UNIVERSIDAD DE CHILE

FACULTAD DE CIENCIA FÍSICAS Y MATEMÁTICAS

DEPARTAMENTO DE GEOLOGÍA

METAL FLUXING IN A LARGE-SCALE INTRA-ARC FAULT SYSTEM: INSIGHTS FROM THE LIQUIÑE-OFQUI FAULT SYSTEM, SOUTHERN CHILE.

TESIS PARA OPTAR AL GRADO DE DOCTOR EN CIENCIAS

MENCIÓN GEOLOGÍA

DANIELE TARDANI

PROFESOR GUÍA:

MARTIN REICH MORALES

MIEMBROS DE LA COMISIÓN:

JOSÉ CEMBRANO PERASSO

DIEGO MORATA CÉSPEDES

LINDA DANIELE

SANTIAGO DE CHILE

2017

RESUMEN DE LA TESIS PARA OPTAR AL GRADO DE:
Doctor en Ciencias, Mención Geología
POR: Daniele Tardani
FECHA: 12/01/2017
PROF. GUÍA: Martin Reich Morales

FLUJO DE METALES EN UN SISTEMA DE FALLA REGIONAL DE INTRA ARCO: NUEVAS PERSPECTIVAS A PARTIR DEL ESTUDIO DE LA FALLA LIQUIÑE-OFQUI, SUR DE CHILE.

La combinación de un análisis estructural a escala regional junto con una extensa base de datos de isótopos de helio, nitrógeno y carbono, composición química y composición de metales traza en manifestaciones volcánicas/geotermales en la parte norte y central de la Zona Volcánica Sur de Chile, revela el rol de las fallas y estructuras en la circulación de fluidos y en el transporte de metales. Las variaciones regionales en la razones isotópicas $^{3}He/^{4}He$, $d^{13}C\text{-}CO_2$ y $d^{15}N$ son consistentes con los datos reportados de $^{87}Sr/^{86}Sr$ en lavas a lo largo del segmento estudiado, los que están fuertemente controlados por la distribución espacial del Sistema de Falla Liquiñe-Ofqui (LOFS), que corresponde a una falla transcurrente de intra-arco, y del Sistema de Fallas Oblicuas al Arco (ALFS), que consiste en un conjunto de fallas transpresivas de rumbo NO. La terminación norte del LOFS muestra las signaturas de $^{3}He/^{4}He$ más primitivas, mientras que en las otras partes de la región las signaturas de isótopos de helio son controladas por la mezcla entre el ^{3}He de derivación mantélica y el ^{4}He de origen cortical, por asimilación magmáticas en la fuente de los fluidos o por contaminación cortical durante la tránsito de los fluidos en la corteza. Ha sido compilada una base de datos de elementos traza (metales base, metales preciosos y metaloides), tomando muestras de fumarolas y aguas termales, donde han sido analizados los isótopos de helio, carbono y nitrógeno. Contrastar las concentraciones de elementos traza con las razones de isótopos de helio ha permitido determinar que los contenidos de metales en fluidos hidrotermales son el resultado de un fuerte control estructural que condiciona la partición selectiva de estos elementos. Las concentraciones más altas de metales base (e.g. Cu, Co, Ni, Pd), provenientes de la lixiviación de la roca caja, se han encontrado en manifestaciones controladas por estructuras NO, mientras que a lo largo del LOFS, las altas vías de permeabilidad permiten el rápido ascenso de metales transportados desde el sistema profundo en fase vapor (e.g. As, Sb, Ge).

El sistema geotermal de alta entalpía Tolhuaca (TGS), ubicado en la parte norte del LOFS se estudió en detalle con el fin de evaluar el desacoplamiento entre Cu y As. Para este fin han sido analizadas una serie de muestras de pirita provenientes de un sondaje de 1km de largo para determinar el contenido de metales traza (e.g. Cu, As, Co, Sb, etc.) y los patrones de zonación de dichos metales dentro de los granos de este sulfuro. Se ha logrado detectar zonaciones en la pirita de la zona de alteración argílica somera, donde bordes ricos en Cu (Co) y núcleos deprimidos en As se alternan con bordes deprimidos en Cu (Co) y núcleos ricos en As. Estos datos de microanálisis se contrastaron con datos químicos de inclusiones fluidas en vetas de cuarzo (altas razones Cu/As) y fluidos del pozo geotermal (bajas razones Cu/As), que muestran una clara correspondencia entre las concentraciones relativas de Cu y As en los fluidos hidrotermales y las zonaciones químicas de la pirita. Estas observaciones proporcionan evidencia directa de captura selectiva de los metales en la pirita como resultado de los cambios en la composición del fluido de formación del mineral, debido probablemente a la separación de un fluido de una sola fase en un vapor de baja densidad y una salmuera más densa, capaz de fraccionar Cu y As.

METAL FLUXING IN A LARGE-SCALE INTRA-ARC FAULT SYSTEM: INSIGHTS FROM THE LIQUIÑE-OFQUI FAULT SYSTEM, SOUTHERN CHILE.

The combination of regional-scale structural analysis and structural background recompilation with a comprehensive dataset of helium, nitrogen and carbon isotope analyses, along with chemical and trace metals composition of volcanic/geothermal manifestations in the northern and central part of Southern Volcanic Zone of Chile unravel the role of faults and structures on fluid circulation and metal transport. The regional variations in $^{3}He/^{4}He$, $d^{13}C–CO_2$ and $d^{15}N$ values are consistent with $^{87}Sr/^{86}Sr$ ratios in lavas reported for the studied segment, which in turn are controlled by the spatial occurrence of the Liquiñe-Ofqui Fault System (LOFS), an intra-arc strike-slip fault and the Arc-oblique Long-lived Basement Fault System (ALFS), a set of transpressive NW-striking faults. The northern ‘‘horsetail” transtensional termination of the LOFS shows uncontaminated MORB-like $^{3}He/^{4}He$ signatures, whereas in the other parts of the region, helium isotope ratios of hydrothermal systems are affected by addition of ^{4}He, derived by magmatic assimilation of country rocks or contamination during the passage of the fluids through the upper crust. The mixing degree is related with the structural features, with the most contaminated values associated with NW-striking faults. A comprehensive dataset of base, precious metals and metalloids have also been compiled, taking samples in exactly the same fumaroles and thermal waters where helium, carbon and nitrogen isotope ratios have been constrained. By contrasting metals concentrations with helium isotope ratios permitted to determine that metals enrichment in hydrothermal fluids is the result of a strong structural control that conditions selective elemental partitioning, enhancing base metals (e.g Cu, Co, Ni, Pd) concentration along oblique, NW-striking ALFS structures by leaching of host rocks, whereas. along the main LOFS, the high vertical permeability pathways allow rapid fluxing of metals transported from the deep seated system by magmatic vapor (e.g., As, Sb, Ge). These contributions furnish new insights towards the knowledge about the impact of tectonics on magmatic degassing, fluid migration and metal flux in active arc settings, and provide a new interpretation that explains the spatial variations of helium, nitrogen and carbon isotopes in thermal fluids in the region and metal partition in different stress regime along a long-lived intra-arc fault system.

The high enthalpy, metal-rich active Tolhuaca Geothermal System (TGS) in the northern part of the LOFS was studied in detail in order to assess the decoupling between Cu and As. Here a set of pyrite samples from a 1km drillhole have been analyzed to determine the trace metals (e.g. Cu, As, Co, Sb, etc.) contents and the zonation patterns of such metals within the mineral grains. Well-developed zonations were detected in pyrite from the shallow argillic alteration zone, where Cu(Co)-rich, As-depleted cores alternate with Cu(Co)-depleted, As-rich rims. These microanalytical data were contrasted with chemical data of fluid inclusion in quartz veins (high Cu/As) and borehole fluids (low Cu/As) reported at the TGS, showing a clear correspondence between Cu and As concentrations in pyrite-forming fluids and chemical zonation in pyrite. These observations provide direct evidence supporting the selective partitioning of metals into pyrite as a result of changes in ore-forming fluid composition, most likely due to separation of a single-phase fluid into a low-density vapor and a denser brine, capable to fractionate Cu and As.

It is the privilege of early youth to live in advance of its days in all the beautiful continuity of hope which knows no pauses and no introspection. One closes behind one the little gate of mere boyishness and enters an enchanted garden. Its very shades glow with promise. Every turn of the path has its seduction. And it isn't because it is an undiscovered country. One knows well enough that all mankind had streamed that way.

It is the charm of universal experience from which one expects an uncommon or personal sensation—a bit of one's own.

One goes on recognizing the landmarks of the predecessors, excited, amused, taking the hard luck and the good luck together—the kicks and the half-pence, as the saying is—the picturesque common lot that holds so many possibilities
for the deserving or perhaps for the lucky.

Joseph Conrad – "The Shadow Line"

To my sister, Bianca.

AGRADECIMIENTOS

Agradezco a mi profesor guía, Martin Reich y a los miembros de mi comisión de tesis, Diego Morata, José Cembrano y Linda Daniele, por haber guiado este trabajo con pasión, paciencia y dedicación. Martin ha sido una excelente guía y tutor muy atento, preocupado tanto de la parte académica, cuanto de lo personal. Diego y José, pródigos de buenos consejos, han sido parte de buenos momentos de discusión durante todo el proceso. Linda ha revisado el trabajo con entusiasmo y competencia, afinando detalles de fundamental importancia.

Quiero agradecer además a Emilie Roulleau, con quien hemos llevado una provechosa relación de trabajo y a Gloria Arancibia por sus revisiones y aportes al Capítulo 2 de la tesis. Agradezco a Yuji Sano y a Naoto Takahata por su extrema disponibilidad y su enseñanzas durante mis dos pasantías en el *Atmosphere and Ocean Research Institute (AORI)* en Japón. Agradezco a Verónica Rodríguez por haber hecho parte de los análisis de agua, por su infinita paciencia y por su extenso adiestramiento de laboratorio. Agradezco a Artur Deditius y Malcolm Roberts por haber realizado los análisis de metales en trazas en pirita y por sus aportes al Capítulo 4 de la tesis.

Esta tesis fue financiada por los proyectos CONICYT FONDAP 15090013 "Centro de Excelencia en Geotermia de los Andes" (CEGA) y FONDECYT 1130030. Financiamientos adicionales provinieron de la Iniciativa Científica Milenio "Trazadores de Metales en Zonas de Subducción" (NC130065), del proyecto FONDECYT de iniciación 11130351 y del *Grant-in-Aid for Science Research* (15H05830) de MEXT, Japón. Agradezco además al proyecto MECESUP0708 por la beca de doctorado.

Un especial agradecimiento va a mis padres y hermana por haberme apoyado en esta búsqueda constante que es la vida y haberme entregado amor, junto con las herramientas para navegar con conciencia en este mar. Agradezco a Manuela por ser mi compañera de viaje y por enriquecer cada día con la maravilla de su amor y sus palabras.

Agradezco a l@s compañer@s de investigación y a aquellos que han participado en este trabajo, compartiendo terrenos y buenas y malas ideas: Pablo, Pame, Schorty, Gerd, Jackie, Vladi, Diego, Claudia, Nicolas, Juan, Carlos, Francisco, Catalina y Valeria.

Un profundo agradecimiento va a los querid@s amig@s de la sala de postgrado, del CEGA y del Milenio, compañeros del día a día y de la cotidiana alegría que acompaña al trabajo. Además quiero dar un agradecimiento especial a Linda-san, Tanaka-san, Ishida-san, Kagoshima-san, Koike-san y Tomonaga-san por su ayuda y su amistad durante mis dos estadías en Japón.

Y por fin, a los querid@s amig@s y compañer@s de la vida, sin los cuales no tendría sentido levantarse y respirar: Pablo, Gabi, Feña, Mauro, Schorty, Clau, Mono, Max, Andrés, Lucho, Poncho, Pame, Rodrigo, Gerd, Pipe, Fran, Skeggia, Cava A, Cava L, Marti, Beppe, Silvia, Cristina, Tommi, Laura, Tommi S., Andrea, Giulia, Sara, Leo, Savo, Daiman, Jappo, Robi, Checco, Gio, Braga, Anto, Marti, Tiziano, Laura, Samu, Totta, Liccia, Riccio, Matte y todos los demás.

TABLE OF CONTENTS

Chapter 1. Introduction

There is a general agreement that fault-related fracture systems, due to its high permeability, play a key role as host structures for geothermal systems and hydrothermal mineralization (Sibson, 1996, 2001; Rowland, 2004; Rowland & Simmons, 2012). There are several examples worldwide where regional-scale fault systems control volcanism and hydrothermal activity, promoting the development of geothermal systems and/or the formation of epithermal Au-Ag deposits (e.g., Taupo Volcanic Zone in New Zealand, and the Cretaceous Atacama Fault System in northern Chile).

However, few studies have focused on determining how regional-scale structures control the composition of hydrothermal fluids from their magmatic source to the shallow geothermal environment (Kennedy et al., 1997; Kennedy and van Soest, 2005; Karlstrom et al., 2013), and how structural meshes influence chemical transport under variable permeability conditions. Such information is of utmost relevance since fluid flow and mineral precipitation play a key role in promoting the development of high enthalpy geothermal reservoirs and hydrothermal ore deposits. Although there is consensus that volcanism and hydrothermal activity are largely controlled by the regional scale tectonic stress field and the architecture of, e.g., a volcanic arc, there is still limited information on how the shallower hydrothermal fluids are connected with the deep magmatic sources, and how metals and volatiles are selectively partitioned.

This thesis aims to unravel the interplay between active regional-scale structures, the circulation of hydrothermal fluids and their link with the parental magmas. In particular, it focuses on disentangling the role of structures on the overall fluxing of metals and volatile species in a subduction-related volcanism setting. To achieve this goal, the main questions addressed here are: (1) How does the structural context affects the helium, nitrogen and carbon isotope signatures in a large-scale, active intra-arc fault system? (2) Does the stress partitioning in a long-lived fault system affect the chemical and isotopic signature of hydrothermal fluids discharged along the fault zone? and (3) Can these processes explain the occurrence of hydrothermal systems endowed with different metals, along a particular segment of the volcanic arc?

In order to answer these relevant questions, it is necessary to unravel if the structural setting exerts a fist-order control on hydrothermal fluid composition by, e.g., conditioning residence times of parental magmas, and influencing the kinetics of magmatic fluid interaction with the host rocks during ascent. The Andean Cordillera of Central-Southern Chile is a perfect natural laboratory to test this hypothesis. In this region, the relationship between tectonics and volcanism is the result of interaction between the crustal structures of the basement and the ongoing regional stress field (Pritchard et al., 2013). As pointed out by several studies, magmatism and volcanism, as well as geothermal activity in the region are spatially associated with tectonic features (e.g. Lara et al., 2006; Cembrano and Lara, 2009; Sánchez et al., 2013). In particular, in the Southern Volcanic Zone (SVZ) between 37° and 46°S, the volcanic and geothermal activity is partially controlled by the ~1000 km long, NNE-striking intra-arc dextral strike-slip Liquiñe-Ofqui Fault System (LOFS), and by the NW-SE Arc-oblique Long-lived Basement Fault System (ALFS). Many geothermal surface manifestations and shallow fumarolic emissions are spatially related to stratovolcanoes and fault segments associated with both fault systems.

In the following pages, I provide a summary of this thesis that includes results of a regional-scale study conducted in the segment of the Southern Volcanic Zone between the 37° and 41°S, and a more local scale study focusing on the Tolhuaca Geothermal System, located in the same segment. The followed approach was multidisciplinary, and involved the integration of

geochemical and isotopic data with updated geological and structural information for the region.

The role of the Liquiñe-Ofqui Fault System (LOFS) and of the Arc-oblique Long-lived Basement Fault System (ALFS) on magma degassing, hydrothermal fluid flow and fluid compositions was studied along a segment of Southern Volcanic Zone (between 37° and 41°S). A combined approach of regional-scale structural analysis of active geothermal areas with isotopic geochemistry of helium, nitrogen and carbon measured in fumaroles and thermal waters allowed to identify that the first order control on helium, carbon and nitrogen isotopes signatures in the region is largely dominated by the degree of crustal assimilation of the magmatic sources, which is in turn controlled by the LOFS and ALFS. The most primitive signatures are related to the NNE-striking LOFS, whereas the isotopic signatures of gases in thermal manifestations along the arc-oblique, NW-striking ALFS, show a higher degree of crustal contamination. Considering the fact that the ALFS inhibit vertical fluid permeability due to its misorientation with respect to the prevailing regional stress field, the $^{3}He/^{4}He$, $\delta^{13}C–CO_2$ and $\delta^{15}N$ data record crustal contributions related to increased fluid/rock interaction and higher residence times.

The compilation of a conceptual model of fluid circulation along the segment was crucial to assess how the different structural orientations of the main and subsidiary faults affect metal transport under variable vertical permeability conditions. A comprehensive dataset of base (Cu, Co, Ni, Mo, Pb, etc.), precious metals (Au, Ag and PGE's) and metalloids (As, Sb, Ge and Te) was obtained from fumaroles and thermal water samples where helium, carbon and nitrogen isotope ratios were also determined. When metal concentrations are contrasted with helium isotope ratios, Has been concluded that despite acid leaching of host rocks plays a relevant role in metal enrichment of the thermal waters (i.e., low, crustal Rc/Ra values correlate with high Ca, Mg, K, Ba, Sr, Co, Ni, Cu, Cd, Rh and Pd), metals such as Mo, W, Ti and Pb and metalloids such as B, As, Sb and Ge are most likely sourced from the deep magmatic system, and transported to the shallow geothermal environment by low density vapors (i.e., high, primitive Rc/Ra values correlate with high. Mo, W, Ti, Pb, As, Sb and Ge). These two different trends of enrichment are the result of a strong structural control that conditions selective elemental partitioning, enhancing water-rock interaction and metal leaching along oblique, NW ALFS structures (e.g Cu, Co, Ni, Pd). In contrast, the high permeability along the main LOFS allows rapid fluxing of metals transported by magmatic vapor (e.g., As, Sb).

These regional-scale studies allow constraining the controls on magma degassing, hydrothermal fluid flow and metal transport in the studied segment. However, it is necessary to explore the effects of chemical partitioning within an active hydrothermal system where anomalous concentrations of metals and metalloids are present. An excellent location to lead such a study is the Tolhuaca Geothermal System (TGS), a young active geothermal system controlled by NW-trending reverse fault, located in the northern termination of the LOFS. Furthermore, the TGS has been drilled down to ~3 km depth, abundant pyrite has been found both in deep propylitic zone and in shallow argillic zone and present-day well fluids carry metals and metalloids including Cu, Au and As among others (Sánchez-Alfaro et al., 2016).

By contrasting the trace element composition and micro-textures of pyrite at the TGS with previously published fluid inclusion and borehole data, has been provided evidences that selective partitioning of metals and metalloids into pyrite is most likely the result of changes in fluid composition. Pyrite from shallow argillic zone present well–developed zonations with Cu(Co)-rich, As-depleted cores, corresponding to Cu-rich, As-depleted paleofluid, whereas the As-rich Cu(Co)-depleted pyrite rims, correspond to the As-rich, Cu-depleted borehole fluids. These changes are most likely related to excursions of single-phased, magmatically derived vapors that

are further separated into a low-density vapor and dense brine capable of selectively scavenging Cu and As. These results are in agreement with how observed at regional scale, where Cu and As decoupling is connected with the different structural direction controlling the hydrothermal fluid of the Southern Volcanic Zone of Chile. Arsenic (i.e. correlated with primitive Rc/Ra) is likely transported by vapor phase up to the surface and associated with NE LOFS structures, permitting high vertical permeability of circulating fluids, whereas Cu (i.e. correlated with lower Rc/Ra ratios) remain confined to the deeper parts of the hydrothermal systems with the dense brine and in shallow thermal springs his enrichment is related with leaching of host rocks along NW ALFS structures, promoting high residence time of fluids in the crust.

Publications and Abstracts resulting from this Dissertation

Publications

Tardani D., Reich M., Roulleau E., Takahata N., Sano Y., Pérez-Flores P., Sánchez-Alfaro P., Cembrano J., Arancibia G.. Exploring the structural controls on helium, nitrogen and carbon isotope signatures in hydrothermal fluids along an intra-arc fault system. *Geochimica et Cosmochimica Acta* v. 184, pp. 193–211. April 2016, **(Chapter 2).**

Tardani D., Reich M., Roulleau E., Sano Y., Takahata N. Large-scale structural controls on metal fluxing in active margins: insights from the Liquiñe-Ofqui intra –arc faults systems, SVZ, Chile. (*in preparation*), **(Chapter 3).**

Tardani D., Reich M., Deditius A., Chryssoulis S., Roberts, M., Sánchez-Alfaro P., Wrage J., Roberts M. Cu-As decoupling in an active geothermal system: a link between pyrite and fluid composition. *Geochimica et Cosmochimica Acta* (*under review*), **(Chapter 4).**

Conference abstracts

Tardani D., Sanchez P., Perez P., Reich M., Tassi F., Capaccioni B., Chiodini G., Vaselli O. Geochemistry of geothermal fluids in the active Liquiñe-Ofqui Fault System (Southern Andes Volcanic Zone, Chile). IAVCEI, Kagoshima, 20-24-June 2013.

Tardani D., Reich M., Roulleau E., Sano Y., Takahata N., Wen H., González-Jiménez J.M., Yang T.F., Sanchez P., Cembrano J., Arancibia G.. Metal fluxing in a large-scale intra-arc fault: insights from the Liquiñe-Ofqui Fault System (LOFS) and associated geothermal fields in southern Chile, AGU Fall Meeting Abstract, San Francisco, December 2014.

Tardani D., Reich M., Roulleau E., Sano Y., Takahata N., Wen H., González-Jiménez J.M., Sanchez P., Cembrano J., Arancibia G.. Metal fluxing in a large-scale intra-arc fault: insights from the Liquiñe-Ofqui Fault System (LOFS) and associated geothermal fields in southern Chile, Goldschmidt, Prague, August 2015.

Tardani D., Reich M., Roulleau E., Takahata N., Sano Y., González J.M., Sánchez P., Cembrano J., Arancibia G.. Metal Fluxing in a Large-Scale Intra-Arc Fault: Insights from the Liquiñe-Ofqui Fault System in Southern Chile. Congreso Geológico Chileno, La Serena (Chile), 4-8 October 2015.

Tardani D., Reich M., Roulleau E., Sano Y., Takahata N., Perez-Flores P., Sanchez-Alfaro P., Cembrano J.M. and Arancibia G. Structural Controls on Helium, Nitrogen and Carbon Isotope Signatures in Geothermal Fluids Along the Liquiñe-Ofqui Fault System, Southern Chile. AGU Fall Meeting Abstract, San Francisco, December 2016.

Reich M., Tardani D., Deditius A., Chryssoulis S., Wrage J. and Sanchez-Alfaro P. Cu-As Decoupling in Hydrothermal Systems: A Link Between Pyrite Chemistry and Fluid Composition. AGU Fall Meeting Abstract, San Francisco, December 2016.

Publications and Abstracts resulting from side-projects

Publications

Reich M., Simon A., Deditius A., Barra F., Chryssoulis S., Lagas G., Tardani D., Knipping J., Bilenker L., Sánchez-Alfaro P., Roberts M.P. and Munizaga R. Trace elements signature of pyrite from the Los Colorados Iron Oxide-Apatite (IOA) deposit, Chile: a missing link between Andean IOA and Iron Oxide Copper-Gold systems? Economic Geology, v. 111, pp. 743–761. January 2016.

Sánchez-Alfaro P., Reich M., Arancibia G., Pérez-Flores P., Cembrano J., Driesner T., Lizama M. Rowland J., Morata D., Heinrich C. A., Tardani D., Campos E. Physical, chemical and mineralogical evolution of the Tolhuaca geothermal system, southern Andes, Chile: insights into the interplay between hydrothermal alteration and brittle deformation. Journal of Volcanology and Geothermal Research v. 324, pp. 88–104. May 2016

Sánchez-Alfaro P., Reich M., Driesner T., Cembrano J., Arancibia G., Pérez-Flores P., Heinrich C. A., Rowland J., Tardani D., Lange D., Campos E. The optimal windows for seismically-enhanced gold precipitation in the epithermal environment. Ore geology review. Ore Geology Reviews v. 79, pp. 463-473. June 2016.

Roulleau E., Tardani D., Sano Y., Takahata N., Vinet N., Berrios C., Bravo F., Muñoz C, Sanchez J. New insight of noble gas and stable isotopes of geothermal/hydrothermal fluids at Caviahue-Copahue Volcanic Complex: boiling steam separation and water-rock interaction at shallow depth. Journal of Volcanology and Geothermal Research 328, 70-83. Oct. 2016.

Roulleau E., Bravo F., Pinti D., Cabusson S., Pizarro M., Tardani D., Muñoz C., Sanchez J., Sano Y., Takahata N., De la Cal F., Esteban C., Morata D. Structural controls on fluid circulation at the Caviahue-Copahue Volcanic Complex (CCVC) geothermal system (Chile-Argentina), revealed by self-potential, soil CO2 and temperature, and helium isotopes. (*in preparation*)

Wrage J., Tardani D., Reich M., Daniele L., Arancibia G., Morata D. Geochemistry of surface waters in the Southern Volcanic Zone, Chile – Implications for structural controls on geothermal fluid development. (*in preparation*).

Conference abstracts

Reich M., Deditius A., Tardani D., Sanchez-Alfaro P. The coupled geochemistry of Au and As in pyrite from ore deposits and geothermal fields: monitoring fluid evolution and external forcing factors in hydrothermal systems. AGU Fall Meeting Abstracts, San Francisco, December 2014.

Reich M., Simon A., Deditius A., Chryssoulis S., Tardani D., Barra F., Knipping J., Bilenker L. & Sanchez-Alfaro P. The Trace Element Signature of Pyrite from the Los Colorados Iron Oxide Apatite (IOA) Deposit: A Missing Link between IOA and IOCG Systems? Goldschmidt, Pragua, August 2015.

Roulleau E., Tardani D., Vinet N., Sano Y., Takahata N., Reich M.. Noble-gas and nitrogen

isotope geochemistry of geothermal fluids from the Caviahue-Copahue volcanic complex in the Southern Andes. Goldschmidt 2015, August 16-21, Prague, Czech Republic.

Vaselli O., Tassi F., Fischer T. Tardani D. Fernandez E., Duarte E., Martinez Cruz M. Seventeen years (1998-2014) of geochemical observations at the Poás volcano (Costa Rica) fumarolic system. Il Pianeta Dinamico: Sviluppi e prospettive a 100 anni da Wegener, At Florence, Italy. September 2015.

Sanchez J., Roulleau E., Tardani D., Sano Y., Takahata N., Esteban C.. Geoquímica e isotópos de He, Sr y Pb en las rocas del Complejo Volcánico Copahue-Caviahue, (Argentina). Congreso Geológico Chileno, La Serena (Chile), 4-8 October 2015

Roulleau E., Bravo F., Barde-Cabusson S., Pizarro M., Muñoz C., Sanchez J., Tardani D., Sano Y., Takahata N., De la Cal F., Esteban C.. The geothermal system of Caviahue-Copahue Volcanic Complex (Chile-Argentina): New insights from self-potential, soil CO_2 degassing, temperature measurements and helium isotopes, with structural and fluid circulation implications. EGU General Assembly 2016, 17-22 April, Vienna Austria, p.2162.

Roulleau E., Tardani D., Bravo F., Pizarro M., Pinti D., Takahata N., Sano Y., Vinet N., Muñoz C., Sanchez J.. The geothermal system of Copahue-Caviahue volcanic complex (Argentina): Relationship between isotopic composition of thermal fluids and fault network. Goldschmidt 2016, 26 June-1 July, Yokohama, Japan.

Chapter 2: Exploring the structural controls on helium, nitrogen and carbon isotope signatures in hydrothermal fluids along an intra-arc fault system.

Abstract

There is a general agreement that fault-fracture meshes exert a primary control on fluid flow in both volcanic/magmatic and geothermal/hydrothermal systems. For example, in geothermal systems and epithermal gold deposits, optimally oriented faults and fractures play a key role in promoting fluid flow through high vertical permeability pathways. In the Southern Volcanic Zone (SVZ) of the Chilean Andes, both volcanism and hydrothermal activity are strongly controlled by the Liquiñe-Ofqui Fault System (LOFS), an intra-arc, strike-slip fault, and by the Arc-oblique Long-lived Basement Fault System (ALFS), a set of transpressive NW-striking faults. However, the role that principal and subsidiary fault systems exert on magma degassing, hydrothermal fluid flow and fluid compositions remains poorly constrained. In this study we report new helium, carbon and nitrogen isotope data ($^3He/^4He$, $\delta^{13}C\text{-}CO_2$ and $\delta^{15}N$) of a suite of fumarole and hot spring gas samples from 23 volcanic/geothermal localities that are spatially associated with either the LOFS or the ALFS in the central part of the SVZ. The dataset is characterized by a wide range of $^3He/^4He$ ratios (3.39 Ra to 7.53 Ra, where $Ra=(^3He/^4He)_{air}$), $\delta^{13}C\text{-}CO_2$ values (−7.44‰ to −49.41‰) and $\delta^{15}N$ values (0.02‰ to 4.93‰). The regional variations in $^3He/^4He$, $\delta^{13}C\text{-}CO_2$ and $\delta^{15}N$ values are remarkably consistent with those reported for $^{87}Sr/^{86}Sr$ in lavas along the studied segment, which are strongly controlled by the regional spatial distribution of faults. Two fumaroles gas samples associated with the northern "horsetail" transtensional termination of the LOFS are the only datapoints showing uncontaminated MORB-like $^3He/^4He$ signatures. In contrast, the dominant mechanism controlling helium isotope ratios of hydrothermal systems towards the south appears to be the mixing between mantle-derived helium and a radiogenic component derived from, e.g., magmatic assimilation of ^4He-rich country rocks or contamination during the passage of the fluids through the upper crust. The degree of ^4He contamination is strictly related with the faults controlling the occurrence of volcanic and geothermal systems, with the most contaminated values associated with NW-striking structures. This is confirmed by $\delta^{15}N$ values that show increased mixing with crustal sediments and meteoric waters along NW faults (AFLS), while $\delta^{13}C\text{-}CO_2$ data are indicative of cooling and mixing driving calcite precipitation due to increased residence times along such structures. Our results show that the structural setting of the region exerts a fist-order control on hydrothermal fluid composition by conditioning residence times of magmas and thus promoting cooling/mixing of magmatic vapor, and therefore, must be taken into consideration for further geochemical interpretations.

Introduction

In arc settings, helium isotopes have been successfully used, coupled with stable isotopes of carbon and nitrogen data, to constrain mantle heterogeneities and mechanisms of volatile recycling (Sano and Marty, 1995; Sano and Williams, 1996; Fischer et al., 1998, 2002; Sano et al., 2001). Subduction zones represent one of the preferential escape routes for primordial ^3He from the mantle, and previous studies have emphasized the role of the mantle wedge in dominating the helium budget in the great majority of cases (Hilton et al., 2002). Furthermore, it has been shown that participation of other contributors to the arc volatile inventory – i.e., the subducting slab and/or arc crust - can be traced using the isotopic composition of noble gases such as $^3He/^4He$ ratios and stable isotopes of carbon and nitrogen (Sano and Marty, 1995; Sano and Williams, 1996, Fischer

et al., 1998, 2002; Sano et al., 2001). Such studies have proved critical to constrain the relative mantle vs. subducted sediment contributions on the isotopic signature of hydrothermal fluids, as well as the degree of contamination by upper crustal rocks. Despite these significant advances, very few studies have focused on deconvolving the regional scale structural and tectonic controls affecting the composition of deep-seated fluids during the separation from the magmatic source and the passage through the crust (Kennedy et al., 1997, Kennedy and van Soest, 2005, Karlstrom et al., 2013). In particular, the local scale control of interconnected faults and associated fractures (fault-fracture meshes; Sibson, 1996) on fluid flow in geothermal and hydrothermal systems has been largely studied over the past twenty years (Sibson, 1994; Sibson, 1996; Manning and Ingebritsen, 1999; Sibson and Rowland, 2003; Fairley and Hinds, 2004; Micklethwaite and Cox, 2004; Rowland and Sibson, 2004; Blenkinsop, 2008; Graf and Thierrien, 2009; Micklethwaite et al., 2010; Baker et al., 2010; Faulkner et al., 2010; Cox, 2010; Gudmundsson et al., 2010; Rowland and Simmons, 2012). These studies have improved our understanding about the structural factors controlling fluid flow, and have provided crucial information to refine conceptual models of the local fault-fracture hydraulic architecture in geothermal and hydrothermal systems.

The goal of this study is to unravel the regional scale structural controls on the isotopic composition of subduction-related magmatic gas, from its source to their pathway toward the surface. Our aim is to assess the nature of the link among fault-fracture meshes, magmatic degassing, crustal assimilation and fluid mixing processes taking place in the upper crust, that affect the composition of hydrothermal fluids discharged along principal and subsidiary structures of a regional scale, intra-arc strike slip fault. Considering the fact that tectonic activity defines the nature, geometry and kinematics of fault-fracture networks, a better understanding of the structural pattern and its link with the chemical evolution of fluids may give significant insights into the processes governing the dynamics of hydrothermal systems associated with such large-scale crustal structures.

The Andean Cordillera of Central-Southern Chile is a perfect natural laboratory to test this hypothesis. In this region, the relationship between tectonics and volcanism is the result of interaction between the crustal structures of the basement and the ongoing regional stress field (Pritchard et al., 2013). As pointed out by several studies, magmatism and volcanism, as well as geothermal activity in the region are spatially associated with tectonic features (Hildreth, 1988; Lopez-Escobar, 1995; Hauser, 1997; Pérez, 1999; Sepúlveda et al., 2004; Lara, 2006; Cembrano & Lara, 2009; Alam et al., 2010; Lahsen et al., 2010; Sánchez et al., 2013). In particular, in the Southern Volcanic Zone (SVZ) between 37° and 46°S, the volcanic and geothermal activity is partially controlled by the ~1000 km long, NNE-striking intra-arc dextral strike-slip Liquiñe-Ofqui Fault System (LOFS), and by the NW-SE Arc-oblique Long-lived Basement Fault System (ALFS). Many geothermal surface manifestations and shallow fumarolic emissions are spatially related to stratovolcanoes and fault segments associated with both fault systems (Fig. 2.1).

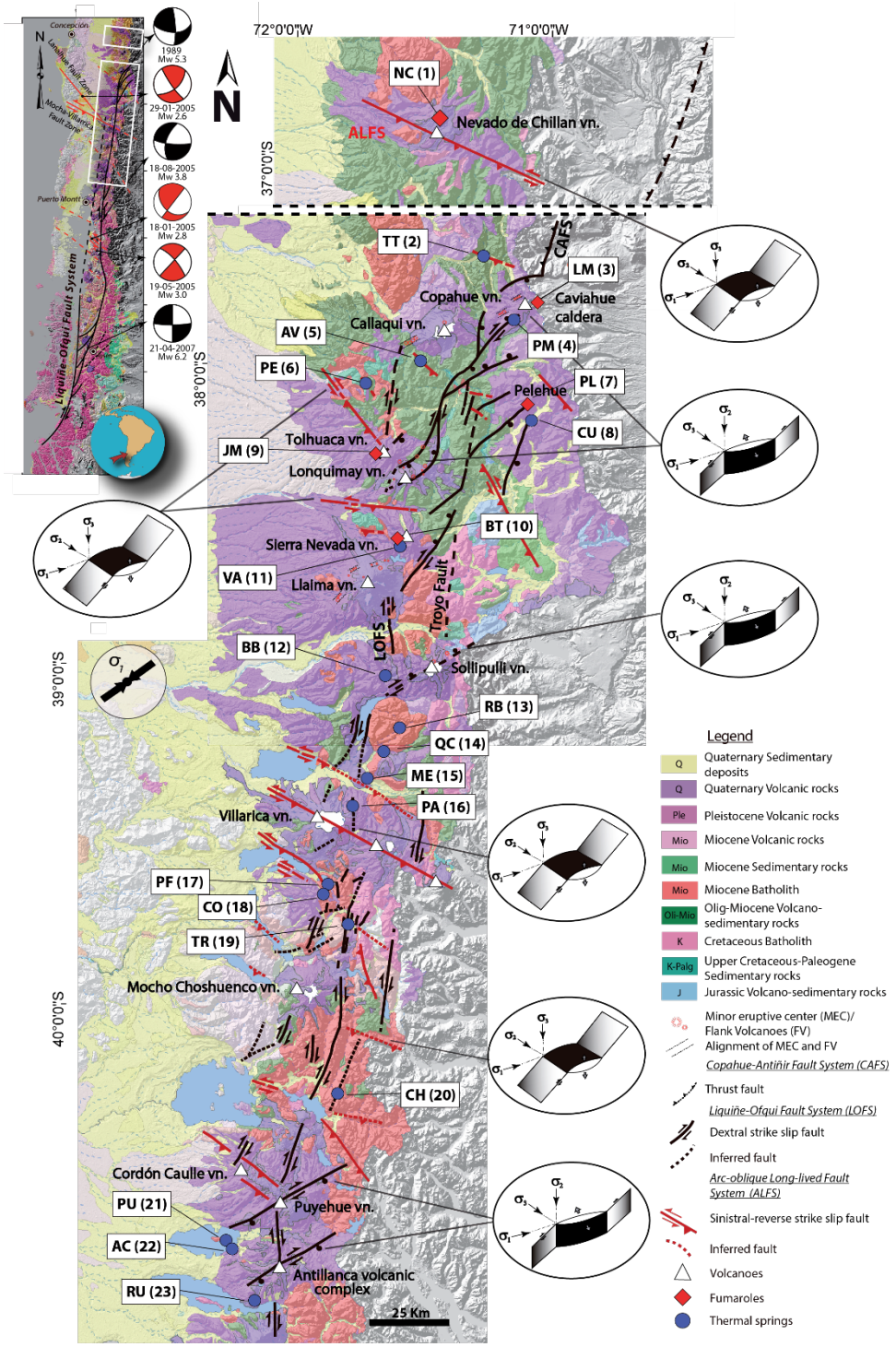

Figure 2.1. *Geologic and structural map of the central part the Southern Volcanic Zone (SVZ) in southern Chile. Solid and dashed lines represent main and secondary faults from Potent (2003), Melnick et al. (2006), Lara et al. (2006), Cembrano & Lara (2009), Sánchez et al. (2013) and Pérez-Flores et al. (2014). Blue circles and red diamonds represent the location of thermal springs and fumaroles samples, respectively. White triangles represent the main stratovolcanoes of the region. Sigma 1 (σ1) represent the maximum regional stress field. CAFS: Copahue-Antiñir Fault System, LOFS: Liquiñe-Ofqui Fault System, ALFS: Arc-oblique Long-lived Fault System. Stress fields for the distinct fault segments are modified from Sánchez et al. (2013) and Pérez-Flores et al. (2014).*

Previous geochemical surveys conducted in this region have recognized a wide range of $^{3}He/^{4}He$ ratios in volcanic/geothermal fluids, suggesting mixing between mantle helium and the radiogenic helium sourced from country rocks (Hilton et al., 1993; Ray et al., 2009, Dobson et al., 2013). However, these studies have focused either on orogen-scale controls on noble gas compositions, or have addressed the local structural controls in individual geothermal systems (Sepúlveda et al., 2007; Agusto et al., 2013). In this study we present a comprehensive dataset of helium, nitrogen and carbon isotope analyses from a suite of about 20 volcanic fumaroles and thermal springs between the 37° and 41°S. The gas samples were collected from fumaroles in active volcanic systems and thermal springs that are closely spatially associated with both the LOFS and the ALFS. Based on new and unpublished mapped structures and as a up-to-date structural background in the region (Potent, 2003; Melnick et al., 2006; Lara et al., 2006; Cembrano & Lara, 2009; Pérez-Flores et al., 2014), we highlight the role of LOFS and ALFS on fluid circulation and provide a new interpretation that explains the spatial variations of helium, nitrogen and carbon isotopes in thermal fluids in the Central Southern Volcanic Zone of Chile.

Geological and structural setting

The Southern Volcanic Zone (SVZ) of south-central Chile lies between 33°S and 46°S (Fig. 2.1). Along with the Central Volcanic Zone (CVZ, 14ºS-28ºS) and the Austral Volcanic Zone (AVZ, 49°S-55°S), it constitutes a three-segment active arc that comprises the Chilean Andes (Parada et al., 2007; Stern et al., 2007).

The Andean region examined in this study is about 450 km-long (37°-41°S), and forms part of the central and southern segments of the Southern Volcanic Zone (SVZ) (Fig. 2.1). In this region, the current geodynamic setting is characterized by slightly oblique convergence between the Nazca and South American plates at a rate of ca. 7–9 cm/year that has prevailed for the last 20 Ma (Angermann et al., 1999; Somoza and Ghidella, 2005). The basement of the volcanic arc, in the northern portion of this segment at 39°S, is made up of extensive outcrops of the Meso–Cenozoic volcano–sedimentary rocks of the Cura Mallin and Cola de Zorro formations, which are locally intruded by Mio–Pliocene plutons (Charrier et al., 2002). South of 39°S, recent volcanic edifices are built directly onto Meso–Cenozoic plutonic rocks of the Patagonian Batholith. Crustal thickness underneath the volcanic arc decreases from 50 km at 33°S to 35 km at 46°S, with an accompanying decrease in the average altitude of the main cordillera, from 5000 m to less than 2000 m (Tassara and Yáñez, 2003).

The structural setting of the studied segment in Figure 2.1 is dominated by the Liquiñe-Ofqui Fault System (LOFS), a NNE-striking, intra-arc transpressional dextral strike-slip fault system that extends between 37°S and 46°S, and associated with ENE-striking second-order intra-arc anisotropies (Cembrano et al. 1996, 2000; Folguera et al. 2002; Adriasola et al. 2006; Rosenau et al. 2006). The ENE-striking structures have been recognized as extensional fractures most likely formed under relatively low differential stress (Lavenu and Cembrano 1999; Cembrano and Lara 2009). Conversely, the arc oblique WNW-striking long-lived basement fault system (ALFS) is severely misoriented with respect to the prevailing stress field, and has been interpreted as crustal weaknesses associated with pre-Andean faults reactivated as sinistral-reverse strike–slip faults during the development of the arc (Cembrano and Moreno 1994; López-Escobar et al. 1995; Lara et al. 2006; Melnick et al. 2006; Rosenau et al. 2006; Glodny et al. 2008; Lange et al. 2008).

The volcanism in the segment is represented by stratovolcanoes and monogenetic cones, many of which are spatially associated with the LOFS or ALFS. Their composition is mainly basaltic-andesitic with minor dacitic-rhyolitic occurrences. The stratovolcanoes and/or

monogenetic cones exhibit mostly primitive magmatic signatures, and are related to secondary structures forming NE-trending volcanic alignments which are directly related to the current dextral transpressional tectonic regime (Lara et al. 2006; Cembrano and Lara 2009). In contrast, the volcanic activity spatially related to the ALFS comprises WNW-trending volcanic alignments, where mostly stratovolcanoes occur. These include a wide range of compositions, with some centers having erupted only rhyolitic products in historical times. Because of their misorientation with respect to the prevailing stress field, the WNW-striking faults require supralithostatic magmatic pressures to become active (see Lara et al., 2004, 2006; Cembrano and Lara 2009).

The northern segment of the LOFS (37.5-39 °S) is characterized by transtensional deformation and shows an accommodation zone individuated by fault splays and graben formation. At 37.5 °S, the interaction of the Liquiñe-Ofqui fault and the Copahue-Antiñir fault results in a NE-striking transitional zone (Melnick et al., 2006). At 38°S, the N–S to NNE-striking LOFS bends eastward and decomposes into a series of NE-striking extensional and transtensional fault splays that form an arrangement characterized by a "horsetail"-like geometry (Potent and Reuther, 2001; Rosenau et al., 2006). These types of structures have long been recognized to play a key role as host structures and high-permeability flow paths for geothermal systems and hydrothermal mineralization (Sibson, 1994; Sibson, 1996; Rowland & Sibson, 2004; Rowland & Simmons, 2012).

Sampling and analytical techniques

Gas samples were collected from fumaroles in active volcanic systems, water samples were taken from bubbling hot springs and thermal water springs in geothermal areas. Fumarole gases were sampled using a titanium tube, inserted into the fumarole or vent, and connected to a condenser and a water separator, to force water condensation. The dry gas obtained was collected in pre-evacuated alkaline glass containers with vacuum valves at both ends. Water and bubbling gas from hot springs were sampled in double valve, pre-evacuated alkaline glass containers, using pure silicone tubes connected to an inverted funnel and a manual pump. Dissolved gases from thermal water samples were extracted using a glass bottle under vacuum in the extraction line. Both methods for volcanic gases and water spring/bubbling gases are exhaustively described in Sano and Fischer (2013).

The $^{3}He/^{4}He$ ratios were measured using a noble gas mass spectrometer (Helix-SFT) at the Atmosphere and Ocean Research Institute (AORI), University of Tokyo, Japan. The $^{4}He/^{20}Ne$ ratios were measured using a quadrupole mass spectrometer. Helium and neon were separated using a cryogenic trap operated at 40 K (see Sano and Wakita, 1988). The measured $^{3}He/^{4}He$ ratios were calibrated against atmospheric helium. Experimental errors of $^{4}He/^{20}Ne$ and $^{3}He/^{4}He$ ratios are about 0.5% and 1% at 1σ, respectively (Sano et al., 2008). Assuming that the Air Saturated Water (ASW) neon content is significantly higher than in mantle and crustal gases, the R/Ra can be corrected for the presence of atmospheric helium using the $^{4}He/^{20}Ne$ ratio of the sample (Craig et al., 1978). The error calculation for air corrected helium was performed using the procedure described in Sano et al. (2006).

The $\delta^{13}C$ and $\delta^{15}N$ values of gas samples were measured using a conventional gas source mass spectrometer (IsoPrim100, Isoprime Ltd.) at AORI. All values were corrected for blanks that represent 0.2% of the measurement contribution (Barry et al., 2012). The error of the delta values is the propagated error of the isotopic measurement of N and C in the sample, the standard and the blank, assumed at 1σ. The carbon isotopic composition was measured in CO_2 and CH_4 gaseous

component and is expressed in delta notation as:

$$\delta^{13}C = \left(\left[{}^{13}C/{}^{12}C \right]_{sample} / \left[{}^{13}C/{}^{12}C \right]_{STD} - 1 \right) \times 1000$$

The nitrogen isotopic composition is given by:

$$\delta^{15}N = \left(\left[{}^{15}N/{}^{14}N \right]_{sample} / \left[{}^{15}N/{}^{14}N \right]_{air} - 1 \right) \times 1000$$

The chemical composition (He, CH_4, N_2, O_2, Ar, H_2S and CO_2) of sampled gases was measured using a quadrupole mass spectrometer at AORI, by comparing peak heights of the sample with those of standard gases. Experimental errors were estimated to be about ±10% by repeated measurements of standard samples. The blank for each component was significantly lower compared to the sample signals.

Results

Table 1 and Table 2 present the chemical composition and isotopic data (R/Ra, $^4He/^{20}Ne$, air-corrected $^3He/^4He$ (Rc/Ra) ratios, $\delta^{15}N$, $\delta^{15}N_C$, $\delta^{13}C–CO_2$ and $\delta^{13}C–CH_4$ values) of gas samples from 23 volcanic/geothermal localities, including 5 fumaroles, 7 bubbling gas and 11 hot springs (water-dissolved gas). In the tables, samples are sorted in latitudinal order and labeled with a sample name and with an ID label, from 1 to 23, from north to south. Furthermore, and for the sake of simplicity, we will refer to samples as fumarole gas and hot spring gas samples. Figure 2.1 shows sample locations and their association with the main structural features of the LOFS and ALFS.

Table 2.1. *chemical composition of SVZ fumarole, bubbling gas and water-dissolved gas samples.*

Sample ID	Sample Name	Location	Latitude S	Longitude O	Sample Type	Temperature °C	He ppm	CH_4	N_2	O_2	Ar	H_2S	CO_2	N_2/He x10^5	N_2/O_2	N_2/Ar	He/Ar
1	NC	Nevado de Chillan Vn.	36° 54.317'	71° 24.085'	F	91.0	8.62	0.09%	11.68%	2.25%	0.14%	12.86%	72.99%	0.14	5.19	82.41	0.01
2	TT	Trapa Trapa	37° 41.971'	71° 17.098'	WD	45.0	89.10	57.10%	42.03%	n.d.	0.56%	n.d.	0.33%	0.05	-	75.44	0.02
3	LM	Las Maquinas (Copahue Vn.)	37° 50.036'	71° 5.055'	F	93.0	10.85	2.80%	2.70%	0.03%	0.00%	0.44%	94.03%	0.02	105.24	544.73	0.22
4	PM	Pucon Mahuida	37° 53.811'	71° 10.536'	WD	47.0	1.99	0.01%	0.67%	0.04%	0.01%	0.01%	99.27%	0.03	16.00	89.79	0.03
5	AV	Termas del Avellano	37° 59.378'	71° 31.938'	BG	65.3	240.60	0.16%	90.42%	8.43%	0.89%	n.d.	0.08%	0.04	10.73	102.17	0.03
6	PE	Termas de Pemehue	38° 4.579'	71° 42.082'	WD	38.5	88.80	1.38%	73.24%	0.42%	0.32%	0.46%	24.17%	0.08	174.01	231.40	0.03
7	PL	Pelehue	38° 7.367'	71° 3.486'	F	93.4	53.52	0.05%	4.11%	0.08%	0.05%	7.71%	87.98%	0.01	51.80	90.58	0.12
8	CU	Termas de Coyuco	38° 11.422'	71° 2.182'	WD	36.0	1.02	0.18%	2.40%	n.d.	0.06%	n.d.	97.35%	0.24	-	38.73	0.00
9	JM	Jaime Muro (Tolhuaca Vn.)	38° 17.409'	71° 40.057'	F	92.0	8.17	0.03%	3.60%	0.04%	0.01%	1.10%	95.22%	0.04	89.41	430.38	0.10
10	BT	Baños del Toro (Sierra Nevada Vn.)	38° 34.487'	71° 36.951'	F	87.0	15.40	0.02%	8.74%	0.02%	0.05%	4.74%	86.42%	0.06	560.17	180.00	0.03
11	VA	Agua de la Vaca	38° 34.809'	71° 37.685'	BG	35.0	29.02	0.08%	93.65%	3.99%	1.32%	n.d.	0.96%	0.32	23.47	70.96	0.00
12	BB	Termas de Balboa	38° 57.628'	71° 42.627'	BG	45.0	6.02	0.03%	32.24%	4.84%	0.44%	n.d.	62.54%	0.54	6.67	73.41	0.00
13	RB	Termas de Rio Blanco	39° 06.468'	71° 36.820'	WD	47.0	96.08	0.08%	20.10%	5.22%	0.46%	n.d.	74.24%	0.02	3.85	43.80	0.02
14	QC	Termas Quimey-Có	39° 13.168'	71° 41.750'	BG	45.0	37.80	0.09%	95.05%	3.54%	1.27%	n.d.	0.04%	0.20	26.81	74.98	0.00
15	ME	Parque Termal Menetùe	39° 19.527'	71° 43.113'	WD	42.0	261.33	0.05%	44.11%	1.39%	1.12%	n.d.	53.45%	0.02	31.74	39.40	0.02
16	PA	Termas de Palguin	39° 25.343'	71° 47.145'	BG	50.0	51.10	8.47%	89.89%	0.23%	1.22%	n.d.	0.19%	0.15	398.94	73.69	0.01
17	PF	Eco Termas Pellaifa	39° 38.030'	71° 55.208'	WD	50.0	48.29	0.01%	9.96%	1.11%	0.25%	n.d.	88.57%	0.02	8.95	40.42	0.02
18	CO	Termas de Coñaripe	39° 38.097'	71° 55.437'	WD	74.6	36.09	2.16%	66.82%	1.47%	1.37%	n.d.	28.42%	0.19	45.35	48.68	0.00
19	TR	Termas de Trafipan	39° 44.175'	71° 51.651'	WD	37.2	45.09	0.09%	96.74%	n.d.	1.44%	n.d.	1.78%	0.21	-	67.23	0.00
20	CH	Termas de Chihuio	40° 11.407'	71° 55.954'	WD	82.5	49.28	0.09%	96.23%	1.64%	1.70%	n.d.	0.34%	0.20	58.51	56.72	0.00
21	PU	Termas de Puyehue	40° 42.645'	72° 19.403'	WD	60.0	21.92	0.12%	78.32%	14.99%	1.37%	n.d.	5.21%	0.03	5.22	56.98	0.00
22	AC	Termas de Aguas Calientes	40° 43.918'	72° 18.357'	BG	66.0	166.60	0.13%	96.62%	1.37%	1.43%	n.d.	0.43%	0.05	70.30	67.44	0.01
23	RU	Termas de Rupanco	40° 51.386'	72° 13.459'	BG	80.0	11.75	1.28%	79.10%	18.65%	0.90%	n.d.	0.07%	0.67	4.24	87.67	0.00

Note. *F fumarole gas; WD water-dissolved gas; BG bubbling pool gas*

Table 2.2. *Isotopic composition of SVZ fumarole, bubbling gas and water-dissolved gas samples.*

Sample ID	Sample Name	Location	$^4He/^{20}Ne$	$^{20}Ne/^4He$	$^3He/^4He^a$	±	$^3He/^4He^b$	±	$CO_2/^4He$	$CO_2/^3He$	$\delta^{15}N$	±	$\delta^{15}N_C$	±	$\delta^{13}C$ (CO_2)	±	$\delta^{13}C$ (CH_4)	±
					Ra		Rc/Ra		$x10^4$	$x10^9$								
1	NC	Nevado de Chillan Vn.	3.05	0.33	3.40	0.07	3.68	0.10	8.47	17.78	0.37	0.20	5.56	0.20	-9.30	0.14	n.a.	-
2	TT	Trapa Trapa	48.77	0.02	4.38	0.09	4.40	0.00	0.00	0.01	2.89	0.21	6.34	0.21	-25.52	0.27	-44.08	0.27
3	LM	Las Maquinas (Copahue Vn.)	67.55	0.01	7.48	0.15	7.52	0.01	8.67	8.27	4.93	0.20	6.16	0.20	-7.96	0.14	-34.38	0.14
4	PM	Pucon Mahuida	27.58	0.04	6.16	0.12	6.23	0.02	49.91	57.83	4.42	0.21	6.28	0.21	-11.87	0.14	n.a.	-
5	AV	Termas del Avellano	21.32	0.05	4.41	0.09	4.46	0.00	0.00	0.00	1.74	0.20	5.56	0.20	-20.40	0.30	n.a.	-
6	PE	Termas de Pemehue	55.52	0.02	4.69	0.10	4.71	0.01	0.27	0.41	3.35	0.20	6.64	0.20	-25.80	0.20	n.a.	-
7	PL	Pelehue	15.70	0.06	7.53	0.15	7.67	0.10	1.64	1.56	1.03	0.20	1.60	0.20	-7.44	0.14	n.a.	-
8	CU	Termas de Coyuco	2.24	0.45	5.89	0.13	6.69	0.10	95.62	116.01	n.a.	-	-	-	-7.75	0.27	n.a.	-
9	JM	Jaime Muro (Tolhuaca Vn.)	16.07	0.06	6.38	0.13	6.49	0.05	11.65	13.04	3.92	0.20	6.52	0.20	-9.75	0.14	n.a.	-
10	BT	Baños del Toro (Sierra Nevada Vn.)	51.34	0.02	4.59	0.09	4.61	0.01	5.61	8.73	2.69	0.20	6.40	0.20	-8.79	0.14	-31.44	1.10
11	VA	Agua de la Vaca	2.49	0.40	3.91	0.08	4.33	0.01	0.03	0.06	0.26	0.22	5.68	0.22	-13.72	0.27	n.a.	-
12	BB	Termas de Balboa	5.22	0.19	6.34	0.06	6.75	0.03	10.39	11.71	n.a.	-	-	-	-19.18	0.28	n.a.	-
13	RB	Termas de Rio Blanco	1.57	0.64	3.56	0.00	4.36	0.04	0.77	1.55	n.a.	-	-	-	-17.00	0.30	n.a.	-
14	QC	Termas Quimey-Có	2.66	0.38	4.67	0.05	5.27	0.03	0.00	0.00	0.02	0.20	-	-	-30.72	0.30	n.a.	-
15	ME	Parque Termal Menetùe	4.47	0.22	5.05	0.01	5.42	0.01	0.20	0.29	n.a.	-	-	-	-27.36	0.53	n.a.	-
16	PA	Termas de Palguin	4.17	0.24	3.58	0.07	3.79	0.00	0.00	0.01	0.10	0.20	-	-	-49.41	0.28	-66.70	0.28
17	PF	Eco Termas Pellaifa	1.28	0.78	3.39	0.04	4.38	0.06	1.83	3.86	n.a.	-	-	-	-23.89	0.36	n.a.	-
18	CO	Termas de Coñaripe	1.73	0.58	3.69	0.10	4.29	0.03	0.79	1.53	0.52	0.23	5.80	0.23	-20.05	0.28	n.a.	-
19	TR	Termas de Trafipan	2.70	0.37	4.43	0.09	4.89	0.02	0.04	0.06	0.24	0.23	5.44	0.23	-23.67	0.58	n.a.	-
20	CH	Termas de Chihuio	3.36	0.30	4.08	0.08	4.40	0.01	0.01	0.01	0.09	0.20	-	-	-23.04	0.36	n.a.	-
21	PU	Termas de Puyehue	1.37	0.73	4.89	0.11	6.07	0.17	0.24	0.34	n.a.	-	-	-	-22.64	0.30	n.a.	-
22	AC	Termas de Aguas Calientes	14.15	0.07	6.77	0.14	6.91	0.01	0.00	0.00	1.32	0.20	5.56	0.20	-20.49	0.27	n.a.	-
23	RU	Termas de Rupanco	4.20	0.24	6.52	0.13	6.97	0.04	0.01	0.01	n.a.	-	-	-	-14.70	0.27	n.a.	-

Note. *$CO_2/^3He$ is calculated from CO_2/He and $^3He/^4He$ ratios. Error for $^4He/^{20}Ne$ is 5%.*

a: $^3He/^4He$ (Ra) ratios are calculated using $^3He/^4He$ of air ($1.40 \times 10{-}6$ ccSTP/g).

b: $^3He/^4He$ (Rc/Ra) is the denomination for corrected $^3He/^4He$ from $^4He/^{20}Ne$.

Gas composition

All five fumarole gas samples are dominated by CO_2, representing at least the 80% of the total gas in each sample. For the hot spring gas, the samples AV (5), PE (6), VA (11), QC (14), PA (16), CO (18), TR (19), CH (20), AC (22) and RU (23) are dominated by N_2, while the others are dominated by CO_2, with the exception of the CH_4-dominated TT (2) sample. Methane was also detected in all other samples, with six of them showing concentrations that are higher than 1%. The reduced sulfur compound H_2S was detected in seven samples. The five fumarole gas samples present the highest H_2S concentrations, while PE (6) and PM (4) are the only two hot spring gas where H_2S concentrations are detectable.

The majority of fumarole and hot spring gas samples have O_2 contents lower than 5%, with the exception of four samples (AV (5), RB (13), PU (21) and RU (23)). Three of these samples (RB (13), PU (21) and RU (23)) have N_2/O_2 close to the air ratio, of 3.73, suggesting a significant atmospheric contamination. In contrast, the helium isotope composition was not strongly affected by atmospheric helium in these three samples, suggesting that the contamination has probably happened during analysis. The $^4He/^{20}Ne$ ratios are 1.57, 1.37 and 4.20 respectively, at least four times higher than the air ratio (0.33).

In Figure 2.2, the inert (He and Ar) and nearly inert (N_2) gas compositions are plotted in a ternary diagram, and used as a source indicator for the origin of volatile components (after Giggenbach and Goguel, 1989; Giggenbach, 1992; Giggenbach and Poreda, 1993). The N_2/Ar ratio of the samples varies between 38.73 and 544.73. All samples, with the exception of sample PL (7), roughly fit a mixing trend between arc-derived fluids ("Arc-type sediments") and a second end-member comprised between the atmospheric value ("Air") and the Air-Saturated Water value ("ASW"). The presence of atmospheric gases in the mixture is visible in Figure 2.2, and is consistent with previously published data by Ray et al. (2009) for the region. Fumarolic outlier gas sample PL (7), instead, shows a mantle-fluid affinity with atmospheric (air) contribution.

The $CO_2/^3He$ ratios were calculated from CO_2/He and $^3He/^4He$ ratios for each sample. The $CO_2/^3He$ ratios for water-dissolved gases and bubbling gases cover an exceptionally wide range between 116.01×10^9 (CU (8)) and 5.08×10^5 (AV (5)) (Fig. 2.3). More than half of the samples show $CO_2/^3He$ ratios lower than MORB ($2.0\pm1.0\times10^9$; Marty and Jambon, 1987) and global arc-like values ($1.5\pm1.1 \times 10^{10}$; e.g. Sano and Williams, 1996), in agreement with previous data for the region (e.g., Ray et al., 2009). All fumarolic gas samples range from 17.78×10^9 (NC (1)) to 1.56×10^9 (PL (7)), and are included in the global arc average field (with the exception of sample PL (7) plotting in the MORB field). The hot spring samples PM (4) (57.83×10^9) and CU (8) (116.01×10^9) are the only ones exceeding the global arc average value.

He, N and C isotope composition

The helium, carbon and nitrogen isotope compositions of thermal manifestations along the SVZ of south-central Chile are highly variable and are not directly correlated with their distance from stratovolcanoes. In contrast, as shown in Figure 2.4, the helium, carbon and nitrogen isotopic ratios show remarkably similar latitudinal tendencies, analogous to the trend of $^{87}Sr/^{86}Sr$ ratios in lavas of principal stratovolcanoes in the segment. Along-arc variations in strontium isotope composition of volcanic rocks are indicative of variable degrees of crustal contamination, most likely due to intracrustal assimilation (Hickey-Vargas et al., 1989; Hildreth and Moorbath, 1988), and/or source region contamination by subducted continental components (Stern, 1991; Kay et al., 2005). The observed variations in helium, carbon and nitrogen isotopes along the studied segment

do not seem to correlate with crustal thickness (Moho depth is represented by the red line in Figure 2.4), but rather with the regional distribution of NE- and NW-striking faults (Figs. 2.1 and 2.4). This observation is in agreement with the fact that these structures play a first order control on the migration and storage of magmas along the SVZ, as studied by Lara et al. (2006) and Cembrano and Lara (2009).

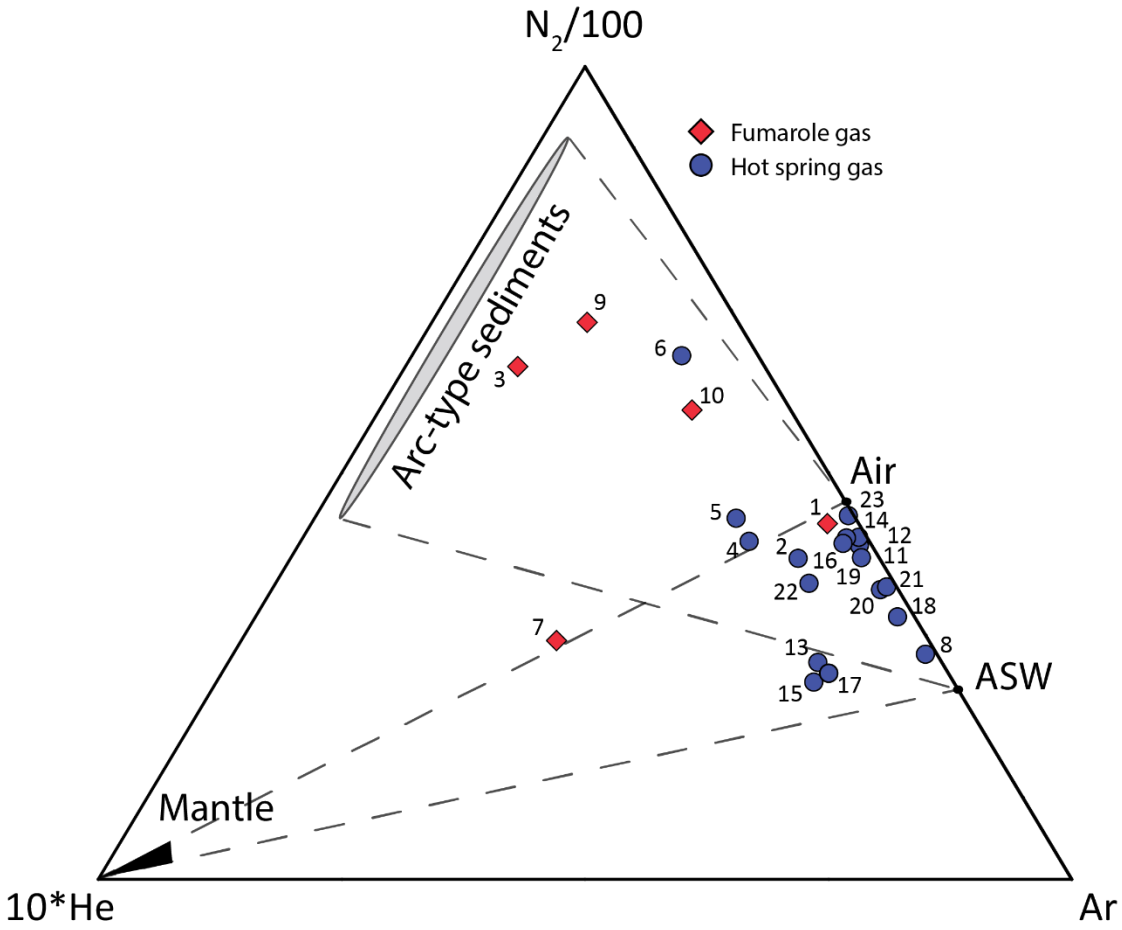

Figure 2.2. *Ternary plot of the relative N2, He and Ar contents of SVZ fumaroles (red diamond) and hot spring (blue circles) gas samples. The end-member components, i.e., mantle, arc-type, air and Air Saturated Water (ASW) are shown for comparison.*

$^{3}He/^{4}He$ ratios

The air-corrected $^{3}He/^{4}He$ ratios (Rc/Ra), given as multiples of the present-day atmospheric ratio ($Ra=1.382 \times 10^{-6}$; Sano et al., 2013; Mabry et al., 2013), range from 3.68 Ra to 7.67 Ra (Table 2). The northern part of the studied segment (~37.5-38.5ºS) shows the widest range of Rc/Ra values, (Fig. 2.4). The highest values were found in two fumarolic gas samples (LM (3) and PL (7)) associated with the transtensional "horsetail" structure in the northern part of the LOFS. High ratios were also found, from north to south, in two bubbling gas samples (PM (4) and CU (8)), in a fumarolic gas sample from the Tolhuaca volcano (JM (9)), and in the bubbling gas sample BB (12), associated with the Sollipulli volcano. Rc/Ra values are also high in the southern part of the studied area, where three hot spring gas samples (PU (21), AC (22) and RU (23)), close to Puyehue-

Cordon Caulle and Casablanca volcanoes, reach MORB-like values. Accordingly, lavas from stratovolcanoes associated with these high Rc/Ra fumaroles and thermal springs show lower strontium isotope ratios ($^{87}Sr/^{86}Sr$) reflecting a low degree of crustal contamination of these magmatic volatile sources (Fig. 2.4).

In contrast, the central part of the studied segment, (~38.5°-40°S), as well as the northernmost limit at the Nevados de Chillán volcano (~37ºS), show lower helium ratios and a narrower distribution of Rc/Ra values, ranging between 5.42 ± 0.01 Ra and 3.68 ± 0,10 Ra. The stratovolcanoes associated with these manifestations present higher values of $^{87}Sr/^{86}Sr$ ratio in lavas, indicating a higher crustal assimilation of the deep magmatic system.

Carbon isotopes ($\delta^{13}C–CO_2$)

The measured $\delta^{13}C–CO_2$ values range from -7.44 ± 0.14‰ to -49.41 ± 0.28‰ (Table 2; Fig. 2.4). Fumarolic gases have the higher values, ranging between -7.44 ± 0.14‰ and -9.75 ± 0.14‰. LM (3) and PL (4) samples, in particular, have MORB-like (-6.5 ± 2.2‰; e.g., Sano and Marty, 1995) and high temperature volcanic gas (-5.5 ± 2.2‰; e.g. Sano and Marty, 1995; Sano and Williams, 1996) signatures. Hot spring gas samples range between -11.87 ± 0.14‰ and -49.41 ± 0.28‰, except for one sample that has more affinity to a fumarolic gas-like signature (sample CU (8), -7.44 ± 0.14‰).

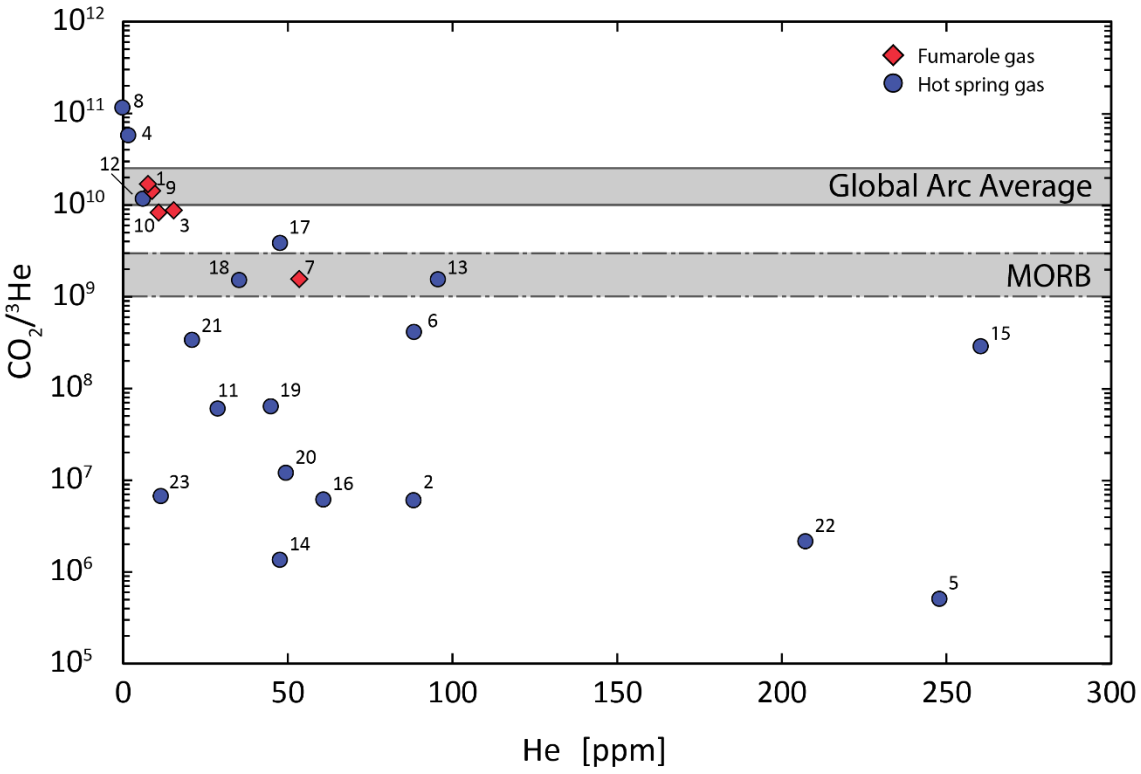

Figure 2.3. *$CO_2/^3He$ versus He concentration plot of SVZ fumaroles (red diamonds) and hot-spring (blue circles) gas samples. Global arc average ($1.5±1.1 \times 10^{10}$; e.g. Sano and Williams, 1996) and MORB ($2.0±1.0×10^9$; e.g. Marty and Jambon, 1987) fields are shown.*

In agreement with Rc/Ra and $^{87}Sr/^{86}Sr$ trends, the stable isotopes of carbon ($\delta^{13}C–CO_2$) show a regional distribution where the highest (heaviest) values are restricted to the northernmost

and southernmost parts of the studied segment. The central part of studied region shows lighter carbon signatures. The lightest value (-49.41‰) corresponds to the bubbling gas sample PA (16) and is coincident with a very low $CO_2/^3He$ value (6.1 x 10^6) and with the second lowest Rc/Ra value in the region (3.78 Ra).

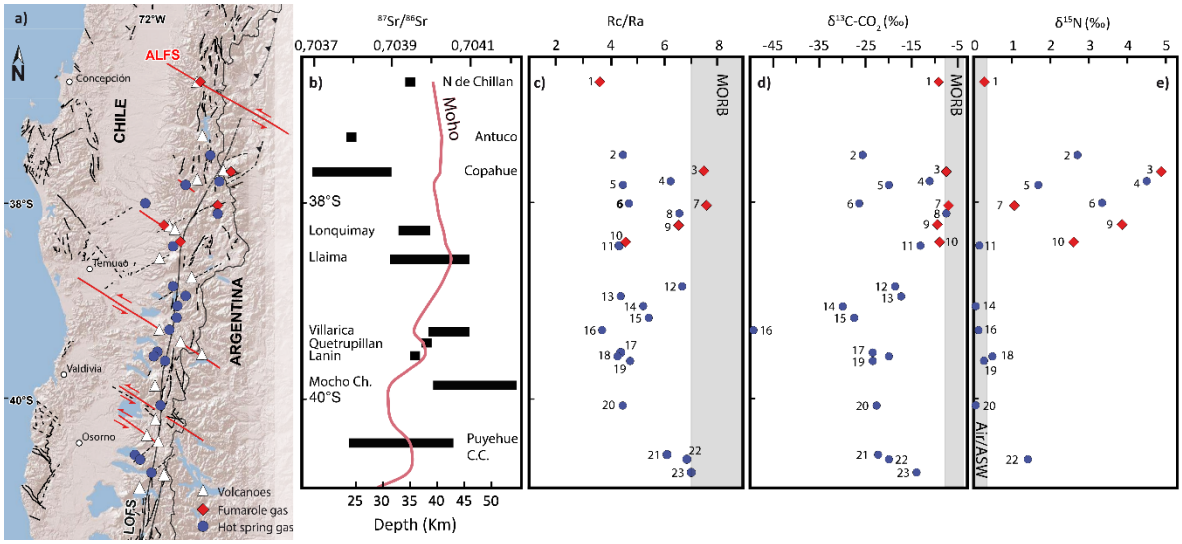

Figure 2.4. *(a) Digital elevation model of the central part of the Southern Volcanic Zone in southern Chile. White triangles represent main stratovolcanoes of the segment. Red diamonds and blue circles represent the location of fumarole and hot spring gas samples, respectively. Solid and dashed lines show simplified faults and lineations from Potent (2003), Lara et al. (2006), Cembrano & Lara (2009), Sánchez-Alfaro et al., (2013) and Pérez-Flores et al., 2014; (b) $^{87}Sr/^{86}Sr$ ratios of lavas from stratovolcanoes of SVZ. Data compiled from Deruelle et al. (1983), Davidson et al. (1987), Gerlach et al. (1988), McMillan et al. (1989), Hickey-Vargas et al. (1989) and Varekamp et al. (2006). The red line represents the depth of the MOHO from Tassara et al. (2006); (c) Latitudinal variation of corrected $^3He/^4He$ (Rc/Ra) ratios; (d) Latitudinal variation of $\delta^{13}C$-CO_2; (e) Latitudinal variation of $\delta^{15}N$.*

Nitrogen isotopes ($\delta^{15}N$)

The $\delta^{15}N$ values range from 0.02 ± 0.20‰ to 4.93 ± 0.20‰, in agreement with subduction-zone signatures (-5‰ to +7‰; Fischer et al., 2002; Hilton et al., 2002). The highest $\delta^{15}N$ values occur in the northern part and the southernmost part of the studied region. The highest $\delta^{15}N$ values, in particular, were measured in the fumarole gas sample LM (3) and the bubbling gas sample PM (4), which are both associated with the Copahue volcano in the northernmost "horsetail" termination of the LOFS. In contrast, all thermal springs in central part of the segment, between 38.5°S and 40°S (and the fumarole gas sample NC (1)) show $\delta^{15}N$ ratios near 0‰.

Discussion

The isotope data of fumaroles and bubbling gas samples presented here show that fluids in the studied segment are characterized by a wide spectrum of Rc/Ra, $\delta^{15}N$, $\delta^{13}C$–CO_2 and $CO_2/^3He$ values. As shown in Figure 2.4, the isotopic compositions are highly variable along the studied area and can be correlated with strontium isotope data in the region. In particular, the northern and southern parts of the studied region are characterized by more primitive helium (Rc/Ra), carbon ($\delta^{13}C$–CO_2) and nitrogen ($\delta^{15}N$) values (Fig. 2.4). This trend is reversed in the central part of the segment (~38.5°-40°S), where Rc/Ra, $\delta^{13}C$–CO_2 and $\delta^{15}N$ values are lower and may be related to secondary processes taking place in the shallow crust.

In the following sections we discuss the possible fractionation processes affecting the helium, nitrogen and carbon isotopic signatures in the region. We evaluate the effects of crustal contamination and meteoric fluid mixing on magmatic volatile compositions during the migration towards the surface, and we explore the link between these processes and the structural/tectonic framework of the region (LOFS and ALFS).

Crustal assimilation and contamination

Crustal contamination can modify the $^{3}He/^{4}He$, $CO_2/^{3}He$ ratios and $\delta^{15}N$, $\delta^{13}C–CO_2$ values through the addition of radiogenic ^{4}He, N_2 and CO_2 from crustal rocks (Sano et al., 1998). In the SVZ, previous studies have pointed out that the main control on the measured $^{3}He/^{4}He$ values is related to a combination of near surface magmatic degassing and crustal contamination of degassed magmas (Hilton et al., 1993, 2002; Ray et al., 2009). However, the aforementioned studies did not address the potential effects of regional and/or local structures on crustal contamination and magmatic degassing. Therefore, the impacts of volcano-tectonic associations on R/Ra variability remain to be tested.

As shown in Figure 2.5, the $^{3}He/^{4}He$ ratios (R/Ra) of analyzed samples in the studied area range between 3.40 Ra and 7.53 Ra. All the fumarole and hot springs gas samples are significantly higher than purely crustal values (~0.05 Ra; e.g. Morrison and Pine, 1955), indicating that the whole segment receives a significant contribution of mantle-derived helium. We calculate that at least 45% of helium in the gas phase is derived from the mantle, representing the baseline of the whole segment (Fig. 2.5). From Figure 2.5, it is evident that well-defined data point clusters may be indicative of variations in the degree of crustal contamination, i.e., coinciding with the different structures that control the volcanic/geothermal manifestations in the region. For example, the two fumarole gas samples in Copahue (LM (3)) and Pelehue (PL (7)) show the highest R/Ra ratios (7.48 Ra and 7.53 Ra, respectively) and are the only samples fitting the MORB field (8±1 Ra; after Farley & Neroda, 1998; Graham, 2002). These samples are characterized by very low degrees of crustal contamination (Fig. 2.5), and are associated with two fault splays located in the northernmost "horsetail" termination of the LOFS (Fig. 2.1). In addition, two hot springs samples (PM (4) and CU (8)) that are associated with the aforementioned fumaroles samples also exhibit high $^{3}He/^{4}He$ values at 6.16 Ra and 5.89 Ra, respectively. Mixing models show additions of crustally derived He that range between 20% and 25% (Fig. 2.5).

The fumarole gas sample JM (9), the three bubbling gas BB (12), AC (22), RU (23) and the water-dissolved gas sample PU (21), also present high $^{3}He/^{4}He$ ratios (6.77 to 4.89 Ra, Table 2). Also, the fumarole gas sample at "Las Sopas", associated with Cordón-Caulle volcano, fit within the same range, with a $^{3}He/^{4}He$ ratio of 6 Ra (Sepúlveda et al., 2007). As shown in Figure 2.5, these samples are characterized by ~15-25% of contamination with crustal helium. All these intermediate to high R/Ra emissions, as shown in Figure 2.1, are associated with volcanoes that are controlled by NE-striking extensional faults (e.g., Sollipulli volcano), or by the intersection between NE- and NW-striking faults (Tolhuaca and Puyehue-Cordon Caulle volcanoes). The aforementioned analysis strongly suggests that R/Ra values in fumaroles and hot springs in the studied area are influenced by crustal contamination processes that are at least partially controlled by regional and/or local structures. In the next paragraphs we use $\delta^{15}N$, $\delta^{13}C–CO_2$ data and mixing models to provide further evidence to support this assumption.

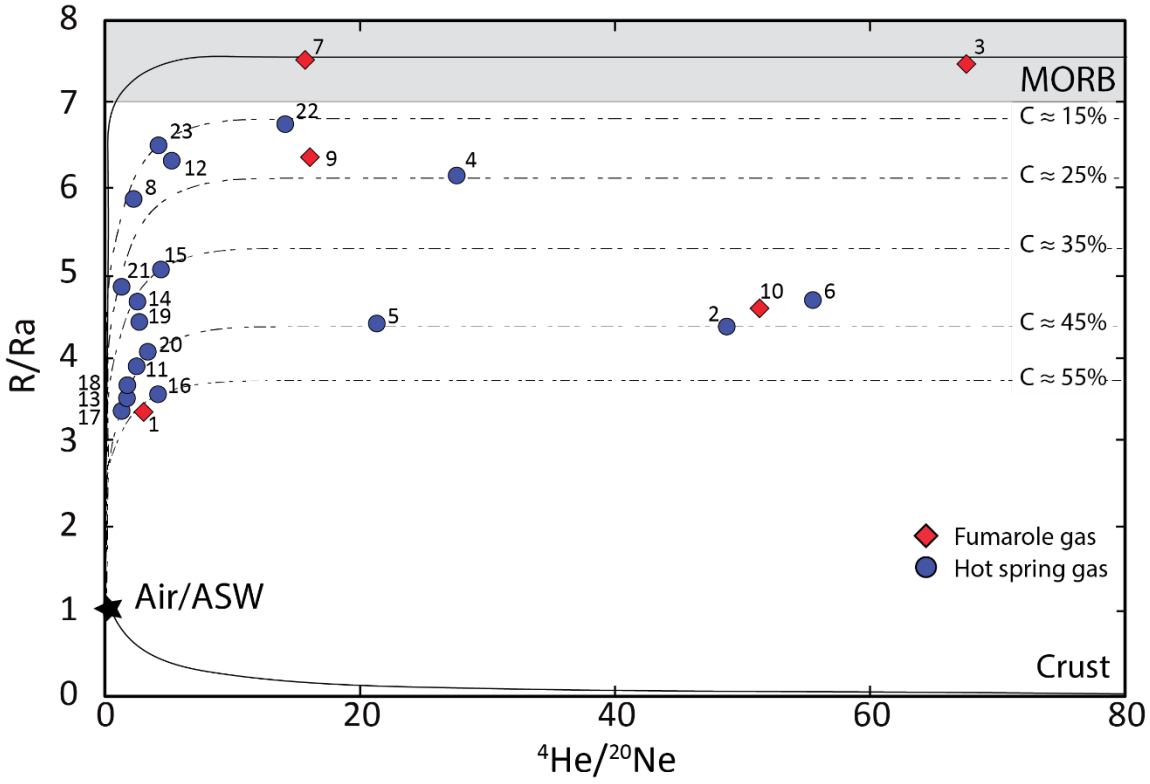

Figure 2.5. *R/Ra versus $^{4}He/^{20}Ne$ plot of SVZ fumaroles (red diamonds) and hot springs (blue circles) gas samples. The end-member MORB, crust, Air and Air-Saturated Water (ASW) are reported. Dashed lines represents the calculated mixing curves between crustal contamination degrees of 15%, 25%, 35%, 45% and 55%, and the Air/ASW endmember.*

In Figure 2.6, the $\delta^{15}N$ is plotted with N_2/He (a) and N_2/Ar (b) ratios. Nitrogen contribution end members from sediments ($\delta^{15}N$ = +7‰; $N_2/He = 1.05 \times 10^4$), MORB ($\delta^{15}N$ = -5‰; $N_2/He = 1.5 \times 10^2$) and air/ASW ($\delta^{15}N$ = 0‰ and $N_2/He = 1.49 \times 10^5$) are reported in Fig. 2.6a (from Sano et al., 1998; Ozima & Podosek, 2002; Fischer et al., 2002; Clor et al., 2005). The mixing curves are defined as:

$$\delta^{15}N_{obs} = A \times \delta^{15}N_{air} + M \times \delta^{15}N_{MORB} + S \times \delta^{15}N_{sed}$$

$$1/(N_2/He)_{obs} = A/(N_2/He)_{air} + M/(N_2/He)_{MORB} + S/(N_2/He)_{sed}$$

$$A + M + S = 1$$

where *obs*, *air*, *MORB* and *sed* refer to the observed values of air, MORB and sediments, respectively, while A, M and S are the fractions of air, MORB and sediments, respectively.

According to the literature, the N_2/He values for volcanic arc samples typically range between 1000 and 10,000, with lowest and highest values reported at 101 and 24,899, respectively (Giggenbach and Corrales, 1992; Giggenbach and Glover, 1992; Giggenbach and Poreda, 1993; Fischer et al., 2002; Clor et al., 2005). These values are significantly higher than those observed in MORBs (N_2/He ~150; Sano et al., 2001).

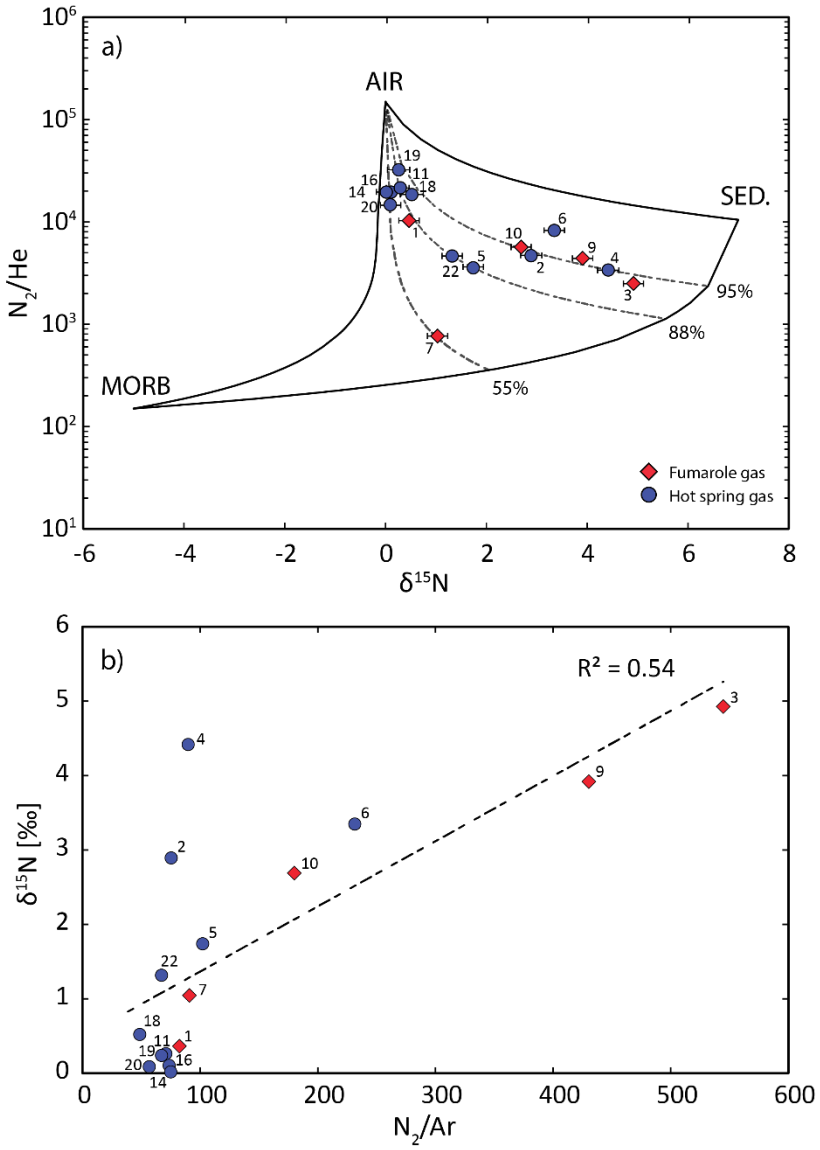

Figure 2.6. *Measured $\delta^{15}N$ (‰) versus N_2/He (a) and N_2/Ar (b) plots of SVZ fumaroles (red diamonds) and hot spring (blue circles) gas samples. In (a), MORB (−5‰, 1.5 × 10^2), sediments (+7‰, 1.05 × 10^4) and air (0‰, 1.489 × 10^5) values are reported (Sano et al., 2001; Fischer et al., 2002; Ozima and Podosek, 2002). Dotted lines reflect air addition to a mixture of mantle and sediment end-members (solid line), with percentages representing the amount of sediments in this mixture.*

The percentage of sediments in the mixture for almost all the samples varies between 88% and 97%, in agreement with gas data from the Copahue volcano (Agusto et al., 2013). Sample PL (7) at Pelehue deviates the general trend, accordingly with the He-N_2-Ar diagram in Figure 2.2, and shows a more pronounced MORB signature with only a 55% contribution from the sediments

endmember. This signature is also confirmed by the corrected $^{3}He/^{4}He$ ratio with the highest value in the region (7.67 Ra) representing a MORB-like signature (Figs. 2.4 and 2.5).

It is noteworthy to mention that at least part of this nitrogen can be also derived from crustal sources such as shallow or deeply buried sediments and added to fluids during their migration towards the surface (Mitchell et al., 2010). However, it is difficult to obtain precise information about crustally derived nitrogen because the N_2/He ratios of our samples are fractionated by air contamination. Despite these limitations, we calculate the fraction of sediment-derived and MORB-derived nitrogen using the following relation (e.g. Fischer et al., 2002):

$$\delta^{15}N_C = (1 - f_{Sed})\delta^{15}N_{MORB} + f_{sed}\delta^{15}N_{Sed}$$
$$f_{MORB} + f_{Sed} = 1$$

where $\delta^{15}Nc$, $\delta^{15}N_{MORB}$, $\delta^{15}N_{Sed}$ are the corrected, MORB (−5 ± 2‰) and sediments (+7 ± 4‰) $\delta^{15}N$ values (Sano et al., 2001; Ozima and Podosek, 2002; Table 2). f_{MORB} and f_{sed} are the fractions of MORB-derived and sediment-derived nitrogen, respectively. In Figure 2.7, the calculated $\delta^{15}Nc$ values were plotted as a function of Rc/Ra ratios. The air-corrected nitrogen values range between 1.60 (sample PL (7)) and 6.64 (sample PE (6)) and fit in the mixing line between MORB and sediments. Samples PL (7), LM (3), PM (4), JM (9) and AC (22) show a nitrogen contribution that is mainly a mixing between the mantle wedge and the subduction sediments in variable amounts, in agreement with Figure 2.6a. In contrast, samples NC (1), TT (2), AV (5), PE (6), BT (10), VA (11), CO (18), TR (19), as also suggested by their lower Rc/Ra ratios, are most likely related to a significant contribution of nitrogen coming from shallow crustal sediments and from a deep crustal source (more than 10%). These samples showing noticeable crustal nitrogen additions are correlated with the highest $^{87}Sr/^{86}Sr$ ratios in their host volcanoes (Fig. 2.4), and those occurring the northern portion of the studied region are also associated with faults that are misoriented for reactivation.

Crustal contamination also contributes to the variation of $\delta^{13}C–CO_2$ values and $CO_2/^{3}He$ ratios observed in SVZ volcanic/geothermal fluids, as presented in Figures 2.3 and 2.4. The crustal contaminant has a $\delta^{13}C$ value between +6 to −28‰ (Faure, 1986; Oehlert and Swart, 2014) and a $CO_2/^{3}He$ ratio between 10^{12} and 10^{14} (Sano and Marty, 1995; Hoefs, 2009). In Figure 2.8, $\delta^{13}C$ values are plotted along air-corrected $^{3}He/^{4}He$ (Rc/Ra) ratios for all the fumarole gas and hot spring samples. Helium and carbon isotopes show a clear positive correspondence. Two samples LM (3) and PL (7) show MORB-like signature consistent with a deep source for carbon. All the other fumarole gas samples (NC (1), JM (9), BT (10)) and four hot spring gas samples (PM (4), CU (8), VA (11), RB (13)) fall in a mixing field between MORB and crustal sediments, showing an important contribution of carbon from crustal sediments (Fig. 2.8). All the other bubbling gas and water-dissolved gas samples plot outside the mixing trend and show fractionation with relative loss

of the heavier isotope that correlates with radiogenic ^{4}He addition.

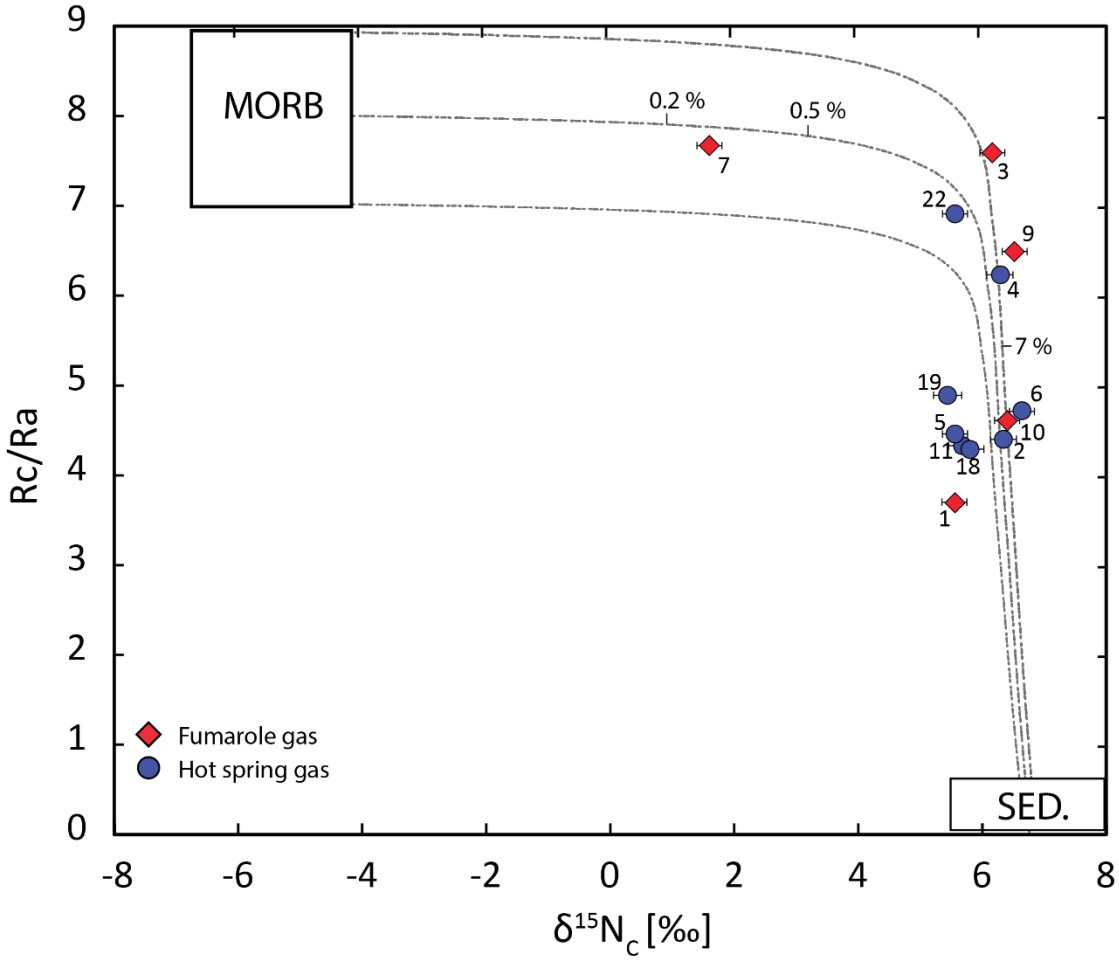

Figure 2.7. *δ^{15}Nc (‰) versus Rc/Ra plot of SVZ fumaroles (red diamonds) and hot springs (blue circles) gas samples. The MORB (−5 ± 2‰, 8 ± 1 Ra; Marty and Humbert, 1997; Sano et al., 2001) and sediments (+7 ± 3‰ and 0.05 Ra; Sano et al., 2001) end-members are shown. Dashed lines represent mixing between MORB and sediments.*

The $CO_2/^3He$ ratios (e.g., Fig. 2.3) are lower than global arc average in most of the hot springs samples, with a minimum value at 5.08×10^5. Those low $CO_2/^3He$ values and the carbon isotope fractionation trend observed in the region seem to be controlled by secondary processes affecting the magmatic/hydrothermal systems, and that can drive the relative loss of CO_2 and a decrease in the $\delta^{13}C$ values (e.g., Fig. 2.8). Magmatic degassing and calcite precipitation may be responsible for such modifications on the isotopic composition of carbon; in fact, Ray et al. (2009) hypothesized that these two processes are currently affecting geothermal emissions in the SVZ, with a stronger influence in the volatile-poor, hot-spring samples. As suggested by the correspondence between Rc/Ra values and $\delta^{13}C$ and $CO_2/^3He$ ratios (Fig. 2.8), magmatic degassing and calcite precipitation may be linked to increased residence times of fluids and crustal assimilation of the magmatic source (magmatic degassing). Therefore, it is likely that structurally-controlled vertical permeability exerts a significant role in modulating residence (and thus reaction) times of migrating fluids, conditioning their geochemical and isotopic signature through degassing or mixing with meteoric water (leading to calcite precipitation). These two processes will be discussed more precisely in further sections.

Mixing with meteoric fluids

As reported in previous studies (e.g., Sánchez et al., 2013), mixing with meteoric waters is one of the main processes affecting the chemical and isotopic signature of hydrothermal fluids in the SVZ. This process impacts the $^{3}He/^{4}He$ and $\delta^{15}N$ values by the addition of radiogenic ^{4}He and N_2, directly from atmospheric gases or from air-saturated water (ASW).

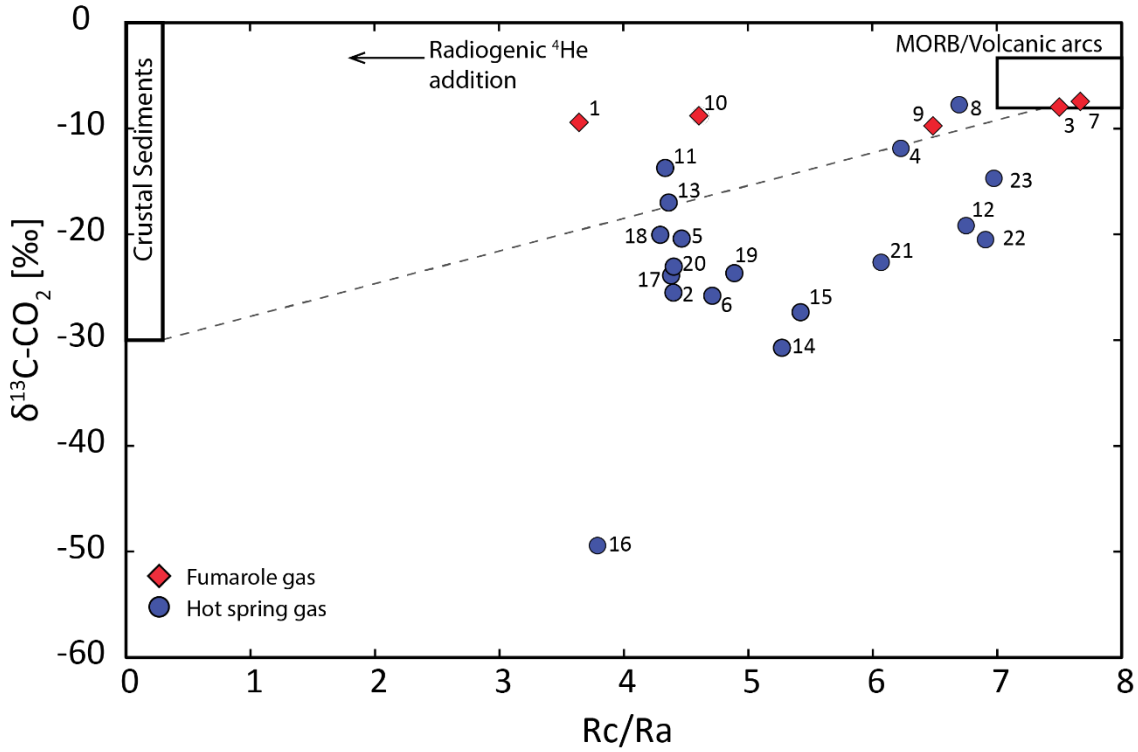

Figure 2.8. *Air-corrected $^{3}He/^{4}He$ ratios versus $\delta^{13}C–CO_2$ plot of SVZ fumaroles (red diamonds) and hot spring (blue circles) gas samples. Crustal sediments (+6 to −28‰, 0.05 Ra; Faure, 1986, Oehlert and Swart, 2014) and MORB (−6.5 ± 2.2‰, 8 ± 1 Ra; Marty et al., 1989, Farley & Neroda, 1998) fields are reported. Dashed line represent the lower limit of mixing field between MORB and crustal sediments.*

In Figure 2.5, the R/Ra ratios are plotted along with $^{4}He/^{20}Ne$ ratios. The $^{3}He/^{4}He$ values are indicative of mixing between a MORB-like gas source, with addition of radiogenic ^{4}He by crustal contamination and air/air-saturated water (ASW). Bubbling gas and water-dissolved gas from hot springs samples in the southern part of the study area (38.5°-40°S), and the fumarole gas sample NC (1) (Nevados de Chillan volcano in the northernmost part of the study area, Figs. 2.1 and 2.4) show in general a higher degree of contamination by air/ASW. Samples NC (1), VA (11), RB (13), QC (14), ME (15), PA (16), PF (17), CO (18), TR (19), CH (20) fall in a range between 6% and 20% of meteoric fluids in the mixture. Samples CU (8), PU (21) and RU (23), from the northern and southern part of the segment also fall within the same range. Samples PU (21) and RU (23), as commented above, have probably undergone direct air contamination during sampling. All other fumaroles and hot springs gas samples from the northern (37.5°-38.5°S) and southern (41°-42°S) segments present a degree of contamination that is significantly lower (< 5%).

As we showed in the previous section, the N_2/He and N_2/Ar ratios in fumaroles and thermal fluids in the studied area cover an exceptionally wide range between 767.52 and 6.7×10^{4}, and

544.73 and 38.73 respectively. These ratios, when plotted along with $\delta^{15}N$ in Figure 2.6a and b, show significant mixing with the atmospheric component. In Figure 2.6b, datapoints show a wider dispersion in the mixing with air-derived nitrogen. The hot springs samples between 38.5°S and 40°S and the fumarole gas sample NC (1) show the highest degree of contamination by Air/ASW (Fig. 2.6b), in agreement with helium isotope data shown in Figure 2.5.

Within a hydrothermal system, gas separation has the potential to fractionate both the gas ratio ($CO_2/^3He$) and the $\delta^{13}C$-CO_2 value (Giggenbach and Poreda, 1993; Barry et al., 2013). The observed $CO_2/^3He$ ratios in gas and water are different and consistent with gas separation. Helium is preferentially partitioned into the gas phase, whereas the more soluble CO_2 is concentrated in the aqueous liquid. This physical process produces an increase of $CO_2/^3He$ in residual water and can induce isotopic fractionation of $^{13}C/^{12}C$ ratios towards lower $\delta^{13}C$-CO_2 values (Vogel et al., 1970). As shown in Figure 2.3, two bubbling gas samples (PM (4), CU (8)) show higher $CO_2/^3He$ values (5.78×10^{10} and 11.6×10^{10}) compared with their associated fumaroles in the Copahue and Pelehue geothermal areas (LM (3), PL (7). These values suggest He loss or CO_2 addition from local sediments. Furthermore, sample CU (8) has a $\delta^{13}C$–CO_2 value (-7.75‰) within the range of arc fumarolic gases (Sano and Marty, 1995), while PM (4) show a lower value (-11.87‰). Both samples have an Rc/Ra ratio of 6.23 (PM (4)) and 6.69 (CU (8)) suggesting only a minor degree of crustal contamination. Therefore, the high $CO_2/^3He$ ratios may reflect both crustal contamination and/or vapor liquid partitioning processes, in close relation with the local scale fault-fracture meshes controlling the permeability in the Copahue and Pelehue geothermal systems (see Fig. 2.1).

Degassing and calcite precipitation

Figures 2.3 show that more than half of the hot spring gas samples present low $CO_2/^3He$ ratios, in comparison to fumarole samples. This observation, also reported in previous studies in the SVZ (e.g., Ray et al., 2009), is suggestive of CO_2 loss from the magmatic/hydrothermal system (Giggenbach and Poreda, 1993). Ray et al. (2009) proposed two mechanisms that can possibly explain the low $CO_2/^3He$ ratios observed in SVG samples: (1) Magma degassing and (2) CO_2 loss driven by calcite precipitation. In the next paragraphs we evaluate these two processes for the studied segment.

Degassing of an andesitic-basaltic magma can produce a decrease in $CO_2/^3He$ in residual melt as well as the $\delta^{13}C$ values (Javoy et al., 1978; Hilton et al., 1998). For the He–CO_2 elemental fractionation, the fractionation factor (α) is defined as $(CO_2/^3He)_{vap}/(CO_2/^3He)_{melt}$, i.e., the inverse ratio of the solubility of He and CO_2 in the parental melt. For a tholeiitic melt, α is ~2.35 (Hilton et al., 1998). A preferential loss of CO_2 occurring during melt degassing will cause a decrease in the $CO_2/^3He$ ratio for the gas remaining in the melt, and a simultaneously decrease in the $\delta^{13}C$ values of the residual CO_2 (isotopic fractionation factor proposed is −4‰ corresponding to α: 0.996 Javoy et al., 1978).

Two models of degassing have been proposed: batch equilibrium (closed system) and Rayleigh distillation (open system). For these two models we assume an initial $CO_2/^3He$ of 11.95×10^9 and a $\delta^{13}C$ value of −8.95‰, corresponding to the average $CO_2/^3He$ and $\delta^{13}C$ values of the four fumarole gas samples falling in the volcanic-arc field in Figure 2.3. By using the Rayleigh distillation equation, $CO_2/^3He_{residual}=(CO_2/^3He_{initial})\times F^{(\alpha - 1)/\alpha}$, we calculate that the system would have needed to undergone a complete loss of CO_2 to achieve the lower $CO_2/^3He$ ratios measured in our samples (i.e., $CO_2/^3He=5.08 \times 10^5$). Moreover, all our samples that have suffered a relative loss of CO_2 are below the Rayleigh distillation degassing curve in Figure 2.9 (labeled "Rayleigh"). Therefore, it is likely that this process does not explain the low $CO_2/^3He$ ratios observed in the

studied segment. Similarly, we tested a case of batch equilibrium degassing using the equations $\delta^{13}C_{residual}=\delta^{13}C_{initial}+(1-F)\times 1000\ln(\alpha)$, and $CO_2/^3He_{residual}=(CO_2/^3He_{initial})\times F^{(\alpha-1)/\alpha}$ (after Javoy et al., 1978; Ray et al., 2009). As shown in Figure 2.9, the batch degassing curve does not fit our data (labeled "Batch"). With this particular mode of degassing, the minimum possible values for $CO_2/^3He$ and $\delta^{13}C$ are 5.0×10^8 and −13‰, respectively (Fig. 2.9).

Consequently, and in agreement with previous studies by Ray et al. (2009) in the SVZ, we dismiss magmatic degassing as a viable process to explain the lower-than-arc-average $CO_2/^3He$ values in our samples. Another alternative mechanism to explain such low $CO_2/^3He$ values is CO_2 loss by calcite precipitation, occurring during cooling/mixing history of the hydrothermal system (e.g., Hilton et al., 1998). Fractionation between $CaCO_3$ and CO_2 gas can be calculated theoretically, and the temperature dependence for C soluble species with respect to $CaCO_3$ is well constrained (Bottinga, 1969). At temperatures less than 192 °C, calcite is enriched in ^{13}C relative to residual CO_2, thus the fractionation factors are −3‰ at 100 °C and −10‰ at 25 °C (Chacko et al., 2001). However, at temperatures greater than 192 °C, calcite is depleted in ^{13}C relative to residual CO_2 and the fractionation factor is around 0‰ (Sano and Marty, 1995; Ray et al., 2009, Barry et al., 2014). In Figure 2.9, the plotted $CO_2/^3He$ and $\delta^{13}C$-CO_2 values illustrate the potential effect of calcite precipitation at two different temperatures, 25 °C and 192 °C (dashed lines). Our samples fall in a field defined by these two lines, showing that the low $CO_2/^3He$ and $\delta^{13}C$-CO_2 values measured in the studied samples can be explained by precipitation of calcite at various temperatures between 25 and 192 °C, as also previously proposed by Ray et al. (2009). Furthermore, evidence of calcite precipitation is present in several outcrop-scale dilational jogs along master and subsidiary faults of the LOFS (e.g., Pérez-Flores et al. 2014). The only two hot spring samples that do not fit this trend are BB (12) and PF (17). These samples were possibly subjected to hydrothermal degassing processes before calcite precipitation; therefore, these two samples may mark a starting point for the calcite precipitation lines which can be defined, as a first approximation, between the global arc-average and samples PM (4) and CU (8).

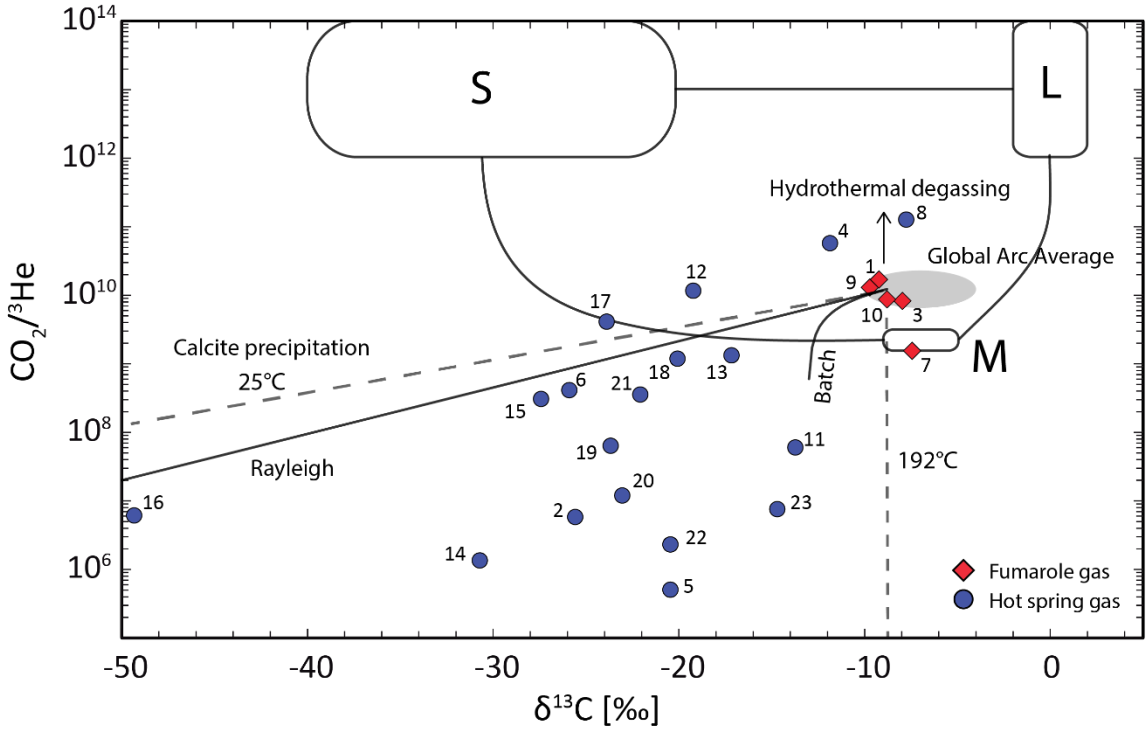

Figure 2.9. *$CO_2/^3He$ versus $\delta^{13}C$–CO_2 plot of SVZ fumaroles (red diamond) and hot springs (blue circles) gas samples compared to MORB (2×10^9, -6.5 ± 2.2‰; Marty et al., 1989; Sano and Marty, 1995; Sano and Williams, 1996), organic sediments (-30 ± 10‰, 1×10^{13}; Sano and Marty, 1995; Hoefs, 2009) and marine limestone (1×10^{13}; 0 ± 2‰; Sano and Marty, 1995; Hoefs, 2009). Dashed lines represent trajectories for CO_2 loss by calcite precipitation at a temperature of 25 °C (fractionation factor = −10‰) and 192 °C (fractionation factor = 0‰). The starting point is $CO_2/^3He = 11.95 \times 10^9$ and a $\delta^{13}C = -8.95$‰. The vertical arrow represent the direction for hydrothermal degassing process. Rayleigh distillation and batch equilibrium curves are also shown.*

Conceptual model of fluid circulation

By combining the volcano-tectonic association of the studied segment of the SVZ (Table 2.3) with the helium, carbon and nitrogen isotope data presented in this study, a conceptual model that summarizes fluid circulation in the central part of SVZ is presented in Figure 2.10.

The northern termination of the LOFS is characterized by a well-developed "horse-tail"-like accommodation zone (Fig. 2.1). The associated accommodation zone of such fault architectures, as asserted by many authors (Sibson, 1994; Sibson, 1996; Kim et al., 2004, Rowland & Sibson, 2004; Rowland & Simmons, 2012), promote high vertical permeability and have long been recognized to play a key role as host structures focusing increased fluid flow in geothermal/hydrothermal systems. In the northern part of the studied segment (Figs. 2.1 and 2.10), the fumarole sample LM (3) and the hot spring sample PM (4) are associated with the Copahue geothermal area, which is set on a "pull apart" like basin, formed by the interplay of the LOFS and the Copahue-Antiñir Fault System (CAFS) (Melnick et al., 2006; Fig. 2.1; Sánchez et al. 2013). A few tens of kilometers towards the south, the occurrence of fumarole sample PL (7) in the Pelehue area and the hot spring sample CU (8) in Coyuco is controlled by a series of NE-striking extensional and transtensional faults that are located east of the main volcanic arc (Fig. 2.1). There are no recognized volcanic centers close to these two thermal manifestations, which seem to be controlled directly by the fault splays of the LOFS (Fig. 2.1). The fumaroles gas samples LM (3) and PL (7), both labeled as "a" in Figure 2.10, show MORB-like $^3He/^4He$ ratios indicating primitive sources

and no significant degrees of crustal contamination (Figs. 2.4, 2.5). Despite this common feature, carbon and nitrogen isotope data point to two completely different signatures for these two systems. $CO_2/^3He$, $\delta^{13}C\text{-}CO_2$ (Fig. 2.9) and $\delta^{15}N$ values (Fig. 2.6a) show a typical volcanic arc signature for LM (3) sample. Carbon and nitrogen signatures most likely originated, in this case, by mixing between mantle and sediments derived from the slab, with almost no contribution from continental crust and mixing with meteoric water. In contrast, the PL (7) sample displays a predominant MORB-like carbon signature and a lower nitrogen contribution from the slab than all the other samples (55%, Fig. 2.6a), with no nitrogen addition from the continental crust. This signature appears consistent with the retro-arc location of the fumarolic field of Pelehue, 20 km far from the closest known eruptive center, and almost 50 km eastward from the present-day location of the active volcanic arc. Water-dissolved gas samples PM (4) and CU (8), also spatially associated with the horse-tail northern termination of the LOFS, are the only two samples affected by hydrothermal degassing and show more crustal additions of helium, nitrogen and carbon with respect to the fumaroles LM (3) and PL (7). The carbon isotope signatures indicate that these hot springs have suffered a vapor-liquid separation and partial gas-phase loss, suggesting that crustal contamination processes are more easily perceived in such volatile-poor samples. These are among the least contaminated samples in the whole region, with air-corrected $^3He/^4He$ ratios ranging between 6 and 7.

Further south, in the central part of the studied segment ("b", Figure 2.10), fumaroles and hot springs are spatially associated with stratovolcanoes controlled by transtensional NE-striking faults (e.g., Sollipulli volcano; Fig. 2.1) or by the intersection between NE- (LOFS) and NW-striking transpressive faults (ALFS) (e.g., Tolhuaca and Cordon Caulle volcanoes; Fig. 2.1, 2.10). These volcanic systems show a higher degree of crustal contamination, with $^{87}Sr/^{86}Sr$ ratios higher than lavas related to volcanoes in the northernmost part of the segment ("a", Fig. 2.10). The associated thermal manifestations in this area are also characterized by a minor degree of crustal contamination of their magmatic source(s). As shown in Figure 2.4, the Rc/Ra ratios in samples JM (9), BB (12), PU (21), AC (22) and RU (23) are among the highest in the region (Rc/Ra~6-7) and correlate with low $^{87}Sr/^{86}Sr$ ratios in their host stratovolcanoes. The nitrogen isotope signature suggests mixing between MORB and sediments, with minor contribution from continental crust (Fig. 2.8). $CO_2/^3He$ and $\delta^{13}C\text{-}CO_2$ show the typical volcanic-arc signature for fumarole sample JM (9), whereas the water-dissolved gas samples are slightly affected by CO_2 loss and $\delta^{13}C\text{-}CO_2$ fractionation for calcite deposition (Fig. 2.9).

Table 2.3. *volcano-tectonic associations along the studied segment of the SVZ*

Group	Name	Location	Description	References	Samples
a: LOFS northern transtensional termination	Copahue-Caviahue volcanic complex	37° 51'S	The Caviahue-Copahue volcanic complex is located at the northern termination of the LOFS in a "horstail"-like acommodation zone. The area is limited by two major fault zones, the Copahue–Antiñir thrust system to the north and the main branch of the LOFS, to the south, wich locally form pull-apart structures. Magmatic products associated with active Copahue volcano vary from basaltic-thrachyandesites to trachyandesites. Several NE-striking strike-slip faults and NE-striking half-graben are located within 40 km to the south of the Caviahue-Copahue complex. One of these structure is forming the Pelehue valley, located in backarc position with respect of the present day active volcanic arc.	Melnick et al., 2006; Varekamp et al., 2006; Rosenau et al, 2006;Peréz-Flores et al., 2014	LM (3), PM (4)
	Pelehue valley	38° 07'S			PL (7), CU (8)
b: LOFS dominant and interplay between LOFS and ALFS	Sollipulli volcano	38° 58'S	Stratovolcanoes and pyroclastic cones that form NE–SW alignments. Mostly basalts have been erupted from these arrays but stratovolcanoes evacuated also dacites or rhyolites.	Gilbert et al., 1996; Lara et al., 2007; Cembrano & Lara, 2009; Lachowycz et al., 2015	BB (12)
	Antillanca volcanic complex	40° 46'S			RU(23)
	Tolhuaca volcano	38° 19'S	Stratovolcanoes or clusters of stratovolcanoes controlled by the interplay of NW-striking sinistral-reverse faults of the ALFS and NE- to NNE-striking dextral-normal faults of LOFS. Volcanic edifices show no asymmetry of the base but they can display flank vents in preferred NW orientation. Magmatic products present a wide compositional range from basaltic to dacitic and rhyolitic.	Lara et al., 2006; Cembrano & Lara, 2009; Peréz-Flores et al., 2014	JM (9)
	Puyehue-Cordón Caulle volcanic complex	40° 35'S			PU (21), AC (22)
	Nevado de Chillan volcano	36° 52'S			NC (1)
c: Dominant ALFS	Sierra Nevada volcano	38° 34'S	Stratovolcanoes built on top of the of NW-striking sinistral-reverse faults from the ALFS. LOFS is represented by the NNE-striking master fault. Volcanic edifices show no or slightly asymmetry of the base and they can display flank vents in NW-preferred orientation. Compositions cover a wide range from basalts to rhyolites.	Melnick et al., 2006; Cembrano & Lara, 2009; Sanchez et al. 2013	BT (10), VA (11) RB (13), QC (14), ME (15), PA (16), PF (17), CO (18), TR (19), CH (20)
	Villarica-Quetrupillan-Lanin volcanic alignment	39° 25"- 39° 38"S			
	Mocho Choshuenco volcano	39° 56'S			
	Trapa Trapa thermal spring	37° 41'S	Thermal springs related NW-trending faults of the ALFS. The hot springs are spatially associated with Callaqui stratovolcano, a N60E elongated volcanic fissure, with parasites and pyroclastic cones alignment in the same direction. The composition of erupted products from Callaqui volcano is mainly basaltic-andesitic.	Moreno et al., 1984; Potent, 2003; Cembrano et al., 2009; Radic, 2010	TT (2)
	Avellano thermal spring	37° 55'S			AV (5)
	Pemehue thermal spring	38° 4'S			PE (6)

Finally, the case "c" in Figure 2.10 represent all those fumaroles and hot springs associated with stratovolcanoes that are controlled by pure transpressive NW-striking faults (Nevado de Chillan, Villarica and Mocho-Choshuenco volcanoes; Fig. 2.1, presenting the highest degrees of crustal contamination (NC (1), BT (10), VA (11), RB (13), QC (14), ME (15), PA (16), PF (17), CO (18), TR (19), CH (20)) and the hot springs spatially related with transpressional fault-fracture zones that do not permit a high fluids permeability (TT (2), AV (5), PE (6)).

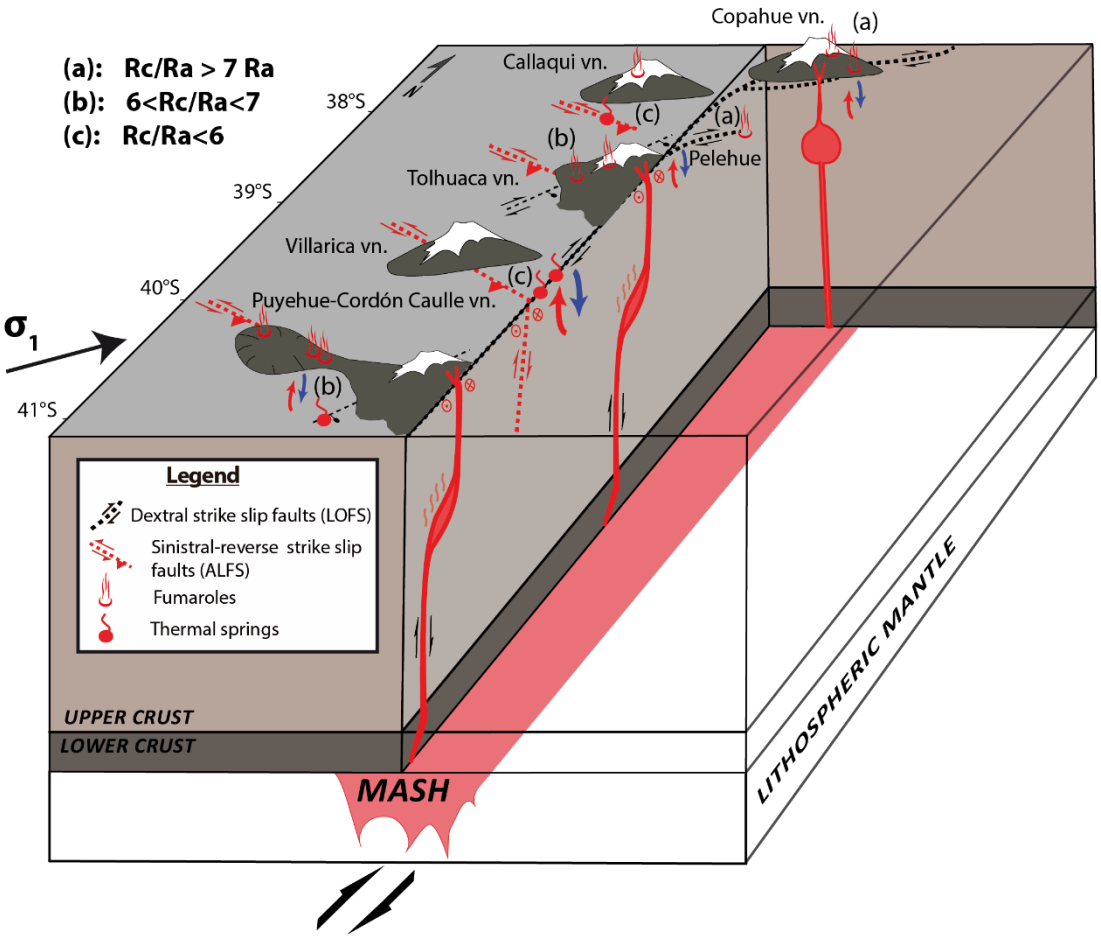

Figure 2.10. *Block model showing the structurally-controlled fluid circulation model proposed for the studied segment of the Southern Volcanic Zone. Black and red dashed lines represent the LOFS and ALFS, respectively. Fumaroles and hot springs are represented along with their relation to volcanic edifices and structural settings. Blue and red arrows represent the mixing between deep and meteoric fluids. Sigma 1 (σ1) represent the maximum regional stress field. Helium ratios (Rc/Ra) ranges are shown in the upper left.*

The hot springs located between Villarica and Mocho-Choshuenco volcanoes (Fig. 2.5, and Fig. 2.6a, b) also show the highest degree of mixing with meteoric water. As also hypothesized by Sánchez et al. (2013), most of these thermal springs are associated with the main traces of the LOFS that, due to their high permeability, allow a deeper circulation of the meteoric fluids, further increasing the dilution process in this already humid and rainy region. The $CO_2/^3He$ and $\delta^{13}C\text{-}CO_2$ indicate a significant loss of CO_2 and ^{13}C for calcite precipitation in almost all the case "c" samples, except for fumaroles gas samples NC (1) and BT (10) and hot spring gas samples VA (11) and RB (13) (Fig. 2.7). As discussed in section 5.4, the CO_2 loss driven by calcite precipitation correlates with $^3He/^4He$ ratios. This trend shows how calcite precipitation may be enhanced by high residence

time of hydrothermal fluids along the LOFS; this process can occur during the cooling/mixing history of the hydrothermal system that increase the reaction time with country rock and the cooling of magmatic vapor, and/or by mixing with cold and shallow infiltrating waters.

Concluding remarks

Our combined isotopic, geochemical and structural data indicate that the NNE-striking intra-arc, strike-slip Liquiñe-Ofqui Fault System (LOFS) and the NW-striking Arc-oblique Long-lived Basement Fault System (ALFS) exert a fundamental control on the helium, nitrogen and carbon isotope signature of thermal manifestations in the Chilean Andes between ~37-41ºS. In this segment of the Southern Volcanic Zone (SVZ), thermal fluids are characterized by a wide range of $^{3}He/^{4}He$, $CO_2/^{3}He$, $\delta^{13}C\text{-}CO_2$ and $\delta^{15}N$ values. We explain these variations by linking the geochemical data of gas in fumaroles and thermal spring water, to a wider geological context that includes the regional distribution of fault-fracture meshes and the isotopic variation of source magmas.

The first order control on helium, carbon and nitrogen isotopes signatures observed in the studied segment seems to be largely dominated by the degree of crustal assimilation of the magmatic sources, which is in turn controlled by the LOFS and ALFS. As shown in Figure 2.4, the air-corrected $^{3}He/^{4}He$, $\delta^{13}C\text{-}CO_2$ and $\delta^{15}N$ fumarole gas data show a strong correspondence with the $^{87}Sr/^{86}Sr$ ratios of lavas from hosting volcanic systems. The thermal spring gas data also show a similar correspondence, although partly masked by secondary processes. Our observations also indicate that the magmatic sources of hydrothermal fluids in the region are highly variable at the regional scale, and more primitive signatures are most likely transmitted to the shallow volcanic/geothermal environment along the NNE-striking LOFS.

In contrast, the isotopic signatures of gases in thermal manifestations along the arc-oblique, NW-striking ALFS, show a higher degree of crustal contamination. Considering the fact that the ALFS inhibit vertical fluid permeability due to its misorientation with respect to the prevailing regional stress field, the $^{3}He/^{4}He$, $\delta^{13}C\text{-}CO_2$ and $\delta^{15}N$ data records crustal contributions related to increased fluid/rock interaction and higher residence times.

Whereas the ALFS promote the formation of long-lived, more evolved high-enthalpy hydrothermal reservoirs (e.g., Tolhuaca geothermal field), the LOFS allow a higher vertical permeability of hydrothermal fluids from more primitive, MORB-like magmatic sources. These large-scale structures are effective *loci* for enhanced fluid flow, providing a "background" $^{3}He/^{4}He$ signal in the area that exceeds by far the crustal helium signature of 0.05 Ra. This crustal-scale fault system also promote the deep circulation of meteoric fluids, as occurring for thermal springs between 38.5°S and 40°S, that partially masks the deep $\delta^{13}C\text{-}CO_2$ and $\delta^{15}N$ signatures due to shallow processes such as mixing with meteoric water and calcite precipitation.

Chapter 3. Large-scale structural controls on metal fluxing in active margins: insights from the Liquiñe-Ofqui intra –arc faults systems, SVZ, Chile.

Abstract

In the present contribution we provide the first dataset of trace elements in geothermal systems of Southern Volcanic Zone of Chile. The aim of this study is to unravel the structural control on transport of metals and metalloids in hydrothermal fluids associated with the Liquiñe-Ofqui Fault System (LOFS), a NNE-trending, intra-arc, dextral strike-slip fault and with the Arc-oblique Long-lived Basement Fault System (ALFS), a series of sinistral transpressive NW-SE trending faults, controlling the volcanism and geothermal activity in southern Chile. The sampled fluids included hot springs and fumarole condensates, where major anions and cations; base and precious metals (PGE's, Ag, Au) and metalloids (B, As, Sb, Ge, Te) contents have been measured. The surface geothermal waters have been divided into two groups based on their pH, temperature and chemical composition: acid-sulfate waters and neutral chlorine waters. The former have the highest concentrations of K, Ca, Ba, Al, Fe, Mn, Co, Ni, Cu, Zn, V, Cr, Sc, Ti, Cd, Y, Zr, Pb, La, Ce, Th and U, whereas neutral-chlorine waters present the highest concentrations of elements such: Na, Mg, B, As, Li, Cs, Rb, Sr, Mo, Sb, Ge, Te, W, Ag, Au, Ru, Rh, Pd, Ir and Pt. Trace elements concentrations have been contrasted with air-corrected helium isotope ratios (Rc/Ra) measured in water-dissolved gas and fumarole gas in the exact same emissions. In acid sulfate waters metals as Ca, Mg, K, Sr, Ba, Co, Ni, Cu, Cd, Rh and Pd show negative correspondence with Rc/Ra, suggesting that its concentration in thermal fluids is dominated by rock leaching, whereas for B, As, Sb, Ge, Mo, W, Ti, Pb and Zr, showing a positive correlation with Rc/Ra, a significant amount of them may come directly from the deep magmatic system, where after deep boiling, can be transported by the low density vapor up to the shallow geothermal domain. These two different trends of enrichment in acid-sulfate waters are the result of a strong structural control that conditions selective elemental partitioning, enhancing water-rock interaction and metal leaching along oblique, NW ALFS structures (e.g., Ni, Co, Cu, Pd among others). In contrast, the high permeability settings along the main LOFS allow rapid fluxing of metals transported by magmatic vapor (e.g., As, Sb, Mo, Ge etc.). In neutral-chlorine waters geochemistry is mainly dominated by shallow processes as mixing with meteoric fluids and mineral precipitation and most of the main and trace elements plots in these waters don't show a clear correlation or display a weak positive correspondence with Rc/Ra ratios. It suggests that dilution and removal processes are more efficient in those contexts where the higher residence time of geothermal fluids in the crust increase the reaction time with country rock and the mixing with cold and shallow infiltrating water. In both acid-sulfate and neutral-chlorine waters has also been found also found exceptionally high amounts of PGE's, with concentrations ranging from 6.00 to 18.00 ppt for Ru, 0.70 to 142.00 ppt for Rh, 0.15 to 1.99 ppb for Pd, 4.00 to 9.00 ppt for Ir and 1.20 to 1.60 ppt for Pt. The PGE's anomaly is restricted to the northern part of studied region, with maximum Pd and Rh concentrations localized in Tolhuaca Geothermal System. The origin of this anomaly may be linked with the interaction of the uprising hydrothermal fluids with ultramafic bodies that exhumed through the subduction channel, were emplaced in the basement of the present volcanic arc.

Introduction

In convergent margins, high-enthalpy geothermal systems and epithermal precious and base metal deposits are closely associated with each other, and both are genetically linked with active volcanism, shallow magmatic reservoirs and overlying hydrothermal circulation cells (Hedenquist and Aoki, 1991; Hedenquist et al., 1993; Einaudi et al., 2003; Sillitoe and Hedenquist, 2003). There are numerous evidences reported in the literature documenting significant flux of volatiles and ore-forming metals from magmatic-hydrothermal systems (Richards, 2011; Pokrovski et al., 2013). In fact, in some active geothermal systems (e.g., Rotokawa in New Zealand or Lihir Island in Papua New Guinea) well fluids carry important concentrations of precious and base metals, reaching 23 ppb of Au, 2.4 ppm of Ag and 19.8 ppm of Cu, among other metals (Simmons et al., 2016). These young, active and metal-rich systems can lead to the formation of giant hydrothermal deposits through a combination of sustained metal flux and efficient metal precipitation (Simmons and Brown, 2006).

Ore deposits form in the crust when specific factors such as distinct tectonic configurations, focused fluid flow and/or reactive host rocks are met to enhance the overall metal concentration (Richards, 2013). Volcanic arc magmas can transport metals from the mantle and from subducted oceanic crust and sediments to the Earth's upper crust and eventually to the surface (Johnson et al., 2013). During ascent and degassing, some metals partition from the magma into a hydrosaline fluid and/or supercritical magmatic vapor phase. This behavior is evident from experimental studies and from analyses of coexisting melt and fluid inclusions (e.g., Heinrich et al., 1999; Pokrovski et al., 2002, 2005; Williams-Jones and Heinrich, 2005; Zajacz et al., 2011; Pokrovski et al., 2013). Furthermore, several studies have reported chemical analyses of base (Cu, Co, Ni, Zn, etc.) and precious (Au, Ag) metals and metalloids (As, Sb) in volcanic fumaroles, hot springs and deep geothermal reservoir fluids (Bernard et al., 1990; Allard et al., 2000; Africano et al., 2002; Aiuppa et al., 2003; Zelenski et al., 2013; Ballantyne and Moore, 1988; McKibben et al., 1990; Brown et al., 1996; Simmons and Brown, 2007; Simmons, et al., 2016a,b; Aiuppa et al., 2000a,b; Kaasalainen and Stefánsson, 2012; Kaasalainen et al., 2015). Despite these fundamental contributions, the origins of giant hydrothermal ore deposits are enigmatic since the concentrations of metals, and more particularly, the flow rates of ore-forming fluids are still poorly quantified. Furthermore, in compressional and extensional settings, shallow magmatic reservoirs and their overlying hydrothermal circulation cells are strongly controlled by structural meshes that permit fluids migration.

The control of fault-fracture meshes on fluid flow in geothermal and hydrothermal systems is important and has been vastly studied over the past ten to fifteen years (e.g. Manning and Ingebritsen, 1999; Cox et al., 2001; Sibson and Rowland, 2003; Fairley and Hinds, 2004; Micklethwaite and Cox, 2004; Rowland and Sibson, 2004; Blenkinsop, 2008; Graf and Thierrien, 2009; Micklethwaite et al., 2010; Baker, et al., 2010; Cox, 2010; Gudmundsson et al., 2010; Rowland and Simmons, 2012). These studies have improved our understanding about the structural factors controlling fluid flow, and have provided crucial information to refine conceptual models of fault/fracture hydraulic architecture in geothermal and hydrothermal systems. Despite these fundamental contributions, our understanding of elemental fluxing in the upper crust is still limited (Richards, 2011; Pokrovski et al., 2013; 2014), and the structural control on metal transport in hydrothermal systems remains poorly constrained in active continental margins (Cox et al., 2001; Rowland and Simmons, 2012).

In the Andean Cordillera of Central-Southern Chile, the nature of the relationship between

tectonics and volcanism is the result of interaction between the crustal structures of the basement and the ongoing regional stress field (Pritchard et al., 2013). Between 37° and 46°S, the volcanic and geothermal activity is controlled by the NNE-trending, 1,000 km long Liquiñe-Ofqui Fault System (LOFS) and by the NW-SE Arc-oblique Long-lived Basement Fault System (ALFS) (Cembrano and Lara, 2009; Perez-Flores et al., 2016). Previous studies have revealed how fault-fracture systems, belonging to both LOFS and ALFS, control the degree of magmatic evolution and crustal assimilation of volcanic systems in the segment (Cembrano and Lara, 2009). Furthermore, several geothermal surface manifestations and shallow fumarolic emissions are spatially related to stratovolcanoes and fault segments associated with both fault systems (Sánchez et al., 2013). In a recent study, Tardani et al. (2016) provided key evidence for significant regional-scale structural controls on the isotopic composition of subduction-related magmatic gas. By determining the helium, nitrogen and carbon isotope signature of thermal fluids discharged along the seismically active Liquiñe-Ofqui Fault System (LOFS) in southern Chile, a ~1000 km long intra-arc, strike-slip fault, Tardani et al. (2016) show that the structural setting of the region exerts a fist-order control on hydrothermal fluid composition by conditioning residence times of magmas and thus promoting cooling/mixing of magmatic vapor.

Despite the abundance of studies describing the geothermal activity and volcanism in the region (Hilton et al., 1993; Cembrano and Lara, 2009; Ray et al., 2009; Dobson et al., 2013; Lahsen et al., 2015; Tardani et al., 2016), very few data are currently available on the concentrations of dissolved metals and metalloids in thermal fluids from southern Chile, and the structural controls that the LOFS and ALFS exert on them remains unknown. In one of these very few studies, Sánchez-Alfaro et al. (2016b) reports high metal concentrations in the deep reservoir fluids of the Tolhuaca Geothermal System (Au: 1.6 μg/kg, Ag: 0.018 μg/kg, Cu: 0.07 μg/kg and Zn: 7.5 μg/kg), although it is not clear how the different structural orientations of the main and subsidiary faults affect metal transport under variable permeability conditions and degrees of mixing with meteoric water. Such information is crucial to better understand how metals are fluxed from the upper crust to the surface, and to improve our knowledge on how metals are efficiently concentrated or dispersed into the environment.

In this study we present the first comprehensive survey of major and trace metal concentration data from shallow thermal waters and volcanic gas condensates, spatially related with both LOFS and ALFS. The reported elements include noble metals (Au, Ag and platinum-group elements, PGE), base metals (Al, Fe, Mn, Co, Ni, Cu, Zn, V, Cr, Sc, Ti, Mo, Cd, Y, Zr and Pb), metalloids (B, As, Sb and Ge), rare earth elements (REE), actinides (U and Th) and alkali and alkaline earth metals (Li, Cs, Rb, Ba and Sr) Results from this study, when combined with recently published helium, nitrogen and carbon isotope data, reveal that geothermal waters and volcanic fumaroles of the Southern Volcanic Zone (SVZ) show anomalous concentrations of trace metals, including high Cu, Co, Zn, As, Sb and PGE's, strongly correlate with major faults and fractures, suggesting that local and regional tectonics may exert a first-order control on metal fluxing and degassing in active margins.

Geological setting

The Andean region examined in this study is about 450 km-long (37°-41°S), and forms part of the central and southern segments of the Southern Volcanic Zone (SVZ) (Fig. 3.1). In this region, the current geodynamic setting is characterized by slightly oblique convergence between the Nazca and South American plates at a rate of ca. 7–9 cm/year that has prevailed for the last 20 Ma (Angermann et al., 1999; Somoza and Ghidella, 2005). The basement of the volcanic arc, in the

northern portion of this segment at 39°S, is made up of extensive outcrops of the Meso–Cenozoic volcano–sedimentary rocks of the Cura Mallin and Cola de Zorro formations, which are locally intruded by Mio–Pliocene plutons (Charrier et al., 2002). South of 39°S, recent volcanic edifices are built directly onto Meso–Cenozoic plutonic rocks of the Patagonian Batholith. Crustal thickness underneath the volcanic arc decreases from 50 km at 33°S to 35 km at 46°S, with an accompanying decrease in the average altitude of the main cordillera, from 5000 m to less than 2000 m (Tassara and Yañez, 2003).

The structural setting of the studied segment in Figure 3.1 is dominated by the Liquiñe-Ofqui Fault System (LOFS), a NNE-striking, intra-arc transpressional dextral strike-slip fault system that extends between 37°S and 46°S, and associated with ENE-striking second-order intra-arc anisotropies (Cembrano et al., 1996, 2000; Folguera et al., 2002; Adriasola et al., 2006; Rosenau et al., 2006). The ENE-striking structures have been recognized as extensional fractures most likely formed under relatively low differential stress (Lavenu and Cembrano, 1999; Cembrano and Lara, 2009). Conversely, the arc oblique WNW-striking long-lived basement fault system (ALFS) is severely misoriented with respect to the prevailing stress field, and has been interpreted as crustal weaknesses associated with pre-Andean faults reactivated as sinistral-reverse strike–slip faults during the development of the arc (Lopez-Escobar et al., 1995; Lara et al., 2006; Melnick et al., 2006; Rosenau et al., 2006; Glodny et al., 2008; Lange et al., 2008).

Stratovolcanoes and monogenetic cones, many of which are spatially associated with the LOFS or ALFS, represent the volcanism in the segment. Their composition is mainly basaltic-andesitic with minor dacitic-rhyolitic occurrences. The stratovolcanoes and/or monogenetic cones exhibit mostly primitive magmatic signatures, and are related to secondary structures forming NE-trending volcanic alignments which are directly related to the current dextral transpressional tectonic regime (Lara et al., 2006; Cembrano and Lara, 2009). In contrast, the volcanic activity spatially related to the ALFS comprises WNW-trending volcanic alignments, where mostly stratovolcanoes occur. These include a wide range of compositions, with some volcanic centers having erupted only rhyolitic products in historical times. Because of their misorientation with respect to the prevailing stress field, the WNW-striking faults require supralithostatic magmatic pressures to become active (see Lara et al., 2004, 2006; Cembrano and Lara, 2009).

The geological and structural map of the studied region (Figure 3.1) shows the location of the main stratovolcanoes, geothermal areas, and fault systems. The geothermal areas are spatially correlated to fault systems, and some of them, in the northern part, occur in the flank of active or dormant stratovolcanoes, presenting also fumarole emissions associated (RV, CR, OM, Nevado de Chillan vn.; LM, LMM, AF, Copahue vn.; JM, Tolhuaca vn.; BT, Sierra Nevada vn.; red diamonds in Fig. 3.1). PL is the only water sample associated with fumarolic activity but not occurring in proximity of volcanic centers (Fig. 3.2a). As discussed by Tardani et al. (2016) it is controlled by one of the fault sprays comprises the ”horsetail” -like northern termination of LOFS. The thermal springs reported as blue circles in Figure 3.1 are relatively low temperature thermal waters (Fig. 3.2b and c) and just few of them are spatially associated with stratovolcanoes (e.g. AV, PM, VA, PA, ER), the others emerge from fractures in plutonic rocks or sediments overlying them and are spatially related with LOFS and ALFS.

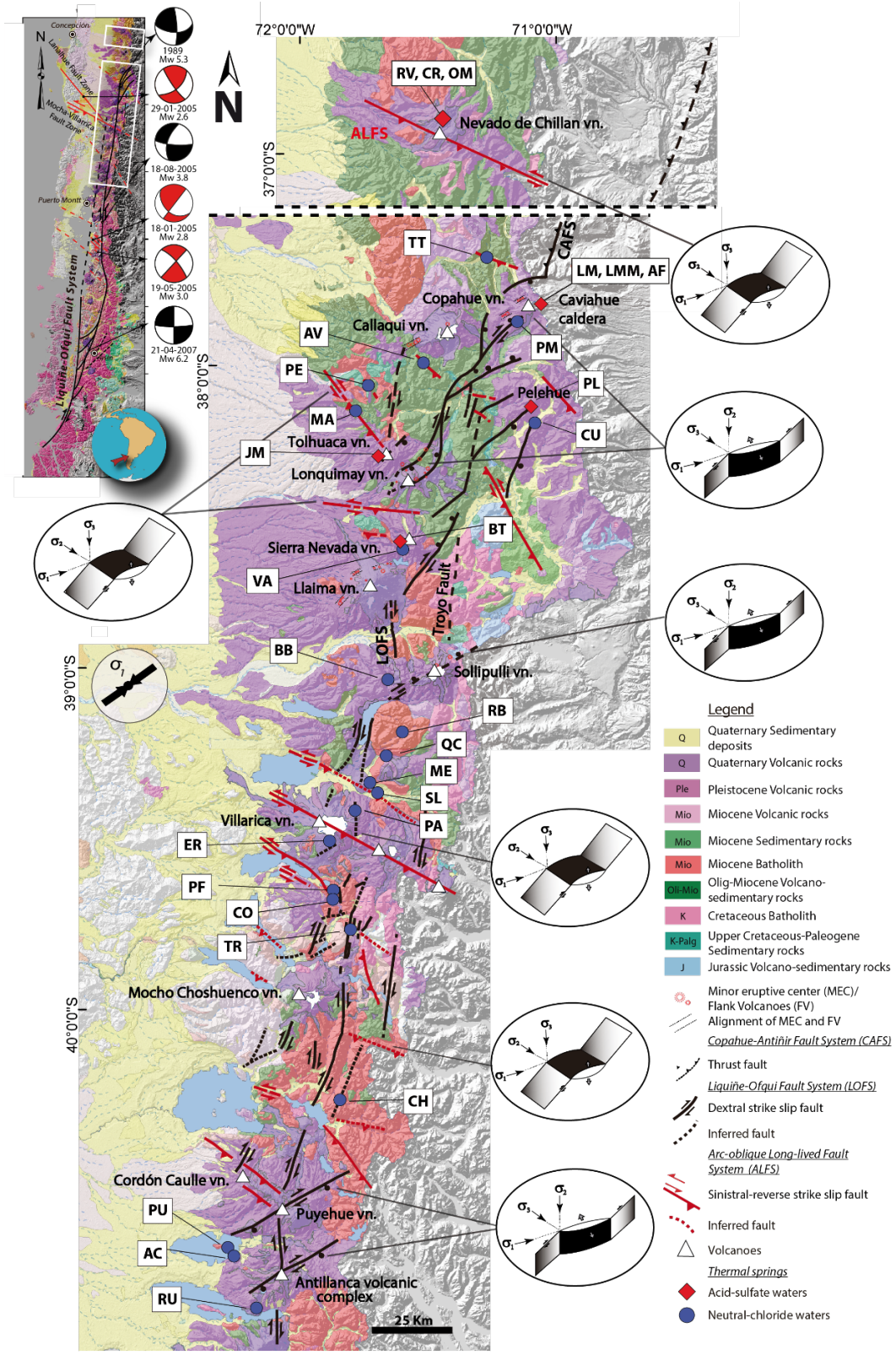

Figure 3.1. *Geologic and structural map of the central part the Southern Volcanic Zone (SVZ) in southern Chile, modified from Tardani et al., (2016). Blue circles and red diamonds represent the location of thermal springs and fumaroles samples, respectively. White triangles represent the main stratovolcanoes of the region. Sigma 1 (r1) represent the maximum regional stress field. CAFS: Copahue-Antiñir Fault System, LOFS: Liquiñe-Ofqui Fault System, ALFS: Arc-oblique Long-lived Fault System. Stress fields for the distinct fault segments are modified from Sánchez et al. (2013) and Pérez-Flores et al. (2016).*

Figure 3.2. *Pictures of geothermal field of Pelehue, PL (a), and the thermal springs of Pucon Mahuida, PM (b) and Malleco, MA (c).*

Samples and methods

Thirty hot spring water samples and fourteen fumarole condensate samples were collected from geothermal surface manifestations in the studied area between 2013 and 2015 (Fig. 3.1). *In situ* measurement techniques used in this study (temperature and pH), and the ionic balance computation have been done follow reported methodologies by Giggenbach and Goguel (1989).

Water samples were filtered through a 0.45 μm filter (cellulose acetate) into pre-cleaned high density polythene bottles. Samples for major cations and trace elements analysis were collected into high density polythene bottles and acidified with HNO_3 (Merck Suprapur®) 4N, 1 ml to 100 ml sample. Fumarole condensates where collected following the methodology by Arnórsson et al. (2006). The steam was condensed by passing it through a glass serpentine, cooled with ice and the condensate gathered in pre-cleaned high density polythene bottles.

Major anions (Cl^-, SO_4^{2-}, F^-, Br^-, and NO^{3-}) were determined using ion chromatography (IC, Dionex ICS 2100) while major cations (Na^+, K^+, Ca^{2+}, and Mg^{2+}) were determined using atomic absorption spectrophotometry (AAS, Perkin-Elmer Pinaacle 900F), at the Andean Geothermal Center of Excellence (CEGA) Laboratories, Universidad de Chile. SiO_2 contents were analyzed by Portable Photometer (Hanna HI96705), and HCO_3^-/CO_3^{2-} contents were analyzed by Volumetric Titration using Giggenbach and Goguel (1989) method. Trace metals contents were analyzed in ACTLABS laboratories using a sector field ICP MS (Element 2 from Thermo). Sample preparation for PGE's analysis has been conducted with 5ml sample solution + 5ml of matrix solution (0.6 M HCl) spiked with 0.1ml of internal standard (10ppb In). As external standards were used solutions

with 10ppt, 25ppt, 50ppt, 100ppt and 250ppt PGE's concentrations. The $^{18}O/^{16}O$ and D/H isotopic ratios ($\delta^{18}O$ and δD ‰ V-SMOW) were determined at Laboratoire de Géochimie des Isotopes Stables (Geotop-UQAM), Université du Québec à Montréal.

For this study, our database is complemented with previously published helium isotope rations recently published by Tardani et al. (2016). A selection of water and condensate sample used in this study was duplicated, and $^{3}He/^{4}He$ ratios were measured along with nitrogen and carbon isotopes ratios ($d^{15}N$, $d^{13}C$).

Results

Major and trace element composition of geothermal water

The major and trace element composition of surface geothermal water in the studied segment of the Southern Volcanic Zone are given in Tables 3.1 and 3.2, respectively. The temperatures of the sampled waters ranges from 36 to 93 °C, the pH is between 2.20 and 9.30, and total dissolved solids between 120 and 3600 ppm. Based on the major element composition, pH, temperature and Cl/SO_4 ratio, the thermal waters are qualitatively categorized into two groups: (1) NaCl waters, and (2) steam-heated acid-sulfate waters (Fig. 3.3). Figure 3.4 shows a concentration plot for major elements in geothermal waters and Figure 3.5 shows bivariate plots for major species. NaCl-rich waters present neutral to alkaline pH values and elevated Cl concentrations that correlate with Na (Fig. 3.5a), with other dominant elemental species including F (0.14-3.67 ppm), HCO_3 (21.30-1550.00 ppm), CO_3 (0.60-10.10 ppm), NO_3 (0.10-6.56 ppm), Br (0.14-2.19 ppm) and Ca (5.04-172.00 ppm) (Table 3.1, Fig. 3.4). In general, calcium and Mg concentrations increase with increasing HCO_3 contents (Figs. 3.5c and d). In contrast, steam-heated acid-sulfate waters have pH values below 4, and have relatively high dissolved SO_4 (174.00-2258.00 ppm). These waters are also characterized by relatively high concentrations of SiO_2 (79.00-370.00 ppm), Ca (2.34-105.40 ppm), K (0.50-26.60 ppm) and Mg (1.88-52.00 ppm) (Table 3.1). Magnesium and K show a positive trend with SO_4 (Fig. 3.5b and c), whereas Ca doesn't show a clear correspondence with the oxidized sulfur specie (Fig. 3.5d).

The concentration of trace elements of thermal springs range from the ppt level to several ppm (Table 3.2, Figs. 3.6, 3.7). Concentrations of alkali metals (Li, Cs, Rb) vary between 2.17 ppb and 2.78 ppm for Li, 0.53–596 ppb for Cs, and 1.29–331 ppb for Rb (Fig. 3.6a). The highest concentrations of Li, Cs and Rb are associated with neutral-chlorine waters, and increase with increasing Cl concentrations in a trend similar to Na and K (Fig. 3.8a, b and c). Barium and Sr range between 0.46–181.00 ppb and 27.40 ppb to 2.82 ppm, respectively (Fig. 3.6a). Barium is higher in acid-sulfate waters and its concentration increases with SO_4 content (Fig. 3.8d). In neutral chlorine waters, barium shows a correspondence with HCO_3 (Fig. 3.8e), similar to Ca and Mg (Fig. 3.5c and d). Strontium is present in higher concentrations in neutral chlorine waters and shows a slightly positive trend with Cl (Fig. 3.8f).

The concentrations of the metalloids B, As, Sb, Ge and Te, range from 2.76 ppb to 72.60 ppm B, 1.20 ppb to 3.92 ppm As, 0.01 to 11.10 ppb Sb, 0.16 to 14.60 ppb Ge, and 1 to 40 ppt Te. Boron, As, Sb and Ge increase with increasing Cl (Fig. 3.8g, h, i and j), and their concentration is highly pH-dependent (Kaasalainen and Stefánsson, 2012).

Table 3.1. *Chemical and isotopic composition of selected surface geothermal waters in Southern Volcanic Zone of Chile*

Sample ID	Sample Name	Location	Latitude	Longitude	T	pH	TDS	$\delta^{18}O$	$\delta^{2}H$	SiO_2	F^-	Cl^-	SO_4^{2-}	Br^-	NO_3^-	HCO_3^-	CO_3^{2-}	Na	K	Ca	Mg	I. Balance
			S	O	°C		ppm	‰	‰	ppm	ppm	ppm	ppm	ppm	ppm	ppm	ppm	ppm	ppm	ppm	ppm	
1	RV	Nevado de Chillan Vn.	36° 54.244'	71° 24.219'	68.00	4.70	570.00	-9.32	-68.20	370.00	0.26	0.25	552.00	n.d.	0.47	18.00	n.d.	56.00	21.48	105.40	33.10	-3.27
2	CR	Nevado de Chillan Vn.	36° 54.330'	71° 24.345'	82.00	2.60	440.00	-9.65	-74.60	178.00	0.24	16.62	293.76	n.d.	0.08	n.d.	n.d.	20.00	4.45	10.00	6.18	-47.64
3	OM	Nevado de Chillan Vn.	36° 54.426'	71° 24.039'	91.00	2.40	890.00	-6.18	-51.90	290.00	0.40	11.82	881.79	n.d.	n.d.	n.d.	n.d.	58.10	26.60	81.30	52.00	-0.31
4	TT	Trapa Trapa	37° 41.971'	71° 17.098'	45.00	7.80	550.00	-11.69	-84.60	50.00	2.60	178.00	14.40	0.47	n.d.	76.88	n.d.	134.00	1.70	29.00	3.20	2.54
5	AF	Copahue Vn.	37° 49.063'	71° 6.987'	87.00	2.70	2000.00	n.a.	n.a.	152.00	0.36	0.22	2258.00	n.d.	n.d.	n.d.	n.d.	22.90	12.50	35.50	24.20	-8.15
6	LMM	Copahue Vn.	37° 49.166'	71° 5.216'	93.00	3.60	470.00	-4.64	-56.10	310.00	0.33	0.32	414.52	n.d.	0.17	n.d.	n.d.	27.70	12.40	20.90	2.40	-40.17
7	LM	Copahue Vn.	37° 50.036'	71° 5.055'	88.00	2.20	1420.00	-0.65	-51.80	134.00	0.14	2.50	1336.19	n.d.	0.09	n.d.	n.d.	4.75	2.75	2.34	1.88	-94.49
8	PM	Pucon Mahuida	37° 53.811'	71° 10.536'	47.00	7.90	3600.00	-11.89	-86.80	156.00	n.d.	274.00	841.00	n.d.	6.56	1550.00	n.d.	440.00	108.00	172.00	294.00	3.85
9	AV	Termas del Avellano	37° 59.378'	71° 31.938'	78.00	7.70	430.00	-10.90	-74.10	45.00	2.47	273.00	173.00	0.59	n.d.	52.00	n.d.	246.00	12.30	34.00	0.20	4.35
10	PE	Termas de Pemehue	38° 4.579'	71° 42.082'	38.50	7.50	2450.00	-9.27	-63.50	95.00	1.43	876.00	155.00	2.19	n.d.	32.00	n.d.	325.00	45.80	122.00	0.44	-3.47
11	PL	Pelehue	38° 7.367'	71° 3.486'	82.00	3.30	120.00	-1.88	-43.80	79.00	0.10	0.24	320.00	n.d.	n.d.	n.d.	n.d.	45.30	3.39	13.90	2.71	2.43
12	CU	Termas de Coyuco	38° 11.422'	71° 2.182'	36.00	6.20	540.00	-12.40	-87.60	156.00	0.14	10.50	17.40	n.d.	n.d.	892.00	n.d.	135.00	13.10	82.20	69.50	2.36
13	MA	Termas Malleco	38°14.079'	71°43.673'	85.50	8.40	350.00	n.a.	n.a.	87.60	n.d.	82.10	40.40	0.14	n.d.	88.50	4.00	108.00	4.80	6.68	0.08	4.20
14	JM	Tolhuaca Vn.	38° 17.409'	71° 40.057'	92.00	2.40	1340.00	-5.34	-45.70	82.00	0.12	0.50	645.00	n.d.	n.d.	n.d.	n.d.	17.30	5.20	31.40	16.00	-22.77
15	BT	Sierra Nevada Vn.	38° 34.487'	71° 36.951'	87.00	3.40	210.00	n.a.	n.a.	120.00	0.08	0.22	174.00	n.d.	n.d.	n.d.	n.d.	4.10	0.50	13.90	3.96	-41.08
16	VA	Agua de la Vaca	38° 34.809'	71° 37.685'	35.00	7.20	360.00	-9.89	-70.20	84.00	0.15	138.00	110.00	0.42	n.d.	56.74	n.d.	99.10	14.90	52.20	2.98	2.82
17	BB	Termas de Balboa	38° 57.628'	71° 42.627'	45.00	7.30	380.00	-9.30	-65.24	110.00	0.64	157.00	28.60	0.48	0.16	84.10	n.d.	135.00	10.90	13.40	2.70	4.42
18	RB	Termas de Rio Blanco	39° 06.468'	71° 36.820'	51.00	7.70	140.00	-10.12	-69.01	53.00	1.03	17.10	78.60	n.d.	n.d.	80.20	n.d.	71.80	1.79	10.60	0.46	3.42
19	QC	Termas Quimey-Có	39° 13.168'	71° 41.750'	45.00	8.10	120.00	-9.66	-68.22	53.00	1.33	15.80	44.40	n.d.	n.d.	37.50	n.d.	39.00	1.09	8.38	0.60	3.24
20	ME	Parque Termal Menetùe	39° 19.527'	71° 43.113'	42.00	9.20	160.00	-9.43	-62.80	64.00	3.67	22.20	49.70	n.d.	n.d.	50.34	7.50	64.00	1.16	5.04	0.57	3.01
21	SL	Termas de San Luis	39° 20.392'	71° 41.394'	40.00	9.30	300.00	-9.53	-64.38	61.00	1.74	9.07	70.60	n.d.	0.14	39.20	10.10	60.40	1.11	5.12	0.12	2.12
22	PA	Termas de Palguin	39° 25.343'	71° 47.145'	50.00	8.90	220.00	-10.19	-72.33	65.00	2.16	19.20	72.20	n.d.	n.d.	60.03	n.d.	67.80	2.13	5.65	0.60	2.95
23	ER	Termas El Rincón	39° 30.475'	71° 51.257'	37.00	7.70	220.00	-10.00	-70.75	84.00	0.85	20.20	109.00	n.d.	n.d.	50.30	n.d.	71.70	4.98	10.90	1.77	2.95
24	PF	Eco Termas Pellaifa	39° 38.030'	71° 55.208'	50.00	8.00	120.00	-8.33	-57.70	63.00	1.12	73.40	74.80	0.21	n.d.	71.70	n.d.	111.00	3.18	6.85	0.28	4.03
25	CO	Termas de Coñaripe	39° 38.097'	71° 55.437'	74.60	8.50	440.00	-8.36	-58.04	91.00	1.57	79.60	98.80	0.24	n.d.	82.40	1.20	132.00	3.97	6.15	0.26	3.33
26	TR	Termas de Trafipan	39° 44.175'	71° 51.651'	37.20	8.70	170.00	-9.06	-59.92	48.00	0.72	23.60	73.20	n.d.	0.10	39.40	n.d.	57.60	1.61	9.82	0.82	3.77
27	CH	Termas de Chihuio	40° 11.407'	71° 55.954'	82.50	9.30	300.00	-10.39	-70.60	90.20	0.74	14.40	188.00	n.d.	n.d.	21.30	3.00	103.00	4.74	13.10	0.01	4.42
28	PU	Termas de Puyehue	40° 42.645'	72° 19.403'	60.00	8.30	430.00	-8.84	-58.40	87.00	1.97	148.00	116.00	0.60	n.d.	63.46	0.60	160.00	5.64	8.78	0.79	-0.88
29	AC	Termas de Aguas Calientes	40° 43.918'	72° 18.357'	66.00	7.80	560.00	-8.97	-53.30	95.00	1.29	191.00	118.00	0.77	n.d.	53.08	n.d.	179.00	8.00	23.20	1.04	2.43
30	RU	Termas de Rupanco	40° 51.386'	72° 13.459'	80.00	7.90	660.00	-9.04	-62.00	109.00	0.86	245.00	113.00	0.92	n.d.	78.71	n.d.	184.00	7.53	23.60	0.30	-4.82

Table 3.2. *Trace elements composition of surface geothermal waters in Southern Volcanic Zone of Chile*

Sample ID	Sample Name	Location	B	As	Li	Cs	Rb	Ba	Sr	Al	Fe	Mn	Co	Ni	Cu	Zn	V	Cr	Sc	Ti	Mo	Cd	Y	Zr	Pb	Sb	Ge	Te	La	Ce	W	Th	U
			ppb	ppb	ppb	ppb	ppb	ppb	ppb	ppb	ppb	ppb	ppb	ppb	ppb	ppb	ppb	ppb	ppb	ppb	ppb	ppb	ppb	ppb	ppb	ppb	ppb	ppb	ppb	ppb	ppb	ppb	ppb
1	RV	Nevado de Chillan Vn.	440.00	1.20	64.30	3.45	12.20	40.00	78.60	800.10	71.00	2500.00	1.86	0.94	8.52	43.30	1.42	2.12	n.d.	1.36	0.14	0.10	0.08	0.11	0.11	0.09	0.93	0.002	0.95	0.12	0.03	0.003	0.01
2	CR	Nevado de Chillan Vn.	15.70	4.07	23.90	4.28	16.10	13.30	47.50	4290.00	2530.00	287.00	0.50	0.70	0.63	68.90	20.90	1.04	0.86	3.42	0.29	0.02	2.38	0.08	0.16	0.02	0.16	n.d.	1.71	1.96	n.d.	0.003	0.02
3	OM	Nevado de Chillan Vn.	88.50	3.05	11.70	2.33	54.30	32.20	143.00	10600.00	69600.00	2690.00	13.80	26.00	25.40	225.00	3.24	4.95	5.06	0.48	0.01	0.10	17.60	0.02	0.07	0.01	0.47	0.004	1.57	6.15	0.05	0.10	0.65
4	TT	Trapa Trapa	276.00	16.10	74.80	1.66	4.25	1.74	305.00	49.10	28.00	35.00	0.03	0.40	0.18	21.80	0.11	0.42	n.d.	1.71	0.41	0.02	0.02	0.02	0.05	0.05	9.27	0.01	0.03	0.04	2.18	0.001	0.001
5	AF	Copahue Vn.	82.70	4.06	5.88	1.73	56.90	31.10	141.00	56200.00	519000.00	2090.00	39.20	100.00	83.10	1480.00	198.00	57.10	31.40	16.70	0.11	0.42	41.90	0.31	0.17	0.33	0.47	n.d.	4.44	14.6	0.23	2.07	1.69
6	LMM	Copahue Vn.	450.00	3.46	8.85	5.08	40.30	23.40	87.20	5060.00	4370.00	188.00	0.25	0.60	0.92	153.00	9.47	1.25	0.93	3.30	0.11	0.02	4.14	0.09	0.10	0.13	0.44	0.01	2.18	3.22	n.d.	0.09	0.12
7	LM	Copahue Vn.	773.00	15.20	2.17	1.24	24.00	9.19	27.40	162.00	4100.00	165.00	0.47	2.41	1.81	178.00	4.58	1.37	1.17	4.42	0.61	0.03	0.25	0.18	0.29	0.31	1.03	0.003	11.40	0.09	n.d.	0.01	0.06
8	PM	Pucon Mahuida	549.00	14.10	810.00	17.60	285.00	30.50	816.00	17.50	702.00	130.00	0.93	5.04	0.35	26.30	0.30	0.81	0.38	1.68	3.04	0.05	0.09	0.18	0.18	0.12	5.31	0.04	0.05	0.05	0.21	0.02	0.07
9	AV	Termas del Avellano	437.00	212.00	691.00	110.00	70.80	2.35	756.00	33.90	8.00	5.80	0.05	0.23	0.33	15.20	0.21	0.35	n.d.	2.09	13.00	0.03	0.01	0.03	0.03	0.91	6.72	0.01	0.03	0.04	29.80	0.001	0.001
10	PE	Termas de Pemehue	17200.00	3920.00	2780.00	596.00	331.00	7.98	2820.00	63.30	47.00	46.60	0.03	0.12	0.59	13.40	0.14	0.11	0.01	1.83	23.50	0.10	0.04	0.06	0.16	11.10	5.80	0.02	0.10	0.05	53.40	0.003	0.001
11	PL	Pelehue	989.30	16.20	119.00	21.30	18.50	12.90	130.00	672.00	370.00	39.70	0.27	0.48	1.13	55.20	2.78	0.49	0.02	5.10	0.71	0.01	0.18	0.09	0.17	0.21	1.08	0.002	1.63	0.31	0.38	0.002	0.01
12	CU	Termas de Coyuco	644.00	36.60	110.00	3.34	28.80	18.10	548.00	29.30	2940.00	166.00	0.25	0.80	0.29	16.90	0.18	0.07	n.d.	0.75	6.11	0.01	0.10	n.d.	0.11	0.01	2.99	0.003	0.04	0.05	0.10	0.001	0.003
13	MA	Termas Malleco	72600.00	4.62	703.00	53.80	39.50	1.38	51.90	264.00	84.00	4.54	n.d.	0.02	n.d.	13.30	0.33	0.05	n.d.	0.56	3.00	0.01	0.05	n.d.	0.12	8.73	14.60	n.d.	n.d.	n.d.	6.30	n.d.	n.d.
14	JM	Tolhuaca Vn.	177.00	6.66	11.70	2.96	29.20	13.60	68.10	41000.00	33700.00	862.00	8.37	5.11	4.78	210.00	114.00	9.11	16.90	5.31	0.08	0.08	18.10	0.13	0.22	0.06	6.59	0.01	1.97	5.86	n.d.	0.61	0.76
15	BT	Sierra Nevada Vn.	127.00	4.05	4.47	0.53	1.29	43.60	128.00	1550.00	2010.00	1.70	1.10	1.43	3.50	119.00	6.00	9.05	0.09	2.94	0.13	0.01	1.87	0.02	0.33	0.09	0.33	0.01	0.55	1.23	n.d.	0.01	0.01
16	VA	Agua de la Vaca	11400.00	840.00	786.00	206.00	111.00	2.99	297.00	9.10	8.00	1.42	0.01	0.09	0.15	17.00	7.46	0.02	0.01	0.74	0.81	0.01	0.00	n.d.	0.09	3.05	2.90	n.d.	0.00	0.01	15.40	n.d.	0.003
17	BB	Termas de Balboa	1840.00	169.00	542.00	54.40	62.50	2.54	106.00	4.10	1.00	0.22	0.03	n.d.	0.14	6.90	13.80	0.18	0.08	0.32	7.69	0.01	0.01	0.01	n.d.	3.57	6.07	0.01	0.01	0.00	6.64	n.d.	0.04
18	RB	Termas de Rio Blanco	115.00	9.21	132.00	5.20	7.05	2.24	278.00	7.30	2.00	0.12	0.03	n.d.	0.11	5.30	0.70	0.02	0.06	0.10	21.70	0.02	0.01	0.02	n.d.	0.39	2.05	0.02	0.01	0.00	5.66	n.d.	0.05
19	QC	Termas Quimey-Có	103.00	12.90	29.70	4.73	6.24	1.56	110.00	12.60	2.00	0.26	0.03	n.d.	0.12	5.70	1.27	n.d.	0.13	0.35	24.60	0.03	0.00	0.02	n.d.	0.22	0.83	0.01	0.01	0.00	13.10	n.d.	0.04
20	ME	Parque Termal Menetùe	304.00	26.00	131.00	17.60	11.00	0.61	56.90	20.60	78.00	13.30	0.04	0.09	0.21	3.50	1.41	n.d.	0.04	1.02	19.60	0.02	0.01	0.10	n.d.	0.14	3.44	n.d.	0.01	0.01	17.50	0.001	0.06
21	SL	Termas de San Luis	126.00	16.50	52.10	6.64	7.40	0.69	74.00	9.40	1.00	0.21	0.02	n.d.	0.52	5.10	2.70	0.01	0.05	0.15	10.90	0.02	0.00	0.02	0.01	0.13	1.58	0.001	0.00	0.00	6.74	n.d.	0.11
22	PA	Termas de Palguin	670.00	76.60	96.20	8.65	9.27	1.79	31.10	194.00	127.00	4.70	0.12	0.25	0.09	7.30	14.40	0.12	0.09	1.10	15.00	0.02	0.05	0.12	0.08	0.54	3.48	n.d.	0.03	0.06	16.00	0.002	0.03
23	ER	Termas El Rincón	851.00	56.40	99.70	5.18	21.80	2.60	34.40	12.30	6.00	0.22	0.02	n.d.	0.09	3.10	22.10	0.08	0.10	1.83	3.79	n.d.	0.01	0.01	n.d.	1.60	3.45	n.d.	0.00	0.01	4.03	n.d.	0.08
24	PF	Eco Termas Pelhifa	3200.00	1070.00	191.00	17.50	16.80	1.23	44.20	26.60	3.00	1.98	0.02	n.d.	0.10	4.80	1.92	n.d.	0.05	n.d.	19.30	0.02	0.00	0.01	n.d.	9.72	6.14	0.001	0.00	0.00	25.50	n.d.	0.02
25	CO	Termas de Coñaripe	3740.00	1370.00	229.00	27.50	24.50	4.36	56.70	151.00	3.00	3.66	0.03	n.d.	0.14	6.30	5.02	n.d.	0.05	1.00	24.30	0.02	0.02	0.02	n.d.	1.72	7.77	0.002	0.01	0.02	34.70	n.d.	0.02
26	TR	Termas de Trafipan	330.00	38.10	25.90	5.48	8.26	0.46	71.20	7.00	n.d.	0.09	0.02	n.d.	n.d.	2.20	1.81	n.d.	0.04	0.23	8.71	0.01	0.00	0.00	n.d.	0.32	2.31	0.004	0.01	0.01	8.32	n.d.	0.02
27	CH	Termas de Chihuio	76.00	13.30	39.10	5.40	15.30	7.50	294.00	31.00	2.00	0.19	0.00	n.d.	n.d.	9.20	0.24	n.d.	0.02	n.d.	20.90	0.00	0.00	0.01	0.03	0.25	2.28	n.d.	0.00	0.00	20.50	n.d.	n.d.
28	PU	Termas de Puyehue	16100.00	724.00	392.00	30.60	31.10	4.12	138.00	19.10	9.00	1.25	0.00	0.10	0.30	16.30	4.01	0.01	0.02	0.34	12.00	0.00	0.00	0.01	0.27	4.15	8.55	0.002	0.01	0.02	66.80	0.001	0.002
29	AC	Termas de Aguas Calientes	18000.00	602.00	583.00	102.00	78.10	7.78	251.00	49.40	13.00	1.71	0.01	0.20	0.39	8.60	4.38	0.08	0.02	0.38	10.40	0.01	0.01	0.02	0.10	3.76	4.18	n.d.	0.01	0.02	55.50	n.d.	0.02
30	RU	Termas de Rupanco	19500.00	279.00	152.00	26.40	30.80	7.37	184.00	35.30	10.00	6.57	0.01	0.18	0.18	9.30	0.68	0.30	0.03	0.16	9.86	0.00	0.01	0.00	0.07	2.17	8.35	n.d.	0.01	0.02	53.30	n.d.	n.d.

Highest concentrations of these elements are commonly associated with neutral chlorine waters. Concentrations of base metals including Al, Fe, Mn, Co, Ni, Cu, Zn, V and Cr show a wide variation (Fig. 3.6a and Table 3.2). Aluminum varies between 4.10 ppb to 56.00 ppm, Fe between 1.00 ppb to 519.00 ppm, Mn between 0.09 ppb to 2.69 ppm, Co between 2.00 ppt to 39.20 ppb, Ni between 0.02 to 100.00 ppb, Cu between 0.09 to 83.10 ppb, Zn between 2.20 ppb to 1.48 ppm, V between 0.11 to 198.00 ppb, and Cr between 0.01 to 57.10 ppb. All these elements invariably reach the highest concentrations in the steam-heated acid-sulfate waters, and at the highest SO_4 concentrations (Fig. 3.9a, b, c, d, e, f, g, h and i).

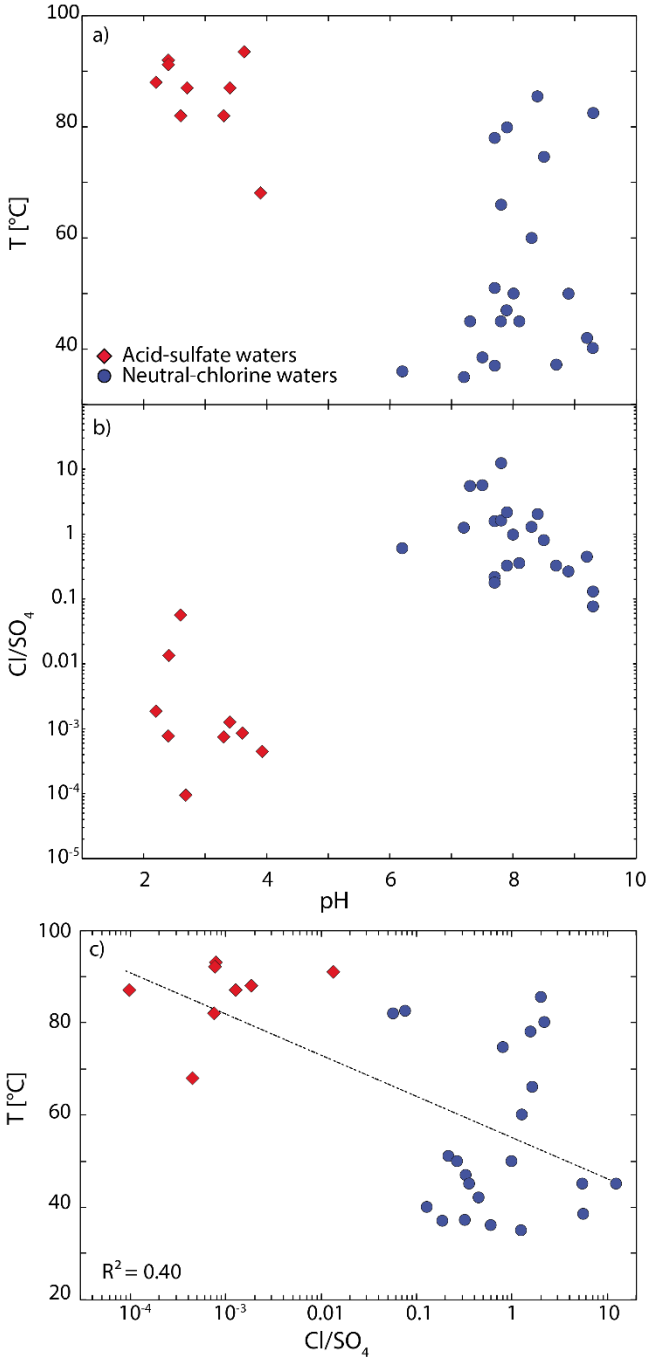

Figure 3.3. *T vs pH (a), Cl/SO_4 vs pH (b) and T vs Cl/SO_4 plots of thermal waters of Southern Volcanic Zone of Chile. Based on their physico-chemical composition and formation mechanism, geothermal waters may be divided into acid-sulfate waters (red diamonds) and neutral-chlorine waters (blue circles).*

The metals Sc, Ti, Mo, Cd, Y, Zr, Pb and W are generally very low (sub ppb) in thermal springs, although the maximum concentrations measured in geothermal waters of SVZ are within the range of 10's of ppb (Fig. 3.6b and Table 2). Maximum concentrations for Sc is 31.40 ppb, 16.70 ppb for Ti, 24.60 ppb for Mo, 0.42 ppb for Cd, 0.31 ppb for Zr, 41.90 ppb for Y, 1.10 ppb for Pb, and 66.80 ppb for W. The highest concentration of Sc, Ti, Cd, Y, Zr and Pb were detected in steam-heated acid-sulfate waters (Fig. 3.6b), and Sc, Ti, Y and Zr show a positive correspondence with SO_4 (Fig. 3.10a, b, c and d). In contrast, the maximum concentrations of molybdenum and W were found in neutral-chlorine waters (Fig 3.6b), and both metals correlate positively with Cl contents (Fig. 3.10e and f). Lanthanum, Ce, Th and U concentrations vary between 1.00 ppt and 11.40 ppb for La, 3.00 ppt and 14.60 ppb for Ce, 1.00 ppt and 2 ppb for Th, and 1.00 ppt and 1.69 ppb for U. The highest concentrations of these elements were measured in acid-sulfate waters (Fig. 3.6b). Figure 3.10g-i shows bivariate plots for La, Ce and U, respectively, all showing a positive correspondence with SO_4.

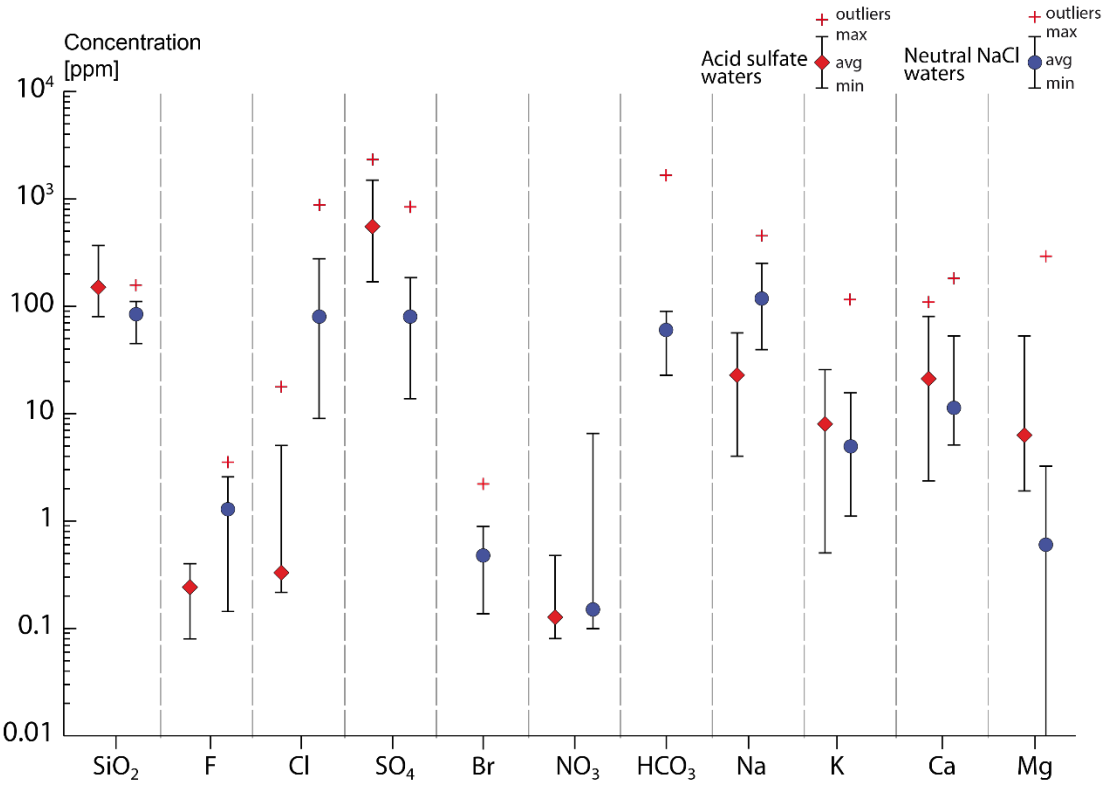

Figure 3.4. *Concentration plot for major chemical species in acid-sulfate waters (red diamonds) and neutral-chlorine waters (blue circles) of Southern Volcanic Zone of Chile. Data are plotted in parts per million (ppm) on a vertical logarithmic scale. For each element, average concentrations are shown together with maximum and minimum values, and with outliers (red cross).*

Finally, the concentration of precious metals vary from sub-ppt to ppb levels (Table 3.3, Fig. 3.7). Silver and Au concentrations range between 5.00 and 120.00 ppt, and 0.10 and 1.30 ppt, respectively. It is noteworthy to mention that appreciable concentrations of Platinum Group Elements (PGE) were detected in selected geothermal water samples. For example, ruthenium, Ir and Pt concentration reach few tens of ppt. In contrast, palladium and Rh display higher concentrations, i.e., between 15.00 and 1990.00 ppt (Pd), and between 0.70 and 142.00 ppt (Rh).

Rhodium displays a positive correlation with SO_4 (Fig. 3.11a), whereas Pd does not show an evident correspondence with SO_4 or Cl anionic species (Fig. 3.11b and c).

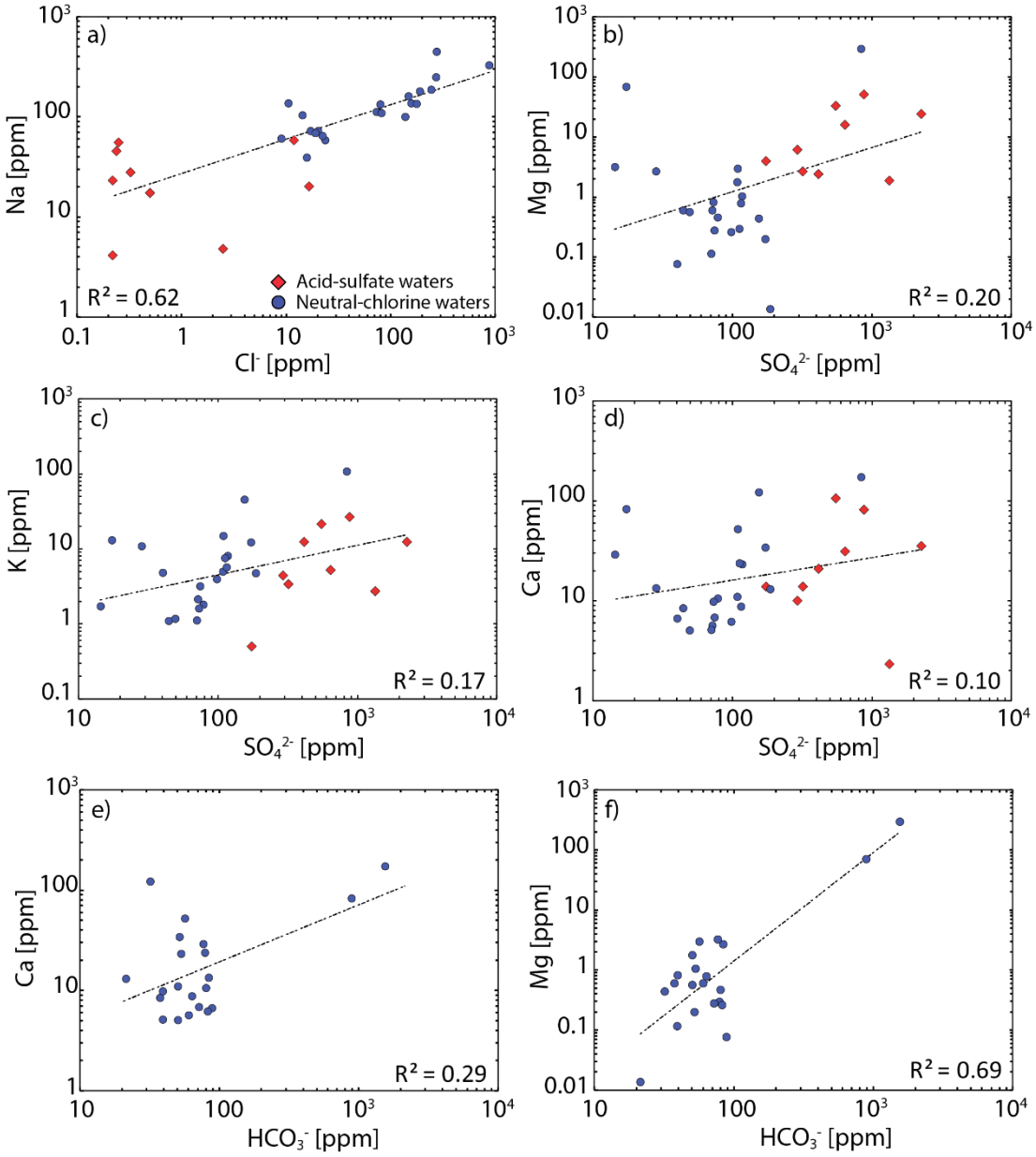

Figure 3.5. *Elemental correlation diagrams of Na-Cl (a), Mg-SO_4 (b), K-SO_4 (c), Ca-SO_4 (d), Ca-HCO_3 (e) and Mg-HCO_3 (f) in acid-sulfate waters (red diamonds) and neutral-chlorine waters (blue circles) of Southern Volcanic Zone of Chile. R-squared (R2) values are shown for every plot.*

Trace element geochemistry of fumarole condensates

The trace element composition of the 13 steam vent discharge samples is listed in Table 3.4 and shown in Figure 3.12. Most elements occur at sub-ppb levels, with the exception of As, B, Al, Mn, Ba, Rb, Sr, Fe, Ni, Zn, Ti, V, Cr and Pb. Among these, boron and Al show the highest concentrations, up to 7.07 and 1.52 ppm, respectively.

Precious metal concentrations (Ag, Au and PGE's) occur at ppt levels (Table 4). Apart from Au (0.10 ppt), palladium and Ir show the highest concentrations, reaching few tens of ppt (Table 4). The major component concentrations of these fumarole condensates were previously reported by Tardani et al., 2016 and occur at sub-ppm levels, with the exception of Na and Ca that reach 1.52 and 1.67 ppm, respectively.

Hydrogen and oxygen stable isotope data

Stable isotopes in water ($\delta^{18}O$, δD) are useful tracers to identify the origin of the geothermal fluids and the secondary processes (e.g. boiling, mixing, water–rock interaction) affecting the thermal waters (Arnórsson, 2000). In SVZ, $\delta^{18}O$ and δD values range from -12.40 ‰ to -0.65 ‰ and from -87.60 ‰ to -43.80 ‰, respectively. In the δD versus $\delta^{18}O$ diagram (Figure 3.13), the neutral-chlorine waters (blue circles) lie on the global meteoric water line (GMWL; Craig 1963), whereas the acid-sulfate waters show a shift towards more positive values of $\delta^{18}O$ and δD respect to the GMWL, in an hypothetical mixing line with Andesitic Waters (Giggenbach and Soto, 1992).

Table 3.3. *Precious metals composition of surface geothermal waters in Southern Volcanic Zone of Chile*

Sample ID	Sample Name	Location	Ag	Au	Ru	Rh	Pd	Ir	Pt
			ppt	ppt	ppt	ppt	ppt	ppt	ppt
1	RV	Nevado de Chillan Vn.	50.00	n.d.	n.d.	28.10	367.00	n.d.	n.d.
2	CR	Nevado de Chillan Vn.	20.00	n.d.	n.d.	2.40	192.00	n.d.	n.d.
3	OM	Nevado de Chillan Vn.	11.00	n.d.	n.d.	n.d.	181.00	n.d.	n.d.
4	TT	Trapa Trapa	n.d.	0.10	n.d.	1.40	n.d.	5.00	n.d.
5	AF	Copahue Vn.	n.d.	n.d.	n.d.	n.d.	n.d.	n.d.	n.d.
6	LMM	Copahue Vn.	20.00	n.d.	n.d.	5.10	322.00	n.d.	1.10
7	LM	Copahue Vn.	30.00	0.30	n.d.	n.d.	15.00	n.d.	n.d.
8	PM	Pucon Mahuida	120.00	0.40	6.00	34.80	220.00	9.00	2.60
9	AV	Termas del Avellano	n.d.	0.40	n.d.	28.40	150.00	4.00	1.20
10	PE	Termas de Pemehue	30.00	0.80	18.00	142.00	1990.00	n.d.	n.d.
11	PL	Pelehue	20.00	n.d.	n.d.	5.60	92.00	n.d.	n.d.
12	CU	Termas de Coyuco	14.00	n.d.	n.d.	n.d.	n.d.	n.d.	n.d.
13	MA	Termas Malleco	5.00	1.30	n.d.	0.90	150.00	n.d.	n.d.
14	JM	Tolhuaca Vn.	20.00	n.d.	n.d.	3.20	1220.00	n.d.	n.d.
15	BT	Sierra Nevada Vn.	30.00	n.d.	n.d.	5.30	202.00	n.d.	n.d.
16	VA	Agua de la Vaca	13.00	0.10	n.d.	n.d.	n.d.	n.d.	n.d.
17	BB	Termas de Balboa	84.00	n.d.	n.d.	1.50	n.d.	n.d.	n.d.
18	RB	Termas de Rio Blanco	34.00	0.20	n.d.	2.50	n.d.	n.d.	n.d.
19	QC	Termas Quimey-Có	35.00	n.d.	n.d.	n.d.	n.d.	n.d.	n.d.
20	ME	Parque Termal Menetùe	33.00	n.d.	n.d.	2.40	n.d.	n.d.	n.d.
21	SL	Termas de San Luis	26.00	0.20	n.d.	1.70	n.d.	n.d.	n.d.
22	PA	Termas de Palguin	30.00	0.20	n.d.	0.80	n.d.	n.d.	n.d.
23	ER	Termas El Rincón	25.00	0.20	n.d.	n.d.	n.d.	n.d.	n.d.
24	PF	Eco Termas Pellaifa	60.00	n.d.	n.d.	0.70	n.d.	n.d.	n.d.
25	CO	Termas de Coñaripe	71.00	0.40	n.d.	1.30	n.d.	n.d.	n.d.
26	TR	Termas de Trafipan	38.00	0.10	n.d.	1.00	n.d.	n.d.	n.d.
27	CH	Termas de Chihuio	n.d.	n.d.	n.d.	n.d.	n.d.	n.d.	n.d.
28	PU	Termas de Puyehue	21.00	0.10	n.d.	n.d.	n.d.	n.d.	n.d.
29	AC	Termas de Aguas Calientes	8.00	0.20	n.d.	n.d.	n.d.	n.d.	n.d.
30	RU	Termas de Rupanco	24.00	n.d.	n.d.	n.d.	n.d.	n.d.	n.d.

Table 3.4. *Major and trace elements composition of fumarole condensates in Southern Volcanic Zone of Chile*

Sample	Location	Latitude S	Longitude O	T °C	Na ppm	K ppm	Ca ppm	Mg ppm	B ppb	As ppb	Li ppb	Cs ppb	Rb ppb	Ba ppb	Sr ppb	Al ppb	Fe ppb	Mn ppb	Co ppb	Ni ppb	Cu ppb	Zn ppb
LN	Nevado de Chillan Vn.	36° 54.107'	71° 24.035'	93.5	n.d.	n.d.	n.d.	0.02	n.d.	n.d.	n.d.	n.d.	n.d.	7.76	n.d.	401.00	107.00	n.d.	n.d.	n.d.	n.d.	n.d.
RV	Nevado de Chillan Vn.	36° 54.244'	71° 24.219'	94.4	1.52	n.d.	n.d.	n.d.	n.d.	2.15	n.d.	0.11	n.d.	14.80	1.15	390.00	n.d.	n.d.	0.10	n.d.	n.d.	n.d.
CR	Nevado de Chillan Vn.	36° 54.330'	71° 24.345'	93.6	n.d.	n.d.	0.95	0.06	11.60	2.48	n.d.	0.29	n.d.	8.93	2.11	1520.00	n.d.	n.d.	0.59	n.d.	n.d.	n.d.
QA	Nevado de Chillan Vn.	36° 54.317'	71° 24.085'	93	0.50	0.11	n.d.	0.04	12.50	n.d.	n.d.	n.d.	n.d.	16.80	1.67	836.00	189.00	n.d.	0.15	n.d.	n.d.	n.d.
OM	Nevado de Chillan Vn.	36° 54.426'	71° 24.039'	93.9	1.25	0.35	1.67	0.55	43.20	2.55	0.74	0.16	1.62	6.43	10.90	183.00	297.00	86.30	0.93	0.50	0.12	39.10
AF	Copahue Vn.	37° 49.063'	71° 6.987'	93	n.d.	0.18	n.d.	n.d.	n.d.	n.d.	n.d.	n.d.	n.d.	12.60	n.d.	1050.00	n.d.	n.d.	n.d.	n.d.	n.d.	54.60
CC	Copahue Vn.	37° 49.158'	71° 9.744'	94.8	0.53	0.17	0.70	n.d.	n.d.	n.d.	n.d.	n.d.	n.d.	13.90	1.15	110.00	n.d.	n.d.	n.d.	n.d.	n.d.	n.d.
LMM	Copahue Vn.	37° 49.166'	71° 5.216'	93.4	n.d.	n.d.	1.27	0.07	67.00	2.15	n.d.	n.d.	n.d.	9.37	2.61	310.00	n.d.	n.d.	0.21	n.d.	n.d.	114.00
CB	Copahue Vn.	37° 49.216'	71° 5.823'	93	n.d.	n.d.	n.d.	n.d.	n.d.	n.d.	n.d.	0.29	n.d.	13.40	1.63	238.00	n.d.	n.d.	0.16	n.d.	n.d.	n.d.
LM	Copahue Vn.	37° 50.036'	71° 5.055'	93.1	0.08	0.06	0.12	0.04	188.00	5.89	n.d.	0.02	0.13	13.50	1.60	204.00	157.00	2.58	0.11	1.02	0.81	14.20
PL	Pelehue	38° 7.367'	71° 3.486'	93.4	0.76	n.d.	0.57	0.04	707.00	14.50	n.d.	0.22	n.d.	15.40	1.76	131.00	n.d.	n.d.	n.d.	n.d.	n.d.	n.d.
JM	Tolhuaca Vn.	38° 17.409'	71° 40.057'	92	n.d.	n.d.	n.d.	n.d.	n.d.	n.d.	n.d.	n.d.	n.d.	7.53	n.d.	507.00	n.d.	n.d.	0.22	n.d.	n.d.	n.d.
BT	Sierra Nevada Vn.	38° 34.487'	71° 36.951'	87	n.d.	n.d.	n.d.	n.d.	n.d.	n.d.	n.d.	0.11	n.d.	13.80	n.d.	168.00	n.d.	n.d.	n.d.	n.d.	n.d.	n.d.

Table 3.4. continue

Sample	V	Cr	Sc	Ti	Mo	Cd	Y	Zr	Pb	Sb	Te	Ge	La	Ce	W	Th	U	Ag	Au	Ru	Rh	Pd	Ir	Pt
	ppb	ppb	ppb	ppb	ppb	ppb	ppb	ppb	ppb	ppb	ppb	ppb	ppb	ppb	ppb	ppb	ppb	ppt	ppt	ppt	ppt	ppt	ppt	ppt
LN	0.36	n.d.	n.d.	n.d.	n.d.	n.d.	n.d.	n.d.	n.d.	n.d.	0.60	0.20	n.d.	n.d.	0.20	0.002	n.d.	n.d.	n.d.	n.d.	n.d.	1.00	n.d.	n.d.
RV	0.29	n.d.	n.d.	n.d.	n.d.	n.d.	n.d.	n.d.	n.d.	n.d.	n.d.	0.98	n.d.	n.d.	n.d.	0.002	n.d.	n.d.	n.d.	n.d.	1.40	n.d.	13.00	n.d.
CR	0.37	1.02	n.d.	1.76	n.d.	n.d.	n.d.	0.12	3.52	n.d.	n.d.	0.19	0.34	0.43	n.d.	0.003	n.d.	n.d.	n.d.	n.d.	n.d.	n.d.	n.d.	n.d.
QA	0.60	n.d.	n.d.	9.66	n.d.	n.d.	n.d.	n.d.	n.d.	n.d.	1.27	0.63	n.d.	n.d.	n.d.	n.d.	n.d.	n.d.	n.d.	n.d.	n.d.	3.00	n.d.	n.d.
OM	1.30	0.10	0.02	0.39	0.03	0.003	0.07	0.06	0.08	0.03	0.02	0.01	0.07	0.19	0.69	n.d.	0.011	8.00	n.d.	n.d.	n.d.	20.00	n.d.	n.d.
AF	0.24	n.d.	n.d.	n.d.	n.d.	n.d.	n.d.	0.19	n.d.	n.d.	0.76	0.20	n.d.	n.d.	n.d.	0.003	n.d.	n.d.	n.d.	n.d.	n.d.	n.d.	n.d.	n.d.
CC	0.30	n.d.	n.d.	n.d.	n.d.	n.d.	n.d.	n.d.	n.d.	n.d.	0.67	0.25	n.d.	n.d.	n.d.	n.d.	n.d.	n.d.	n.d.	n.d.	n.d.	n.d.	n.d.	n.d.
LMM	0.36	1.01	n.d.	1.09	n.d.	n.d.	n.d.	0.36	2.73	n.d.	n.d.	n.d.	0.76	0.89	0.45	0.006	n.d.	n.d.	0.10	n.d.	n.d.	n.d.	n.d.	n.d.
CB	0.32	n.d.	n.d.	n.d.	n.d.	n.d.	n.d.	n.d.	n.d.	n.d.	n.d.	1.60	n.d.	n.d.	n.d.	n.d.	n.d.	n.d.	n.d.	n.d.	n.d.	n.d.	n.d.	n.d.
LM	0.27	0.30	0.01	2.57	0.05	0.004	0.04	0.27	0.41	0.04	0.03	0.59	0.05	0.13	0.02	n.d.	0.002	n.d.	0.10	n.d.	n.d.	n.d.	n.d.	n.d.
PL	0.17	n.d.	n.d.	n.d.	n.d.	n.d.	n.d.	0.12	0.56	n.d.	n.d.	0.46	n.d.	n.d.	n.d.	0.002	0.012	n.d.	n.d.	n.d.	0.60	n.d.	2.00	n.d.
JM	0.31	n.d.	n.d.	n.d.	n.d.	n.d.	n.d.	n.d.	n.d.	n.d.	n.d.	0.86	4.06	3.44	n.d.	0.002	n.d.	n.d.	n.d.	n.d.	n.d.	n.d.	n.d.	n.d.
BT	0.34	n.d.	n.d.	n.d.	n.d.	n.d.	n.d.	n.d.	n.d.	n.d.	n.d.	0.58	n.d.	n.d.	n.d.	n.d.	n.d.	n.d.	n.d.	n.d.	1.10	n.d.	n.d.	0.90

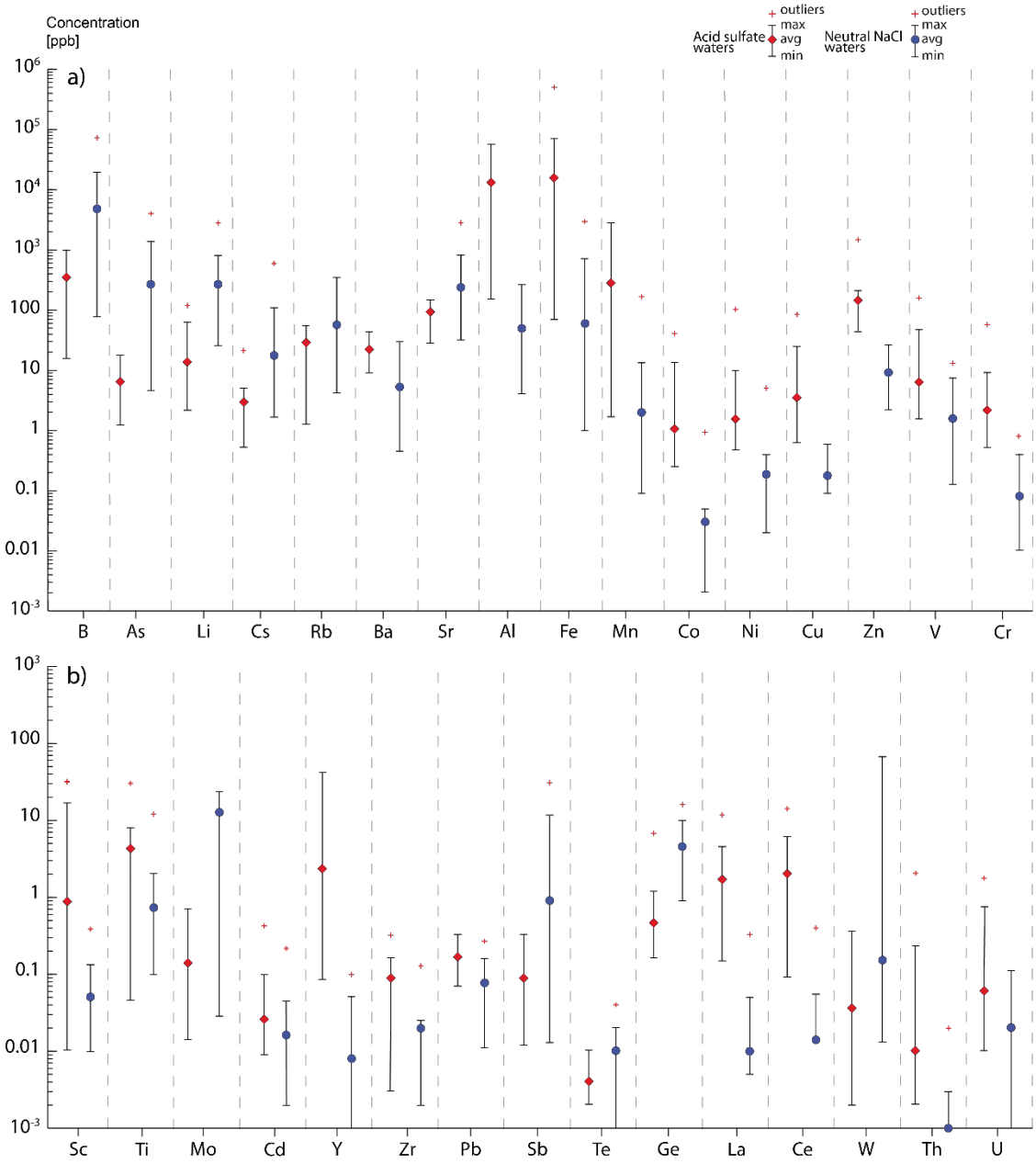

Figure 3.6. *Concentration plot for trace elements in acid-sulfate waters (red diamonds) and neutral-chlorine waters (blue circles) of Southern Volcanic Zone of Chile. Data are plotted in parts per billion (ppb) on a vertical logarithmic scale. For each element, average concentrations are shown together with maximum and minimum values, and with outliers (red cross).*

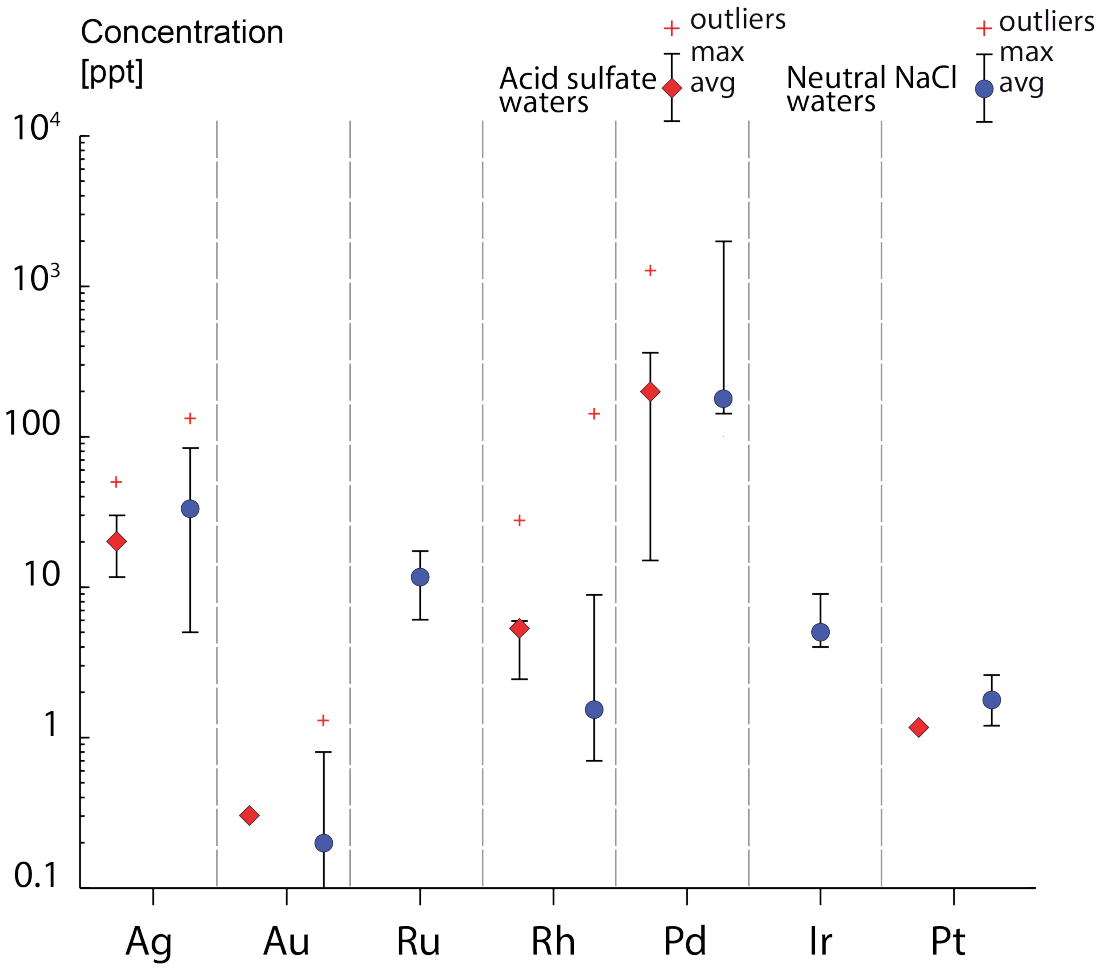

Figure 3.7. *. Concentration plot for precious metals in acid-sulfate waters (red diamonds) and neutral-chlorine waters (blue circles) of Southern Volcanic Zone of Chile. Data are plotted in parts per trillion (ppt) on a vertical logarithmic scale. For each element, average concentrations are shown together with maximum and minimum values, and with outliers (red cross).*

Discussion

In the following section we discuss the main geochemical features of geothermal fluids in the studied segment, and we focus on exploring the relation between the trace element concentrations and the structural features associated with the LOFS and ALFS. For this purpose, we compare the trace element database presented above with helium isotope data ($^3He/^4He$) recently reported by Tardani et al. (2016). In this segment of the Southern Volcanic Zone (SVZ), thermal fluids are characterized by a wide range of $^3He/^4He$ ratios (3.39 Ra to 7.53 Ra, where Ra = $(^3He/^4He)_{air}$) that are strongly controlled by the regional distribution of fault-fracture meshes and the variation of source magma compositions. The first-order control on helium isotopes signatures of thermal fluids in the studied segment is the degree of crustal assimilation of the magmatic sources, which is governed by the LOFS and ALFS spatial distribution (Tardani et al., 2016). Furthermore, as reported by (Tardani et al., 2016), mixing with meteoric waters is a relevant processes affecting the chemical and isotopic composition of hydrothermal fluids in the studied

segment of the SVZ. Mixing with meteoric fluids is particularly relevant in the neutral-chlorine hot springs located between Villarica and Mocho-Choshuenco volcanoes (Fig. 3.1). Within this region, most of the neutral-chlorine thermal waters are associated with the main traces of the LOFS that, due to their high vertical permeability, allow a deeper circulation of the meteoric fluids, further increasing the dilution process in this already humid and rainy region. Our δD and $\delta^{18}O$ isotope data (Fig. 3.13) are in agreement with the aforementioned studies. All neutral-chlorine water samples (blue circles) lie on the Global Meteoric Water Line (GMWL), showing a significant meteoric contribution for H and O. In contrast, the acid-sulfate waters (red diamonds in Fig. 3.13) plot between the GMWL and the andesitic water field (grey box, after Giggenbach and Soto, 1992), displaying a variable mixing degree between waters of magmatic and meteoric derivation. In sections 5.1 and 5.2, we discuss the controls on trace element composition of acid-sulfate waters and neutral chlorine waters, respectively.

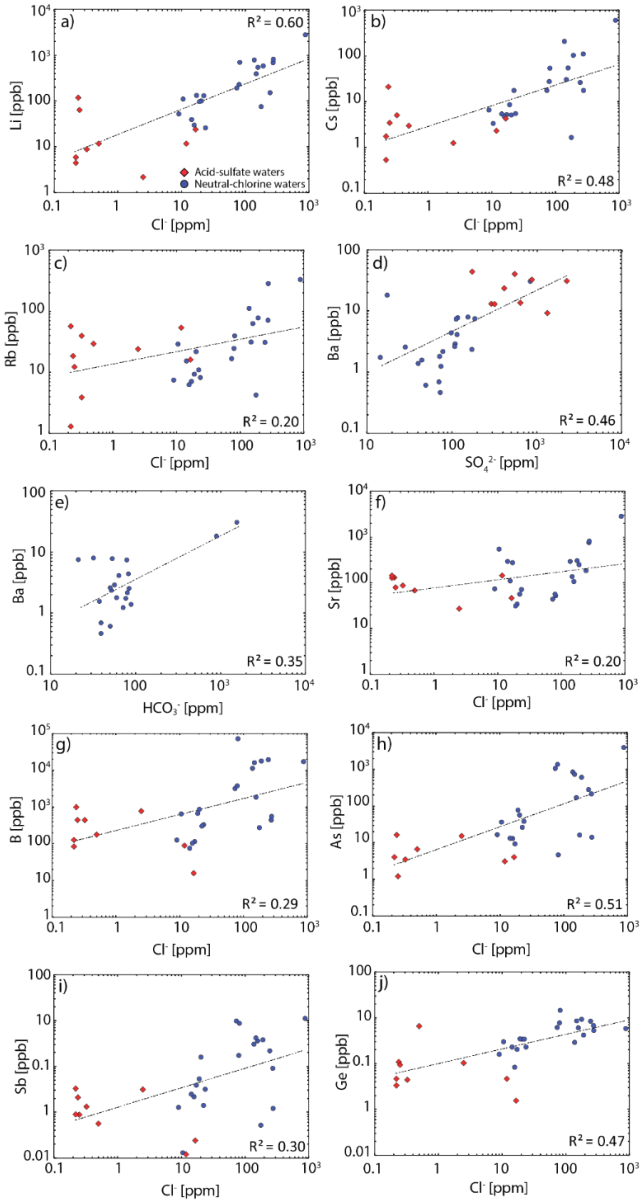

Figure 3.8. *Elemental correlation plots for Li-Cl (a), Cs-Cl (b), Rb-Cl (c), Ba-SO4 (d), Ba-HCO3 (e), Sr-Cl (f), B-Cl (g), As-Cl (h), Sb-Cl (i) and Ge-Cl (j) in in acid-sulfate waters (red diamonds) and neutral-chlorine waters (blue circles) of Southern Volcanic Zone of Chile. R-squared (R2) values are shown in each plot.*

Structural controls on degassing: acid-sulfate water composition

Figures 3.14 and 3.15, show the concentrations of SiO_2, alkali, alkaline earth metals, heavy metals, PGEs and metalloids of acid-sulfate waters, plotted as a function of Rc/Ra (air-corrected $^3He/^4He$) ratios measured in the exact same samples, and previously reported by Tardani et al. (2016) and Roulleau et al. (2016).

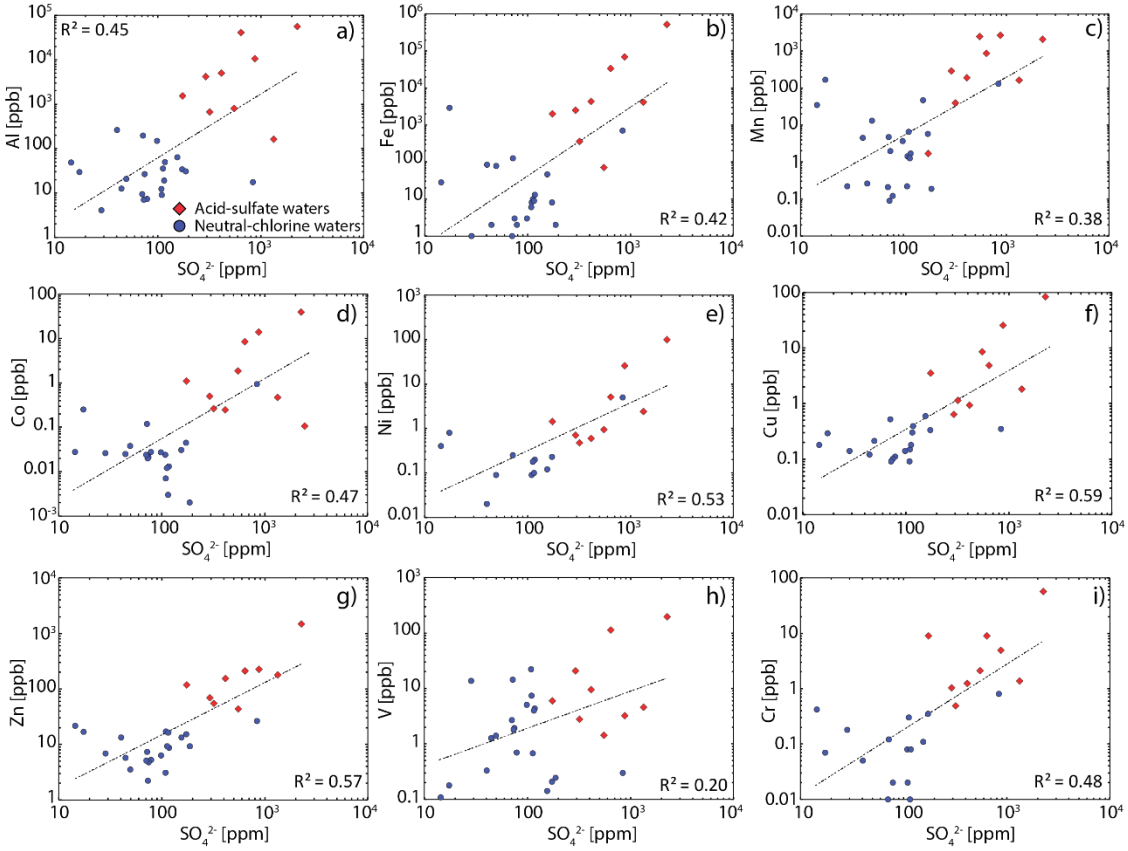

Figure 3.9. *Elemental correlation plots for Al-SO4 (a), Fe-SO4 (b), Mn-SO4 (c), Co-SO4 (d), Ni-SO4 (e), Cu-SO4 (f), Zn-SO4 (g), V-SO4 (h) and Cr-SO4 (i) in in acid-sulfate waters (red diamonds) and neutral-chlorine waters (blue circles) of Southern Volcanic Zone of Chile. R-squared (R2) values are shown in each plot.*

In general, the highest concentrations of SiO_2, Ca, Mg, K, Ba, Sr, Co, Ni, Cu, Cd, Rh and Pd correlate with lower He isotopes ratios, i.e., a dominant crustal component (Fig. 3.14). This observation suggests that the occurrence of these elements is associated with higher degrees of evolution/crustal assimilation of the parental magmas, and/or with increased water-rock interaction. As described by Tardani et al. (2016) for the studied segment, the degree of crustal contamination (^4He addition) is related with the faults controlling the occurrence of volcanic and geothermal systems, with the most contaminated values associated with NW-striking structures. In contrast, B, As, Sb, Ge, Mo, W, Ti, Pb and Zr show the opposite trend, i.e., high concentrations are related with higher He ratios (Fig. 3.15). This trend suggests that the aforementioned elements are related to less evolved magmas, and/or their occurrence may be modulated by high permeability pathways that enhance vertical fluids circulation, inhibiting reaction (and hence neutralization) with wall rocks. According to Tardani et al. (2016), the higher $^3He/^4He$ ratios are associated with the northern "horsetail" like termination of the LOFS and with NNE-trending transtensional

structures of the LOFS.

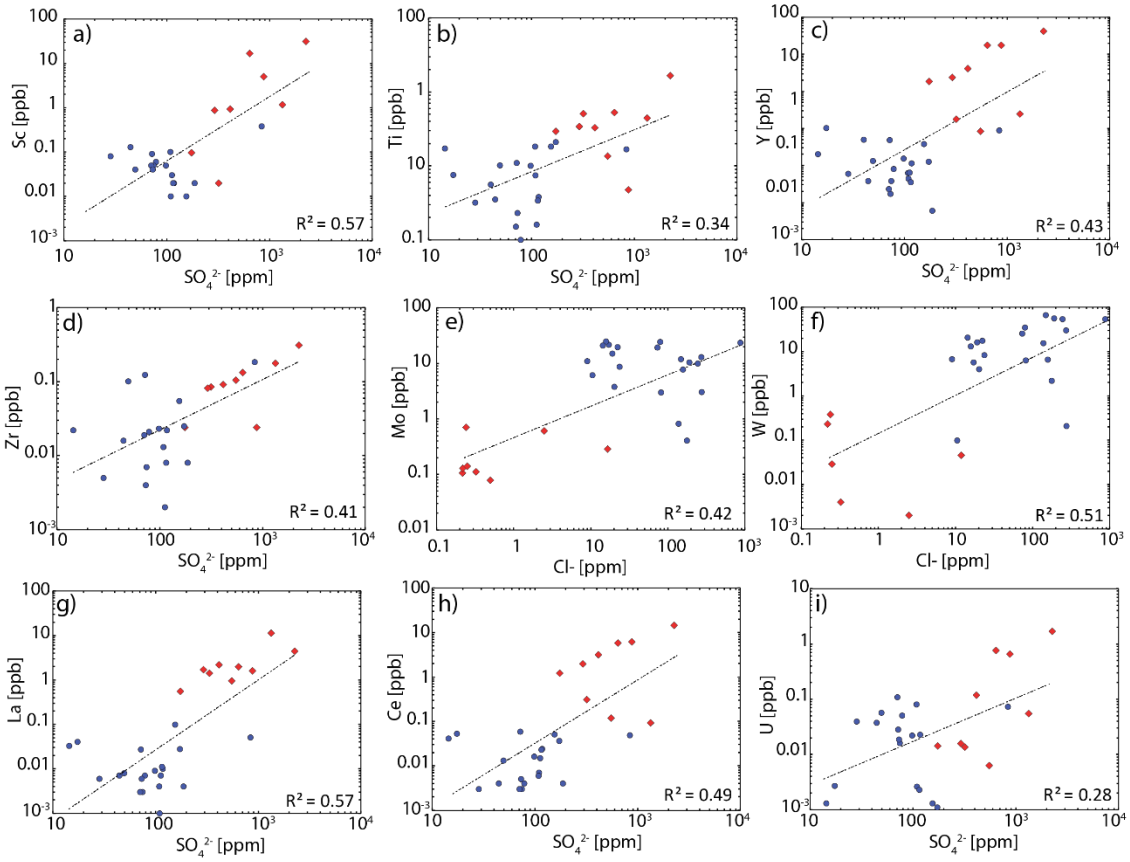

Figure 3.10. *Elemental correlation plots for Sc-SO4 (a), Ti-SO4 (b), Y-SO4 (c), Zr-SO4 (d), Mo-Cl (e), W-Cl (f), La-SO4 (g), Ce-SO4 (h) and U-SO4 (i) in acid-sulfate waters (red diamonds) and neutral-chlorine waters (blue circles) of Southern Volcanic Zone of Chile. R-squared (R2) values are shown in each plot.*

However, and despite the fact that water-rock interaction and fluid leaching has a significant control on trace metal composition of surface thermal waters, the elements concentration vs. Rc/Ra plots presented in Figures 3.14 and 3.15 suggest that other processes may be fractionating, e.g., base metals and PGEs from metalloids in steam heated acid-sulfate waters. This observation is summarized in Figure 3.16, where Cu/As ratios of the acid sulfate waters are plotted against He isotope data, represented by Rc/Ra values (Fig. 3.16). The Cu/As ratios show a negative correlation with the Rc/Ra values, i.e., high Cu/As ratios are related with low, "crustal" He signatures while lower Cu/As ratios are associated with higher, "mantle-like" He values. As reported by Tardani et al. (2016), the regional variations in $^{3}He/^{4}He$ ratios are remarkably consistent with those reported for $^{87}Sr/^{86}Sr$ in lavas along the studied segment, which in turn are strongly controlled by the regional spatial occurrence of transpressive (ALFS) and transtensive (LOFS) faults.

The two processes that more likely affect trace element fractionation in hydrothermal fluids are the degree of magmatic evolution and the timing of separation of a magmatic vapor from the silicate melt; however, magmatic/hydrothermal fluid circulation can be significantly impacted by the tectonic activity and structural architecture of the upper crust, in particular in this seismically regions (e.g., Sánchez-Alfaro et al., 2016b).

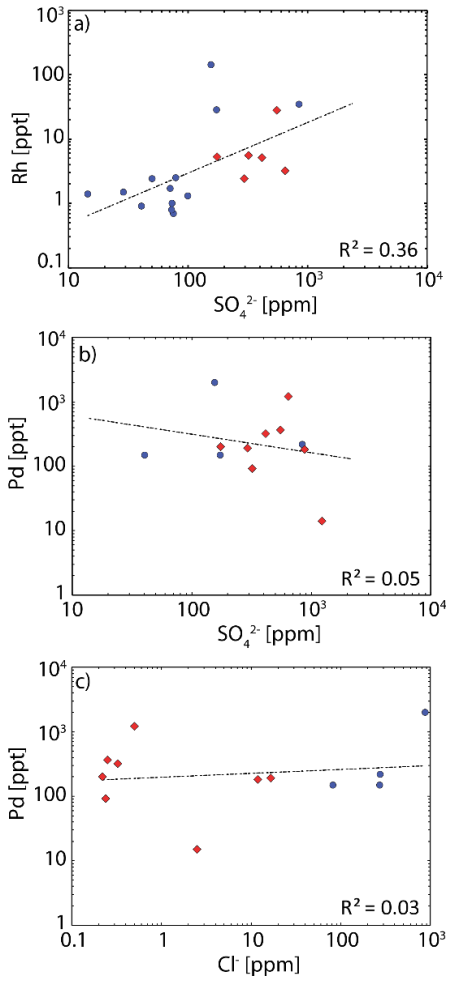

Figure 3.11. *Elemental correlation plots for Rh-SO4 (a), Pd-SO4 (b) and Pd-Cl (c), in acid-sulfate waters (red diamonds) and neutral-chlorine waters (blue circles) of Southern Volcanic Zone of Chile. R-squared (R2) values are shown in each plot.*

In the northern segment of our study area (Copahue volcano geothermal area, Fig. 3.1), samples LM and LMM show mantle-like helium signatures (Tardani et al., 2016; Roulleau et al., 2016), whereas the AF sample has an Rc/Ra ratio of about 5 (Roulleau et al., under review). The geothermal fields of the Copahue volcano, despite the wide range of Rc/Ra ratios reported in the surface fluids, have been supposed that are fed by the same magmatic source (Agusto et al., 2013; Roulleau et al., under review). These differences are attributed to the upper crust structures that promote or inhibit the vertical migration of fluids and the reaction with host rock affect helium isotope signature (Roulleau et al., under review). Within this context, the thermal springs LM, LMM and AF shows very different Cu/As ratio, of about 0.2 for the first two, whereas the latter show a ratio of about 20 (Table 2; Fig. 3.16). These data strongly suggest that the fractionation of base metals and metalloids in this system (e.g., Cu and As) may be related with the uprising of magmatic vapor through the upper crust, after the separation from the parental mafic magma.

Volatile exsolution, during magma ascent and cooling, is a continuous process starting at depth with the exsolution of the relatively insoluble CO_2 (Lowenstern, 2001; Wallace, 2005; Blundy et al., 2010). However, the bulk of the magmatic water content exsolves relatively rapidly as the magma approaches its solvus, at depths of ~5–10 km, depending on magma composition and water content (Richards, 2011, 2015 and references therein). During this process, both metals and metalloids (e.g., Cu and As, for which robust experimental data are available) partition into a low-chlorine vapor phase, relative to a silicate magma (Zajacz et al., 2011). Besides chlorine contents, sulfur concentrations are also relevant, playing an important role in the complexation of Cu and other base metals in magmatic vapors at P–T conditions characteristic of felsic plutons and related hydrothermal systems, whereas for metalloids (i.e., As), vapor phase affinity is enhanced by the availability of hydroxyl complexes (Heinrich et al., 1999; Simon et al., 2006; Zajacz et al., 2011; Pokrovski et al., 2013). In contrast, mafic magmas generally release magmatic volatiles that contain lower concentration of Cl and may have relatively high sulfur concentrations available to for the early separation a magmatic vapor capable to scavenge Cu from silicate melt (Williams-Jones and Heinrich, 2005; Stelling et al., 2008).

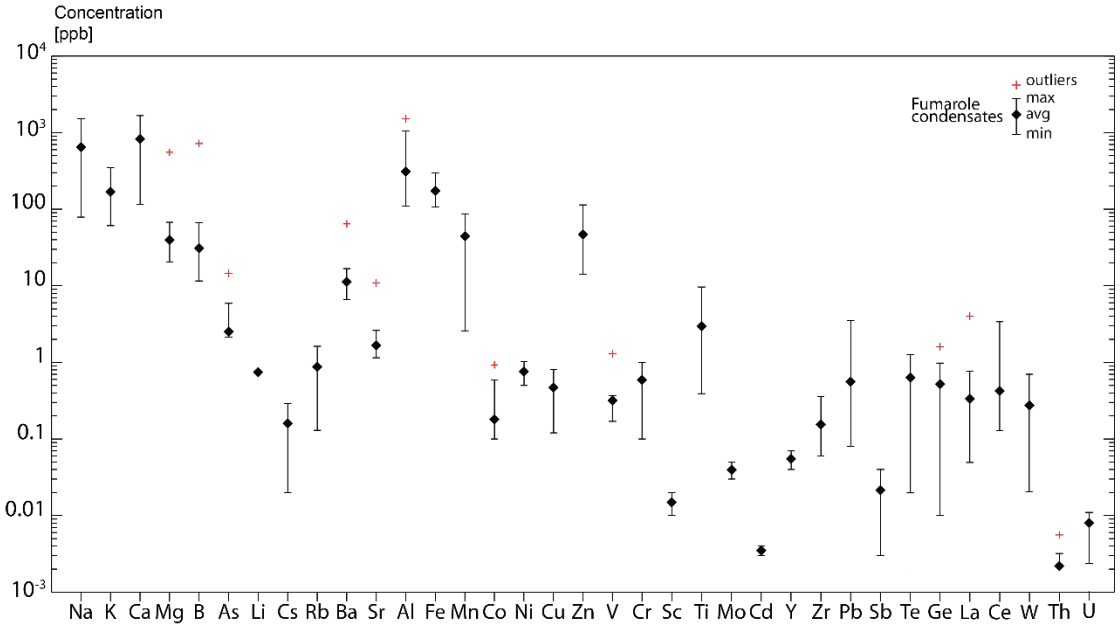

Figure 3.12. *Concentration plot for trace elements in fumarole condensates (white diamonds) associated with acid-sulfate waters of Southern Volcanic Zone of Chile. Data are plotted in parts per billion (ppb) on a vertical logarithmic scale. For each element, average concentrations are shown together with maximum and minimum values, and with outliers (red cross).*

Magmatic vapors, formed in these systems by separation from the parental silicate magma, could separate into a saline brine and vapor, a process that could take place during the upward migration through the upper crust (Heinrich et al., 2004). The vapor-liquid partition coefficients compilation published by Pokrovski et al. (2013) for surface geothermal springs, show that elements such as B and Pb have the highest vapor affinity, while As, Sb and W also exhibit among the highest $\log P_{v/l}$ values. Furthermore, Planer-Friedrich et al. (2006) have recognized in low temperature (< 60 °C) geothermal springs of Yellowstone Park that high volatilities of some metalloids may also be due to the formation of particular compounds as methyl-chloride species such as $(CH_3)_2AsCl$, $(CH_3)_3As$, $(CH_3)_2AsSCH_3$, and CH_3AsCl_2.

These species may predominate over major inorganic forms ($As(OH)_3$) and may be responsible for high As concentrations in the gas phase.

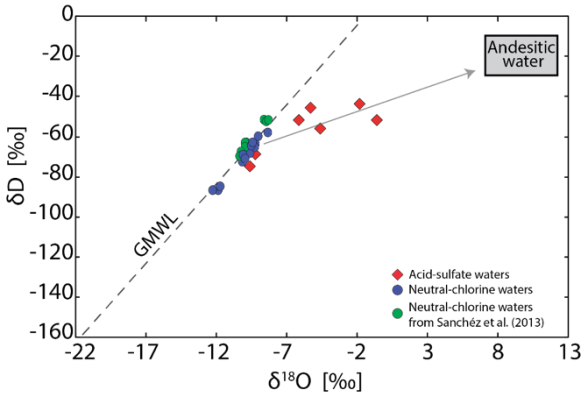

Figure 3.13. *$\delta^{18}O$-δD plot of acid-sulfate waters (red diamonds) and neutral-chlorine waters (blue circles) of Southern Volcanic Zone of Chile. Data of neutral-chlorine waters from Sánchez et al. (2013) are reported (Green circles). Global Meteoric Water Line (GMWL; Craig, 1963) and Andesitic Water box (Giggenbach and Soto, 1992) are shown for comparison.*

In Figure 3.17, we plotted the arithmetic mean of partition coefficients between the vapor and liquid phase ($K_D = C_{vapor}/C_{liquid}$) calculated in eight samples (RV, CR, OM, LMM, LM, PL, JM; Table 5) where we have collected in the same point both steam condensate and thermal water samples. Our empirical vapor/liquid partition coefficients are in good agreement with those published by Pokrovski et al. (2013) for Kamchatka geothermal springs and reported as grey bars in Fig. 3.17. Just for W our data are slightly higher than what reported by Pokrovski et al. (2016). It is relevant to note that those elements that positively plot with Rc/Ra in Figure 3.17, i.e., display $logP_{v/l}$ values close to unity (B, As, Mo and Ti) and higher than 1 (Sb, W, Pb, Zr and Ge), indicating a marked vapor affinity. At the contrary those metals that show a negative correlation with Rc/Ra also display a Kd<1 (e.g. Ca, Mg, K, Ba, Sr, Cu, NI, Co, Cd, Rh and Pd) This suggests that in acid-sulfate waters, the concentrations of Ca, Mg, K, Ba, Sr, Co, Ni, Cu, Cd, Rh and Pd are mainly controlled by reaction with host rocks during hydrothermal fluids ascent, whereas B, As, Sb, Ge, Mo, W, Ti, Pb and Zr may be sourced directly from the deep-seated magma chambers and transported towards the geothermal environment by a vapor phase.

Neutral-chlorine waters

Similarly to the previous analysis, the concentrations of SiO_2, and selected major and trace elements in neutral-chlorine waters are plotted vs. Rc/Ra (Fig. 3.18). Silica concentration and Na, K, Ca, Mg, B, Rb, Ba, Ni, Cu and Pb concentrations show a positive correspondence with Rc/Ra values, whereas As, Sr, Co and Mo do not a clear trend. In general, the concentration data of neutral-chlorine waters present a higher dispersion that the sulfate waters when plotted against Rc/Ra ratios (Figs. 3.14 and 3.15). These features suggest that that the chemistry of chlorine-neutral waters is heavily modulated by secondary water-rock interaction processes that deplete selected species (e.g. base metals) by removal due to mineral precipitation or incorporation/adsorption into secondary

minerals.

Table 3.5. *Calculated partition coefficients between vapor and liquid phase (KD = C vapor/C liquid) in samples RV, CR, OM, LMM, LM, PL, JM. AVG: arithmetic mean.*

	Na	K	Ca	Mg	B	As	Li	Cs	Rb	Ba	Sr	Al	Fe	Mn	Co	Ni	Cu	Zn	V	Cr	Sc	Ti	Mo	Cd	Y	Zr	Pb	Sb	Te	Ge	La	Ce	W	Th	U	Ag	Rb	Pd
LM	0.02	0.02	0.05	0.02	0.24	0.39	-	0.02	0.01	1.47	0.06	1.26	0.04	0.02	0.23	0.42	0.45	0.08	0.06	0.22	0.01	0.58	0.08	0.13	0.18	1.51	1.45	0.14	0.03	196.67	0.00	1.36	-	0.00	0.04	-	-
LMM	-	-	0.06	0.03	0.15	0.62	-	-	-	0.40	0.03	0.06	-	-	0.86	-	-	0.75	0.04	0.81	-	0.33	-	-	-	3.96	26.25	-	-	-	0.35	0.28	-	0.06	0.00	-	-	-
OM	0.02	0.01	0.02	0.01	0.49	0.84	0.06	0.07	0.03	0.20	0.08	0.02	-	0.03	0.07	0.02	0.00	0.17	0.40	0.02	0.00	0.82	1.86	0.03	0.00	2.38	1.20	2.50	0.04	2.75	0.04	0.03	14.96	0.00	0.02	0.73	-	0.11
CR	-	-	0.09	0.01	0.74	0.61	-	0.07	-	0.67	0.04	0.35	-	-	1.20	-	-	-	0.02	0.98	-	0.51	-	-	-	1.50	21.46	-	-	-	0.20	0.22	-	0.92	0.00	-	-	-
AF	-	0.01	-	-	-	-	-	-	-	0.41	-	0.02	-	-	-	-	-	0.04	0.00	-	-	-	-	-	-	0.59	-	-	1.63	-	-	-	-	0.00	-	-	-	-
JM	-	-	-	-	-	-	-	-	-	0.55	-	0.01	-	-	0.03	-	-	-	0.00	-	-	-	-	-	-	-	-	-	-	122.57	2.06	0.59	-	0.00	-	-	-	-
RV	0.03	-	-	-	-	1.79	-	0.03	-	0.37	-	0.49	-	-	0.05	-	-	-	0.20	-	-	-	-	-	-	-	-	-	-	490.00	-	-	-	0.71	-	-	0.05	-
PL	-	-	-	-	-	0.71	-	0.01	-	1.19	0.01	0.19	-	-	0.00	-	-	-	0.06	-	-	-	-	-	-	-	-	-	-	230.00	-	-	-	-	-	-	0.11	-
AVG	0.02	0.02	0.06	0.02	0.47	0.85	0.06	0.04	0.02	0.66	0.04	0.30	0.04	0.02	0.35	0.22	0.23	0.26	0.10	0.51	0.01	0.56	0.97	0.08	0.09	1.99	12.59	1.32	0.57	208.40	0.53	0.49	14.96	0.24	0.01	0.73	0.08	0.11

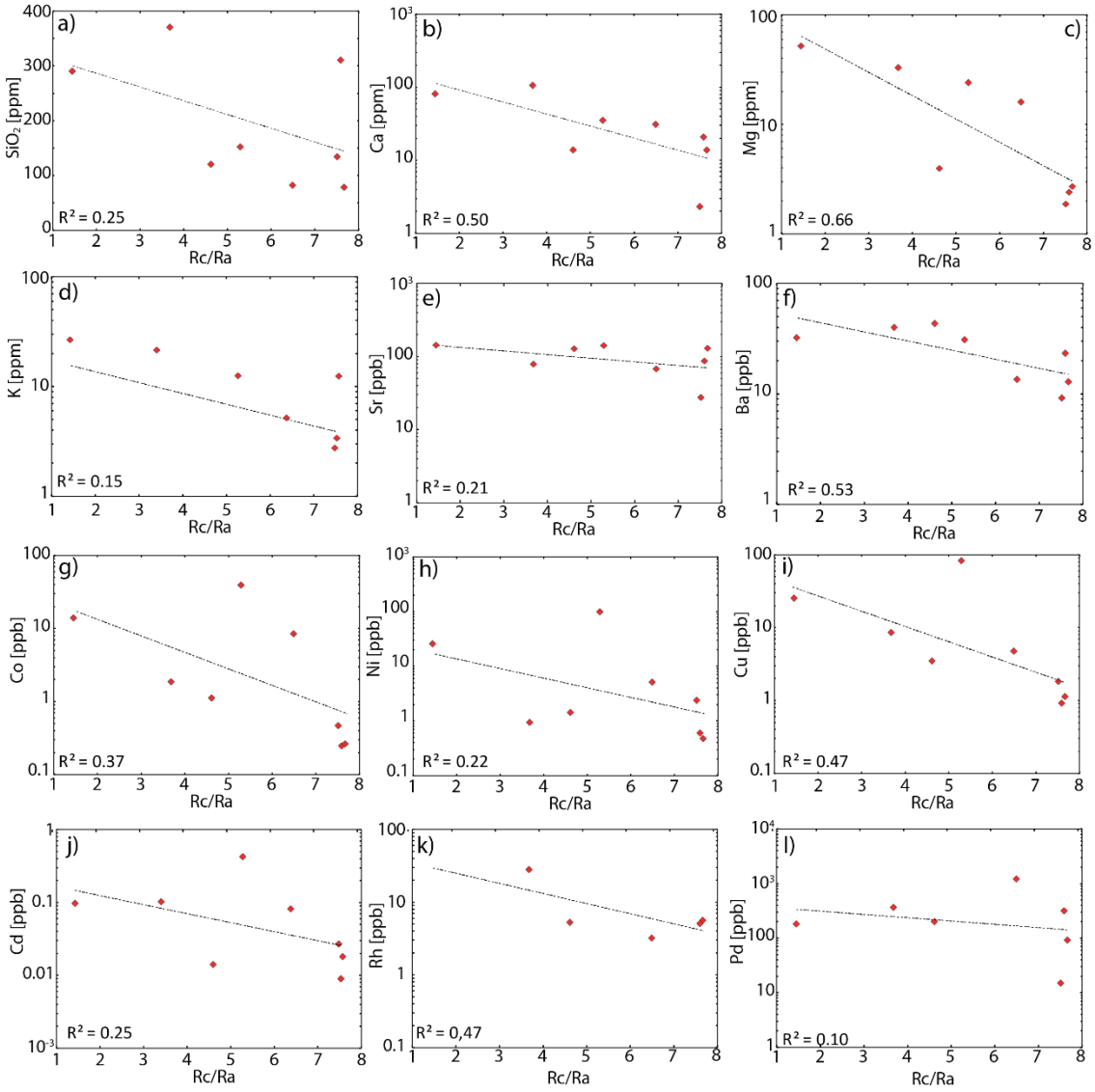

Figure 3.14. *Air-corrected, helium isotopes ratios (Rc/Ra) plotted with concentrations of SiO2 (a), Ca (b), Mg (c), K (d), Sr (e), Ba (f), Co (g), Ni (h), Cu (i), Cd (j), Rh (K) and Pd (l) in acid-sulfate waters (red diamonds) of Southern Volcanic Zone of Chile. R-squared (R2) values are shown in each plot.*

Elements such Ca, Mg, Ba and Sr can be removed by incorporation into minerals, such as carbonates, and possibly in major alteration minerals such as epidote and zeolites (Kaasalainen and Stefánsson, 2012). Calcite precipitation is a common mechanism described in neutral-chlorine thermal waters of Southern Volcanic Zone, and has been recognized as the main cause of $\delta^{13}C$ fractionation of dissolved CO_2 and of unusual $CO_2/^3He$ variability in dissolved gas samples , (Ray et al., 2009; Tardani et al., 2016). In Figure 3.19, the concentrations of Ca, Mg, Ba, and Sr are plotted with $CO_2/^3He$ ratios of exactly the same neutral-chlorine waters, from Tardani et al. (2016) and Roulleau et al. (2016). The positive correspondence of all four elements with $CO_2/^3He$ ratios suggest that calcite precipitation is one of the main processes controlling alkaline-earth metal composition of shallow thermal springs in the studied area.

Elements such As, Sb, Mo, Al, Fe, Mn, Co, Ni, Zn, Cd, Cu, Pb, Cr, V, Zr and W may be

easily extracted from the fluid into Al and Fe oxi-hydroxides and/or clays, and/or incorporated into Fe(Cu) sulfides and sulfates, whereas SiO_2 may precipitate as quartz or amorphous silica. In neutral-chlorine waters, many of these metals may not be present at concentrations high enough to form pure phases, but may be incorporated into major oxides and hydroxides, silicates, sulfides, carbonates and clay minerals (Simmons and Browne, 2000; Reyes et al., 2002; Abraitis et al., 2004; Markússon and Stefánsson, 2011; Kaasalainen and Stefánsson, 2012; Libbey and Williams-Jones, 2016). Therefore, and as proposed by Tardani et al. (2016), it is likely that mineral precipitation and increased water-rock interaction had controlled the composition of neutral chloride waters, as result of cooling/mixing processes that have affected the hydrothermal systems increasing the reaction time with country rock and the cooling of magmatic vapor, and/or by mixing with cold and shallow infiltrating water.

Shallow dilution processes by meteoric water are also affecting neutral-chlorine waters in the Southern Volcanic Zone of Chile (Sánchez et al., 2013; Tardani et al., 2016). As shown in Figure 3.13, the $\delta^{18}O$ and δD isotopic signatures of thermal waters, lie on the GMWL and are mainly dominated by meteoric fluid sources. In Figure 3.20, concentrations of metals such Na, Ca, Li, Sr, Mn, Cu, Zn, Cd and Ti are plotted along with $^{4}He/^{20}Ne$ ratios measured in dissolved gas samples collected in the same thermal waters where trace metals analysis have been conducted and already published by Tardani et al. (2016) and Roulleau et al. (2016). The $^{4}He/^{20}Ne$ ratio is a proxy indicative of contamination by air of volcanic/geothermal fluid. Air have a fixed $^{4}He/^{20}Ne$ ratio of

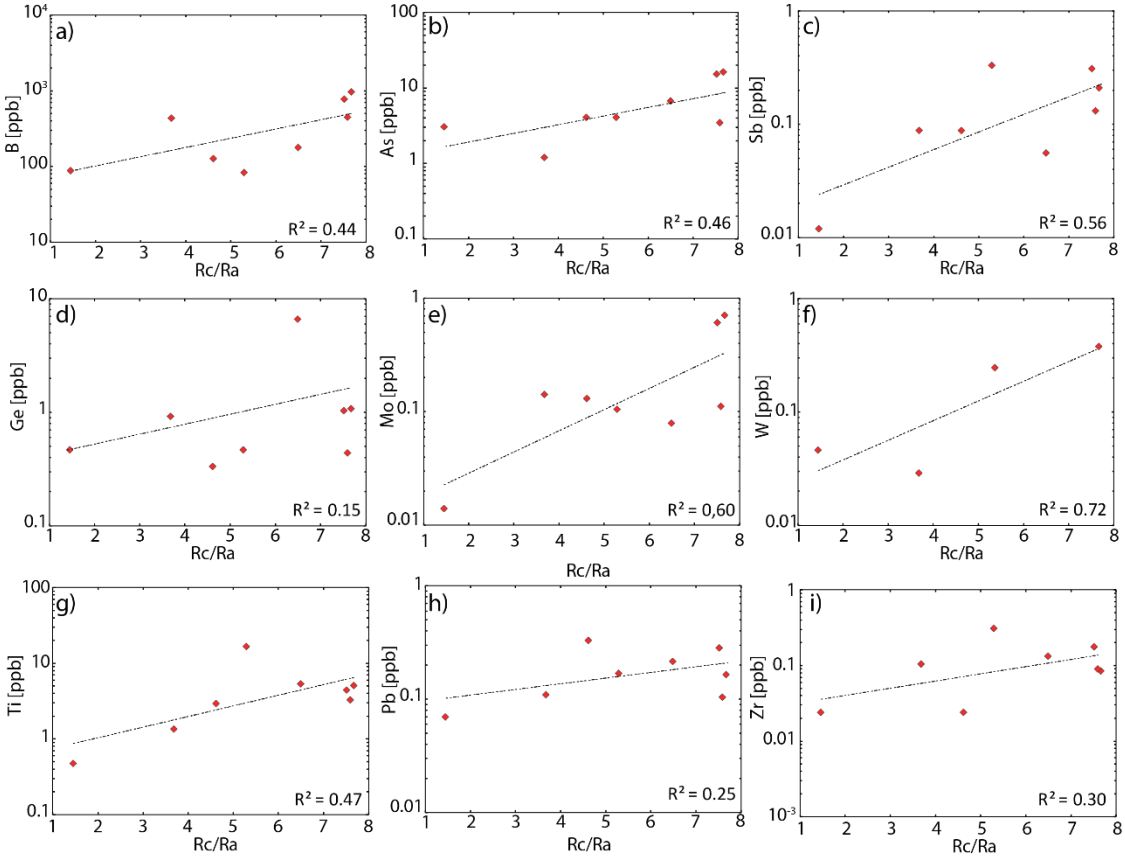

Figure 3.15. *Air-corrected, helium isotopes ratios (Rc/Ra) plotted with concentrations of B (a), As (b), Sb (c), Ge (d), Mo (e), W (f), Ti (g), Pb (h) and Zr (i) in acid-sulfate waters (red diamonds) of Southern Volcanic Zone of Chile. R-squared (R2) values are shown in each plot.*

0.33, whereas hydrothermal fluid present usually higher values due to lack of ^{20}Ne in the magmatic source. The positive correspondence between concentrations and $^{4}He/^{20}Ne$ ratios suggest that metal contents in neutral-chlorine waters are significantly controlled by dilution of thermal waters in the shallow crustal level.

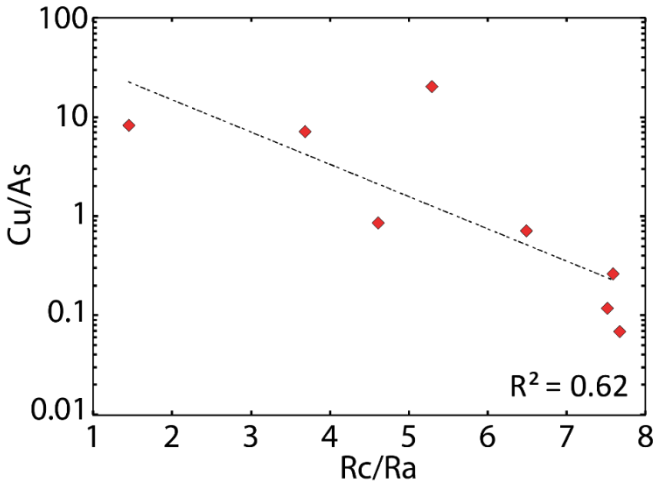

Figure 3.16. *Air-corrected, Helium isotopes ratio (Rc/Ra) plotted with Cu/As ratio in acid-sulfate waters (red diamonds) of Southern Volcanic Zone of Chile. R-squared (R2) value is shown.*

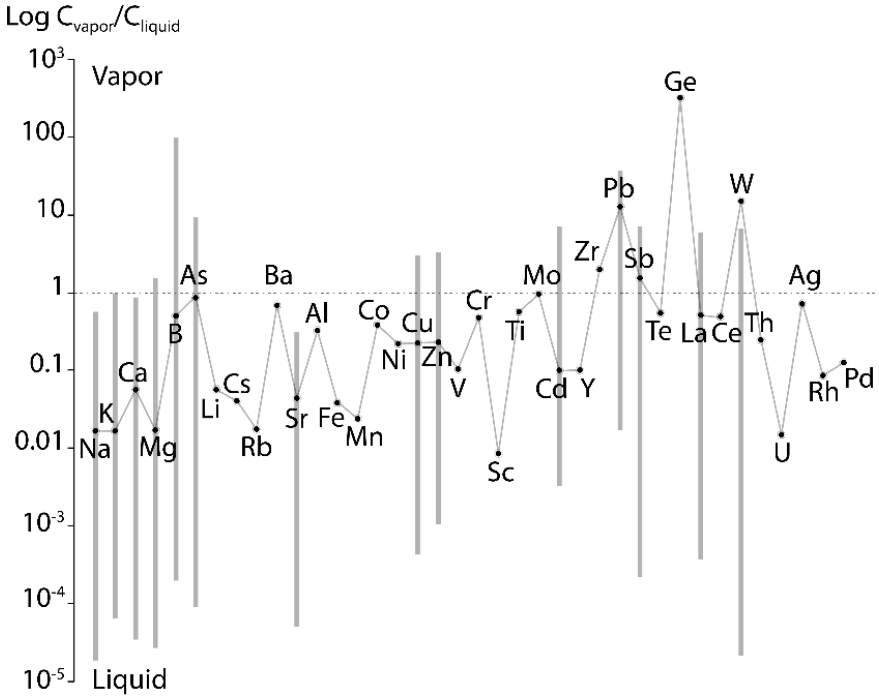

Figure 3.17. *Diagram representing the partition coefficients between vapor and liquid, calculated for each datapoint which was possible to take water and condensate sample in the same place. Data are plotted on a vertical logarithmic scale. For each element is shown the arithmetic mean of partition coefficients calculated for single datapoints. Grey bars represent the partition coefficients vapor-liquid from Pokrovski et al. (2013)*

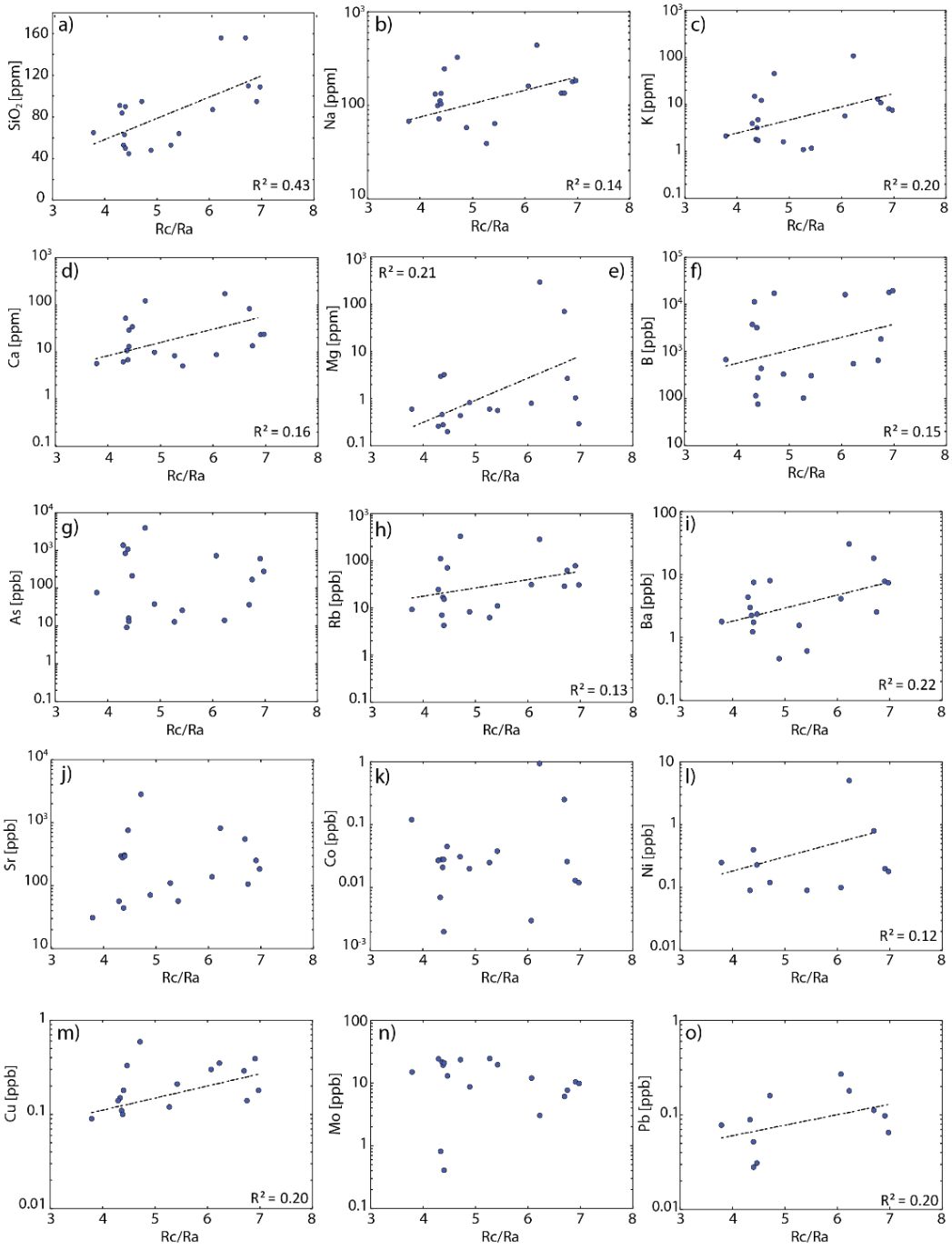

Figure 3.18. *Air-corrected, helium isotopes ratios (Rc/Ra) plotted with concentrations of SiO2 (a), Na (b), K (c), Ca (d), Mg (e), B (f), As (g), Rb (h), Ba (i), Sr (j), Co (k), Ni (l), Cu (m), Mo (n) and Pb (o) in neutral-chlorine waters (blue circles) of Southern Volcanic Zone of Chile. R-squared (R^2) values are shown in those diagrams where trend line has been calculated.*

Anomalous PGE concentrations in thermal waters: a pre-enriched basement?

The measured concentrations of PGEs in acid sulfate, neutral chlorine waters and fumarole condensates are unusually elevated (Table 3 and 4, Figs. 3.7 and 3.12), and may provide additional insight on the metal sources and processes controlling metal concentrations and distribution in thermal waters of the studied segment. Figures 3.21 to 3.25 show the spatial distribution of concentrations of Ru, Rh, Pd, Ir and Pt, respectively, in thermal springs along the LOFS in the Southern Volcanic Zone of Chile. Of the six PGEs, Pd and Rh are the most anomalous. The contents of Pd, the most mobile element among the PGEs, are high and range between 0.01 and 2.00 ppb. Rhodium concentrations are also relatively elevated ranging between 0.001 and 0.150 ppb. Ruthenium, Pd, Ir and Pt concentrations are above detection only in the northern part of the studied region, in an area between the Copahue and Sierra Nevada volcanoes. Rhodium, instead, is also detectable in the central part of studied region, near Villarica volcano, but with concentrations in thermal waters two orders of magnitude lower than the northern part of the segment.

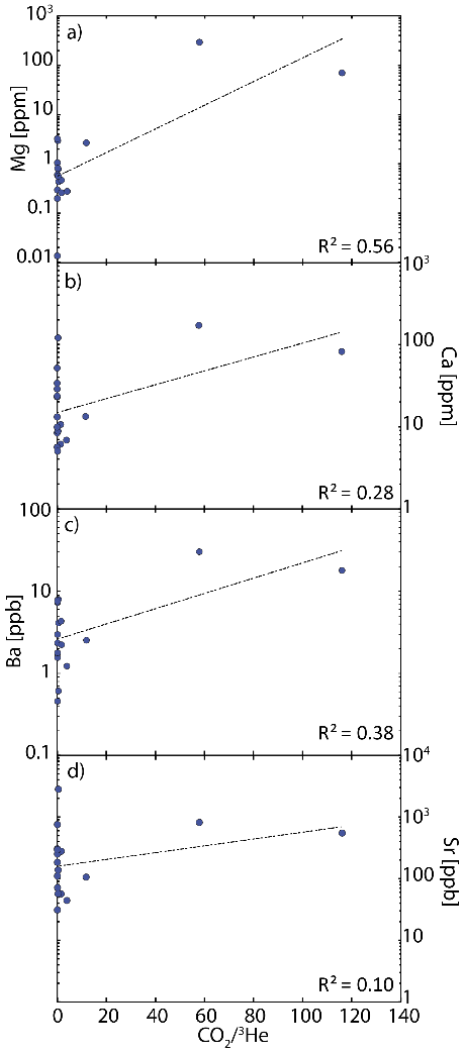

Figure 3.19. *$CO_2/^3He$ ratios plotted with concentrations of Mg (a), Ca (b), Ba (c) and Sr (d) in neutral-chlorine waters (blue circles) of Southern Volcanic Zone of Chile. R-squared (R^2) values are shown in each plot.*

PGE concentration data in geothermal waters worldwide are scarce. Similar Pd and Rh concentrations have been reported in deep, high temperature (300°C), high salinity (19-25% TDS) brines at the Salton Sea geothermal system (up to 2.0 ppb Pd and 0.5 ppb Rh; McKibben et al., 1990) and in mud pots in Mutnovsky volcano in South Kamchatka, where the temperatures of fumarolic emissions range between 150°C and 570°C (up to 2.2 ppb Pd and 0.13 ppb Rh; Bortnikova et al., 2008). Our data in fumarole condensates are also relatively high for low temperature gas emissions (<100 °C). Zelenski et al. (2013) also PGE's contents in high temperature fumaroles (1084 °C) in Erta Ale volcano in Ethiopia reported Pt content of about 0.5 ppb and Os contents of 0.27 ppb in the gas phase. Platinum and Rh were found just in the sublimates, whereas Ru and Ir are not reported in any phase. Our Pt data are about 1 ppt, thousand times lesser than how reported for Erta Ale, but we could determine also Pd (20.00 ppt), Ir (13.00 ppt) and Rh (1.40 ppt) in the gas condensate. Ruthenium is below the detection limit.

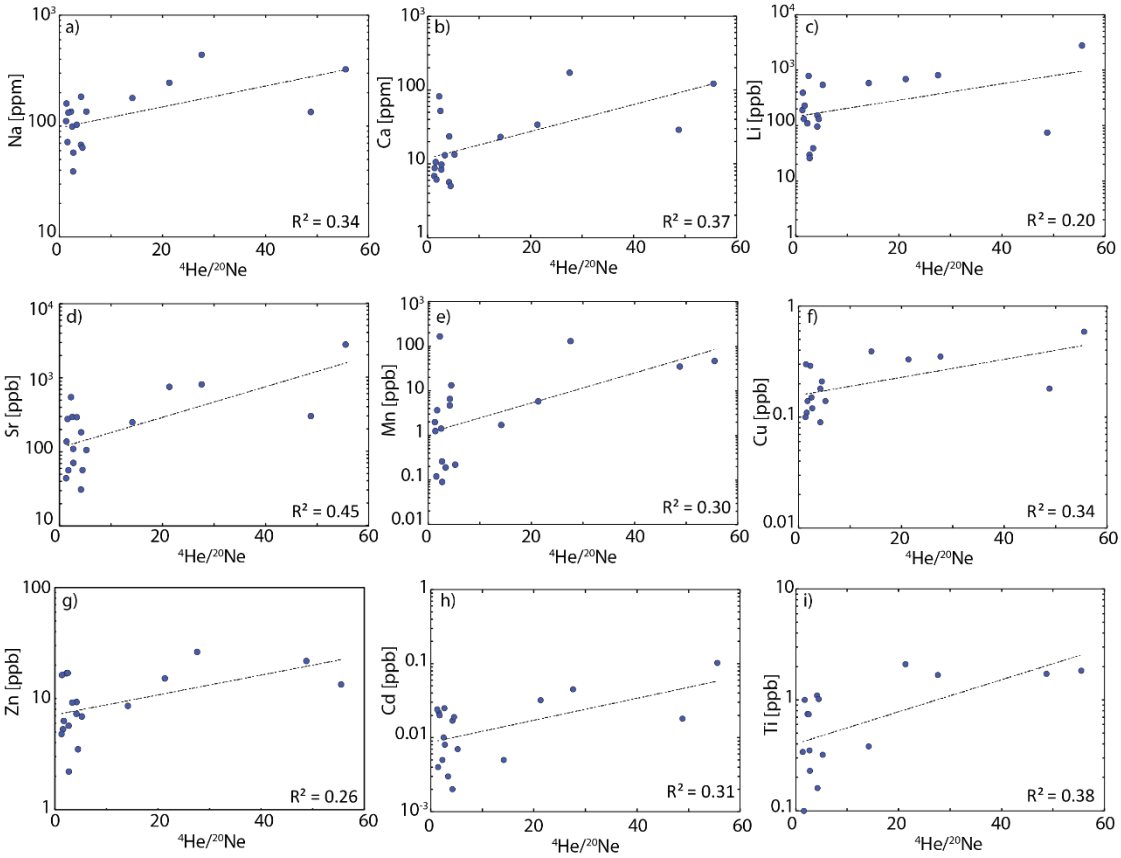

Figure 3.20. *$^{4}He/^{20}Ne$ ratios plotted with concentrations of Na (a), Ca (b), Li (c), Sr (d), Mn (e), Cu (f), Zn (g), Cd (h) and Ti (i) in neutral-chlorine waters (blue circles) of Southern Volcanic Zone of Chile. R-squared (R^2) values are shown in each plot.*

Palladium and Rh concentrations from the studied springs were plotted along Rc/Ra He ratios in Figure 3.14 (K and L, respectively). The observed trends are similar to those for alkali, alkaline-earth and transitional metals (Fig. 3.14), suggesting that fluid-rock interaction during ascent is the most probable cause of Pd enrichment in thermal springs. Considering that anomalous (ppb levels) Pd and Rh concentrations are likely related to a PGE-rich mafic source of mantle affinity, PGE enrichment of thermals fluids from the studied area might require PGE-rich source rocks of mafic affinity.

The basement in the northern portion of the studied region (north of 39°S) is composed mainly by Meso–Cenozoic volcano-sedimentary rocks (Cura Mallín and Cola de Zorro), above which basaltic to rhyolitic volcanic edifices are constructed. These units are intruded by granidioritic plutons of Mio-Pliocene age (Charrier et al., 2002). South of 39°S, the basement is dominated by the Meso–Cenozoic plutonic rocks of the Patagonian Batholith. Therefore, potential source rock units for PGEs would be restricted to the most primitive lavas of Miocene to Holocene volcanoes around which thermal springs occur (Fig. 3.1). However, bulk-rock geochemical analysis conducted in lavas of the main volcanic centers in the region (i.e., Copahue, Callaqui, Lonquimay and Tolhuaca volcanoes) have revealed low PGEs contents, i.e., below 1 ppb (Appendix A1). The low PGE contents of these mafic volcanic rocks preclude a scenario where the elevated PGE concentrations found in geothermal fluids can be attributed to leaching due to water-rock interaction.

A more probable source of PGEs in thermal fluids may be related to hidden ultramafic bodies that have been documented to occur between 38°-40°S (Salazar, 2015; see Figs 3.21 to 3.25). These chromite-bearing ultramafic orebodies have been described by González-Jiménez et al. (2016) at La Cabaña, Recent analyses conducted in chromitites from these ultramafic bodies have reveal significant amounts of PGEs (up to 347 ppb total) and Au (up to 24 ppb), present as inclusions of platinum-group minerals (PGM) and alloys, as well as native gold. The PGM identified include native osmium, laurite (RuS_2), irarsite (IrAsS), osarsite (OsAsS), omeiite ($OsAs_2$) and Pt–Fe alloys. González-Jiménez et al. (2016) proposed is that these exhumed ultramafic bodies were emplaced into the sediments of the Paleozoic accretionary prism after transport throughout the subduction channel. Many of these bodies were emplaced into the upper crust and currently forming part of the basement beneath the present volcanic arc (e.g., Voipire, Madre de Dios). Although more detailed studies are needed, it is likely that the anomalous concentrations of PGEs in thermal fluids, in particular Pd (ppb levels), are related to increased leaching of PGEs from hidden ultramafic bodies or blocks.

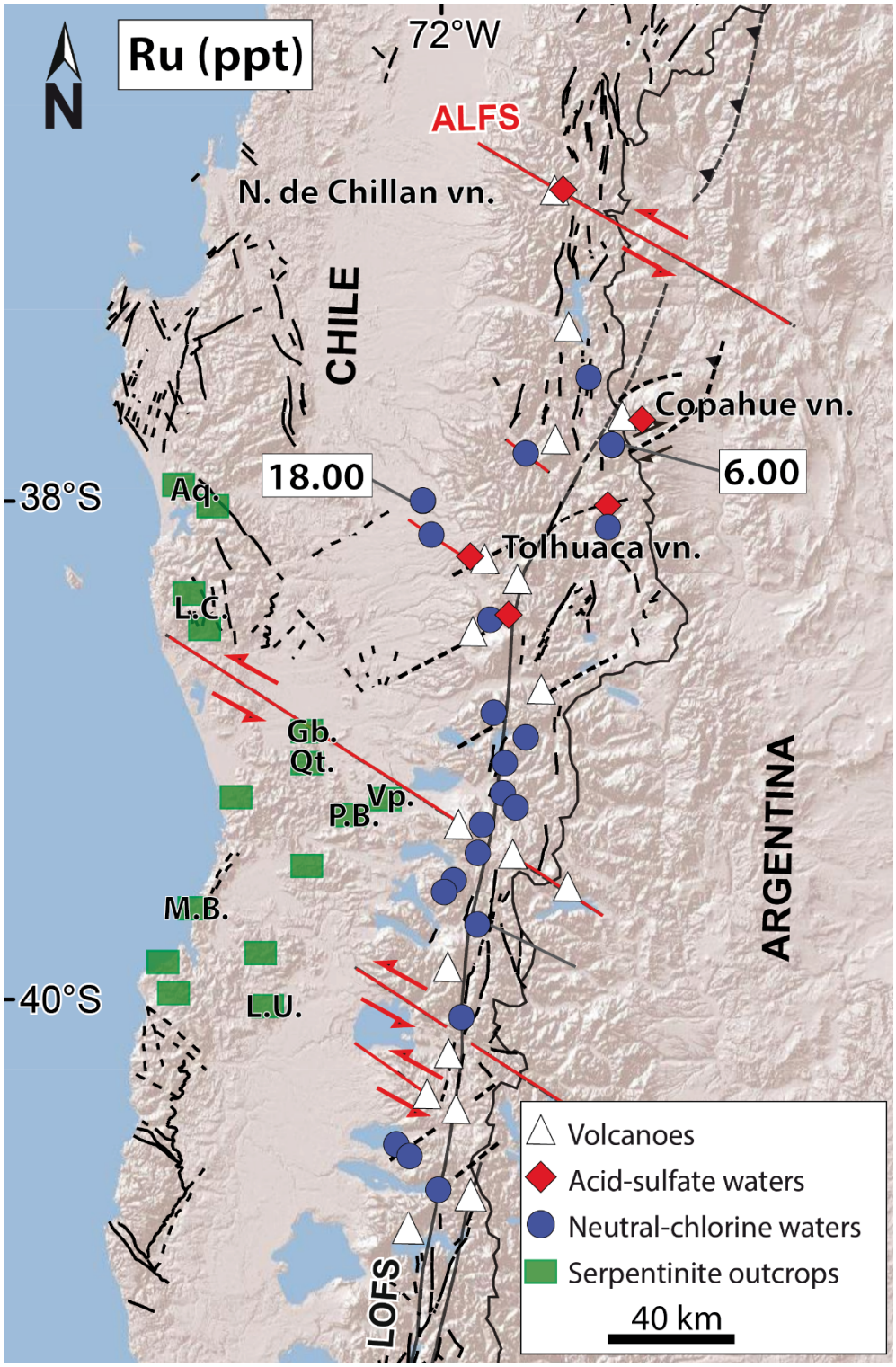

Figure 3.21. *Digital elevation model of the central part of the Southern Volcanic Zone in southern Chile with regional distribution of Ru concentrations in part per trillion (ppt), in acid-sulfate waters (red diamonds) and neutral-chlorine waters (blue circles). White triangles represent main stratovolcanoes of the segment. Solid and dashed lines show simplified faults and lineations from Lara et al. (2006), Cembrano and Lara (2009), Sánchez et al. (2013) and Pérez-Flores et al., 2016. Green squares represent ultramafic bodies of southern Chile from Salazar (2015). Aq.: Antiquina, L.C.: La Cabaña, Gb.: Gorbea, Qt.: Quitratue, Vp.: Voipire, P.B.: Palo Blanco, M.B.: Morro Bonifacio, L.U.: Los Ulmos.*

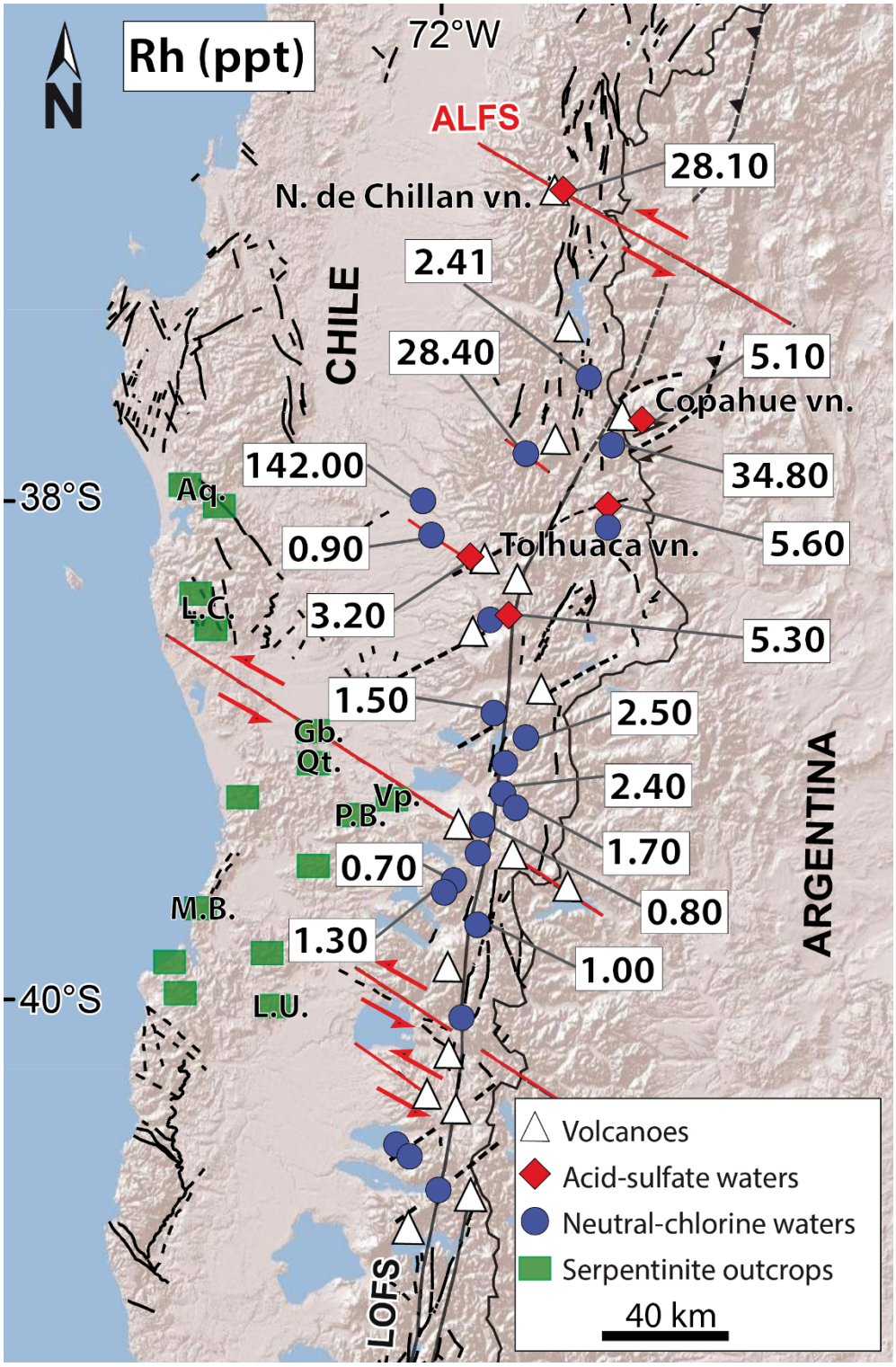

Figure 3.22. *Digital elevation model of the central part of the Southern Volcanic Zone in southern Chile with regional distribution of Rh concentrations in part per trillion (ppt), in acid-sulfate waters (red diamonds) and neutral-chlorine waters (blue circles). White triangles represent main stratovolcanoes of the segment. Solid and dashed lines show simplified faults and lineations from Lara et al. (2006), Cembrano and Lara (2009), Sánchez et al. (2013) and Pérez-Flores et al., 2016. Green squares represent ultramafic bodies of southern Chile from Salazar (2015). Aq.: Antiquina, L.C.: La Cabaña, Gb.: Gorbea, Qt.: Quitratue, Vp.: Voipire, P.B.: Palo Blanco, M.B.: Morro Bonifacio, L.U.: Los Ulmos.*

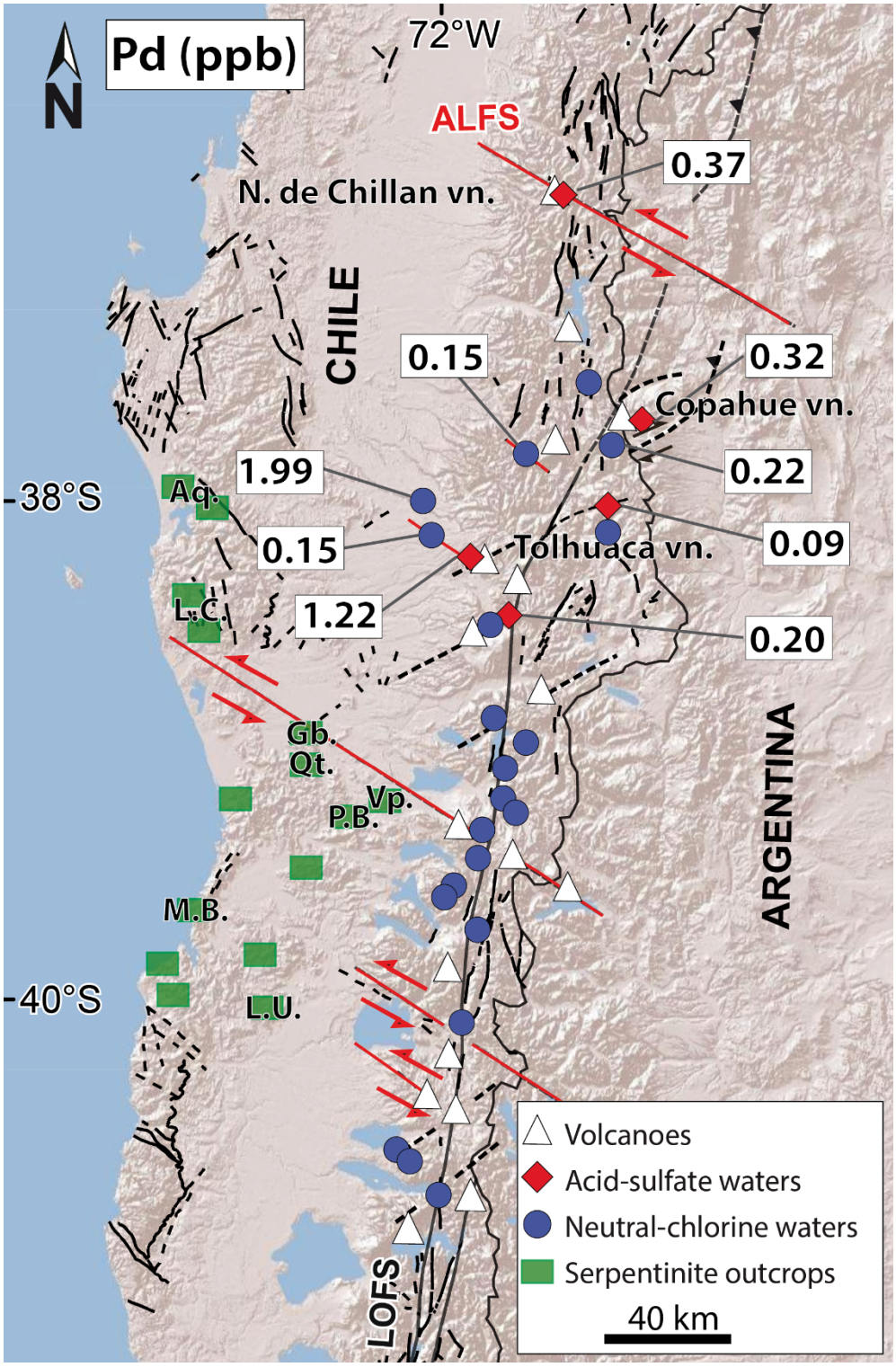

Figure 3.23. *Digital elevation model of the central part of the Southern Volcanic Zone in southern Chile with regional distribution of Pd concentrations in part per billion (ppb), in acid-sulfate waters (red diamonds) and neutral-chlorine waters (blue circles). White triangles represent main stratovolcanoes of the segment. Solid and dashed lines show simplified faults and lineations from Lara et al. (2006), Cembrano and Lara (2009), Sánchez et al. (2013) and Pérez-Flores et al., 2016. Green squares represent ultramafic bodies of southern Chile from Salazar (2015). Aq.: Antiquina, L.C.: La Cabaña, Gb.: Gorbea, Qt.: Quitratue, Vp.: Voipire, P.B.: Palo Blanco, M.B.: Morro Bonifacio, L.U.: Los Ulmos.*

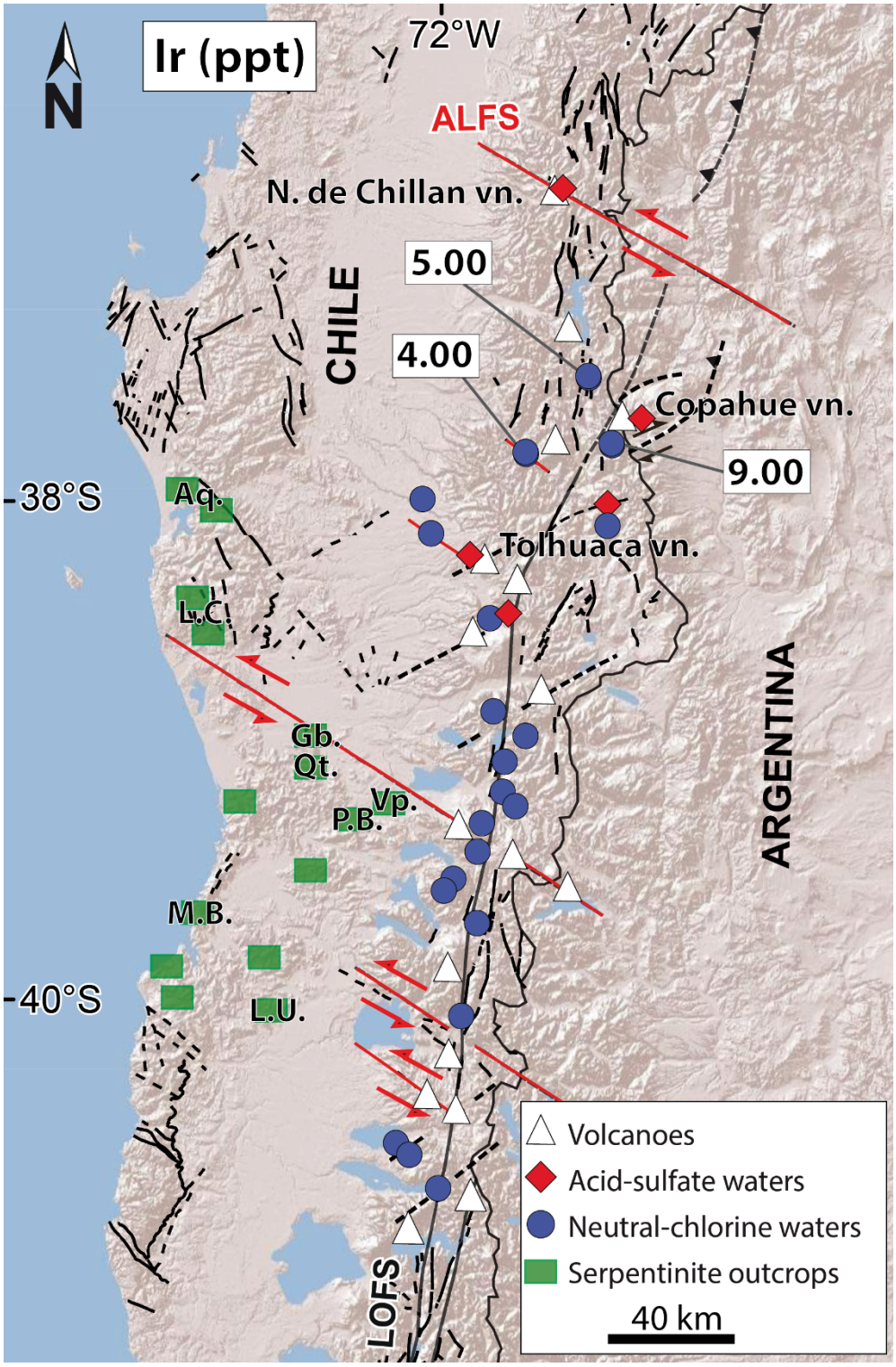

Figure 3.24. *Digital elevation model of the central part of the Southern Volcanic Zone in southern Chile with regional distribution of Ir concentrations in part per trillion (ppt), in acid-sulfate waters (red diamonds) and neutral-chlorine waters (blue circles). White triangles represent main stratovolcanoes of the segment. Solid and dashed lines show simplified faults and lineations from Lara et al. (2006), Cembrano and Lara (2009), Sánchez et al. (2013) and Pérez-Flores et al., 2016. Green squares represent ultramafic bodies of southern Chile from Salazar (2015). Aq.: Antiquina, L.C.: La Cabaña, Gb.: Gorbea, Qt.: Quitratue, Vp.: Voipire, P.B.: Palo Blanco, M.B.: Morro Bonifacio, L.U.: Los Ulmos.*

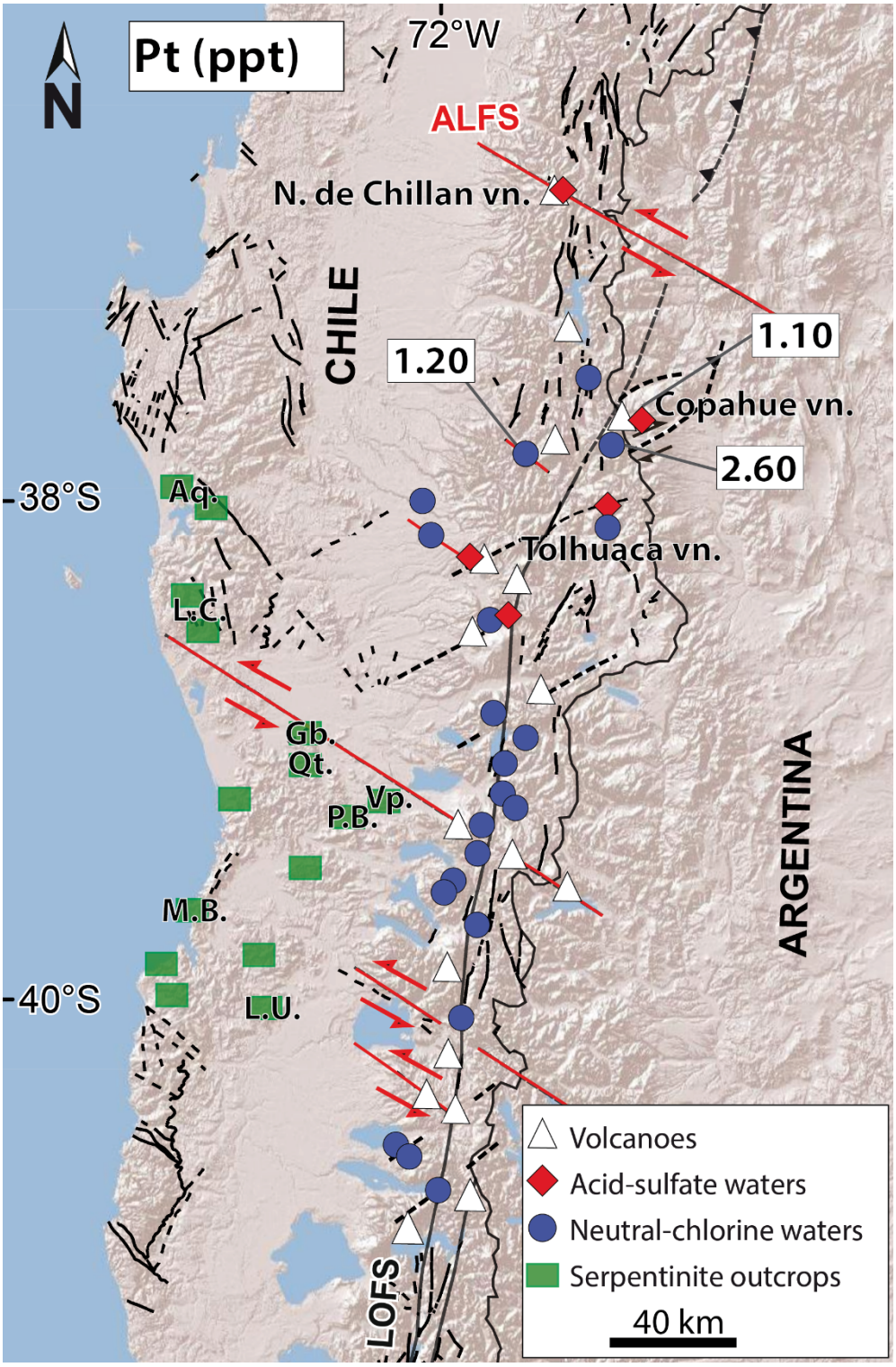

Figure 3.25. *Digital elevation model of the central part of the Southern Volcanic Zone in southern Chile with regional distribution of Pt concentrations in part per trillion (ppt), in acid-sulfate waters (red diamonds) and neutral-chlorine waters (blue circles). White triangles represent main stratovolcanoes of the segment. Solid and dashed lines show simplified faults and lineations from Lara et al. (2006), Cembrano and Lara (2009), Sánchez et al. (2013) and Pérez-Flores et al., 2016. Green squares represent ultramafic bodies of southern Chile from Salazar (2015). Aq.: Antiquina, L.C.: La Cabaña, Gb.: Gorbea, Qt.: Quitratue, Vp.: Voipire, P.B.: Palo Blanco, M.B.: Morro Bonifacio, L.U.: Los Ulmos.*

Concluding remarks and further implications

This study presents major and trace element concentrations of thermal springs that occur along the Liquiñe-Ofqui Fault Zone in the Southern Volcanic Zone, Chile. Acid-sulfate waters, formed by condensation and mixing of steam with meteoric waters, show the highest concentrations of metal and metalloid species including K, Ca, Mg, Ba, Al, Fe, Mn, Co, Ni, Cu, Zn, V, Cr, Sc, Ti, Cd, Y, Zr, Pb, La, Ce, Th and U. Neutral-chlorine waters, considered to represent aquifer fluids that have undergone boiling and subsequently mixed with meteoric water in the shallower part of the crust, present the highest concentrations of F, Cl, Br, NO_3, carbonates/bicarbonates, as well as Na, B, As, Li, Cs, Rb, Sr, Mo, Sb, Te, Ge and W. In both acid-sulfate and neutral-chlorine waters, PGE concentrations are elevated, in particular Pd (>1 ppb) and Rh (0.15 ppb). In order to constrain metal sources and processes, our major and trace element database was combined with previously published He isotope (Rc/Ra) and stable isotope (delta C, N) data obtained the exact water samples. The results for acid-sulfate waters show that despite that acid leaching of host rocks plays a role in metal enrichment (i.e., low, crustal Rc/Ra values correlate with high Ca, Mg, K, Ba, Sr, Co, Ni, Cu, Cd, Rh and Pd), metals such Mo, W, Ti and Pb and metalloids such as B, As, Sb and Ge are most likely to be directly sourced from the deep magmatic system and transported to the shallow geothermal environment by low density vapors (i.e., high, primitive Rc/Ra values correlate with high. Mo, W, Ti, Pb, As, Sb and Ge). These two different trends of enrichment of acid-sulfate waters are the result of a strong structural control that conditions selective elemental partitioning, enhancing water-rock interaction and metal leaching along oblique, NW ALFS structures (e.g., Ni, Co, Cu, Pd among others). In contrast, high vertical permeability along the main LOFS allow rapid fluxing of metals transported by magmatic vapor (e.g., As, Sb, Mo, Ge etc.)

Neutral-chlorine water chemistry, in contrast, is mostly dominated by shallow processes including mixing with meteoric fluids and mineral precipitation. Most of the major and trace element data of these waters do not show a clear correlation with Rc/Ra ratios (or display a weak positive correspondence). This is interpreted that dilution by meteoric fluids and precipitation processes are dominant, leading to a "loss" of metals concentrations by (co)precipitation and dilution. These removal processes are enhanced in low permeability settings, where the higher residence time of geothermal fluids in the crust increase the reaction time with country rock and the cooling of reservoir waters, by mixing with cold and shallow infiltrating water.

A particular feature of both acid-sulfate and neutral chlorine is the elevated PGE tenor, especially in the northern part of the studied region (north of 39°S). Although PGE's contents are relatively high in almost all the thermal springs between 37° and 39°S, the highest concentrations of Pd and Rh in water are related with the thermal springs PE and JM (Tolhuaca volcano), controlled by a NW ALFS structures and its origin is likely associated with leaching of host rocks (negative correspondence between Pd and Rh with Rc/Ra). Between 38°-40°S have been documented various outcrops of ultramafic bodies that have been proposed that were emplaced into the sediments of the Paleozoic accretionary prism after transport throughout the subduction channel. These bodies are the most suitable source of PGEs in thermal fluids, which by acid leaching of hidden bodies beneath the volcanic arc may be enriched in PGE's during the ascent through the upper crust.

Our study reveals a strong structural control on metal fluxing along the Liquiñe-Ofqui fault in Southern Volcanic Zone of Chile. The two main structural features controlling the volcanism and geothermal activity in the region i.e. transtensional NE-trending LOFS and transpressive NW-trending ALFS, control the occurrence of base and precious metals and metalloids in hydrothermal

fluids. Highest concentrations of base metals (e.g. Cu, Co, Ni) are associated with NW ALFS controlled thermal springs, whereas those thermal springs spatially associated with NE LOFS show the highest concentrations of metalloids (e.g. As, Sb) and metals as Pb, W, Ti and Zr.

This study conducted in active hydrothermal system may shed new light on metals partition and hydrothermal ore deposit distribution along long lived fault structures. For example in the Atacama Fault System, a 1000 km sinistral fault cutting across the Chilean Coastal Cordillera, which are associated the origin of many ore deposit of northern Chile, the IOCG-IOA deposits occur mainly along the main track, whereas porphyry Cu-Au deposits occur along secondary NW-trending structures.

Chapter 4: Cu-As decoupling in an active geothermal system: a link between pyrite and fluid composition

Abstract

Over the past few decades several studies have reported that pyrite hosts appreciable amounts of trace elements which commonly occur forming complex zoning patterns within a single mineral grain. These chemical zonations in pyrite have been recognized in a variety of hydrothermal ore deposit types (e.g., porphyry Cu-Mo-Au, epithermal Au deposits, iron oxide–copper–gold, Carlin-type and Archean lode Au deposits, among others), showing in some cases marked oscillatory alternation of metals and metalloids in pyrite growth zones (e.g., of Cu-rich, As-(Au, Ag)-depleted zones and As-(Au, Ag)-rich, Cu-depleted zones). This decoupled geochemical behavior of Cu and As has been interpreted as a result of chemical changes in ore-forming fluids, although direct evidence connecting fluctuations in hydrothermal fluid composition with metal partitioning into pyrite growth zones is still lacking. In this study, we report a comprehensive trace element database of pyrite from the Tolhuaca Geothermal System (TGS) in southern Chile, a young and active hydrothermal system where fewer pyrite growth rims and mineralization events are present and the reservoir fluid (i.e. ore-forming fluid) is accessible. We combined the high-spatial resolution and X-ray mapping capabilities of electron microprobe analysis (EMPA) with low detection limits and depth-profiling capacity of secondary-ion mass spectrometry (SIMS) in a suite of pyrite samples retrieved from a ~1 km drill hole that crosses the argillic (20 to 450 m) and propylitic (650 to 1000 m) alteration zones of the geothermal system. We show that the concentrations of precious metals (e.g., Au, Ag), metalloids (e.g., As, Sb, Se, Te), and base and heavy metals (e.g., Cu, Co, Ni, Pb) in pyrite at the TGS are significant. Among the elements analyzed, arsenic and Cu are the most abundant with concentrations that vary from sub-ppm levels to a few wt. % (i.e., up to ~5 wt. % As, ~1.5 wt. % Cu). Detailed wavelength-dispersive spectrometry (WDS) X-ray maps and SIMS depth vs. isotope concentration profiles reveal that pyrites from the TGS are characterized by chemical zoning where the studied elements occur in different mineralogical forms. Arsenic and cobalt occur as structurally bound elements in pyrite, Cu and Au in pyrite can occur as both solid solution and submicron-sized particles of chalcopyrite and native Au (or Au tellurides), respectively. Pyrites from the deeper propylitic zone do not show significant zonation and high Cu-(Co)-As concentrations correlate with each other. In contrast, well-developed zonations were detected in pyrite from the shallow argillic alteration zone, where Cu(Co)-rich, As-depleted cores alternate with Cu(Co)-depleted, As-rich rims. These microanalytical data were contrasted with chemical data of fluid inclusion in quartz and calcite veins (high Cu/As ratios) and borehole fluids (low Cu/As ratios) reported at the TGS, showing a clear correspondence between Cu and As concentrations in pyrite-forming fluids and chemical zonation in pyrite. These observations provide direct evidence supporting the selective partitioning of metals into pyrite as a result of changes in ore-forming fluid composition, most likely due to separation of a single-phase fluid into a low-density vapor and a denser brine, capable of fractionating Cu and As.

Introduction

Sulfide minerals are common in many active geothermal systems worldwide, including Salton Sea in California (Skinner et al., 1967; McKibben and Elders, 1985; McKibben et al., 1988a,

b; Hulen et al., 2004), Rotokawa, Ngawha and Broadlands-Ohaaki in New Zealand (Krupp and Seward, 1987; Cox and Browne, 1995; Simmons and Browne, 2000), Kirishima and Yanaizu-Nishiyama in Japan (Shoji et al., 1989, 1999), Mataloko in Indonesia (Koseki and Kazuo, 2006; Koseki and Nakashima, 2006), Joaquina in Guatemala (Libbey et al., 2015) and Reykjanes in Iceland (Libbey and William Jones, 2016). Among sulfides, pyrite is ubiquitous in geothermal systems although most studies have focused on their metal-rich fossil counterparts (i.e., ore deposits). Mineral chemistry studies of pyrite in hydrothermal ore deposits, including Carlin-type and Archean lode Au deposits, porphyry Cu deposits, epithermal Au-Ag deposits and iron oxide–copper–gold deposits (IOCG), among others, have pointed out that this sulfide is a major host of metals and metalloids such as Au, Ag, Cu, Pb, Zn, Co, Ni, As, Sb, Se, Te, Hg, Tl, and Bi (Cook and Chryssoulis, 1990; Fleet et al., 1993; Huston et al., 1995; Simon et al., 1999; Large et al., 2009; Palenik et al., 2004; Vaughan and Kyin, 2004; Reich et al., 2005, 2006; Barker et al., 2009; Cook et al., 2009; Deditius et al., 2009a,b, 2011, 2014; Sung et al., 2009; Koglin et al., 2010; Ulrich et al., 2011; Peterson and Mavrogenes, 2014; Steadman et al., 2015; Gregory et al., 2016; Reich et al., 2016; Tanner et al., 2016). These studies have also provided analytical and spectroscopic evidence showing that the incorporation and micro-textural distribution of these elements is complex in pyrite, occurring in both solid solution and/or as metal nanoparticles or nano-inclusions forming chemically-heterogeneous growth and sector zones. This variation in the chemical composition of pyrite has been used to elucidate the chemical evolution of hydrothermal systems and ore deposits at various scales (Muntean et al. 2011), but also been evaluated as a vectoring tool in mineral exploration (Baker et al., 2006; Belousov et al., 2014; Franchini et al., 2015; Gregory et al., 2016; Soltani Dehnavi et al., 2015). More recently, trace element contents in marine sulfides, particularly pyrite, are being used to answer some fundamental questions about the evolution of the Earth's ocean-atmosphere system, including how nutrient trace element cycles relate to geodynamic cycles, biological evolution and mass extinction events (Large et al., 2014, 2015a, b; Gregory et al., 2015a, b; Long et al., 2015).

Recent studies have reported complex oscillatory growth and sector zoning in pyrite from hydrothermal ore deposits where elements such Cu, Au and As are preferentially enriched and show a decoupled geochemical behavior (Deditius et al., 2008, 2009, 2011; Reich et al., 2013). Arsenic-rich zones containing Au, Ag, Sb, Te, and Pb, can alternate with Cu-rich zones with significantly lower concentrations of these elements, and barren pyrite zones with no other elements. These chemical zoning features have been related to selective partitioning of metals into pyrite as the result of physico-chemical changes in the ore-forming fluids (Deditius et al., 2009; Peterson and Mavrogenes, 2014; Reich et al., 2013, 2016). Furthermore, in low-temperature sedimentary environments, recent studies have shown that diagenetic pyrite formed within the anoxic sediments can record the composition of pore water, which is generally enriched in heavy metals (Berner et al., 2006, 2013; Gregory et al., 2014).

In particular, the presence of finely spaced multiple growth zones in pyrite where Cu and As are geochemically decoupled provide evidence that the composition of shallow hydrothermal systems can be affected intermittently and repetitively by vapors, probably from underlying magmas (Deditius et al., 2009; Reich et al., 2013). However, direct observations linking the alternating metal concentrations in pyrite zonations and the chemical evolution of the ore-forming fluid are still lacking. Furthermore, in active geothermal systems very few studies report trace metal concentrations in pyrite (Reykjanes geothermal system; Libbey & William-Jones, 2016), and no data linking sulfide composition, paleofluid and present-day fluid chemistry are currently available. Such information is relevant and is feasible to obtain in a young, active geothermal system where fewer mineralization events are present, pyrite show fewer growth zones and/or chemical

oscillations, and the reservoir fluid (i.e. ore-forming fluid) is accessible. This evidence is crucial to interpret the reportedly complex zoning of pyrite in fossil hydrothermal systems.

In this paper we report a comprehensive major and trace element database of pyrite from the active Tolhuaca Geothermal System (TGS) in the Andes of southern Chile, a high enthalpy geothermal reservoir that has been drilled down to ~3 km depth, but it is not affected by geothermal production or re-injection (Melosh et al., 2012; Sánchez-Alfaro et al., 2016a). At the TGS fine-grained pyrite is abundant, present-day geothermal fluids carry metals and metalloids including Cu, Au and As, among others, and paleofluid compositions are also available from fluid inclusions studies (Sánchez-Alfaro et al., 2016a). Therefore, the TGS provides an excellent opportunity to link the chemical and textural features of pyrite with paleofluid and borehole fluids composition data. In situ concentrations of precious metals (e.g., Au, Ag), metalloids (e.g., As, Sb, Se, Te) and base and heavy metals (e.g., Cu, Co, Ni, Pb) were measured using a combination of electron microprobe analysis (EMPA) and secondary-ion mass spectrometry (SIMS) in a suite of well constrained pyrite samples retrieved from a ~1 km drill core. Furthermore, we correlated our pyrite trace element data with geochemical data of present-day borehole fluids samples and LA-ICP-MS analyses of fluid inclusion assemblages hosted in paragenetically-linked quartz and calcite veins from Sánchez-Alfaro et al. (2016a). By integrating these three sources of data, i.e., elemental concentrations in pyrite, fluid inclusion data and borehole fluid chemistry, we provide evidence that fluctuations in the trace element budget of pyrite are directly linked to changes in hydrothermal fluid composition resulting from episodic inputs of magmatic vapor and/or phase separation (or boiling) of a single-phase hydrothermal fluid.

Geological background

In the Andean Cordillera of the central-southern Chile, hydrothermal systems occur in close spatial relationships with active volcanism as well as with major seismically active fault systems (Cembrano and Lara, 2009). In southern Chile, geothermal features are spatially related with the Liquiñe-Ofqui Fault System and with the NW-trending Arc-oblique Long-lived Basement Fault System (Sánchez et al., 2013; Tardani et al., 2016). The active TGS is located in the northern termination of the Liquiñe-Ofqui Fault System (Fig. 4.1) and is spatially associated with both NE- and NW-striking faults.

The Tolhuaca volcano is a glacially scoured composite stratovolcano of late-Pleistocene to Holocene age that rises ~900 m over a Miocene volcano-sedimentary rock basement (Lohmar et al., 2012; Thiele et al., 1987). In the summit, several NW-trending aligned craters with different preservation states indicate a migration of the volcanic activity from the SE towards the NW (Thiele et al., 1987). Lavas are predominantly basaltic andesites and andesites, with minor presence of basalts and dacites (Thiele et al. 1987, Lohmar et al., 2012). The latest eruptive phases occur in the NW portion of the volcanic edifice and correspond to a ~2 km long NW-trending fissure and a pyroclastic cone. The Tolhuaca volcano is likely to be related to the ALFS, which provides the suitable conditions for the development of magma reservoirs and magma differentiation (Cembrano and Lara, 2009, Pérez-Flores et al., 2016).

The TGS is located in the northwest flank of the Tolhuaca volcano and is characterized by several surficial thermal manifestations including fumaroles, boiling pools and hot springs (Fig. 4.1). Geothermal exploration campaigns have revealed the existence of a high-enthalpy reservoir in the system (Melosh et al., 2010, 2012). Two slim holes (Tol-1 and Tol-2) and two larger diameter wells (Tol-3 and Tol-4) were drilled down to 2117 m vertical depth (Fig. 4.1). Temperature logging and fluid samples suggest the presence of a geothermal reservoir at c.a. 1.5 km depth, at liquid-

saturated conditions with temperatures up to 300 °C and a relatively high meteoric water component (Melosh et al., 2012). The main reservoir is overlain by a steam heated aquifer at shallow depths that reaches up to 160 °C and controls the chemical nature of most of the hot springs (Melosh et al., 2010, 2012).

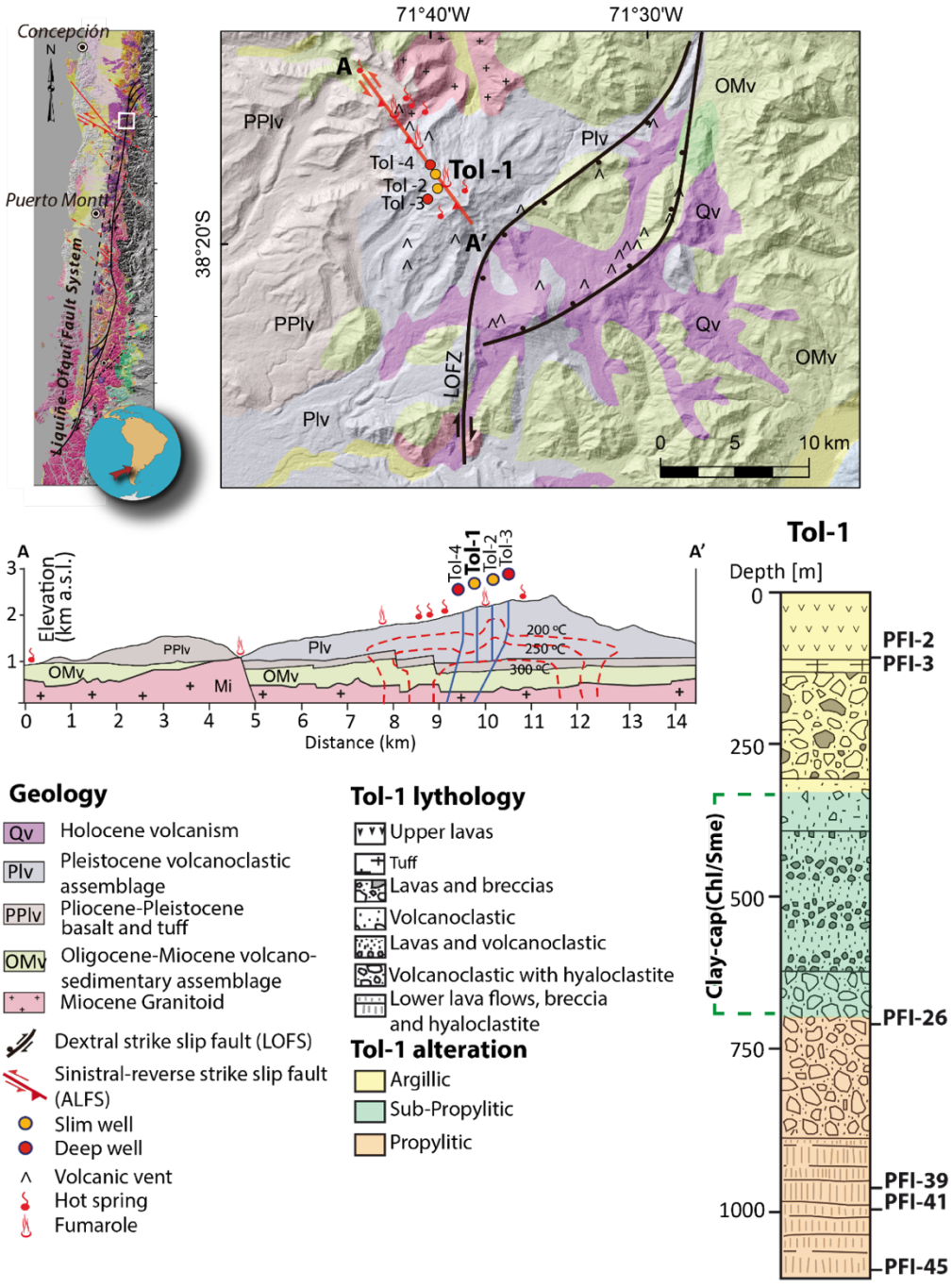

Figure 4.1. *Geological map of the Tolhuaca Geothermal System (TGS), modified from Aravena et al. (2016) and Sánchez-Alfaro et al. (2016a). The main geologic units, structures, surface thermal features and geothermal well locations, as well as the schematic cross section, were modified from Sánchez-Alfaro et al. (2016a). Simplified lithology of the Tol-1 well and hydrothermal alteration zones were taken from Melosh et al. (2010; 2012) and Sánchez et al. (2013). Depth location is indicated for pyrite-bearing samples PFI-2, PFI-3, PFI-26, PFI-39, PFI-41 and PFI-45. LOFZ: Liquiñe Ofqui Fault Zone; ALFS: Arc-oblique Long-lived Basement Fault System.*

The different geologic units, observed in the Tol-1 drill core material, are mainly lavas and related breccias, volcanoclastic and minor tuffs (Fig. 4.1). Hyaloclastites and pillow breccias also occur at different levels in the Tol-1 core (Lohmar et al., 2012; Sánchez-Alfaro et al., 2016a). Based on thin section petrography and X-ray diffraction (XRD) analyses of the Tol-1 core, three alteration zones were defined: 1) an upper zone of argillic alteration (20 to 450 m); 2) an intermediate zone with sub-propylitic alteration (450 to 650 m); and 3) a deeper zone of propylitic alteration (≥ 650 m) (Fig. 4.1) (Melosh et al., 2012). Lohmar et al. (2012) and Sánchez-Alfaro et al. (2016a) characterized argillic alteration facies by Fe-oxides + chlorite + calcite + clay + quartz + pyrite (+apatite), whereas the mineral assemblages in high temperature propylitic facies are composed of chlorite + epidote + calcite + pyrite + quartz + zeolites.

Melosh et al. (2012) and Sánchez-Alfaro et al. (2016a) recognized four stages (S1 to S4) of hydrothermal alteration in the TGS. The S1 stage represents an early heating event characterized by precipitation of iron oxides, quartz, and chalcedony as a result of widespread boiling and flushing. An episode of pervasive hydrothermal alteration of the volcanic and volcaniclastic rocks defines the S2 stage, where low temperature (<200 °C) argillic alteration assemblages (smectite; illite/smectite; interlayered chlorite/smectite, pyrite, calcite and chalcedony/amorphous silica) developed at the shallower levels (<670 m), while propylitic alteration assemblages (chlorite, epidote, quartz, calcite and pyrite) were formed under higher temperature (≥250 °C) conditions in the deep upflow zone (>700 m). Between the S2 and S3 stages, a low-permeability clay cap composed of chlorite and smectite was formed, separating the deep part of the system (propylitic alteration) from the shallower one (argillic alteration) (Fig. 4.1). The S3 stage was characterized by an increase in magmatic heat that promoted hydro-fracturing and brecciation of the clay-cap. The homogenization temperature data from fluid inclusions indicate diffuse boiling in the upper and lower zones. Finally, the S4 stage reveals a phase of fluid mixing and gentle boiling.

Samples and methods

Six representative pyrite-bearing samples from the argillic and propylitic alteration zones were selected (PFI-2, PFI-3, PFI-26, PFI-39, PFI-41, and PFI-45) from different depths of the drill core, as shown in Figure 4.1. Scanning electron microscope (SEM) observations were undertaken at the Andean Geothermal Centre of Excellence (CEGA), Universidad de Chile, using a FEI Quanta 250 SEM equipped with secondary electron (SE), energy-dispersive X-ray spectrometry (EDS), backscattered electron (BSE) and cathodoluminescence (CL) detectors. The analytical parameters were: spot size of 1-3 μm, an accelerating voltage of 10-20 keV, a beam intensity of 80 μA, and a working distance of 10 mm.

Pyrite is present as euhedral or sub-euhedral disseminated grains (<1 mm) at the TGS, occurring in millimeter-sized monomineralic veinlets and in micrometer-sized crystals in the rim of veins of amorphous silica and Fe-oxides (Fig. 4.2). Pyrite is generally fine-grained in the deeper propylitic zone (<30 μm). In the sub-propylitic zone (clay cap), pyrite is almost absent and is replaced by minor chalcopyrite and bornite. Minor amounts of sphalerite and galena are also identified. For detailed descriptions of the alteration and mineralization assemblages at Tolhuaca, the reader is referred to Sánchez-Alfaro et al. (2016a).

Electron microprobe analysis (EMPA) of pyrite grains (152 spot analyses total) was performed using a field-emission gun JEOL 8530F hyperprobe equipped with five wavelength-dispersive spectrometers at the Center for Microscopy, Characterization and Analysis (CMCA), University of Western Australia in Crawley, WA. Operating conditions were 40 degrees take-off angle and beam energy of 20 keV. The beam current was 50 nA, and the beam was fully focused.

Elements were acquired using the following analyzing crystals: LiF for Fe Kα, Au Lα, Te Lα, Cu Kα, Ni Kα, Zn Kα and Co Kα; PETJ for S Kα, Ag Lα, and Cd Lα; PETH for Sb Lα, and Pb Mα; and TAP for As Lα and Se Lα. The standards employed were commercially available metals, oxides, sulfides, selenides, and tellurides. Counting time was 20 seconds for S Kα and Fe Kα, 60 seconds for Cu Kα, Ni Kα, Zn Kα, and Co Kα, 80 seconds for Se Lα and Te Lα, 100 seconds for As Lα, Sb Lα, and Pb Mα, 120 seconds for Ag Lα and Cd Lα, and 200 seconds for Au Lα. Mean atomic number background corrections were employed throughout (Donovan and Tingle, 1996). Unknown and standard intensities were corrected for dead time and the ZAF algorithm was used for matrix absorption (Armstrong, 1988). On-peak interference corrections were applied as appropriate (Donovan et al., 1993). Detection limits ranged from 0.006 wt. % for Sb to 0.032 wt. % for Au.

Wavelength-dispersive spectrometry (WDS) X-ray maps were acquired using the calibration set up described above. Detection limit maps were acquired for these elements and applied as the minimum cut-off values. Map acquisition utilized a 100 nA beam current with 2 x 2 μm pixel dimension and 40 msec dwell time per pixel. Data were processed using the Calcimage software package and output to Surfer® for further processing and enhancement.

Additionally, 152 secondary-ion mass spectrometry (SIMS) spot analyses were acquired on individual pyrite grains from selected samples from the argillic and propylitic alteration zones (Table 4.2). SIMS analyses were performed at the Advanced Mineral Technology Laboratories (AMTEL) in London, Ontario, using a Cameca IMS-3f ion microprobe. Secondary ions monitored were ^{63}Cu, ^{65}Cu, ^{75}As, ^{78}Se, ^{80}Se, ^{107}Ag, ^{109}Ag, ^{121}Sb, ^{123}Sb, ^{128}Te, ^{130}Te, and ^{197}Au. In addition, the major sulfide-matrix constituent isotopes, ^{56}Fe and ^{34}S were monitored. A 10 kV and 8 nA primary Cs+ beam source was used for measurements, with a 4.5 kV accelerating voltage used for the negative secondary ions. The analytical spot size of the primary beam was ~25 μm; depth of analysis was 3.5-7.0 μm. Mineral standards used were produced experimentally by implanting a known dosage of the element of interest into the pyrite matrix using the Tandetron accelerator at the University of Western Ontario, Canada. The detection limits were ~0.03 ppm for Au, 3 ppm for As, 0.1 ppm for Cu, 0.02 ppm for Ag, 0.2 ppm for Sb, 0.01 ppm for Te, and 0.1 ppm for Se. For depth-concentration profiles, the minimum detectable size of sub-micron mineral inclusions was 500 nm at a 5 sec counting time. Thus, if more than one nanoparticle or inclusion is intercepted simultaneously, they register as a single particle in the depth profile.

Results

Representative EPMA and SIMS analyses of pyrite are reported in Tables 4.1 and 2, respectively. A summary of the trace elements concentrations in pyrite is presented in Figure 4.3. Back-scattered electron (BSE) images and quantitative WDS X-ray maps of representative samples from the shallow argillic alteration zone (PFI-2 and PFI-3) are shown in Figure 4.4, while Figure 4.5 displays WDS X-ray maps of pyrite grains from the deeper propylitic alteration zone (PFI-39 and PFI-41). Although no marked vertical variation in the trace element concentrations was generally observed in pyrite from the TGS, the average concentrations of some metals (Cu, Co, Pb, ,and Ni) and metalloids (As, Sb, Te) are slightly higher in the shallower argillic alteration zone (first 250 m of the drillcore).

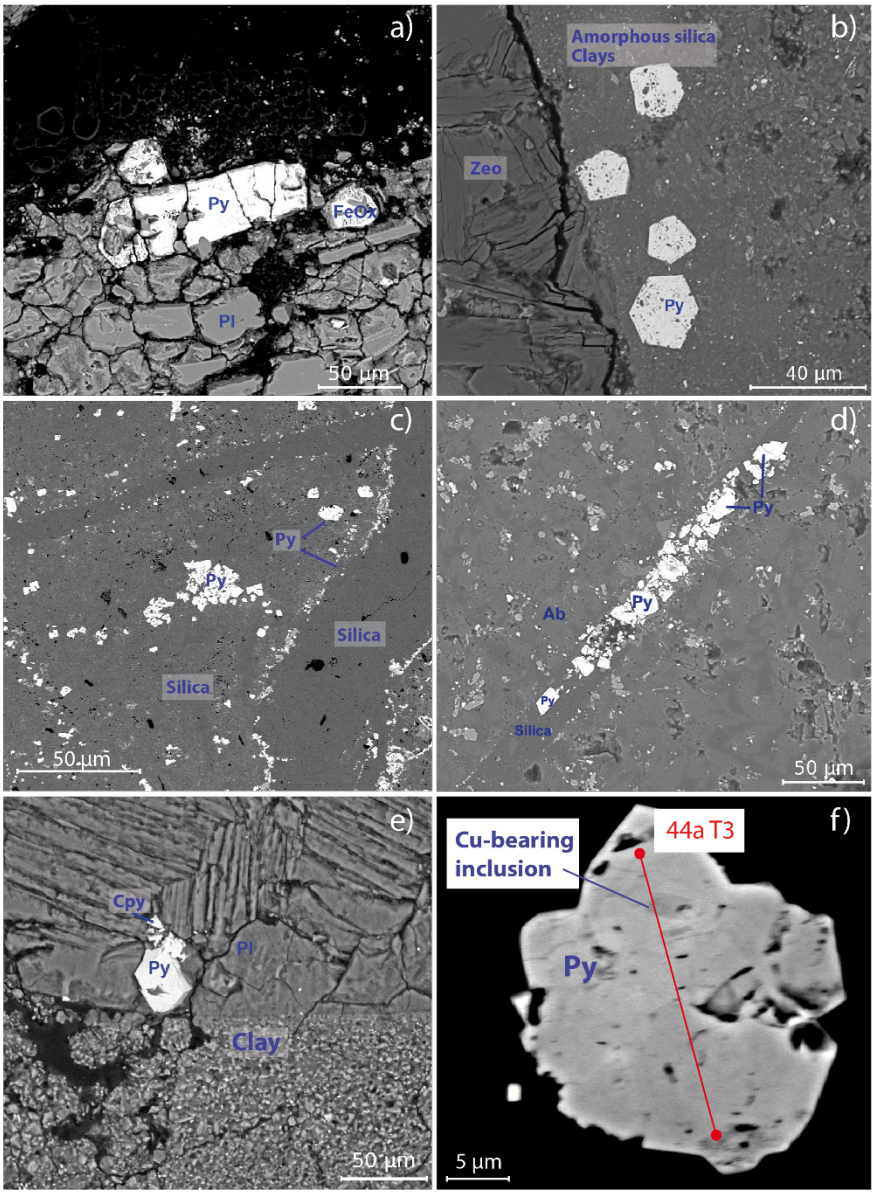

Figure 4.2. *Backscattered electron (BSE) images showing representative textural relationships of pyrite-bearing samples from the TGS. Pyrite occurs as disseminated grains (A, B, C, E, F) and in silica veinlets (C, D), and is mainly associated with Fe-oxide (A) and chalcopyrite (E). Chalcopyrite inclusions in pyrite are visible in selected grains (F). Py: pyrite; FeOx: Fe-oxide; Zeo: zeolite; Ab: albite, Cpy: chalcopyrite. The red line (F) shows an EMPA traverse (see table 4.1, sample PFI-39, datapoints 44a T3).*

Pyrite from the TGS is characterized by high concentrations of As, Pb and Cu, up to ~5 wt. %, ~2 wt. % and ~1.5 wt. %, respectively (Fig. 4.3). Cobalt and Sb contents are also relatively high and vary from 200 ppb to ~1 wt. % and from ~300 ppb to ~0.5 wt. %, respectively, spanning five orders of magnitude in concentration. Arsenic, Cu and Co show distinct zoning in the shallower argillic alteration zone (Fig. 4.4). WDS X-ray maps indicate that arsenic is enriched in the rims of pyrite crystals and depleted in the center (Fig. 4.4b, f, i, l and o), while Cu and Co show the opposite distribution with the highest concentrations found in the pyrite cores (Fig. 4.4c, d, g, j, k, m, n, p and q). WDS X-ray maps of fine-grained pyrite from the deeper, propylitic alteration zone (Figs. 5a-f) do not display the well-defined zonation patterns observed in pyrite grains from the argillic

alteration zone samples. Only one pyrite grain from the propylitic zone shows As-enriched cores (Fig. 4.5a), although these higher concentrations do not correlate with increased Cu or Co (Fig. 4.5b and c).

Concentrations of Au in pyrite are detectable using SIMS. Only one data point was detected by EPMA with a concentration of 1500 ppm (Table 4.1). SIMS data show Au values that vary between 10 ppb to ~10 ppm. Silver concentrations range between 70 ppb and ~400 ppm, with one data point reaching ~0.5 wt. %. Cadmium, Ti and Se contents of pyrite range from 200 and 160 ppm, and 30 ppb, respectively, to maximum concentrations within the range of 1000's of ppm. Nickel and Te concentrations vary between ~60 to 600 ppm, and ~10 ppb to 500 ppm, respectively.

Discussion

Mineralogical incorporation of metals and metalloids in pyrite from the TGS

Pyrite from the TGS can be classified as "arsenian" in terms of its As contents (i.e., up to 5 wt. % levels), which is also in agreement with the high As concentrations documented in the well fluids and thermal springs (up to 25 ppm; Sánchez-Alfaro et al., 2016a). The generally homogeneous distribution of As in pyrite, as detected by WDS X-ray maps (Figs. 4.4b, f, i, l, o and Figs. 4.5a and d), strongly suggests that As is structurally bound (solid solution), even if the As-Fe-S ternary diagram in Figure 4.6 suggests minor presence of As^0. Correlation plots showing As-S and As-Fe inverse trends (Figs. 4.7a and b) and the ternary diagram of Figure 4.6 does not show a conclusive trend of As substitution at the TGS, and it is likely that As^{1-}, As^{2+} and As^{3+} ionic species are present (Deditius et al., 2008; 2014; Qian et al., 2013). No significant clustering distribution of As are observed in WDS maps, where As is markedly enriched in the pyrite rims (Figs. 4.4b, f, i, l and o). Also, no noticeable differences in As speciation are observed in pyrite from the shallower or deeper zones, as suggested using SIMS depth profiling, where each successively deeper layer of the material is analyzed as a function of time. The flat ^{75}As depth profile in Figure 4.8b strongly suggests that As is mainly incorporated within the pyrite structure.

The high Cu concentrations (up to ~2 wt. %) measured by EMPA are related to two dominant mineralogical forms of Cu, as observed on SIMS depth profiles: (i) structurally bound Cu, and (ii) as micro- to nano-sized inclusions of chalcopyrite (Figs. 4.8c and d). Both forms of Cu can also be observed in the elemental maps in Figures 4.4d, g, k, n and q, and in Figures 4.5c and f. Structurally bound Cu is distributed homogeneously, forming the light blue-colored areas usually restricted to the core of the pyrite crystals, which contrasts with the dark-blue, low-Cu background (Fig. 4.4d, g and k, WDS maps).

The elemental plot in Figure 4.7c shows a negative correspondence between Cu and Fe (R^2=0.60), suggesting that $Cu^{2+} \Leftrightarrow Fe^{2+}$ as a possible substitution, although the precise mechanism of Cu incorporation cannot be deduced (Shimazaki and Clark, 1970; Schmid-Beurmann and Bente, 1995). It is likely that most of the structurally bound Cu replaces Fe in octahedral sites, which may be due to considerable distortion of the pyrite symmetry by the presence of other elements such as As, Sb or Co (Radcliffe and McSween, 1969; Bayliss, 1989).

Table 4.1. *Representative EPMA Analyses (wt %) of Pyrite from the Tolhuaca Geothermal System. Detection limits (DL) are shown in wt. %.*

	S WT%	Fe WT%	Co WT%	Cu WT%	Ni WT%	Pb WT%	Ti WT%	As WT%	Sb WT%	Se WT%	Te WT%	Au WT%	Ag WT%	Cd WT%	TOTAL
DL	0.01	0.02	0.01	0.01	0.01	0.01	0.01	0.01	0.01	0.01	0.01	0.03	0.01	0.02	
PFI-2															
p1-1	50.83	45.07	0.01	0.03	b.d.	0.03	b.d.	2.72	0.01	b.d.	b.d.	b.d.	b.d.	b.d.	98.75
p1-2	51.67	44.70	0.01	b.d.	0.01	0.02	b.d.	3.93	0.02	0.01	b.d.	b.d.	b.d.	0.03	100.47
p3-1	52.18	44.42	0.11	0.02	0.04	0.11	b.d.	2.35	0.01	0.01	b.d.	b.d.	0.02	0.03	99.30
p2-1	51.37	44.62	b.d.	b.d.	b.d.	0.03	b.d.	2.95	0.01	b.d.	b.d.	b.d.	b.d.	b.d.	99.09
p5-1	53.16	44.51	0.10	0.33	0.02	0.24	b.d.	b.d.	0.01	b.d.	b.d.	b.d.	0.03	0.04	98.43
p4-1	53.16	44.88	0.02	0.47	b.d.	0.10	b.d.	0.30	b.d.	b.d.	b.d.	b.d.	0.02	b.d.	98.99
p8-1	53.09	45.01	0.10	0.09	0.01	0.17	b.d.	0.50	0.02	0.03	b.d.	b.d.	0.02	b.d.	99.13
p8-2	51.79	43.93	0.05	0.36	0.01	0.08	b.d.	0.43	b.d.	b.d.	b.d.	b.d.	b.d.	0.02	96.70
p8-3	53.09	44.52	0.06	0.05	0.01	0.08	b.d.	0.15	b.d.	b.d.	b.d.	b.d.	0.02	0.02	98.02
p8-4	52.78	43.90	0.02	0.06	b.d.	0.04	b.d.	0.89	b.d.	b.d.	b.d.	b.d.	0.02	0.04	97.75
p7-1	50.01	45.23	0.11	0.03	0.06	0.06	b.d.	b.d.	0.01	b.d.	0.04	b.d.	b.d.	b.d.	95.60
p7-2	52.79	45.47	b.d.	0.14	b.d.	0.02	b.d.	b.d.	0.01	b.d.	0.05	b.d.	b.d.	b.d.	98.58
p7-3	53.54	45.17	0.01	0.03	b.d.	b.d.	b.d.	0.33	b.d.	b.d.	b.d.	b.d.	0.03	0.02	99.13
p6-1	50.17	43.53	0.04	0.33	b.d.	0.16	b.d.	4.88	0.03	0.04	0.04	b.d.	b.d.	b.d.	99.26
PFI-3															
p3-1	52.76	44.82	0.06	0.08	b.d.	0.15	b.d.	b.d.	0.01	0.01	b.d.	b.d.	b.d.	b.d.	97.92
p3-4	51.67	44.27	b.d.	0.24	b.d.	0.07	b.d.	b.d.	0.01	b.d.	b.d.	b.d.	b.d.	0.02	96.31
p4-1	52.15	44.94	0.24	0.06	0.03	0.07	b.d.	0.08	0.02	b.d.	b.d.	b.d.	0.02	b.d.	97.67
p4-2	52.07	44.88	0.06	0.08	b.d.	0.12	b.d.	b.d.	0.01	b.d.	b.d.	b.d.	b.d.	0.02	97.29
p4-3	51.46	44.55	0.04	0.11	b.d.	0.19	b.d.	b.d.	0.01	b.d.	b.d.	b.d.	0.02	b.d.	96.43
p4-4	51.74	45.04	0.05	0.03	b.d.	0.06	b.d.	b.d.	0.01	b.d.	b.d.	b.d.	b.d.	b.d.	96.98
p4-5	51.27	44.20	0.18	0.12	0.02	0.15	b.d.	b.d.	0.02	b.d.	b.d.	b.d.	0.02	b.d.	96.04
p1-2	51.60	44.95	0.18	0.09	0.02	0.07	b.d.	b.d.	0.01	b.d.	b.d.	b.d.	0.02	b.d.	96.97
p1-4	51.95	45.84	0.03	0.13	0.01	0.06	b.d.	0.19	0.01	b.d.	b.d.	b.d.	b.d.	b.d.	98.26
p1-5	51.16	45.46	0.01	0.03	b.d.	0.01	b.d.	0.86	0.02	b.d.	b.d.	b.d.	b.d.	b.d.	97.58
p2-4	51.29	45.59	0.04	0.06	b.d.	0.03	b.d.	0.07	0.02	b.d.	b.d.	b.d.	b.d.	b.d.	97.12
p2-5	52.03	45.74	0.03	0.08	b.d.	0.02	b.d.	0.06	0.01	b.d.	b.d.	b.d.	b.d.	b.d.	98.00
p2-7	51.08	44.78	0.10	0.04	b.d.	0.17	b.d.	b.d.	0.01	b.d.	b.d.	b.d.	b.d.	b.d.	96.20
p2-8	51.72	45.25	0.06	0.10	b.d.	0.04	b.d.	0.19	0.02	b.d.	b.d.	b.d.	b.d.	b.d.	97.43
p5-2	51.55	45.42	0.06	0.09	b.d.	0.08	b.d.	0.08	0.01	b.d.	0.05	b.d.	b.d.	b.d.	97.38
p5-5	51.79	44.66	0.07	0.08	b.d.	0.12	b.d.	b.d.	0.01	b.d.	b.d.	b.d.	0.02	b.d.	96.82
p7-1	50.01	44.39	0.05	0.07	b.d.	0.07	b.d.	0.53	0.02	0.01	b.d.	b.d.	b.d.	b.d.	95.17
p7-4	51.49	45.44	b.d.	0.20	b.d.	0.03	b.d.	0.11	0.02	b.d.	b.d.	b.d.	b.d.	b.d.	97.33
p7-5	51.93	45.06	0.03	0.07	b.d.	0.02	b.d.	0.29	0.02	b.d.	b.d.	b.d.	0.02	b.d.	97.47
PFI-39															
8a	53.76	45.45	0.03	b.d.	b.d.	b.d.	b.d.	b.d.	0.01	0.04	b.d.	b.d.	0.03	0.07	99.38
9a	52.54	45.95	0.03	b.d.	b.d.	b.d.	b.d.	b.d.	b.d.	b.d.	b.d.	b.d.	b.d.	0.02	98.54
10a	53.32	46.24	0.08	b.d.	b.d.	b.d.	b.d.	0.16	b.d.	b.d.	b.d.	b.d.	b.d.	0.04	99.85
12a	54.75	46.52	0.04	0.10	b.d.	b.d.	b.d.	0.12	b.d.	b.d.	b.d.	b.d.	0.03	0.05	101.62
19a	52.56	45.37	0.05	b.d.	b.d.	b.d.	b.d.	0.06	b.d.	b.d.	b.d.	b.d.	b.d.	0.04	98.08
24a	54.01	46.63	0.04	b.d.	b.d.	b.d.	b.d.	b.d.	0.01	b.d.	b.d.	b.d.	b.d.	0.04	100.72
26a	54.08	46.17	0.04	b.d.	b.d.	b.d.	b.d.	0.15	b.d.	b.d.	b.d.	b.d.	0.02	0.04	100.49
29a	52.75	45.96	0.05	b.d.	b.d.	0.06	b.d.	1.77	0.02	b.d.	b.d.	b.d.	0.02	0.03	100.65
30a	53.73	46.07	0.10	b.d.	b.d.	0.03	b.d.	0.18	b.d.	b.d.	b.d.	b.d.	0.02	0.04	100.18
31a	54.37	46.80	0.07	b.d.	b.d.	0.02	b.d.	0.04	0.01	b.d.	b.d.	b.d.	b.d.	0.03	101.34
32a(T1)	53.25	46.93	0.06	b.d.	b.d.	0.01	b.d.	b.d.	b.d.	b.d.	b.d.	b.d.	b.d.	0.03	100.27
32a(T1)	53.03	46.59	0.08	b.d.	b.d.	0.03	b.d.	0.22	b.d.	b.d.	b.d.	b.d.	b.d.	0.03	99.99
32a(T1)	53.73	46.79	0.07	b.d.	b.d.	b.d.	b.d.	b.d.	b.d.	b.d.	b.d.	b.d.	b.d.	0.03	100.62
32a(T1)	54.25	46.87	0.06	b.d.	b.d.	b.d.	b.d.	0.04	b.d.	b.d.	b.d.	b.d.	b.d.	0.03	101.25
32a(T1)	53.63	46.74	0.07	b.d.	b.d.	0.06	b.d.	0.66	0.01	b.d.	b.d.	b.d.	b.d.	0.04	101.20
32a(T1)	53.67	46.71	0.06	b.d.	b.d.	0.02	b.d.	0.05	b.d.	b.d.	b.d.	b.d.	0.02	0.03	100.56
32a(T1)	53.40	46.61	0.07	b.d.	b.d.	0.04	b.d.	0.35	b.d.	b.d.	b.d.	b.d.	b.d.	0.04	100.50
33a	52.52	46.50	0.08	b.d.	b.d.	0.03	b.d.	0.13	b.d.	b.d.	b.d.	b.d.	b.d.	0.04	99.28
34a(T2)	53.18	46.25	0.11	b.d.	b.d.	0.05	b.d.	0.21	b.d.	b.d.	b.d.	b.d.	0.02	0.05	99.88
34a(T2)	53.62	46.67	0.04	b.d.	b.d.	b.d.	b.d.	b.d.	b.d.	b.d.	b.d.	b.d.	b.d.	0.04	100.36
34a(T2)	53.56	46.75	0.04	b.d.	b.d.	b.d.	b.d.	b.d.	b.d.	b.d.	b.d.	b.d.	0.02	0.05	100.42
34a(T2)	53.24	46.39	0.06	b.d.	b.d.	b.d.	b.d.	0.06	b.d.	b.d.	b.d.	b.d.	0.02	0.04	99.81
36a	53.80	46.50	0.04	b.d.	b.d.	0.02	b.d.	0.25	0.01	b.d.	b.d.	b.d.	b.d.	0.04	100.67
39a	53.85	46.41	0.03	b.d.	b.d.	b.d.	b.d.	b.d.	b.d.	b.d.	b.d.	b.d.	b.d.	0.05	100.34
40a	53.80	46.17	0.04	0.01	b.d.	0.01	0.02	0.03	0.01	0.01	b.d.	b.d.	0.03	0.05	100.18
41a	52.64	46.12	0.04	0.02	b.d.	b.d.	0.07	b.d.	b.d.	b.d.	b.d.	b.d.	b.d.	0.04	98.92
42a	53.56	46.15	0.03	b.d.	b.d.	b.d.	b.d.	b.d.	b.d.	b.d.	b.d.	b.d.	0.02	0.04	99.81
44a(T3)	53.51	46.64	0.06	b.d.	b.d.	b.d.	b.d.	b.d.	b.d.	b.d.	b.d.	b.d.	b.d.	0.04	100.25
44a(T3)	53.00	45.89	0.07	1.58	b.d.	0.05	b.d.	b.d.	0.01	b.d.	b.d.	b.d.	b.d.	0.03	100.64
44a(T3)	53.72	46.87	0.07	0.06	b.d.	0.04	b.d.	b.d.	b.d.	b.d.	b.d.	b.d.	0.02	0.04	100.81
44a(T3)	52.95	46.64	0.08	b.d.	b.d.	0.03	b.d.	0.03	b.d.	b.d.	b.d.	b.d.	b.d.	0.02	99.74
44a(T3)	52.80	45.99	0.07	b.d.	b.d.	0.01	b.d.	b.d.	b.d.	b.d.	b.d.	b.d.	b.d.	0.03	98.91
44a(T3)	53.25	46.34	0.05	b.d.	b.d.	b.d.	b.d.	b.d.	b.d.	b.d.	b.d.	b.d.	b.d.	0.04	99.69
45a(T4)	52.84	46.01	0.06	0.02	b.d.	0.02	b.d.	1.19	0.03	b.d.	b.d.	b.d.	0.02	0.04	100.22
45a(T4)	51.77	44.93	0.05	0.05	b.d.	2.04	b.d.	1.17	0.02	b.d.	b.d.	b.d.	b.d.	0.04	100.07
45a(T4)	51.38	45.23	0.04	b.d.	b.d.	1.34	b.d.	1.32	0.02	b.d.	b.d.	b.d.	b.d.	b.d.	99.33
46a(T5)	53.95	46.40	0.05	b.d.	b.d.	b.d.	b.d.	0.39	b.d.	b.d.	b.d.	b.d.	0.02	0.05	100.85
46a(T5)	53.98	46.51	0.04	b.d.	b.d.	b.d.	b.d.	0.36	b.d.	b.d.	b.d.	b.d.	0.02	0.04	100.95
46a(T5)	53.83	46.81	0.04	b.d.	b.d.	b.d.	b.d.	0.26	0.01	b.d.	b.d.	b.d.	0.02	0.04	101.01
46a(T5)	53.32	46.44	0.05	0.04	b.d.	0.02	b.d.	0.22	0.01	b.d.	b.d.	b.d.	b.d.	0.04	100.14
46a(T5)	53.79	46.97	0.11	b.d.	b.d.	0.02	b.d.	0.43	0.01	b.d.	b.d.	b.d.	b.d.	0.04	101.38
46a(T5)	53.33	46.66	0.07	b.d.	b.d.	0.02	b.d.	0.36	0.01	b.d.	b.d.	b.d.	b.d.	0.03	100.47
46a(T5)	53.48	46.75	0.07	b.d.	b.d.	b.d.	b.d.	0.26	0.01	b.d.	b.d.	b.d.	b.d.	0.03	100.60
47a	53.42	45.71	0.14	b.d.	b.d.	b.d.	0.06	0.62	0.03	b.d.	b.d.	b.d.	0.02	0.04	100.04
49a	53.09	46.26	0.19	b.d.	b.d.	b.d.	0.04	0.98	0.01	b.d.	b.d.	b.d.	b.d.	0.03	100.60
50a	52.97	46.82	0.07	b.d.	b.d.	b.d.	b.d.	0.62	0.03	b.d.	b.d.	b.d.	b.d.	0.03	100.53

Table 4.1. *Continue.*

PFI-41															
1b(T1)	54.46	46.43	0.04	b.d.	b.d.	b.d.	b.d.	b.d.	b.d.	b.d.	b.d.	b.d.	0.04	0.04	101.02
1b(T1)	54.16	46.69	0.04	b.d.	b.d.	b.d.	b.d.	b.d.	b.d.	b.d.	b.d.	b.d.	0.03	0.06	100.98
1b(T1)	54.05	46.92	0.04	b.d.	b.d.	b.d.	b.d.	b.d.	b.d.	b.d.	b.d.	b.d.	b.d.	0.04	101.04
1b(T1)	53.72	46.75	0.04	b.d.	b.d.	b.d.	b.d.	b.d.	b.d.	b.d.	b.d.	b.d.	b.d.	0.04	100.55
1b(T1)	53.68	46.69	0.04	b.d.	b.d.	b.d.	b.d.	b.d.	0.01	b.d.	b.d.	b.d.	b.d.	0.03	100.44
1b(T1)	53.44	46.63	0.04	b.d.	b.d.	0.01	b.d.	b.d.	b.d.	b.d.	b.d.	b.d.	b.d.	0.03	100.15
1b(T1)	53.43	46.72	0.05	b.d.	b.d.	0.01	b.d.	b.d.	0.01	b.d.	b.d.	b.d.	b.d.	0.02	100.24
2b	53.87	46.48	0.04	b.d.	b.d.	0.01	b.d.	b.d.	b.d.	b.d.	b.d.	b.d.	b.d.	0.04	100.45
4b	54.09	46.77	0.05	b.d.	b.d.	0.02	b.d.	b.d.	b.d.	b.d.	b.d.	b.d.	0.02	0.04	100.99
5b	53.53	46.43	0.08	b.d.	b.d.	0.04	b.d.	b.d.	b.d.	b.d.	b.d.	b.d.	b.d.	0.03	100.11
6b	53.51	46.42	0.03	b.d.	b.d.	0.01	b.d.	b.d.	b.d.	b.d.	b.d.	b.d.	b.d.	0.04	100.02
7b	53.53	46.59	0.04	b.d.	b.d.	b.d.	b.d.	b.d.	0.01	b.d.	b.d.	b.d.	b.d.	0.03	100.20
8b	53.90	46.13	0.04	b.d.	b.d.	b.d.	b.d.	0.37	b.d.	b.d.	b.d.	b.d.	0.03	0.05	100.51
9b	54.08	46.56	0.04	b.d.	b.d.	b.d.	b.d.	0.12	b.d.	b.d.	b.d.	b.d.	0.03	0.04	100.87
10b	52.95	46.24	0.05	b.d.	b.d.	b.d.	b.d.	0.55	0.01	b.d.	b.d.	b.d.	b.d.	0.04	99.82
11b	53.07	46.24	0.08	b.d.	b.d.	0.04	0.15	b.d.	b.d.	b.d.	b.d.	b.d.	b.d.	b.d.	99.58
12b	54.51	46.40	0.06	b.d.	b.d.	b.d.	0.08	0.16	0.01	b.d.	b.d.	b.d.	0.03	0.03	101.27
13b	52.68	45.70	0.04	b.d.	b.d.	b.d.	0.06	0.10	b.d.	b.d.	b.d.	b.d.	0.02	0.03	98.63
14b	53.62	46.71	0.06	b.d.	b.d.	0.02	0.12	b.d.	b.d.	b.d.	b.d.	b.d.	0.02	0.03	100.57
15b	53.61	46.47	0.05	b.d.	b.d.	0.02	0.07	0.13	b.d.	b.d.	b.d.	b.d.	b.d.	0.03	100.38
16b	53.69	46.26	0.11	b.d.	b.d.	0.02	0.13	b.d.	b.d.	b.d.	b.d.	b.d.	b.d.	0.03	100.24
17b	52.41	45.62	0.11	b.d.	b.d.	0.02	0.11	0.10	0.01	b.d.	b.d.	b.d.	b.d.	0.03	98.42
20b	53.40	46.28	0.05	b.d.	b.d.	0.04	0.04	b.d.	0.01	b.d.	b.d.	b.d.	b.d.	0.02	99.84
21b	53.25	45.92	0.04	b.d.	b.d.	0.02	0.06	0.22	0.01	b.d.	b.d.	b.d.	0.02	0.04	99.57
22b	53.72	46.17	0.08	b.d.	b.d.	b.d.	0.20	0.14	0.01	b.d.	b.d.	b.d.	0.03	0.03	100.38
23b	53.15	46.28	0.04	b.d.	b.d.	0.02	0.02	0.06	b.d.	b.d.	b.d.	b.d.	b.d.	0.03	99.61
24b	52.56	45.69	0.04	b.d.	b.d.	b.d.	b.d.	b.d.	b.d.	b.d.	b.d.	b.d.	0.02	0.03	98.33
25b	52.81	45.78	0.04	b.d.	b.d.	b.d.	0.05	0.02	b.d.	b.d.	b.d.	b.d.	b.d.	0.03	98.72
27b	53.54	45.85	0.09	0.02	0.03	0.05	0.14	0.60	0.04	0.50	0.11	0.15	0.48	0.60	102.28
30b	53.44	45.84	0.07	b.d.	b.d.	b.d.	0.04	0.02	0.01	b.d.	b.d.	b.d.	0.03	0.04	99.47
31b(T2)	53.60	46.66	0.03	b.d.	b.d.	0.02	b.d.	0.24	0.01	b.d.	b.d.	b.d.	b.d.	0.03	100.60
31b(T2)	53.35	46.37	0.04	0.21	b.d.	0.12	b.d.	0.61	b.d.	b.d.	b.d.	b.d.	0.02	0.04	100.76
31b(T2)	52.59	45.89	0.04	0.23	b.d.	0.13	b.d.	0.24	b.d.	b.d.	b.d.	b.d.	b.d.	0.03	99.14
31b(T2)	53.28	46.43	0.04	0.14	b.d.	0.09	b.d.	0.23	b.d.	b.d.	b.d.	b.d.	b.d.	0.03	100.23
31b(T2)	53.12	46.49	0.04	b.d.	b.d.	0.07	b.d.	0.46	b.d.	b.d.	b.d.	b.d.	0.02	0.04	100.23
31b(T2)	53.70	46.46	0.04	0.17	b.d.	0.05	b.d.	0.45	b.d.	b.d.	b.d.	b.d.	0.02	0.04	100.92
31b(T2)	53.17	46.77	0.05	b.d.	b.d.	0.03	b.d.	0.41	b.d.	b.d.	b.d.	b.d.	b.d.	0.02	100.45
31b(T2)	52.62	46.59	0.09	b.d.	b.d.	0.16	b.d.	0.18	b.d.	b.d.	b.d.	b.d.	b.d.	0.03	99.67
31b(T2)	53.18	46.34	0.10	b.d.	b.d.	0.13	0.14	0.08	b.d.	b.d.	b.d.	b.d.	b.d.	0.03	100.01
31b(T2)	52.78	45.82	0.04	1.34	b.d.	0.26	0.07	0.24	b.d.	b.d.	b.d.	b.d.	b.d.	0.04	100.59
31b(T2)	52.31	46.77	0.03	b.d.	b.d.	b.d.	b.d.	0.17	b.d.	b.d.	b.d.	b.d.	b.d.	0.03	99.31
32b(T3)	53.59	46.60	0.04	b.d.	b.d.	b.d.	b.d.	0.35	b.d.	b.d.	b.d.	b.d.	b.d.	0.03	100.61
32b(T3)	53.82	46.56	0.04	b.d.	b.d.	b.d.	b.d.	0.23	b.d.	b.d.	b.d.	b.d.	b.d.	0.04	100.68
32b(T3)	53.71	46.50	0.04	b.d.	b.d.	0.01	b.d.	0.19	b.d.	b.d.	b.d.	b.d.	b.d.	0.03	100.49
32b(T3)	53.45	46.22	0.04	b.d.	b.d.	0.02	b.d.	0.34	b.d.	b.d.	b.d.	b.d.	b.d.	0.04	100.12
32b(T3)	52.30	45.10	0.03	0.13	b.d.	0.05	0.26	0.23	b.d.	b.d.	b.d.	b.d.	0.02	0.04	98.17
32b(T3)	53.19	46.30	0.04	b.d.	b.d.	0.01	0.02	0.01	b.d.	b.d.	b.d.	b.d.	b.d.	0.04	99.61
32b(T3)	53.19	46.45	0.06	b.d.	b.d.	0.02	0.02	0.16	b.d.	b.d.	b.d.	b.d.	b.d.	0.03	99.93
32b(T3)	53.69	46.42	0.05	b.d.	b.d.	0.04	0.02	0.17	0.01	b.d.	b.d.	b.d.	b.d.	0.04	100.44
PFI-45															
33b(T4)	52.66	45.91	0.04	b.d.	b.d.	0.02	b.d.	0.23	0.01	b.d.	b.d.	b.d.	0.02	0.04	98.92
33b(T4)	53.44	46.61	0.05	b.d.	b.d.	b.d.	0.11	0.27	b.d.	b.d.	b.d.	b.d.	0.02	0.03	100.53
33b(T4)	53.27	45.62	0.05	b.d.	b.d.	0.04	0.76	0.15	b.d.	b.d.	b.d.	b.d.	0.03	0.05	99.97
33b(T4)	54.95	46.49	0.04	b.d.	b.d.	b.d.	b.d.	0.20	b.d.	0.02	b.d.	b.d.	0.05	0.06	101.80
34b	53.34	46.20	0.03	b.d.	b.d.	b.d.	0.02	0.13	b.d.	b.d.	b.d.	b.d.	b.d.	0.04	99.77
35b	53.40	45.63	0.05	b.d.	b.d.	0.01	0.41	0.17	b.d.	b.d.	b.d.	b.d.	0.02	0.05	99.75
36b	55.01	46.38	0.03	b.d.	b.d.	b.d.	b.d.	0.15	b.d.	b.d.	b.d.	b.d.	b.d.	0.04	101.62
40b	53.85	46.36	0.05	b.d.	b.d.	b.d.	b.d.	0.38	b.d.	b.d.	b.d.	b.d.	0.02	0.06	100.71
41b(T5)	53.06	46.30	0.03	b.d.	b.d.	0.01	b.d.	0.50	0.01	b.d.	b.d.	b.d.	b.d.	0.03	99.95
41b(T5)	52.29	45.78	0.03	b.d.	b.d.	b.d.	b.d.	0.29	b.d.	b.d.	b.d.	b.d.	0.03	0.05	98.46
41b(T5)	52.26	45.63	0.03	b.d.	b.d.	b.d.	b.d.	1.23	0.01	b.d.	b.d.	b.d.	0.03	0.05	99.24
41b(T5)	53.23	45.56	0.03	b.d.	b.d.	0.02	b.d.	1.46	0.02	0.02	b.d.	b.d.	0.03	0.06	100.42
41b(T5)	53.24	46.18	0.03	b.d.	b.d.	b.d.	b.d.	1.09	0.01	b.d.	b.d.	b.d.	0.02	0.04	100.62
41b(T5)	53.15	46.19	0.03	b.d.	b.d.	b.d.	b.d.	1.20	b.d.	b.d.	b.d.	b.d.	0.03	0.06	100.65
41b(T5)	53.42	45.75	0.03	b.d.	b.d.	b.d.	0.07	0.74	b.d.	b.d.	b.d.	b.d.	0.03	0.06	100.11
41b(T5)	53.09	45.86	0.03	b.d.	b.d.	b.d.	b.d.	1.12	b.d.	b.d.	b.d.	b.d.	0.02	0.06	100.19
41b(T5)	53.48	45.47	0.03	b.d.	b.d.	b.d.	b.d.	0.60	b.d.	b.d.	b.d.	b.d.	0.03	0.05	99.66
42b(T6)	53.73	46.41	0.03	b.d.	b.d.	b.d.	b.d.	0.12	b.d.	b.d.	b.d.	b.d.	0.02	0.04	100.35
42b(T6)	53.80	46.35	0.04	b.d.	b.d.	b.d.	b.d.	0.14	b.d.	b.d.	b.d.	b.d.	b.d.	0.03	100.35
42b(T6)	53.77	46.19	0.03	b.d.	b.d.	0.02	b.d.	0.02	0.01	b.d.	b.d.	b.d.	0.02	0.03	100.08
42b(T6)	53.09	46.15	0.03	b.d.	b.d.	b.d.	b.d.	0.83	0.01	b.d.	b.d.	b.d.	b.d.	0.04	100.16
42b(T6)	53.12	46.29	0.03	b.d.	b.d.	b.d.	b.d.	0.48	b.d.	b.d.	b.d.	b.d.	b.d.	0.03	99.95
42b(T6)	53.40	46.13	0.03	b.d.	b.d.	b.d.	b.d.	0.29	b.d.	b.d.	b.d.	b.d.	b.d.	0.03	99.88
42b(T6)	51.87	46.20	0.04	b.d.	b.d.	b.d.	b.d.	0.50	b.d.	b.d.	b.d.	b.d.	b.d.	b.d.	98.61

Table 4.2. *Secondary Ion Mass Spectrometry (SIMS) Analyses of Au, Ag, Co, Cu, As, Sb, Se and Te in Pyrite from the Tolhuaca Geothermal System. Detection limits (DL) are shown in ppm.*

	Au (ppm)	Ag (ppm)	Co (ppm)	Cu (ppm)	As (ppm)	Sb (ppm)	Se (ppm)	Te (ppm)
DL	0.14	0.38	0.28	0.55	1.62	5.45	0.05	0.30
PFI-2								
01pyc131	0.40	2.21	10.3	444	24	b.d.	0.15	b.d.
01pyc133	b.d.	3.74	116	1123[a]	226	22.7	b.d.	b.d.
01pyc135	b.d.	2.26	34.2	277	1132	36.2	b.d.	b.d.
01pyc138	b.d.	10.5	274	21	16347	6.33	0.53	b.d.
01pyc139	b.d.	4.05	141	837	384	23.5	b.d.	b.d.
01pyc140	b.d.	2.21	114	1091	206	13.8	0.15	b.d.
01pyc142	b.d.	6.33	105	553	14729	45.3	0.08	b.d.
01pyc144	0.17	6.53	101	472	11242	16.9	3.43	b.d.
01pyc148	b.d.	3.13	223	420	4535	34.0	b.d.	b.d.
01pyc150	b.d.	10.6[a]	14.6	234	21647	35.0	0.95	b.d.
01pyc151	0.16	b.d.	13.4	71.4	244	b.d.	b.d.	b.d.
01pyp129	b.d.	1.25	73.3	862	839	22.4	0.10	b.d.
01pyp130	0.25	4.18	705	1425	158	7.98	0.13	b.d.
01pyp132	b.d.	7.20	261	1165	9887	58.4	0.48	b.d.
01pyp134	b.d.	10.4	426	5980	11565	88.0	0.43	b.d.
01pyp136	b.d.	6.98	457	3112	235	12.0	0.18	b.d.
01pyp137	b.d.	8.16	1173	2950	824	10.8	0.40	b.d.
01pyp141	b.d.	b.d.	1220	2243	288	b.d.	b.d.	b.d.
01pyp143	b.d.	7.77	653	2175	11187	71.1	0.40	b.d.
01pyp145	0.17	10.7	1544	2847	4484	47.6	1.70	b.d.
01pyp146	b.d.	4.72	247	1988	834	25.2	0.13	b.d.
01pyp147	b.d.	4.96	222	1490	2248	34.7	0.30	b.d.
01pyp149	b.d.	4.08	92.4	809	2246	55.7	b.d.	b.d.
PFI-3								
01pyc01	0.15	4.6	182	274.0	2136	24.9	1.33	1.35
01pyc06	3.58	30.9	5.7	3354.0	136	68.4	1.20	22.50
01pyc07	b.d.	1.04	243	422.0	1193	9.9	0.85	b.d.
01pyc08	b.d.	1.82	247	471.0	2805	41.0	0.55	b.d.
01pyc15	b.d.	3.45	423	1124.0	1893	54.8	1.18	b.d.
01pyc18	b.d.	b.d.	3.4	4.5	12.50	b.d.	14.30	0.88
01pyc19	b.d.	2.66	239	196.0	5355	28.9	2,68[a]	0.33
01pyc22	b.d.	3.45	117	654.0	988	57.5	0.43	0.58
01pyc23	b.d.	1.44	136	323.0	3615	22.0	0.63	b.d.
01pyp02	0.15	3.51	900	2202.0	2925	81.9	2.70	b.d.
01pyp04	b.d.	4.84	406	1405.0	1505	59.4	3.20	0.90
01pyp05	15.4[a]	5.54	6	3572.0	158	10.2	1.58	13.80
01pyp09	0.24	5.24	1055	3928.0	1817	94.1	5.93	0.30
01pyp10	0.43	5.66	669	1708.0	1963	80.9	2.45	0.58
01pyp12	0.26	4.86	823	5155.0	1303	76.3	3.03	b.d.
01pyp13	b.d.	1.78	199	1335.0	2727	74.4	0.88	1.08
01pyp14	b.d.	1.51	720	1202.0	2907	55.8	3.90	b.d.
01pyp16	4,63[a]	1.32	7.9	4962.0	31.7	b.d.	1.60	0.60
01pyp17	b.d.	3.86	1292	3184.0	2440	44.6	2.38	b.d.
01pyp20	b.d.	1.52	304	461.0	4058	57.5	0.13	b.d.
01pyf03	0.28	7.54	120	296.0	672	40.9	0.75	1.55
01pyf11	b.d.	0.62	142	805.0	517	20.3	1.98	b.d.
01pyf21	0.19	2.35	147	448.0	490	29.5	0.83	0.38
PFI-26								
01pyc104	b.d.	b.d.	59.9	13.7	1346[a]	b.d.	2.28	b.d.
01pyc117	b.d.	b.d.	168	186.0	834	b.d.	5.58	0.30
01pyc119	b.d.	b.d.	62.5	22.0	568	6.0	28.20[a]	6.78
01pyc122	b.d.	b.d.	13.4	85.4	278	b.d.	12.20	1.13
01pyc127	b.d.	1.01	9.8	134.0	1670	49.6	1.03	b.d.
01pyp100	b.d.	b.d.	22.7	22.6	19.40	b.d.	34.60	b.d.
01pyp101	b.d.	0.61	47.6	33.7	1035	b.d.	18.70	b.d.
01pyp105	b.d.	1.87	53.8	24.3	115	b.d.	24.50	1.30
01pyp113	b.d.	0.8	1117[a]	45.6	2033	19.5	2.00	b.d.
01pyp114	b.d.	b.d.	40.8	30.7	402	b.d.	24.50	b.d.
01pyp115	b.d.	0.83	18.0	21.3	1923	8.88	7.28	b.d.
01pyp116	b.d.	0.51	43.3	30.5	651	b.d.	13.60	b.d.
01pyp118	b.d.	0.75	49.8	58.7	1155	b.d.	23.50	b.d.
01pyp120	b.d.	b.d.	73.3	17.7	131	b.d.	34.90	1.80
01pyp121	b.d.	0.54	43.6	38.9	1299	8.30	7.15	b.d.
01pyp123	b.d.	0.48	24.7	42.0	142	b.d.	17.40	0.70
01pyp126	0.20	2.52	561	149.0	3429	85.6	6.73	0.35
01pyp128	0.26	5.25	81	112.0	883	23.3	26.90	4.90
01pyf98	b.d.	0.85	84.6	35.7	211	12.65	15.20	b.d.
01pyf99	b.d.	b.d.	79.5	62.7	64.1	b.d.	20.60	b.d.
01pyf102	b.d.	b.d.	89.3	49.5	299	11.08	19.20	1.68
01pyf103	b.d.	b.d.	75.9	62.1	97.5	9.93	28.30	1.03
01pyf106	0.19	1.64	21.9	41.7	2196	15.33	1.05	b.d.
01pyf107	0.50	10.1	260	169.0	886	32.2	28.40	6,88[a]
01pyf109	0.17	0.51	175	157.0	451	9.58	10.60	1.23
01pyf110	b.d.	0.65	140	68.4	420	b.d.	15.30	b.d.
01pyf111	b.d.	b.d.	99	56.3	469	12.9	15.30	1.88
01pyf112	b.d.	2.62	352	383.0	886	46.2	15.00	1.35
01pyf124	b.d.	0.51	147	235.0	193	13.8	9.63	1.10
01pym108	0.77	8.42	978	892.0	1099	118.0	12.50	6.98
01pym125	0.33	4.41	659	403.0	985	117.0	14.10	3.85

Table 4.2. *Continue*

01pyc24	b.d.	b.d.	21.7	38.2	234	b.d.	0.13	b.d.
01pyc25	0.39	1.42	10.7	5.7	2792	b.d.	2.33	1.03
01pyc36	0.60	b.d.	149	2.5	133	b.d.	3.90	3.03
01pyc40	0.26	2.19	25.7	44.5	1535	112.0	1.28	b.d.
01pyc54	0.28	5.67	b.d.	3.6	11298	b.d.	1.83	b.d.
01pyp27	0.41	10.6	51.2	26.3	4441	99.1	2.00	3.83
01pyp28	0.52	4.31	210	55.4	3533	232.0	2.78	b.d.
01pyp30	0.15	2.13	276	102.0	1162	208.0	1.25	b.d.
01pyp38	0.54	3.05	192	115.0[a]	4058	262.0	1.95	0.30
01pyp39	0.33	2.36	89.8	38.7	3124	156.0	2.13	b.d.
01pyp43	b.d.	1.27	317	53.4	1140	266.0	1.98	b.d.
01pyp49	0.14	1.05	87.2	58.7	857	174.0	2.18	b.d.
01pyp50	0.58	3.92	29.7	117.0	5355	6.18	6.98	b.d.
01pyp56	b.d.	2.03	217	94.7	1250	263.0	2.48	b.d.
01pyf26	b.d.	b.d.	257	67.8	5754	b.d.	b.d.	b.d.
01pyf29	0.44	4.82	315	161.0	3735	89.9	0.68	0.70
01pyf31	0.23	2.67	114	111.0	789	154.0[a]	0.88	b.d.
01pyf32	b.d.	b.d.	287	163.0	730	b.d.	b.d.	b.d.
01pyf33	0.27	1.79	111	74.3	1616	33.3	0.45	b.d.
01pyf34	0.36	8.95	353	126.0	1082	57.3	0.58	1.43
01pyf35	0.46	3.54	219	196.0	2240	46.1	1.05	b.d.
01pyf37	1.27	6.6	1317	381.0	8390	178.0	5.98	b.d.
01pyf41	b.d.	b.d.	42.2	59.5	2715	b.d.	b.d.	b.d.
01pyf42	0.58	8.1	46.4	62.9	1938	62.2	1.08	7.15
01pyf44	0.47	6.04	633	273.0	3152	162.0	2.85	b.d.
01pyf45	0.27	3.88	218	289.0	3924	328.0	1.70	b.d.
01pyf46	0.35	2.24	207	84.9	1174	28.5	0.63	b.d.
01pyf47	0.25	1.56	83.1	35.5	1508	88.2	1.10	b.d.
01pyf48	0.38	5.32	127	62.9	336	26.1	0.13	1.00
01pyf51	0.47	5.31	323	272.0	4851	104.0	3.90	b.d.
01pyf52	0.35	4.83	361	75.9	6742	77.3	0.73	b.d.
01pyf53	b.d.	0.51	84.1	39.5	714	12.5	0.23	b.d.
01pyf55	b.d.	1.53	133	36.7	1910.0[a]	b.d.	0.68	b.d.
PFI-45								
01pyc57	b.d.	5.12[a]	1.1	25.5	10617	265.0	0.05	b.d.
01pyc75	b.d.	3.49	50.4	50.2	5659	22.0	b.d.	b.d.
01pyc92	b.d.	5.59	7.5	22.2	10764	25.5	b.d.	b.d.
01pyc94	b.d.	6.32	9.1	37.2	11223	83.2	0.13	b.d.
01pyc95	b.d.	3.58	19.8	29.8	7192	24.4	0.13	b.d.
01pyp59	b.d.	3.92	2.2	41.8	6971	44.6	0.13	b.d.
01pyp62	b.d.	1.89	21.7	18.2	3131	6.28	0.45	b.d.
01pyp70	b.d.	3.06	35.0	21.3	6379	6.9	0.68	b.d.
01pyp72	0.15	6.14	13.8	43.9	12718	41.1	0.98	b.d.
01pyp74	b.d.	1.83	17.2	18.3	4357	6.05	1.83	b.d.
01pyp78	b.d.	2.74	b.d.	61.1	5387	86.4	b.d.	b.d.
01pyp79	0.14	8.85	22.0	37.2	15756	58.2	0.75	b.d.
01pyp83	b.d.	6.69	1.4	4.8	12968	171.0	b.d.	b.d.
01pyp85	b.d.	3.67	25.0	29.7	6446	17.5	0.63	b.d.
01pyp86	b.d.	1.47	35.0	18.2	3002	b.d.	0.45	b.d.
01pyp90	b.d.	3.52	21.1	17.5	6377	12.2	1.00	b.d.
01pyf60	b.d.	7.14	196	105.0	10874	74.7	1.08	b.d.
01pyf63	0.15	5.91	87.7	116.0	8952	119.0	1.53	b.d.
01pyf64	b.d.	6.33	69.2	111.0	7983	47.4	1.15	b.d.
01pyf65	0.37	6.09	26.2	108.0	8741	80.4	1.15	b.d.
01pyf67	b.d.	1.39	103	54.2	2195	11.7	0.45	b.d.
01pyf69	0.16	5.74	49.4	46.1	9277	44.3	0.95	b.d.
01pyf71	b.d.	1.39	80	46.3	2443	19.5	0.33	b.d.
01pyf76	b.d.	2.53	74.3	77.2	2298	48.3	0.83	b.d.
01pyf80	b.d.	4.81	36.8	42.0	7464	13.3	1.78	b.d.
01pyf89	b.d.	3.04	127	63.7	6123	38.7	0.23	b.d.
01pyf91	b.d.	9.04	398	136.0	12162	139.0	1.20	b.d.
01pyf96	b.d.	4.56	42.2	57.7	8296	44.9	0.60	b.d.
01pyf98	b.d.	0.85	84.6	35.7	211	12.7	15.20	b.d.
01pym58	b.d.	3.20	50.7	148.0	1899	b.d.	5.15	b.d.
01pym61	0.33	11.02	507	698.0	5186	34.4	13.10	b.d.
01pym66	b.d.	2.94	105	276.0	3420	27.9	19.50	b.d.
01pym68	b.d.	7.50	36.5	70.7	15395	75.9	0.48	b.d.
01pym73	b.d.	4.17	55.8	171.0	2952	47.3	5.68	b.d.
01pym77	0.17	6.72	70.2	361.0	5661	40.2	25.00	b.d.
01pym81	0.23	3.79	31.0	158.0	1632	14.1	1.98	b.d.
01pym82	b.d.	3.37	44.3	159.0	6637	59.4	4.75	b.d.
01pym84	0.16	4.07	49.6	120.0	7587	4604.0	1.38	b.d.
01pym87	0.16	8.32	102	108.0	10171	50.7	0.70	0.50
01pym88	0.36	5.12	38.6	278.0	2321	16.7	12.80	b.d.
01pym93	0.33	9.50	29.3	293.0	4295	29.8	17.80	1.45
01pym97	0.30	3.25	68.2	170.0	2019	23.8	3.15	b.d.

a: Samples (and elements) that were depth-profile using SIMS

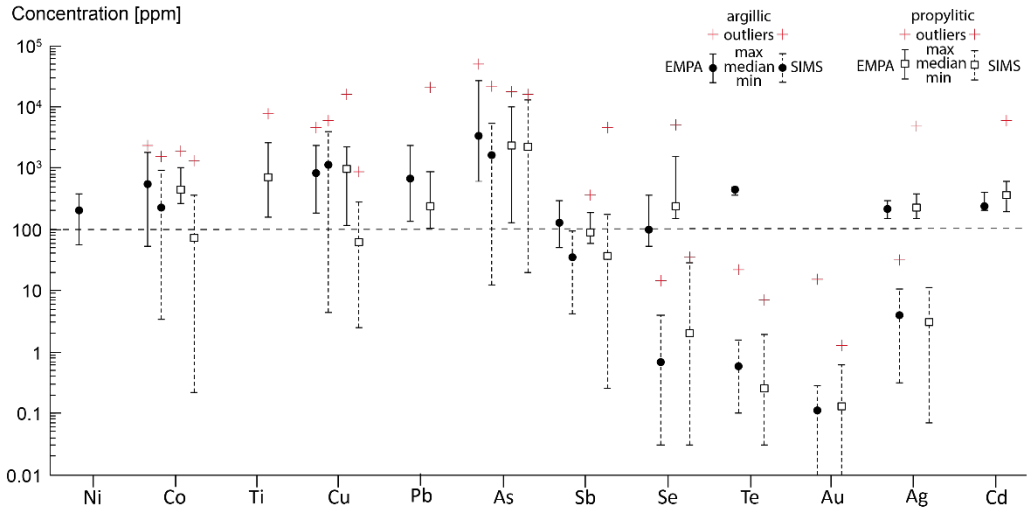

Figure 4.3. *Concentration plot for minor and trace elements in pyrite (samples PF-2, PF-3, PF-26, PF-39, PF-41 and PF-45). Pyrite data from argillic and propylitic alteration zones are identified by black circles and open squares, respectively. Data are plotted in parts per million (ppm) on a vertical logarithmic scale. For each element, median concentrations measured by EPMA (solid lines) and SIMS (segmented lines) are shown together with maximum and minimum values. Outliers are shown as red crosses. The horizontal dotted line is the mean detection limit (mdl) of EPMA analysis for all elements (~100 ppm).*

Micro- to nano-sized Cu-bearing inclusions occur as scattered discrete particles and blebs along the growth zones (Fig. 4.4d, k, n and Fig. 4.5c; yellow-to-red-colored). The size of the particles is less than 5 µm, and they occur as individual inclusions and/or as aggregates of abundant micrometer- to submicrometer-sized particles. The occurrence of the two mineralogical forms of Cu in pyrite in the TGS is confirmed by SIMS depth profiling. In Figure 4.8c and d, depth–concentration profiles are presented for the pyrite matrix isotopes (^{56}Fe, ^{34}S) and copper (^{63}Cu). When Cu is present in solid solution (structurally bound), the depth–concentration profile of ^{63}Cu is flat (Fig. 4.8c, 1100 ppm Cu), whereas at higher concentrations the spiky ^{63}Cu profile confirms the presence of individual particles or clusters of particles of 500 nm in size (Fig. 4.8d, ~100 ppm Cu). Previous experimental studies have pointed out that the solid solution of CuS_2 in FeS_2 is thermodynamically unstable in nature and the solubility of Cu in FeS_2 decreases considerably with temperature (from 4.5 mol% Cu at 900 °C to ~0.6 mol% Cu at 700 °C, at 45 kbar; Shimazaki and Clark, 1970; Schmid-Beurmann and Bente, 1995). However, the solubility of Cu in pyrite has not been determined at the lower temperatures relevant for most hydrothermal systems (e.g., <500 °C). Analogously to Reich et al. (2005), it may be suggested that the incorporation of As could influence Cu incorporation in both solid solution and as Cu-bearing nanoparticles in pyrite (Reich et al., 2013). At the TGS, Cu and As concentrations do not show a correspondence (Fig. 4.7d), and the micrometric chalcopyrite inclusions are found associated with both low and high As-bearing concentration zones. At very low temperatures (i.e., sedimentary settings) Cu is incorporated within the pyrite structure at low concentrations (ppm levels), while Cu-bearing microinclusions at present at higher concentrations (wt % levels; Gregory et al., 2015a). Factor analysis has shown that Cu is associated with large cations that disrupt the pyrite structure enhancing Cu incorporation. However, it likely that the total concentration of the metals in fluids play a key role on Cu incorporation into pyrite as evidenced in studies such as Gregory et al. (2015a).

As shown in Tables 4.1 and 4.2 and Figure 4.3, cobalt concentrations in pyrite are variable, ranging from hundreds of ppb to thousands of ppm. Despite the fact that the plot of Co-Fe in Figure 4.7e does not show a clear correlation trend, the SIMS depth profile (Fig. 4.8a) and WDS X-ray

maps (Fig. 4.4c, j, m and p) suggest that cobalt in the studied pyrites is in solid solution. This is in agreement with the fact that Co extensively substitutes for Fe in pyrite, due to the similar ionic radii of Co^{2+} and Fe^{2+}, and that the CoS_2 endmember adopts the pyrite structure (Vaughan and Craig, 1978; Tossell et al., 1981, Abraitis et al., 2004, Gregory et al., 2015a, b).

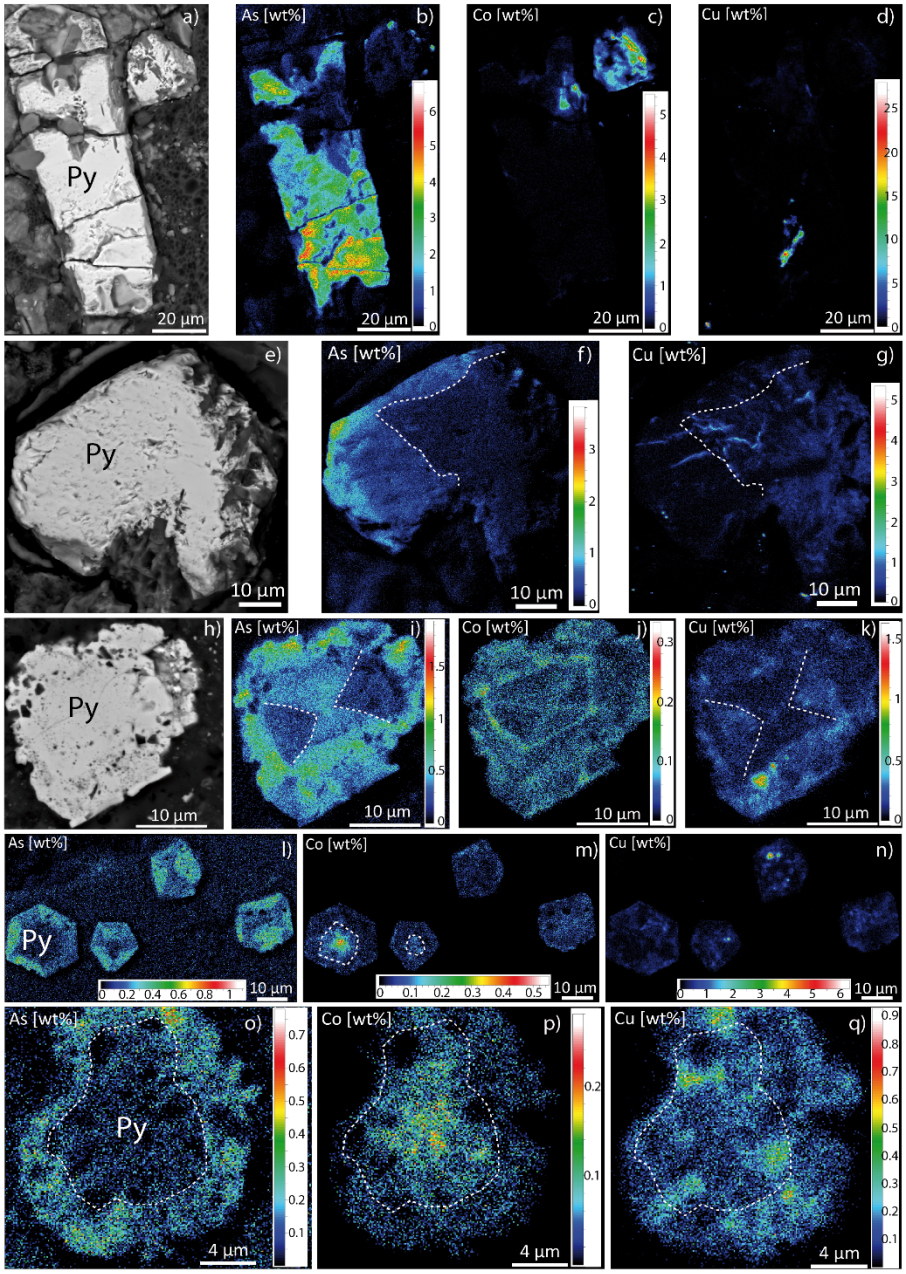

Figure 4.4. *Representative microtextures and chemical zonations of pyrite from the (shallow) argillic alteration zone of the Tolhuaca Geothermal System. Samples: PFI-2 (a, b, c, d, e, f and g) and PFI-3 (h, i, j, k, l, m, n, o, p and q). (a), (e) and (h): backscattered electron (BSE) image showing pyrite (Py) crystals. (b), (c), and (d): quantitative wavelength dispersive spectrometry (WDS) X-ray maps of area in (a) for As (Ka), Co (Ka), and Cu (Ka), respectively. (f) and (g) show WDX maps of area in (e) for As (La) and Cu (Ka), respectively. (i), (j) and (k) show WDX maps of area in (h) for As (La), Co (Ka), and Cu (Ka), respectively. (l) and (o); (m) and (p); and (n) and (q) show WDX maps of disseminated pyrite grains for As (La), Co (Ka), and Cu (Ka), respectively. Quantitative WDX maps for As (La) Co (Ka), and Cu (Ka) show zonations of these metals. Cu (Ka) distributions in (d), (k) and (n) show discrete inclusions of chalcopyrite. A color scale bar for concentration (in wt %) is shown for each WDS map. Py: pyrite.*

WDS X-ray maps in Figure 4.4c, j, n, p, show that chemical zoning of Co, like Cu, is spatially correlated to cores and/or thin bands within pyrite crystals. The positive correspondence between Co and Cu in Figure 4.7f supports the hypothesis that these two metals may be included in pyrite in similar mineralogical form. The relatively high Co concentrations (up to ~0.2 wt. %) and high Co/Ni ratios between 1 and 10 in pyrite from the TGS (Fig. 4.9a) are indicative of a magmatic-hydrothermal origin associated with a greater mafic affinity (Large et al., 2009; Koglin et al., 2010; Reich et al., 2016), in agreement with the composition of the lavas from Tolhuaca volcano, which have mainly basaltic to andesitic compositions (Sánchez-Alfaro et al., 2016a).

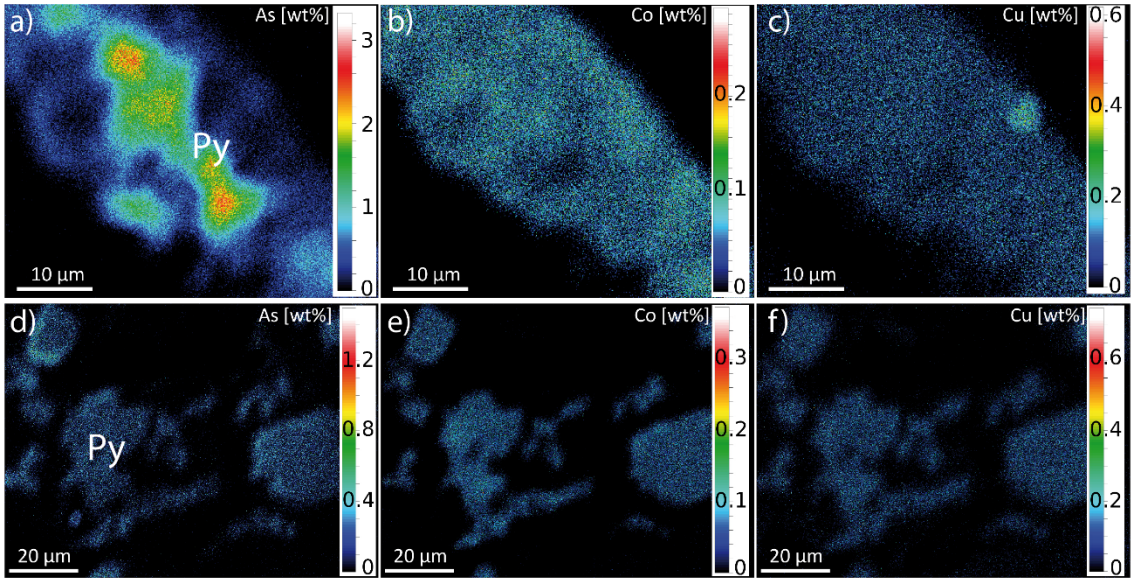

Figure 4.5. *Representative microtextures and chemical features of pyrite from the deep (propylitic) alteration zone. Samples: PFI-39 (a, b, c) and PFI-41 (d, e, f). (a) and (d) show quantitativeWDX maps for As. (b) and (e) show maps for Co (Ka). (c) and (f) show WDX maps for Cu (Ka). Cu (Ka) distribution in (c) shows discrete inclusions of chalcopyrite. Color scale bars for concentration (in wt %) are shown. Py: pyrite.*

Apart from the base metals, precious metals (Au, Ag) concentrations in the studied pyrite are at least one order of magnitude higher when compared to pyrite from other active geothermal systems (Libbey and William-Jones, 2016), ranging from 10's of ppb to 10's of ppm for Au and from 10's of ppb to 1000's of ppm for Ag (Tables 4.1 and 4.2). Gold and silver incorporation into pyrite structure is favored by the substitution of anionic or cationic As, due to a structural distortion and/or decrease in the size of pyrite grains, increasing the surface/volume ratio (e.g., Simon et al., 1999; Palenik et al., 2004; Deditius et al., 2008, 2014). Several different incorporation mechanisms for Au and As have been proposed for pyrite. The most validated model involves the coupled substitution of cationic Au for Fe in distorted octahedral sites and anionic As for S in tetrahedral sites (Simon et al., 1999). It is relevant to note that the highest concentrations of Au in pyrite are usually related to the presence of Au-bearing micro- to nano-sized inclusions and clusters of Au nanoparticles (Reich et al., 2005; Deditius et al., 2014, Gregory et al., 2015a; Gregory et al., 2016).

As shown in Table 4.2 and Figure 4.3, SIMS data show Au concentrations in pyrite that varies between 10 ppb and ~10 ppm. Only one EMPA data point reported in Table 4.1 shows Au concentration of 1500 ppm. In Figure 4.9b, most Au–As analyses plot below the solubility limit defined by Reich et al. (2005), suggesting that Au occurs as structurally bound ions (Au^{1+}). Only

three data points plot above the As-dependent solubility limit, indicating the presence of nanoparticles of native Au^0 and/or Au-tellurides. Although SIMS depth–concentration profiles do not confirm the presence of nanoinclusions (Fig. 4.8e and f), the occurrence of nanoparticles smaller than the SIMS depth-profiling detection capabilities (<500 nm) is possible, and higher concentrations of Au (e.g., >10 ppm) measured by EMPA and SIMS may be related to micro- to nano-sized Au-bearing mineral particles. The similar incorporation behavior of Au and Te, both as solid solution or gold-telluride, is also assessed by the positive correlation between Au and Te, shown in Figure 4.9c.

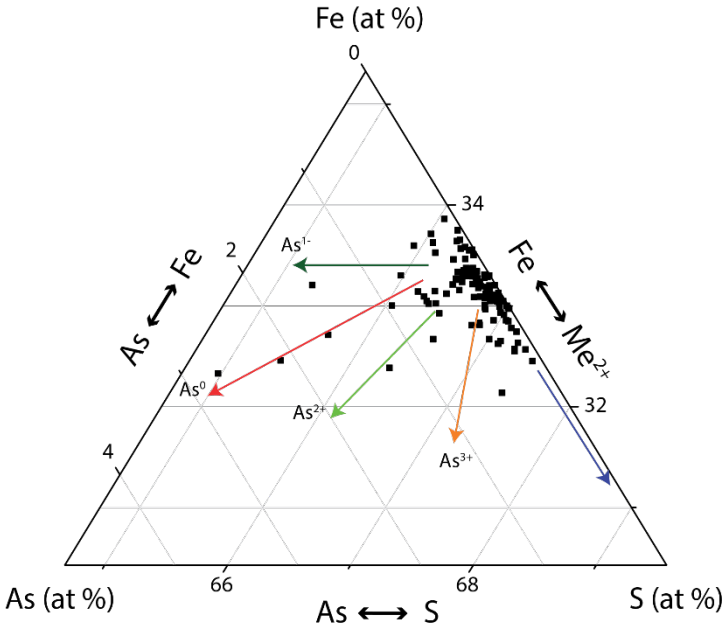

Figure 4.6. *Ternary diagram showing the As-Fe-S composition of pyrite in the Tolhuaca Geothermal System. Five different trends show substitution of (i) As for S (As^{1-} - pyrite; green arrow); (ii) As0 nano-inclusions (As^0 red arrow); (iii) As^{2+} for Fe (As^{2+} -pyrite; light green arrow); (iv) As^{3+} for Fe (As^{3+}-pyrite; orange arrow); and (v) divalent metals Me^{2+} for Fe (blue arrow). The composition of As^{2+}-pyrite (after Qian et al., 2013, Deditius et al., 2014) was calculated based on the assumption of ideal occupancy of S (66.66 at.%). n = 2924.*

As shown in Tables 4.1 and 4.2 and summarized in Figure 4.3, the measured Ag content of pyrite varies between ~70 ppb and 5000 ppm. Previous studies have shown that Ag is widely present in pyrite in both solid solution (replacing Fe^{2+} as Ag^+) and/or forming micro and nano-sized Ag-sulfide and sulfosalt inclusions (Abraitis et al., 2004, Deditius et al., 2011). At the TGS, SIMS depth profiles show that Ag occurs in both mineralogical forms. In Figure 4.10a and b, depth–concentration profiles are presented for ^{109}Ag. The flat profile in Figure 4.10a (at 11 ppm Ag) support the presence of Ag in solid solution, whereas the spiky ^{109}Ag profile confirms the presence of individual particles or clusters of Ag-bearing particles <500 nm in size (Fig. 4.10b, 5 ppm Ag). The generally positive trend between Ag and Au (Figure 4.9d) suggests a similar incorporation behavior of these two metals, as documented in previous studies (e.g., Reich et al., 2010). Furthermore, Ag-As data points in Figure 4.9e show two groups at higher (~200 ppm) and lower (<100 ppm) Ag contents. The lower Ag concentration group display a positive correspondence with As, while the high-Ag concentrations do not vary with As contents, showing a line parallel to the Y axis. These data, in addition to SIMS depth profiles in Figure 4.10a and b, suggest that Ag incorporation into pyrite is dependent on As and follow a similar behavior than Au (Reich et al., 2005, 2013, Deditius et al., 2014).

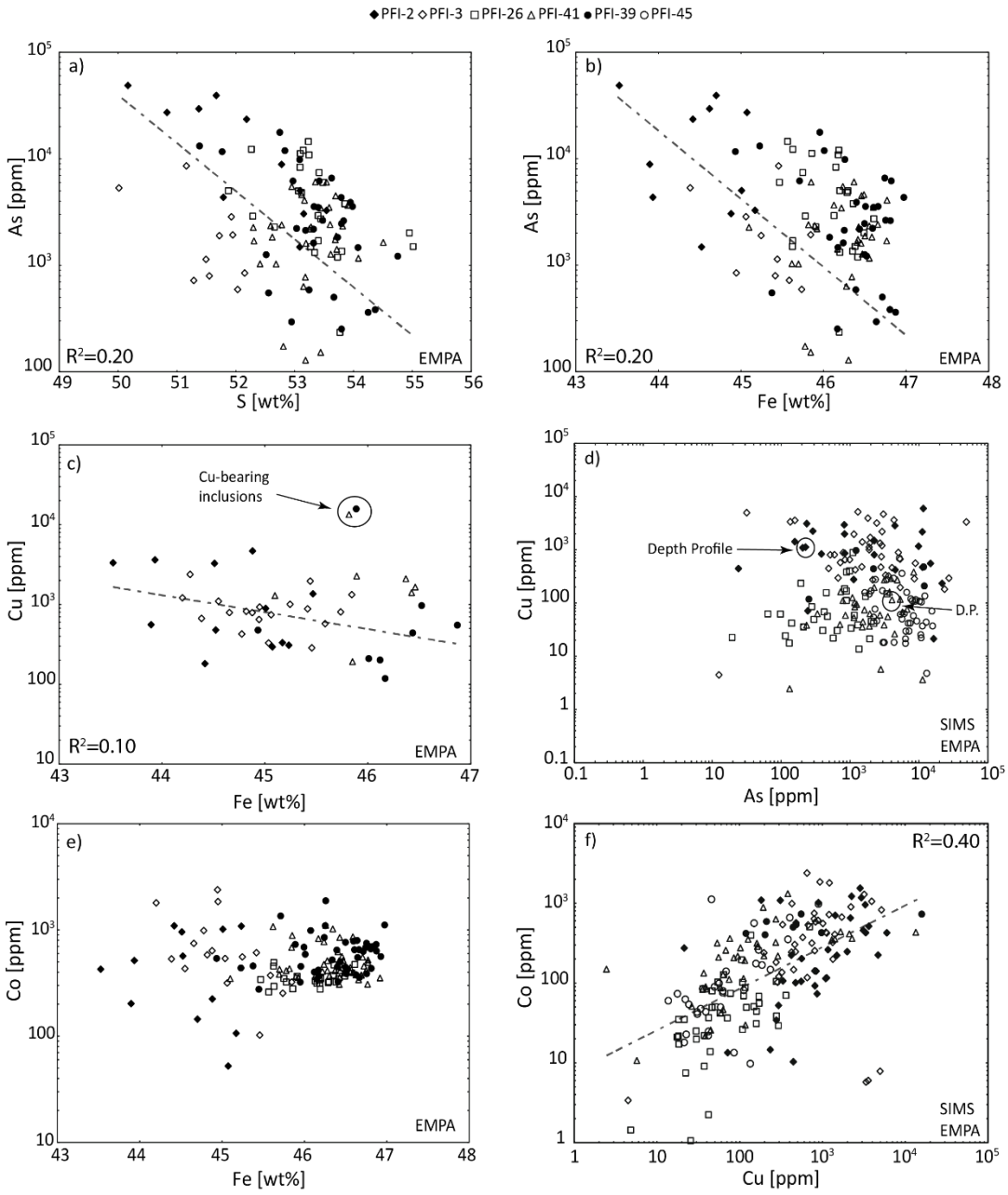

Figure 4.7. *Elemental correlation plots of (a) As vs. S, (b) As vs. Fe, (c) Cu vs. Fe, (d) Cu vs. As, (e) Co vs. Fe, and (f) Co vs. Cu. Black diamonds, open diamonds, open squares, open triangles, black circles and open circles represents pyrite samples PFI-2, PFI-3, PFI, 26, PFI, 39, PFI, 41 and PFI-45, respectively. R2 values are shown.*

All other trace elements measured in pyrite at the TGS (e.g. Pb, Ni, Ti, Sb, Se, Te, Cd) also occur in relatively high amounts, e.g., 100-ppm levels for Ni and Te, 1000-ppm levels for Ti, Sb, Se and Cd, and up to wt. % levels for Pb. Lead may be incorporated in solid solution by the substitution of Pb^{2+} for Fe^{2+}, as suggested by the negative relation shown in the elemental plot of Figure 4.9f. However, the high concentrations of Pb (up to 2 wt. %) may also be attributed to the presence of sub-micron sized Pb-bearing inclusions, most likely galena (Griffin et al., 1991; Huston et al., 1995; Abraitis et al., 2004; Pacevski et al., 2012, Gregory et al., 2015a). Tellurium and Se

are likely hosted in solid solution, as shown in the flat SIMS profiles (Figs. 4.10c and d), although the presence of micro- or nano-inclusions cannot excluded. In fact, the SIMS depth profiles in Figure 4.10e and f indicate that Se is probably incorporated in pyrite as both solid solution and Se-bearing mineral inclusions.

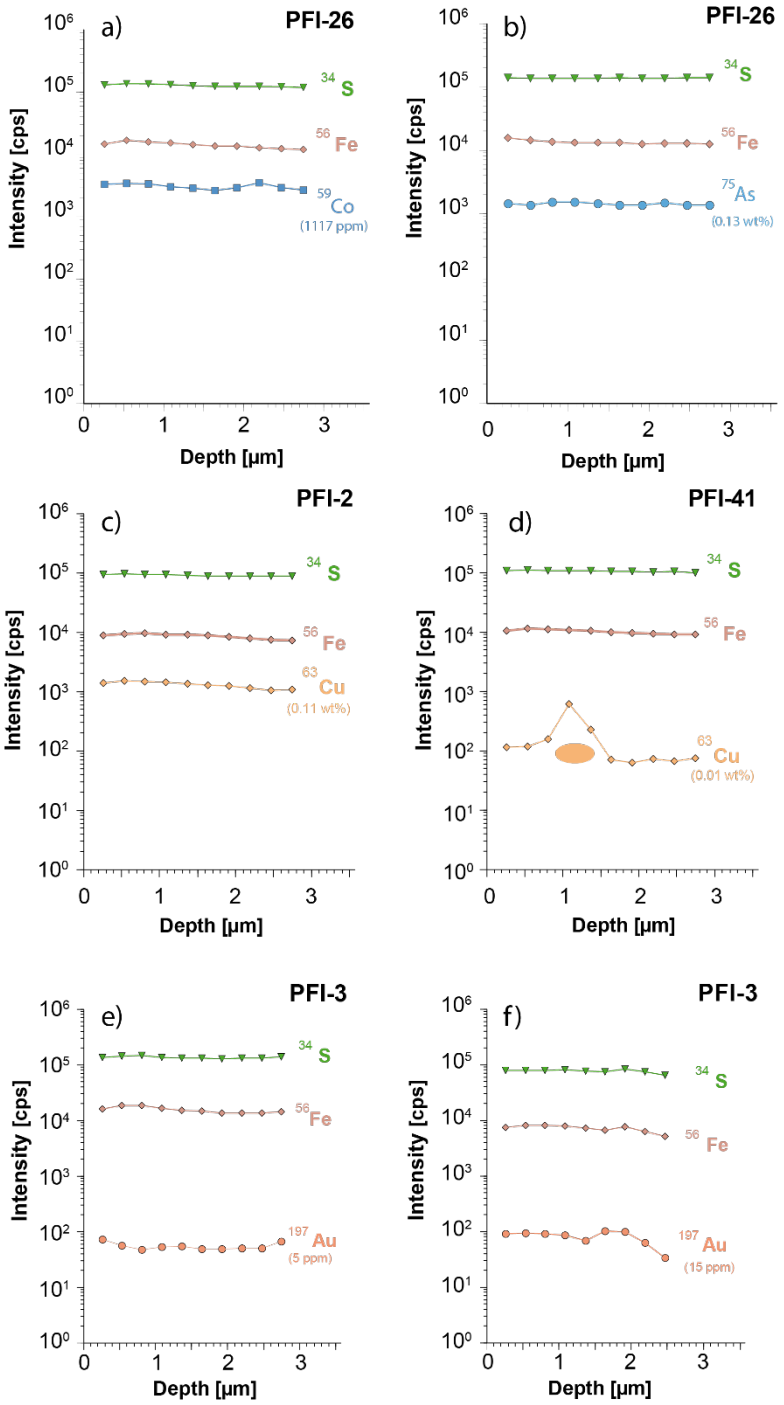

Figure 4.8. *SIMS depth-concentration profiles (time vs. intensity) of trace elements in pyrite from Tolhuaca Geothermal System. Spiky profiles for 63Cu reflect the presence of individual nanoinclusions or clusters of mineral nanoparticles (colored circles and ovals), whereas 59Co, 75As, and 197Au show a more homogeneous (solid-solution) distribution. Major sulfide-matrix constituent isotopes, 56Fe and 34S, were monitored during each run (top). Vertical intensity scale is in counts per second (cps); horizontal (depth) scale is in micrometers (µm).*

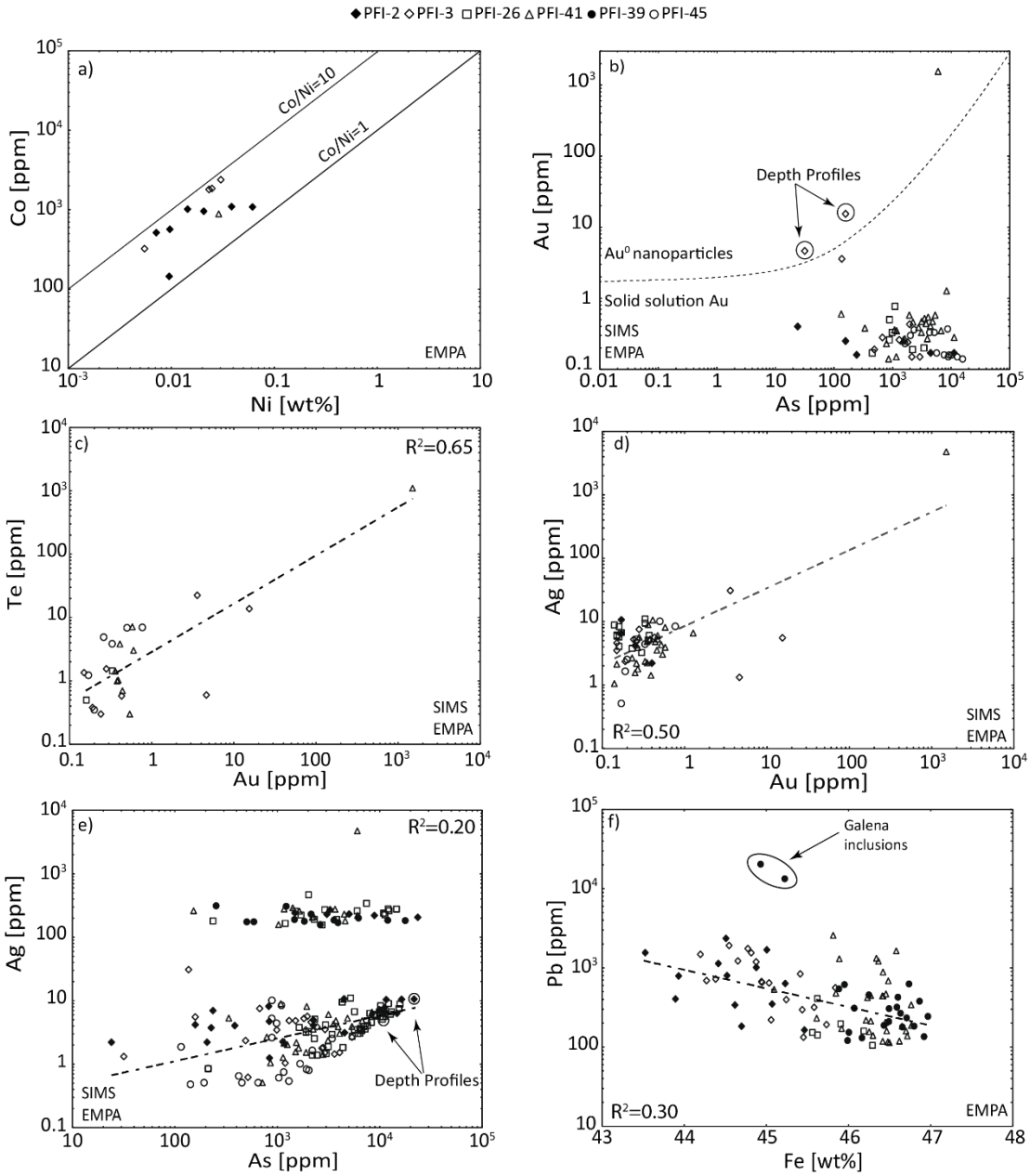

Figure 4.9. *Elemental correlation plots of (a) Co vs. Ni, (b) Au vs. As, (c) Te vs. Au, (d) Ag vs. Au, (e) Ag vs. As and (f) Pb vs. Fe. Black diamonds, open diamonds, open squares, open triangles, black circles and open circles represents pyrite samples PFI-2, PFI-3, PFI, 26, PFI, 39, PFI, 41 and PFI-45, respectively. Solid lines in (a) represent Co/Ni=1 and Co/Ni=10. The curve in (b) is the As-dependent solubility of Au in pyrite as determined by Reich et al. (2005). R2 values are shown.*

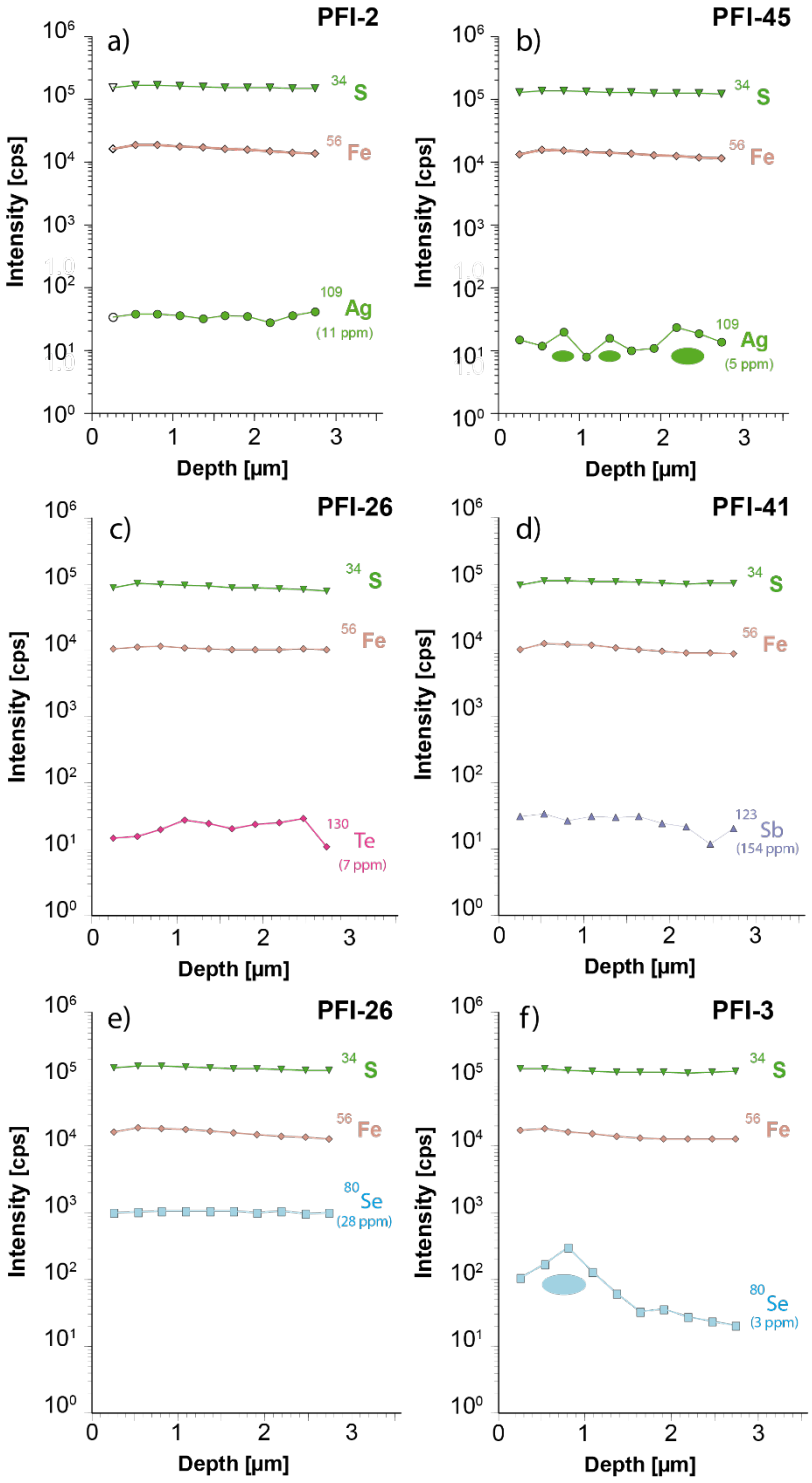

Figure 4.10. *SIMS depth-concentration profiles (time vs. intensity) of trace elements in pyrite from the TGS. Spiky profiles for 109Ag, and 80Se reflect presence of individual nanoinclusions or clusters of mineral nanoparticles (colored circles and ovals), whereas 130Te and 123Sb show a more homogeneous (solid-solution) distribution. Major sulfide-matrix constituent isotopes, 56Fe and 34S, were monitored (top). Vertical intensity scale is in counts per second (cps); horizontal (depth) scale is in micrometers (µm).*

Cu-As decoupling in the TGS: linking pyrite chemistry with paleofluid and borehole fluid composition

The trace element geochemistry of pyrite has proven useful in accessing the history of complex processes undergone by a single sample. In magmatic-hydrothermal settings, pyrite has been used to fingerprint ore sources, vector towards mineralization and infer changes in fluid composition (e.g., Franchini et al., 2014; Mukherjee and Large, 2016). Similar observations are reported in lower temperature sedimentary environments where pore waters progressively enrich in trace elements as they desorb from organic matter, resulting in a sequential enrichment of trace elements in pyrite with increasing sediment depth (Huerta-Diaz and Morse, 1994; Gregory et al., 2014).

Abrupt changes in As and Cu concentrations in pyrite growth zones have been observed in the Pueblo Viejo and Yanacocha high sulfidation Au-Ag deposits (Deditius et al., 2009). Arsenic-rich zones, also enriched in Au, Ag, Sb, Te, and Pb, alternate with Cu-rich zones with significantly lower concentrations of these elements and barren pyrite zones with no other elements. In situ trace element and sulfur isotope ($\delta^{34}S$) data by Peterson and Mavrogenes (2014) in pyrite at the Porgera Au deposit in Papua New Guinea uncovered a stratigraphy of repeated high-Au negative $\delta^{34}S$ and low-Au positive $\delta^{34}S$ zones, recognized with a 3 μm spot size laser ablation, within individual pyrite crystals present in the highest grade gold event. These zonations are less likely to reflect changes in substitutional mechanisms of As and Cu into pyrite forming from a fluid of constant composition, and chemical and isotopic data provide strong evidence pointing to sharp variations in the pyrite-forming fluid composition (Deditius et al., 2009; Kouzmanov et al., 2010).

In high-temperature hydrothermal settings, these abrupt chemical changes have been interpreted as the result of mixing between the pyrite-forming fluids and magmatic vapors, the latter capable to geochemically decouple As and Cu during its separation from the parental magma (Deditius et al., 2009). Indeed, although it has been observed that both As and Cu partition into the magmatic vapor, they respond differently to P-T-X conditions of the system, especially in terms of ligands (Cl and S) availability (Heinrich et al., 1999, 2004; Pokrovski et al., 2002, 2005; Williams-Jones et al., 2002; Williams-Jones and Heinrich, 2005; Simon et al., 2006, 2007; Pokrovski et al., 2013). Magmatic vapors, formed by direct separation from the parental silicate magma, may remain a single phase or separate into a brine and a lower density vapor, a process that can take place more than once during the upward migration of the magmatic vapor (Heinrich, 2004, 2005). These phase separation processes are capable of fractionating As and Cu in the porphyry-epithermal environment. Pokrovski et al. (2005; 2013) compiled experimental data of vapor-liquid partition coefficients between 300 and 450 °C for various metalloids, base and precious metals. They determined that As partitions preferentially into the low density, low salinity vapor phase than Cu which has a higher affinity for the high-density saline brine. This selective metal partitioning has been extensively reported in experiments and fluid inclusion studies in ore deposits, from the deeper magmatic-hydrothermal porphyry roots to the shallower epithermal domain (Kouzmanov and Pokrovski, 2012, and references therein).

For most hydrothermal systems it remains difficult to determine how the compositions of hydrothermal fluids change with time and how those changes affect the precipitation of ore minerals, including pyrite (Rusk et al., 2008). Several studies have reported LA-ICP-MS data of fluid inclusions from porphyry systems (e.g., Heinrich et al., 2005; Audetat et al., 2008), epithermal Au(-Ag) deposits (e.g., Pudak et al., 2009), and from fluid inclusions hosted in sulfide ore minerals (e.g., Wilkinson et al., 2009; Kouzmanov et al., 2010). All these studies have reported significant variations in metal concentrations related to chemical fluctuation of hydrothermal ore fluids.

Despite such evidence, a direct correlation between chemical changes in ore-forming fluids and the trace metal chemical zonations recorded in pyrite (e.g. Cu, As, Co, Au, Sb, Ni) remains to be confirmed beyond trace element analyses of the sulfide phase (Large et al., 2009; Deditius et al., 2009; Thomas, 2011; Reich et al., 2013, 2016; Peterson and Mavrogenes, 2014; Deditius et al., 2014; Steadman, 2015; Gregory et al., 2016).

By combining our EMPA/SIMS pyrite data with 1) LA-ICP-MS analyses of fluid inclusion that are paragenetically linked in calcite/quartz veins, and 2) borehole fluid chemical data at the TGS, we provide evidence that the observed zonations in pyrite are likely related to chemical changes in the pyrite-forming hydrothermal fluid. Borehole fluids in the TGS have trace metal contents that are broadly similar to those measured in the Taupo Volcanic Zone in New Zealand and in the active Lihir gold deposit in Papua New Guinea (Simmons and Browne, 2000; Simmons et al., 2016a, b; Sánchez-Alfaro et al., 2016b). Furthermore, and unlike pyrites from ore deposits that commonly show multiple growth bands and complex oscillatory zoning patterns, pyrite in the shallow argillic zone of the TGS presents the advantage of having only two growth zones as observed in the WDS X-ray maps (Figures 4.4 and 4.11).

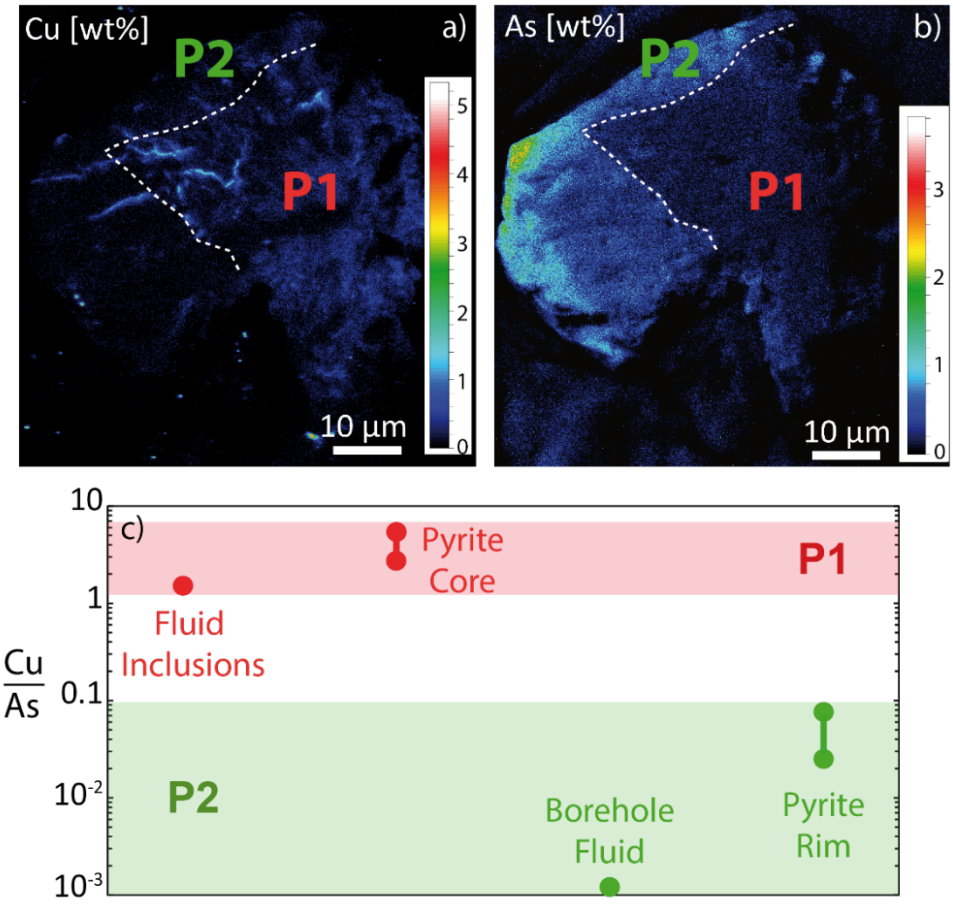

Figure 4.11. *Combination of pyrite data (WDS X-ray maps) with LA-ICP-MS analyses of fluid inclusions in pyrite-bearing veins and borehole fluids chemical data at the TGS, The panels (a) and (b) show a pyrite grain from the argillic zone that contains a Cu-rich, As-poor core (P1), and an As-rich, Cu-poor rim (P2). The panels (c) shows the Cu/As ratio of fluid inclusions (red circles) and borehole fluids samples (green circles), respectively, reported by Sánchez-Alfaro et al. (2016a). The Cu-rich, As-poor pyrite core (P1) correlates with the high Cu/As ratios measured in fluid inclusions in calcite-quartz-pyrite veins. Conversely, As-rich and Cu-poor pyrite rims (P2) correlate with the low Cu/As and ratio measured in the present-day borehole fluids.*

The fluid inclusions data used in this study were reported by Sánchez-Alfaro et al. (2016a). In particular, the LA-ICP-MS data were obtained in fluid inclusion assemblages observed in pyrite-bearing, calcite/quartz veins retrieved from the shallower part of the drillcore (first 400 m), which represents the upwelling paleo-hydrothermal fluid. In contrast, the present-day borehole fluid composition (measured using ICP-MS) is likely to represent the resulting fluid after the condensation of a low-density vapor that separated from a magmatic-hydrothermal fluid sourced in the deeper parts of the hydrothermal system. This distinction allows us to correlate the composition of paleo- and present-day fluids with measured concentrations of trace metals in cores and rims of pyrite in the shallow argillic zone, which are the only pyrite grains that show clear zonation patterns.

As shown in Figure 4.11a and b, we will refer in the following discussion to the pyrite growth zones as P1 for pyrite cores, and P2 for the pyrite rims. Copper-arsenic ratios of pyrite cores (red) and rims (green) are compared in Figure 4.11c with the Cu/As ratios of fluid inclusion (red circles) and borehole fluids samples from the TGS (green circles). The textural and chemical data in Figure 4.11 point that a Cu-rich, As-depleted fluid was involved in pyrite core formation (P1), followed by a late-stage low-Cu and high-As fluid was related to the precipitation of pyrite rims (P2). In the same way, the comparison between (present-day) borehole fluids and fluid inclusion data reveals significant differences. Fluid inclusions are Cu-rich but poor in As (Cu/As~1) while borehole fluids are rich in As, but Cu-poor (Cu/As~10^{-3}). According to Sánchez-Alfaro et al. (2016a), simple boiling models cannot explain the aforementioned differences in fluid chemistry because non-volatile elements such as Cu and As remain in the liquid phase during boiling ($K_d=C_{vapor}/C_{liquid}$, K_{As}=0.001-0.01; $K_{Cu}< 10^{-3}$; $K_{Na}<10^{-3}$) under epithermal conditions (100<T<280 °C; Pokrovski et al., 2013). In Figure 4.11, the relatively high-Cu, low-As concentrations in fluid inclusions (Cu/As~1, Fig. 4.11c) can be paragenetically linked to the formation of the Cu-rich, As-depleted pyrite cores (Cu/As~1-10, Fig. 4.11c). In contrast, the As-rich, Cu-depleted pyrite rims (Cu/As~0.1-0.01, Fig. 4.11c) correlate with the high-As and low Cu concentrations measured of borehole fluids (Cu/As~10^{-3}, Fig. 4.11c) at the TGS. These observations strongly suggest that the zonations reported in pyrite from TGS are the result of a compositional change of the pyrite-forming hydrothermal fluid during continuous pyrite precipitation.

EMPA data and WDS X-ray maps also show that pyrite cores are significantly enriched in Co (up to 4 wt. %). Unfortunately, no experimental partitioning data are available for Co, and Sánchez-Alfaro et al. (2016a) do not report Co concentrations in fluid inclusion or borehole fluids. However, and as shown by Pokrovski et al. (2013), most base metals present a marked affinity for a high-density saline brine; therefore it is reasonable to assume that Co may display a similar behavior than Cu (see maps in Fig. 4.4c, j, m and p).

The pyrite core precipitation stage P1 at Tolhuaca was most likely related to Cu(Co)-rich supercritical magmatic vapors that segregated during a stage of magmatic diking and sill intrusion as reported for the TGS. The episodic separation of these magmatic vapors produced fluid overpressure conditions inducing fracturing and brecciation of the low permeability clay-cap, as observed by Sánchez-Alfaro et al. (2016a). This magmatically derived single-phase fluid ascended and following phase separation (or boiling) (Sánchez-Alfaro et al., 2016b), precipitated pyrite (cores) with high concentrations of Cu and Co, in both the deep and shallower parts of the TGS. Pyrite in the argillic (shallower) zone hosts higher concentrations of Cu and Co than pyrite in the propylitic (deeper) zone (Fig. 4.3; Tables 4.1 and 4.2). This may be due to the neutralization of acid hydrothermal fluids in the upper argillic zone, as proposed by Sánchez-Alfaro et al. (2016a), producing a concomitant decrease of metal solubility in the fluid phase.

During a later phase of evolution of the TGS (P2), the fluid pressure was lower than the lithostatic pressure and the clay-cap acted as a low-permeability barrier (Sánchez-Alfaro et al., 2016a). Phase separation took place in the deeper part of the system, partitioned the magmatic/hydrothermal fluid into a low-density vapor and high-density brine capable of fractionating Cu (and Co) and As. During this phase, only the As-rich vapor was able to migrate upwards, reaching the dominantly-meteoric aquifer in the argillic zone and possibly contracting into an As-rich hydrothermal fluid that precipitated the As-rich, Cu(Co)-poor pyrite rims, over the previously formed Cu(Co)-rich, As-depleted cores (Fig 4.4f, g, i, k, o and q). The Cu(Co)-rich, As-poor brine, on the other hand, remained in the deep (propylitic) part of the system where it continued precipitating pyrite with similar Cu, Co and As concentrations as the pyrite core deposited during P1 phase. In the sub-propylitic zone, the local accumulation of the brine, now blocked by the low permeability barrier or clay-cap, may have triggered local supersaturation of Cu in the fluid phase with the consequent deposition of chalcopyrite and bornite instead of pyrite as the main sulfide phase.

Our results are in agreement with recent studies discussed by Simmons et al. (2016a, b) in the Taupo Volcanic Zone, New Zealand, where significant amounts of metals are reported in geothermal fluids. The authors report that boiled chloride waters are strongly depleted in Cu, Pb, Ag, Au, and Te, because these metals deposit in sharp response to gas loss and cooling in the well. In contrast, As, Sb, and other metals and metalloids are measurably less depleted in boiled waters, making them available to form metal anomalies at shallow depths (Simmons et al., 2016a, b).

The precipitation of Cu minerals might have also been reached locally in the argillic zone during the P2 phase. As previously documented, kinetic effects can trigger the formation of micro to nano-particulate inclusions of chalcopyrite that co-precipitate with pyrite during rim formation (Fig. 4.4k and n). (Deditius et al., 2011; Reich et al., 2011). Therefore, Cu-bearing nanoparticle nucleation in pyrite might be, in this case, favored by the high As concentration on the mineral surface, or electrochemical effects as it has been previously proposed for precious and base metals (e.g., Au, Ag, Pb and Zn) (Oberthur et al., 1997; Abraitis et al., 2004; Mikhlin et al., 2007, 2011).

Concluding remarks

Our EMPA–SIMS database show that significant concentrations of base and heavy metals (e.g., Cu, Co, Ni, Pb), precious metals (e.g., Au, Ag) and metalloids (e.g., As, Te, Se, Sb) are hosted in pyrite at the Tolhuaca Geothermal System. Detailed WDS X-ray maps and SIMS depth vs. isotope concentration profiles reveal that pyrites in the shallower argillic zone in the TGS are characterized by two chemically distinct zones where Cu(Co) and As are geochemically decoupled, while pyrites in the deeper part of the system (propylitic zone) do not display significant textural or chemical zonations.

When contrasting Cu-As contents in pyrite cores and rims with LA-ICP-MS fluid inclusion data and borehole fluids composition (Sánchez-et al., 2016) in the TGS, we provide evidence that selective partitioning of metals and metalloids into pyrite is most likely the result of changes in fluid composition. The aforementioned changes are interpreted as being related to excursions of single-phased, magmatically-derived vapors that are further separated into a low-density vapor and dense brine capable of selectively scavenging Cu and As. During the first stage of pyrite formation (P1), fracturing of the impermeable clay-cap resulted in the formation of Cu(Co)-rich, As-depleted pyrite cores in both the deep and shallower parts of the TGS. This stage preceded the formation of As-rich Cu(Co)-depleted pyrite rims (P2) in the shallower (argillic) part of the system. Although the absolute timing between these two main (and consecutive) pyrite formation events is yet to be

constrained, the high As and low Cu contents of the present-day borehole fluids suggest that the late-stage, pyrite-forming fluids were compositionally similar to the present-day fluid in the Tolhuaca deep reservoir.

The results presented in this study show that significant variations in fluid composition may be related to abrupt changes in the P-T-X conditions at the TGS. However, experimental studies and more observations in natural systems are needed to assess the precise nature of the triggers leading to such changes – i.e., magmatic input of metal rich fluids, system overpressure, and externally-forced perturbations such as earthquakes (e.g., Cox and Ruming, 2004; Peterson and Mavorgenes, 2014, and Sánchez-Alfaro et al., 2016b). Finally, results from this work confirm that pyrite composition and micro-textures are valuable complements to other geochemical tools used to investigate the evolution of hydrothermal systems.

Chapter 5. Conclusions

The results presented in this thesis provide new insights on the interplay between structures, fluid composition and metal transport in hydrothermal systems. In particular, this thesis contributes to better understand the role of large-scale fault systems on magma degassing and hydrothermal fluid circulation, the structural control on metal transport in hydrothermal fluids, and metal and metalloid partitioning due to vapor-brine separation from a magmatic vapor.

This study focused on the segment between 37° and 41°S of the SVZ, and combined regional-scale sampling of thermal fluids with a structural study along the LOFS and ALFS domains. The isotopic (helium, carbon and nitrogen) data of fumaroles and thermal waters reveal that the structural segments associated with the Liquiñe-Ofqui fault system (LOFS) and with the long-lived basement fault systems (ALFS) are controlling the circulation and the composition of hydrothermal fluids. This approach allowed to identify four volcano-tectonic domains presenting different helium, nitrogen and carbon isotope compositions, based on the degree of crustal contamination and mixing with meteoric waters. Furthermore, it is observed that the geothermal manifestations related to the two main fault systems (LOFS and ALFS) are also characterized by a different trace metal/metalloid signature.

The regional variations in $^{3}He/^{4}He$, $\delta^{13}C–CO_2$ and $\delta^{15}N$ values (3.39 Ra to 7.53 Ra, -7.44‰ to -49.41‰ and 0.02‰ to 4.93‰, respectively) are remarkably consistent with those reported for $^{87}Sr/^{86}Sr$ in lavas along the studied segment (from 0.737 to 0.742), which are strongly controlled by the regional spatial distribution of faults. The two fumaroles gas samples PL and LM associated with the northernmost ‘‘horsetail” transtensional termination of the LOFS are the only datapoints showing uncontaminated MORB-like $^{3}He/^{4}He$ signatures (7.67 Ra and 7.52 Ra, respectively). Towards the south, the dominant mechanism controlling helium isotope ratios of fumaroles and thermal springs (3.68 Ra to 6.97 Ra) appears to be the mixing between mantle-derived helium and a radiogenic component derived from magmatic assimilation of ^{4}He-rich country rocks or contamination during the passage of the fluids through the upper crust. The degree of ^{4}He contamination is strictly related with the faults controlling the occurrence of volcanic and geothermal systems, and the most contaminated values associated with NW-striking structures (3.68 Ra to 5.42 Ra). This is confirmed by $\delta^{15}N$ values that show increased mixing with crustal sediments and meteoric waters along NW faults (AFLS), while $\delta^{13}C–CO_2$ data are indicative of cooling and mixing driving calcite precipitation due to increased residence times along such structures.

The trace elements concentrations in surface thermal waters were contrasted with the helium isotope ratios (Rc/Ra) measured in the exact same emissions. In the acid sulfate waters metals as Ca, Mg, K, Sr, Ba, Co, Ni, Cu, Cd, Rh and Pd show negative correspondence with Rc/Ra, suggesting that its concentration in thermal fluids is dominated by rock leaching. In contrast, B, As, Sb, Ge, Mo, W, Ti, Pb and Zr show a positive correlation with Rc/Ra. This is interpreted as a deep magmatic source for these elements, which are transported upwards to the shallow geothermal domain by low density vapors after deep phase-separation or boiling. These two different trends of enrichment of acid-sulfate waters are the result of a strong structural control that conditions selective elemental partitioning, enhancing water-rock interaction and metal leaching along oblique, NW-striking ALFS structures (e.g. Cu, Co, Ni, Pd etc.). In contrast, the high permeability regime along the main LOFS allow rapid fluxing of metals transported by magmatic vapors (e.g., As, Sb etc.). The geochemistry of neutral-chlorine waters is mainly dominated by shallow processes as mixing with meteoric fluids and mineral precipitation controlling the metal contents of these waters. The weak positive correspondences of some metals with Rc/Ra suggest that these

removal processes are more efficient in NW ALFS structures where the higher residence time of geothermal fluids in the crust increase the reaction time with country rock and the mixing with cold and shallow infiltrating waters.

The geochemical decoupling of Cu and As was studied in detail at the active Tolhuaca Geothermal System (TGS), a high enthalpy, metal-rich hydrothermal system associated with a NW-striking structure in the northern termination of the LOFS. This metals-rich system provided the opportunity to contrast the trace element composition of a suite of pyrite samples retrieved from a ~1 km drill hole, with chemical composition of present-day fluids and paleofluids trapped in fluid inclusions. Well-developed zonations were detected in pyrite from the shallow argillic alteration zone, where Cu(Co)-rich, As-depleted cores alternate with Cu(Co)-depleted, As-rich rims. Contrasting these results with chemical data of fluid inclusion in quartz veins (high Cu/As) and borehole fluids (low Cu/As) reported at the TGS, a correspondence between Cu and As concentrations in pyrite-forming fluids and chemical zonation in pyrite is clear. These observations provide direct evidence supporting the selective partitioning of metals into pyrite as a result of changes in ore-forming fluid composition, most likely due to separation of a single-phase fluid into a low-density vapor and a denser brine, capable to fractionate Cu and As.

These results remark how observed at regional scale, where Cu and As fractionate with different structural features controlling the volcanism and thermal emissions occurrence in the Southern Volcanic Zone of Chile. Arsenic (i.e. correlated with primitive Rc/Ra) is transported by vapor phase from the deep magmatic domain up to the surface and the highest concentrations are associated with NE LOFS structures, permitting high vertical permeability of circulating fluids. In contrast Cu (i.e. correlated with lower Rc/Ra ratios) remain probably confined to the deeper parts of the magmatic/hydrothermal systems due to his affinity with the dense brine and the shallow thermal springs enrichment observed in surface emissions is related with leaching of host rocks, especially along NW ALFS structures, promoting high residence time of fluids in the crust.

The interpretation regarding the effects of structural features on the circulation and composition of geothermal/hydrothermal fluids in the Southern Volcanic Zone may be applicable in other fault systems worldwide and the study of active hydrothermal systems may lead to new interpretations regarding metals partition and hydrothermal ore deposits distribution along long-lived fault structures. In fact, the occurrence of a differential metal distribution in fossil hydrothermal systems associated with regional scale faults have been long time observed. For example in the Atacama Fault System, a 1000 km sinistral fault, which are associated the genesis of many ore deposit of northern Chile, a differential occurrence of ore deposits related with different stress directions has been recognized, where the Iron Oxide Apatite (IOA) deposits commonly occur along the main track of the fault, whereas the Iron Oxide Copper-Gold (IOCG) deposits, are mainly associated with secondary NW-trending structures.

Biblography

Abraitis P. K., Pattrick R. A. D., Vaughan D. J. (2004) Variations in the compositional, textural and electrical properties of natural pyrite: a review. Int. J. Miner. Process. 74, 41–59.

Adriasola A. C., Thomson S. N., Brix M. R., Hervé F. and Stockhertckhert B. (2006) Postmagmatic cooling and late Cenozoic denudation of the North Patagonian Batholith in the Los Lagos region of Chile, 41°-42°15'S. *Int. J. Earth Sci.* 95, 504–528.

Africano F., Rompaey G. Van, Bernard A. and Guern F. Le (2002) Deposition of trace elements from high temperature gases of Satsuma-Iwojima volcano. *Earth Planet. Sci. Lett.* 54, 275–286.

Agusto M., Tassi F., Caselli A. T., Vaselli O., Rouwet D., Capaccioni B., Caliro S., Chiodini G. and Darrah T. (2013) Gas geochemistry of the magmatic-hydrothermal fluid reservoir in the Copahue-Caviahue Volcanic Complex (Argentina). *J. Volcanol. Geotherm. Res.* 257, 44–56.

Aiuppa A., Allard P., D'Alessandro W., Michel A., Parello F., Treuil M. and Valenza M. (2000) Mobility and fluxes of major, minor and trace metals during basalt weathering and groundwater transport at Mt. Etna volcano (Sicily). *Geochim. Cosmochim. Acta* 64, 1827–1841.

Aiuppa A., Dongarrà G., Capasso G. and Allard P. (2000) Trace elements in the thermal groundwaters of Vulcano Island (Sicily). *J. Volcanol. Geotherm. Res.* 98, 189–207.

Aiuppa A., Dongarra G., Valenza M., Federico C. and Pecoraino G. (2003) Degassing of trace volatile metals during the 2001 eruption of Etna. *Geophys. Monogr.* 139, 41–54.

Alam, M. A., Sánchez, P., Parada, M. A. (2010) Interplay of volcanism and structural control in defining the geothermal system(s) along the Liquiñe-Ofqui Fault Zone, in the south-central Chile. Geothermal Resources Council (GRC) Transactions 34, 747-750.

Allard P., Aiuppa A., Loyer H., Carrot F., Gaudry A., Pinte G., Michel A. and Dongarrá G. (2000) Acid Gas and Metal Emission Rates during Long-lived Basalt Degassing at Stromboli Volcano Carrot. *Geophys. Res. Lett.* 27, 1207–1210.

Angermann D., Klotz J. and Reigber C. (1999) Space-geodetic estimation of the Nazca-South America Euler vector. *Earth Planet. Sci. Lett.* 171, 329–334.

Aravena D., Muñoz M., Morata D., Lahsen A., Parada M. A., Dobson P. (2016) Assessment of high enthalpy geothermal resources and promising areas of Chile. Geothermics 59, 1–13. doi:10.1016/j.geothermics.2015.09.001.

Armstrong J. T. (1988) Quantitative analysis of silicates and oxide minerals: Comparison of Monte-Carlo, ZAF and Phi-Rho-Z procedures, in Newbury, D.E., ed., Microbeam analysis: San Francisco, CA, San Francisco Press, 239–246.

Arnórsson S. (1985) The Use of Mixing Models and Chemical Geothermometers For Estimating Undergorund Temperatures in Geothermal Systems. *J. Volcanol. Geotherm. Res.* 23, 299–335.

Arnórsson S., Bjarnason J. Ö., Giroud N., Gunnarsson I. and Stefánsson A. (2006) Sampling and analysis of geothermal fluids. *Geofluids* 6, 203–216.

Arnórsson S., Stefansson A. and Bjarnason J. O. (2007) Fluid-Fluid Interactions in Geothermal Systems. *Rev. Mineral. Geochemistry* 65, 259–312.

Audetat A., Pettke T., Heinrich C. A. and Bodnar R. J. (2008) The composition of magmatic-hydrothermal fluids in barren and mineralized intrusions. Econ. Geol. 103, 1–32.

Bajwah Z. U., Secombe P. K., and Offler R. (1987) Trace element distribution, Co:Ni ratios and genesis of the Big Cadia iron-ore deposit, New South Wales, Australia Miner. Deposita 22,

292–300.
Baker T., Mustard R., Brown V., Pearson N., Stanley C. R., Radford N. W., and Butler I. (2006) Textural and chemical zonation of pyrite at Pajingo: A potential vector to epithermal gold veins. Geochem. Explor. Environ. Anal. 6, 283–293.
Baker, Y., Bertelli, M., Blenkinsop, T., Cleverley, J.S., McLellan, J., Nugus, M., Gillen, D. (2010). P-T-X condictions of fluids in the Sunrise Dan Gold Deposit, Western Australia, and implications for the interplay between deformation and fluids. Econ. Geol. 105, 873-894.
Ballantyne J. M. and Moore J. N. (1988) Arsenic geochemistry in geothermal systems. *Geochim. Cosmochim. Acta* 52, 475–483.
Barker S. L. L., Hickey K. A., Cline J. S., Dipple G. M., Kilburn M. R., Vaughan J. R. and Longo A. A. (2009) Uncloaking invisible gold: use of nano-SIMS to evaluate gold, trace elements, and sulphur isotopes in pyrite from Carlin-type gold deposits. Econ. Geol. 104, 897–904.
Barnes S. J., Boyd R., Korneliussen A., Nilson L. P., Often M., Pedersen R. B., Robins B. (1988) The use of mantle normalization and metal ratios in discriminating between the effects of partial melting, crystal fractionation and sulphide segregation on platinum-group elements, gold, nickel and copper: examples from Norway. In: Prichard H. M., Boowles J. W., Potts P., Scribb, editors. Geoplatinum-87. London: Elsevier; p. 113-143.
Barry, P. H., Hilton, D. R., Halldórsson, S. A., Hahm, D., Marti, K. (2012) High precision nitrogen isotope measurements in oceanic basalts using a static triple collection noble gas mass spectrometer. Geochem. Geophys. Geosyst. 13 (Q01019).
Barry, P. H., Hilton, D. R., Fischer, T. P., De Moor, J. M., Mangasini, F., Ramirez, C. (2013) Helium and carbon isotope systematics of cold "mazuku" CO_2 vents and hydrothermal gases and fluids from Rungwe Volcanic Province, southern Tanzania. Chemical Geology 339 (2013) 141–156.
Barry, P. H., Hilton, D. R., Furi, E., Halldórsson, S. A., Gronvold, K. (2014) Carbon isotope and abundance systematics of Icelandic geothermal gases, fluids and subglacial basalts with implications for mantle plume-related CO_2 fluxes. Geochimica et Cosmochimica Acta 134 (2014) 74–99.
Bayliss P. (1989): Crystal chemistry and crystallography of some minerals within the pyrite group. Am. Mineral. 74, 1168-1176.
Belousov I., Large R., Meffre S., Danyushevsky L., and Beardsmore T. (2014) Pyrite trace element compositions for ore deposits from Western Australia [abs.]. Goldschmidt Conference, Sacramento, California, Abstracts, 167.
Bernard A., Symonds R. B. and Rose Jr W. I. (1990) Volatile transport and deposition of Mo, W and Re in high temperature magmatic fluids. *Appl. Geochemistry* 5, 317–326.
Berner, Z., Pujol, F., Neumann, T., Kramar, U., Stüben, D., Racki, G., and Simon, R. (2006) Contrasting trace element composition of diagenetic and syngenetic pyrites: implications for the depositional environment. In Proceedings Geophysical Research Abstracts 8, 08281.
Berner, Z. A., Puchelt, H., Noltner, T., and Kramar, U. T. Z. (2013) Pyrite geochemistry in the Toarcian Posidonia Shale of south-west Germany: Evidence for contrasting trace-element patterns of diagenetic and syngenetic pyrites. Sedimentology 60, no. 2, 548-573.
Blenkinsop, T.G. (2008). Relationships between faults, extension fractures and veins, and stress. J. Struct. Geol. 30, 622-632.
Blundy J., Cashman K. V., Rust A. and Witham F. (2010) A case for CO2-rich arc magmas. *Earth Planet. Sci. Lett.* 290, 289–301. Available at: http://dx.doi.org/10.1016/j.epsl.2009.12.013.
Bortnikova S. B., Bessonova E. P., Gavrilenko G. M., Vernikovskaya I. V, Bortnikova S. P., Palchik N. A. and Field D. (2008) Hydrogeochemistry of Thermal Sources , Mutnovsky Volcano , South Kamchatka (Russia). In *Thirty-Third Workshop on Geothermal Reservoir*

Engineering Stanford University, Stanford, California, January 28-30, 2008
Bottinga, Y. (1969) Calculated fractionation factors for carbon and hydrogen isotope exchange in the system calcite-CO2-graphite–methane–hydrogen and water vapor. Geochim. Cosmochim. Acta 33, 49–64.
Bralia A., Sabatini G., and Troja P. (1979) A reevaluation of the Co/Ni ratio in pyrite as geochemical tool in ore genesis problems. Miner. Deposita 14, 353–374.
Brown K. L., Webster J. G. and Christenson B. W. (1996) Precious metal sampling at the Ohaaki geothermal field. *Proceeding 18th New Zeal. Geotherm. Work.*, 169–174.
Campbell F. A, and Ethier V. G. (1984) Nickel and cobalt in pyrrhotite and pyrite from the Faro and Sullivan orebodies. Can. Mineral. 22, 503–506.
Cembrano, J., Moreno, H. (1994) Geometría y naturaleza contrastante del volcanismo Cuaternario entre los 38° S y 46° S: ¿Dominios compresionales y tensionales en un régimen transcurrente? Congreso Geológico Chileno, No. 7, Actas, Vol. 1. Universidad de Concepción, Chile, pp. 240–244.
Cembrano J. (1996) The Liquiñe Ofqui fault zone: a long-lived intra-arc fault system in 800 southern Chile. Tectonophysics 259, 55–66.
Cembrano J., Hervé F. and Lavenu A. (1996) The Liquiñe Ofqui fault zone: a long-lived intra-arc fault system in southern Chile. *Tectonophysics* 259, 55–66.
Cembrano J., Schermer E., Lavenu A. and Sanhueza A. (2000) Contrasting nature of deformation along an intra-arc shear zone, the Liquine-Ofqui fault zone, southern Chilean Andes. *Tectonophysics* 319, 129–149.
Cembrano J. and Lara L. (2009) The link between volcanism and tectonics in the southern volcanic zone of the Chilean Andes: A review. *Tectonophysics* 471, 96–113.
Chacko, T., Cole, D. R., Horita, J. (2001) Equilibrium Oxygen, Hydrogen and Carbon Isotope Fractionation Factors Applicable to Geologic Systems. In Valley JW, Cole DR (eds) Stable Isotope Geochemistry. Rev Mineral Geochem 43:1-81.
Charrier R., Baeza O., Elgueta S., Flynn J. J., Gans P., Kay S. M., Muñoz N., Wyss A. R. and Zurita E. (2002) Evidence for Cenozoic extensional basin development and tectonic inversion south of the flat-slab segment, southern Central Andes, Chile (33°-36°S.L.). *J. South Am. Earth Sci.* 15, 117–139.
Chryssoulis S. (1990) Detection and quantification of "invisible" gold by microprobe techniques, in Hausen, D.M., Halbe, D.N., Petersen, E.U., and Tafuri, W.J., eds., Proceedings Symposium Gold 90: Littleton, CO, Society for Mining, Metallurgy, and Exploration, 323–331.
Ciobanu C. L., Cook N. J., Utsunomiya S., Kogagwa M., Green L., Gilbert S. and Wade B. (2012) Gold-telluride nanoparticles in arsenic-free pyrite. Am. Mineral. 97, 1515–1518.
Cline J. S. (2001) Timing of gold and arsenic sulfide mineral deposition at the Getchell Carlin-type gold deposit, North- Central Nevada. Econ. Geol. 96, 75–89.
Clor, L. E., Fischer, T. P., Hilton, D. R., Sharp, Z. D., Hartono, U. (2005) Volatile and N isotope chemistry of the Molucca Sea collision zone: tracing source components along the Sangihe Arc, Indonesia. Geochemistry, Geophysics, Geosystems 6, Q03J14.
Cook N.J. and Chryssoulis S.L. (1990) Concentrations of invisible gold in the common sulfides. Can. Mineral. 28, 1–16.
Cook N. J., Ciobanu C. L. and Mao J. (2009) Textural controls on gold distribution in As-free pyrite from the Dongping, Huangtuliang and Hougou gold deposits, North china Craton (Hebei Province, China). Chem. Geol. 264, 101–121.
Cox M. E., Browne P.R.L. (1995) The occurrence of pyrrhotite in the Ngawha geothermal system, New Zealand. Proc. New Zealand Geotherm. Workshop 17, 35–40.

Cox, S. (2010) The application of failure mode diagrams for exploring the roles of fluid pressure and stress states in controlling styles of fracture-controlled permeability enhancement in faults and shear zones. Geofluids 10, 217–233.

Cox, S, Knackstedt, M & Braun, J (2001), 'Principles of Structural Control on Permeability and Fluid Flow in Hydrothermal Systems', Reviews in Economic Geology, vol. 14, pp. 1-24.

Cox, S.F., and Ruming, K. (2004) The St. Ives mesothermal gold system, Western Australia—a case of golden aftershocks? J. Struct. Geol. 26, 1109–1125.

Craig, H. (1963) The isotopic geochemistry of water and carbon in geothermal areas in Tongiorgi, E., eds., Nuclear geology on geothermal areas: Pisa, Consiglio Nazionale delle Ricerche, Laboratorio di Geologia Nucleare, p. 17–53.

Craig, H., Lupton, J. E., Horibe, Y. (1978) A mantle helium component in Circum-Pacific volcanic gases: Hakone, the Marianas, and Mr. Lassen. In: Alexander, Ozima, M. (Eds.), Terrestrial Rare GasesE.C. Advances in Earth and Planetary Science. Academic Publication, Japan, pp. 3–16.

Davidson, J., Dungan, M. A., Ferguson, K. M., Colucci, M. T. (1987) Crust–magma interactions and the evolution of arc magmas: the San Pedro–Pellado volcanic complex, southern Chilean Andes. Geology 15, 443–446.

Deditius A. P., Utsunomiya S., Renock D., Ewing R. C., Ramana C. V., Becker U., Kesler S. E. (2008) A proposed new type of arsenian pyrite: composition, nanostructure and geological significance. Geochim. Cosmochim. Acta 72, 2919–2933.

Deditius A. P., Utsunomiya S., Ewing R. C., Chryssoulis S. L., Venter D. and Kesler S. E. (2009a) Decoupled geochemical behavior of As and Cu in hydrothermal systems. Geology 37, 707–710.

Deditius A. P., Utsunomiya S., Ewing R. C. and Kesler S. E. (2009b) Nanoscale “liquid” inclusions of As–Fe–S in arsenian pyrite. Am. Mineral. 94, 391–394.

Deditius A., Utsunomiya S., Kesler S. E., Reich M. and Ewing R. C. (2011) Trace elements nanoparticles in pyrite. Ore Geol. Rev. 42, 32–46.

Deditius A., Reich M., Kesler S.E., Utsunomiya S., Chryssoulis S., Walshe J.L., Hough R., and Ewing R.C. (2014) The coupled geochemistry of Au and As in pyrite from hydrothermal ore deposits. Geochim, Cosmochim. Acta 140, 644–670.

Deruelle, B., Harmon, R. S., Moorbath, S. (1983) Combined Sr–O isotopes relationships and petrogénesis of Andean volcanics of South America. Nature 302, 814–816.

Dobson P. F., Kennedy B. M., Reich M., Sanchez P. and Morata D. (2013) Effects of Volcanism, Crustal Thickness, and Large Scale Faulting on the He Isotope Signatures of Geothermal Systems in Chile. *38th Work. Geotherm. Reserv. Eng.*, SGP–TR–198.

Donovan J. J., and Tingle T. N. (1996) An improved mean atomic number correction for quantitative microanalysis. J. Micros. 2, 1, 1–7.

Donovan J. J., Snyder D. A., and Rivers M. L. (1993) An improved interference correction for trace element analysis. Microbeam Anal. 2, 23–28.

Einaudi M. T., Hedenquist J. W. and Inan E. E. (2003) Porphyry to Epithermal Environments. *Soc. Econ. Geol. Geochemical Soc. Spec. Publ.* 10, 285–313.

Emsbo P., Hofstra A. H., Lauha E. A., Griffin G. L. and Hutchinson R. W. (2003) Origin of high-grade gold ore, source of ore fluid components, and genesis of the Miekle and neighboring Carlin-type deposits, Northern Carlin Trend, Nevada. Econ. Geol. 98, 1069–1105.

Farley, K. A., Neroda, E. (1998) Noble gases in the Earth's mantle. Annu Rev Earth Planet Sci 26:189-218.

Fairley, J. P., Hinds, J. J. (2004) Rapid transport pathways for geothermal fluids in an active Great Basin fault zone. *Geology* 32, 825-828.

Faulkner, D. R., Jackson, C. A. L., Lunn, R. J., Schlische, R. W., Shipton, Z. K., Wibberley, C. A. J., Withjack, M. O. (2010) A review of recent developments concerning the structure, mechanics and fluid flow properties of fault zones. Journal of Structural Geology, vol 32, p. 1557-1575.

Faure, G. (1986) Principles of Isotope Geology, 2nd ed. John Wiley and Sons, Inc., Canada, p. 501

Fischer, T. P., Giggenbach, W. F., Sano, Y., Williams, S. N. (1998) Fluxes and sources of volatiles discharged from Kudryavy, a subduction zone volcano, Kurile Islands. Earth and Planetary Science Letters 160, 81–96.

Fischer, T. P., Hilton D. R., Zimmer M. M., Shaw A. M., Sharp Z. D., Walker J. A. (2002) Subduction and recycling of nitrogen along the Central American margin. Science 297, 1154–1157.

Fischer, J.M., Amosse, J., Leblanc, M. (1988) PGE distribution in some ultramafic rocks and minerals from the Bou-Azzer ophiolite complex (Morocco). In: Prichard,H.M., Potts, P.J., Bowles, J.F.W., Cribb, S.J. (Eds.), Geo-Platinum, pp. 199–210.

Fleet M. E., Chryssoulis S. L., Maclean P. J., Davidson R., Weisener G. (1993) Arsenian pyrite from gold deposits: Au and As distribution investigated by SIMS and EP, and color staining and surface oxidation by XPS and LIMS. Can. Miner. 31, 1–17.

Fleet M. E. and Mumin A. H. (1997) Gold-bearing arsenian pyrite and marcasite and arsenopyrite from Carlin Trend gold deposits and laboratory synthesis. *Am. Mineral.* 82, 182–193.

Folguera A., Ramos V. A. and Melnick D. (2002) Partición de la deformación en la zona del arco volcánico de Los Andes neuquinos (36-39°S) en los ultimos 30 millones de años. *Rev. Geol. Chile* 29, 227–240.

Franchini M., McFarlane C., Maydagán L., Reich M., Lentz D. R., Meinert L., and Bouhier V. (2015) Trace metals in pyrite and marcasite from the Agua Rica porphyry-high sulfidation epithermal deposit, Catamarca, Argentina: Textural features and metal zoning at the porphyry to epithermal transition. Ore Geol. Rev. 66, 366–387.

Gerlach, D., Frey, F., Moreno, H., López-Escobar, L. (1988) Recent volcanism in the Puyehue–Cordón Caulle Region, Southern Andes, Chile (40.5°S): petrogénesis of evolved lavas. Journal of Petrology 29, 333–382

Giggenbach W.F. and Goguel R.L. (1989) Collection and analysis of geothermal and volcanic water and gas discharges. Report No. CD 2401. Department of Scientific and Industrial Research. Chemistry Division. Petone, New Zealand.

Giggenbach, W. F., Corrales, S. R. (1992) Isotopic and chemical composition of water and steam discharges from volcanic-magmatic-hydrothermal systems of the Guanacaste Geothermal Provinc. Costa Rica. Appl. Geochem 7:309-332.

Giggenbach W. F. and Soto R. C. (1992) Isotopic and chemical composition of water and steam discharges from volcanic-magmatic-hydrothermal systems of the Guanacaste Geothermal Province, Costa Rica. *Appl. Geochemistry* 7, 309–332.

Giggenbach, W. F., Glover, R. B. (1992) Tectonic regime and major processes governing the chemistry of water and gas discharges from the Rotorua geothermal field, New Zealand. Geothermics 21, 121–140.

Giggenbach W. F. and Stewart M. K. (1982) Processes controlling the isotopic composition of steam and water discharges from steam vents and steam-heated pools in geothermal areas. *Geothermics* 11, 71–80.

Giggenbach, W. F., Poreda, R. J. (1993) Helium isotopic and chemical composition of gases from volcanic hydrothermal systems in the Philippines. Geothermics 22:369-380e,

Gilbert J. S., Stasiuk M. V., Lane S. J., Adam C. R., Murphy M. D., Sparks R. S. J. and Naranjo J. A. (1996) Non-explosive constructional evolution of the ice-filled caldera at Volcan

Sollipulli. Chile. Bull. Volcanol. 58, 67–83.
Glodny, J., Gräfe, K., Echtler, H., Rosenau, M. (2008) Mesozoic to Quaternary continental margin dynamics in South-Central Chile (36°–42°S): the apatite and zircon fission track perspective. International. Journal of Earth Sciences 97, 1271–1291.
González-Jiménez J. M., Barra F., Garrido L. N. F., Reich M., Satsukawa T., Romero R., Salazar E., Colás V., Orellana F., Rabbia O., Plissart G. and Morata D. (2016) A secondary precious and base metal mineralization in chromitites linked to the development of a Paleozoic accretionary complex in Central Chile. *Ore Geol. Rev.* 78, 14–40.
Graf, T., Therrien R. (2009) Stable-unstable flow of geothermal fluids in fractured rock. Geofluids 9, 138-152.
Graham, D. W. (2002) Noble gas isotope geochemistry of mid-ocean ridge and ocean island basalts: Characterization of mantle source reservoirs. Rev Mineral Geochem 47:247-318.
Griffin W. L., Ashley P. M., Ryan C. G., Soey H. S., Suter G. F. (1991) Pyrite geochemistry in the North Arm epithermal Ag–Au deposit, Queensland, Australia: a proton-microprobe study. Can. Mineral. 29, 185–198.
Gregory, D., Meffre, S., and Large, R. (2014) Comparison of metal enrichment in pyrite framboids from a metal-enriched and metal-poor estuary. Am. Mineral. 99, no. 4, 633-644.
Gregory, D. D., Large, R. R., Halpin, J. A., Baturina, E. L., Lyons, T. W., Wu, S., Danyushevsky, L., Sack, P. J., Chappaz, A., and Maslennikov, V. V. (2015a) Trace Element Content of Sedimentary Pyrite in Black Shales. Econ. Geol. 110, no. 6, 1389-1410.
Gregory, D. D., Large, R. R., Halpin, J. A., Steadman, J. A., Hickman, A. H., Ireland, T. R., and Holden, P. (2015b) The chemical conditions of the late Archean Hamersley basin inferred from whole rock and pyrite geochemistry with d33 S and d34 S isotope analyses. Geochim. Cosmochim. Acta 149, 223-250.
Gregory, D. D., Large, R. R., Bath, A. B., Steadman, J. A., Wu, S., Danyushevsky, L., Bull, S. W., Holden, P., and Ireland, T. R. (2016) Trace Element Content of Pyrite from the Kapai Slate, St. Ives Gold District, Western Australia. Econ. Geol. 111, no. 6, 1297-1320.
Gudmundsson, A., Simmenes, T.H., Larsen, B., Philipp, S.L. (2010) Effects of internal structure and local stresses on fracture propagation, deflection, and arrest in fault zones. J. Struct. Geol. 32, 1643-1655.
Günther, D., Audétat, A., Frischknecht, R., Heinrich, C.A. (1998) Quantitative analysis of major, minor and trace elements in fluid inclusions using laser ablation-inductively coupled plasmamass spectrometry. J. Anal. At. Spectrom. 13, 263–270.
Hauser, A., 1997. Catastro y caracterización de las fuentes de agues minerals y termales de Chile. Boletin, vol. 50. Servicio Nacional de Geologia y Mineria-Chile. 89 p.
Hedenquist J. W. and Aoki M. (1991) Meteoric interaction with magmatic discharges in Japan and the significance for mineralization. *Geology* 19, 1041–1044.
Hedenquist J. W., Simmons S. F., Giggenbach W. F. and Eldridge C. S. (1993) White Island, New Zealand, volcanic-hydrothermal system represents the geochemical environment of high-sulfidation Cu and Au ore deposition. *Geology* 21, 731–734.
Heinrich C. A. (2007). Fluid – fluid interactions in hydrothermal ore formation. Rev. Mineral. Geochem. 65, 363–387.
Heinrich C. A., Gunther D., Audetat A., Ulrich T. and Frischknecht R. (1999) Metal fractionation between magmatic brine and vapor, determined by microanalysis of fluid inclusions. Geology 27, 755–758.
Heinrich C. A., Driesner T., Stefansson A. and Seward T. M. (2004) Magmatic vapour contraction and the transport of gold from porphyry environment to epithermal ore deposits. Geology 32, 761–764.

Heinrich C. A., Halter W. E. and Pettke T. (2005) The formation of economic porphyry copper (gold) deposits: constraints from microanalysis of fluid and melt inclusions. In Mineral Deposits and Earth Evolution (ed. I. McDonald, et al.). Geol. Soc. (London) Spec. Publ. 248, 247–263.

Hickey-Vargas, R., Moreno, H., López Escobar, L., Frey, F. (1989) Geochemical variations in Andean basaltic and silicic lavas from the Villarrica–Lanín volcanic chain (39.5°S): an evaluation of source heterogeneity, fractional crystallization and crustal assimilation. Contributions to Mineralogy and Petrology 103, 361–386.

Hildreth, W., and Moorbath, S. (1988) Crustal contributions to arc magmatism in the Andes of Central Chile: Contributions to Mineralogy and Petrology, v. 98, no. 4, p. 455–489.

Hilton, D. R., Hammerschmidt, K., Teufel, S., Friedrichsen, H. (1993) Helium isotope characteristics of Andean geothermal fluids and lavas. Earth Planet Sci Lett 120:265-28.

Hilton, D. R., McMurtry, G. M., Goff, F. (1998) Large variations in vent fluid $CO_2/^3He$ ratios signal rapid changes in magma chemistry at Loihi Seamount, Hawaii. Nature 396, 359–362.

Hilton, D. R., Fischer, T. P., Marty, B. (2002) Noble gases and volatile recycling at subduction zones. In: Porcelli, D.P., Ballentine, C.J., Wieler, R. (Eds.), Reviews in Mineralogy and Geochemistry: Noble Gases in Geochemistry and Cosmochemistry, vol. 47, pp. 319–370.2.

Hoefs, J., 2009. Stable Isotope Geochemistry (288 pp.).

Huerta-Diaz, M. A., and Morse, J. W. (1992) Pyritization of trace metals in anoxic marine sediments. Geochim. Cosmochim. Acta 56, 7, 2681-2702

Hulen J. B., Norton D. L., Moore J. N., Kaspereit D. (2004) Epithermal vein-hosted and stratabound Pb–Zn mineralization in an active hydrothermal system: the southern Salton Sea geothermal field, California. Geotherm. Resour. Counc. Trans. 28, 415–424.

Huston D.L., Sie S.H., Suter G.F., Cooke D.R., and Both R.A. (1995) Trace elements in sulfide minerals from eastern Australian volcanic-hosted massive sulfide deposits: Part I. Proton microprobe analyses of pyrite, chalcopyrite, and sphalerite, and Part II. Selenium levels in pyrite: Comparison with δ34S values and implications for the source of sulfur in volcanogenic hydrothermal systems. Econ. Geol. 90, 1167–1196.

Javoy, M., Pineau, F., Iiyama, I. (1978) Experimental determination of the isotopic fractionation between gaseous CO2 and carbon dissolved in tholeiitic magma; a preliminary study. Contrib. Mineral. Petrol. 67, 35–39.

Johnson E., Kamenetsky V.S., McPhiep J. (2013) The Behavior of Metals (Pb, Zn, As, Mo, Cu) During Crystallization and Degassing of Rhyolites from the OkatainaVolcanic Center, Taupo Volcanic Zone, New Zealand. Journal of Petrology 54, 1641-1659.

Kaasalainen H. and Stefánsson A. (2012) The chemistry of trace elements in surface geothermal waters and steam, Iceland. *Chem. Geol.* 330-331, 60–85.

Kaasalainen H., Stefánsson A., Giroud N. and Arnórsson S. (2015) The geochemistry of trace elements in geothermal fluids, Iceland. *Appl. Geochemistry* 62, 207–223.

Kay, S. M., Godoy, E., Kurtz, A. (2005) Episodic arc migration, crustal thickening, subduction erosion, and magmatism in the south-central-Andes. Geological Society of America Bulletin 117, 67–88. doi:10.1130/B25431.1.

Karlstrom K. E., Crossey L. J., Hilton D. R. and Barry P. H. (2013) Mantle ^3He and CO_2 degassing in carbonic and geothermal springs of Colorado and implications for neotectonics of the Rocky Mountains. Geology 41(4), 495–498.

Kennedy B. M., Kharaka Y. K., Evans W. C., Ellwood A., DePaolo D. J., Thordsen J., Ambats G. and Mariner R. H. (1997) Mantle fluids in the San Andreas fault system, California. Science 278, 1278–1281.

Kennedy B. M. and van Soest M. C. (2005) Regional and local trends in helium isotopes, Basin

and Range Province, western North America: evidence for deep permeable pathways. Geotherm. Resour. Council Trans. 29, 263–268.
Kim, Y. S., Peacock, D. C. P., Sanderson, D. J. (2004) Fault damage zones. Journal of Structural Geology 26 (2004) 503–517.
Kirk Nordstrom D., Blaine McCleskey R. and Ball J. W. (2009) Sulfur geochemistry of hydrothermal waters in Yellowstone National Park: IV Acid-sulfate waters. *Appl. Geochemistry* 24, 191–207.
Koglin N., Frimmel H.F., Lawrie Minter W.E. and Bratz H. (2010) Trace-element characteristics of different pyrite types in Mesoarchean to Paleoproterozoic placer deposits. Miner. Deposita 45, 259–280.
Koseki T., Kazuo N. (2006) Sulfide minerals and sulfur isotope compositions from wells MT-1 and MT-2 in the Bajawa Geothermal Field, Flores Island, Indonesia. J. Geotherm. Res. Soc. Jpn. 28, 223–236.
Koseki T., Nakashima K. (2006) Geothermal structure and feature of sulfide minerals of the Mataloko geothermal field, Flores Island, Indonesia. Proc. of the Asian Geothermal Symposium. 7, 105–109.
Kouzmanov K., Pettke T. and Heinrich C.A. (2010). Direct analysis of ore-precipitating fluids: combined IR microscopy and LA-ICP-MS study of fluid inclusions in opaque ore minerals. Econ. Geol. 105, 351–373.
Kouzmanov, K. and Pokrovski, G. (2012) Hydrothermal Controls on Metal Distribution in Porphyry Cu (-Mo-Au) Systems. Society of Economic Geologists, Inc. Special Publication 16, 573–618.
Krupp R.E., Seward T.M. (1987) The Rotokawa geothermal system, New Zealand; an active epithermal gold-depositing environment. Econ. Geol. 82, 1109–1129.
Lachowycz S. M., Pyle D. M., Gilbert J. S., Mather T. A., Mee K., Naranjo J. A. and Hobbs L. K. (2015) Glaciovolcanism at Volca´n Sollipulli, southern Chile: Lithofacies analysis and interpretation. J. Volcanol. Geoth. Res. 303, 59–78.
Lahsen A., Rojas J., Morata D. and Aravena D. (2015) Geothermal Exploration in Chile: Country Update. *World Geotherm. Congr. 2015*, 1–7.
Lahsen, A., Muñoz, N., Parada, M. A. (2010) Geothermal development in Chile. Proceedings World Geothermal Congress, Bali, Indonesia, Paper Nº 25.
Lange D., Cembrano J., Rietbrock A., Haberland C., Dahm T. and Bataille K. (2008) First seismic record for intra-arc strike-slip tectonics along the Liquiñe-Ofqui fault zone at the obliquely convergent plate margin of the southern Andes. *Tectonophysics* 455, 14–24.
Lara L. E., Lavenu A., Cembrano J. and Rodríguez C. (2006) Structural controls of volcanism in transversal chains: Resheared faults and neotectonics in the Cordón Caulle-Puyehue area (40.5°S), Southern Andes. *J. Volcanol. Geotherm. Res.* 158, 70–86.
Lara L. E., Naranjo J. A. and Moreno H. (2004) Rhyodacitic fissure eruption in Southern Andes (Cordón Caulle; 40.5°S) after the 1960 (Mw:9.5) Chilean earthquake: A structural interpretation. *J. Volcanol. Geotherm. Res.* 138, 127–138.
Large R.R., Danyushevsky L., Hollit C., Maslennikov V., Meffre S., Gilbert S., Bull S., Scott R., Emsbo P., Thomas H., Singh B., and Foster J. (2009) Gold and trace element zonation in pyrite using a laser imaging technique: Implications for the timing of gold in orogenic and Carlin-style sediment-hosted deposits. Econ. Geol. 104, 635–668.
Large, R. R., Halpin, J. A., Danyushevsky, L. V., Maslennikov, V. V., Bull, S. W., Long, J. A., Gregory, D. D., Lounejeva, E., Lyons, T. W., and Sack, P. J. (2014) Trace element content of sedimentary pyrite as a new proxy for deep-time ocean-atmosphere evolution. Earth Planet. Sci. Lett. 389, 209-220.

Large, R. R., Halpin, J. A., Lounejeva, E., Danyushevsky, L. V., Maslennikov, V. V., Gregory, D., Sack, P. J., Haines, P. W., Long, J. A., and Makoundi, C. (2015a) Cycles of nutrient trace elements in the Phanerozoic ocean. Gond. Res. 28, 1282–1293.

Large, R.R., Gregory, D.D., Steadman, J.A., Tomkins, A.G., Lounejeva, E., Danyushevsky, L.V., Halpin, J.A., Maslennikov, V.V., Sack, P.J., Mukherjee, I., Berry, R., Hickman, A. (2015b) Gold in the oceans through time. Earth Planet. Sci. Lett. 428, 139–150.

Lavenu A., Cembrano J. (1999). Compressional- and transpressional-stress pattern for Pliocene and Quaternary brittle deformation in fore arc and intra-arc zones (Andes of Central and Southern Chile). J. Struct. Geol. 21, 1669–1691.

Libbey R.B., Williams-Jones A.E., Melosh B.L., Backeberg N.R. (2015) Characterization of geothermal activity along the North American–Caribbean Plate boundary in Guatemala: The Joaquina geothermal field. Geothermics 56, 17–34.

Libbey R.B., Williams-Jones A.E. (2016) Relating sulfide mineral zonation and trace element chemistry to subsurface processes in the Reykjanes geothermal system, Iceland. J. Volcanol. Geoth. Res. 310, 225–241.

Loftus-Hills G., and Solomon M. (1967) Cobalt, nickel and selenium in sulphides as indicators of ore genesis. Miner. Deposita 2, 228–242.

Lohmar S., Stimac J., Colvin A., González A., Iriarte S., Melosh G., Wilmarth M. (2012) Tolhuaca volcano (Southern Chile, 38.3°S): New learnings from surface mapping and geothermal exploration wells. In Proceedings Congreso Geológico Chileno 2012 Antofagasta, Chile, 5-9. 443–445.

Long, J.A., Large, R.R., Lee, M.S.Y., Benton, M.J., Danyushevsky, L.V., Chiappe, L.M., Halpin, J.A., Cantrill, D., Lottermoser, B. (2015) Severe selenium depletion in the Phanerozoic oceans as a factor in three global mass extinctions. Gond. Res. 36, 209–218.

Lopez-Escobar L., Cembrano J. and Moreno H. (1995) Geochemistry and tectonics of the Chilean southern Andes basaltic Quaternary volcanism (37-46°S). *Rev. Geol. Chile* 22, 219–234.

Lowenstern J. (2001) Carbon dioxide in magmas and implications for hydrothermal systems. *Miner. Depos.* 36, 490–502.

Mabry, J., Lan, T., Burnard, P., Marty, B. (2013) High-precision helium isotope measurements in air. Journal of Analytical Atomic Spectrometry 28 (12), 1903–1910.

Manning, C.E., Ingebritsen, S.E. (1999) Permeability of the continental crust: implications of geothermal data and metamorphic systems. Rev. Geophys. 37, 127-150.

Markússon S. H. and Stefánsson A. (2011) Geothermal surface alteration of basalts, Krýsuvík Iceland-Alteration mineralogy, water chemistry and the effects of acid supply on the alteration process. *J. Volcanol. Geotherm. Res.* 206, 46–59.

Marty B. and Humbert F. (1997) Nitrogen and argon isotopes in oceanic basalts. Earth Planet. Sci. Lett. 152, 101–112.

Marty B., Jambon A. (1987) C/^{3}He in volatile fluxes from the solid Earth: Implication for carbon geodynamics. Earth Planet Sci Lett 83:16-26.

Marty B., Jambon A. and Sano Y. (1989) Helium isotopes and CO_2 in volcanic gases of Japan. Chem. Geol. 76, 25–40.

McKibben M.A., Elders W.A. (1985) Fe–Zn–Cu–Pb mineralization in the Salton Sea geothermal system, Imperial Valley, California. Econ. Geol. 80, 539–559.

McKibben M. A., Andes J. P., Williams A. E. (1988a) Active ore formation at a brine interface in metamorphosed deltaic lacustrine sediments; the Salton Sea geothermal system, California. Econ. Geol. 83, 511–523.

McKibben M.A., Eldridge C.S., Williams A.E. (1988b) Sulfur and base metal transport in the Salton Sea geothermal system. Geotherm. Resour. Counc. Trans. 12, 121–125.

McKibben M. a., Williams A. E. and Hall G. E. M. (1990) Solubility and transport of platinum-group elements and Au in saline hydrothermal fluids: Constraints from geothermal brine data. *Econ. Geol.* 85, 1926–1934.

McMillan, N. J., Harmon, R. S., Moorbath, S., Lopez-Escobar, L., Strong, D. (1989) Crustal sources involved in continental arc magmatism: a case study of Volcan Mocho–Choshuenco, southern Chile. Geology 17, 1152–1156.

Melnick D., Folguera A. and Ramos V. A. (2006) Structural control on arc volcanism: The Caviahue-Copahue complex, Central to Patagonian Andes transition (38°S). *J. South Am. Earth Sci.* 22, 66–88.

Melosh G., Cumming W., Benoit D., Wilmarth M., Colvin A., Winick J., Soto E., Sussman D., Urzúa-Monsalve L., Powell T., Peretz A. (2010) Exploration results and resource conceptual model of the Tolhuaca Geothermal Field, Chile, in: Proceedings World Geothermal Congress, Bali, Indonesia, 25-29 April 2010.

Melosh G., Moore J., Stacey R. (2012) Natural reservoir evolution in the Tolhuaca geothermal field, southern Chile, in: 37th Workshop on Geothermal Reservoir Engineering Stanford University, Stanford, California, January 31 - February 1, 881 2012. SGP-TR-194.

Meyer F. M., Oberthür T., Robb L. J., Saager R., and Stupp H.D. (1990) Cobalt, nickel and gold in pyrite from primary gold deposits and Witwatersrand reefs. S. Afr. J. Geol. 93, 70–82.

Micklethwaite, S., Cox, S.F. (2004) Fault-segment rupture, aftershock-zone fluid flow, and mineralization. Geology 32, 813-816.

Mickelthwaite, S., Sheldon, H., Baker, T. (2010) Active fault and shear processes and their implications for mineral deposit formation and discovery. J. Struct. Geol. 32, 151-165.

Mikhlin, Y.L., and Romanchenko, A.S. (2007) Gold deposition on pyrite and the common sulfide minerals: an STM/STS and SR-XPS study of surface reactions and Au nanoparticles. Geochim. Cosmochim. Acta 71, 5985–6001.

Mikhlin, Y., Romanchenko, A., Likhatski, M., Karacharov, A., Erenburg, S., and Trubina, S. (2011) Understanding the initial stages of precious metals precipitation: Nanoscale metallic and sulfidic species of gold and silver on pyrite surfaces. Ore Geol. Rev. 42, 47-54.

Mitchell, E. C., Fischer, T. P., Hilton, D. R., Hauri, E. H., Shaw, A. M., de Moor, J. M., Sharp, Z. D., Kazahaya, K. (2010) Nitrogen sources and recycling at subduction zones: insights fromthe Izu–Bonin–Mariana arc. Geochemistry, Geophysics, Geosystems 11, Q02X11.

Mookherjee A., and Philip R. (1979) Distribution of copper, cobalt and nickel in ores and host-rocks, Ingladhal, Karnataka, India. Miner. Deposita 14, 33–55.

Moreno H., Lahsen A., Thiele R. and Varela J. (1984) Estudio del Volcán Callaqui, Contrato 01CB-01. Geología del Área del Volcán Callaqui, Escala 1:50.000. Endesa. Departamento de Geología y Geofísica, Facultad de Ciencias Físicas y Matemá ticas,Universidad de Chile.

Morrison, P., Pine, J. (1955) Radiogenic origin of the helium isotopes in rock. Ann. NY Acad. Sci. 62, 71–92.

Morey A.A., Tomkins A.G., Bierlin F.P., Wienberg R.F. and Davidson G. J. (2008) Bimodal distribution of gold in pyrite and arsenopyrite: Examples from the Archean Boorara and Bardoc shear systems, Yilgarn craton, Western Australia. Econ. Geol. 103, 599–614.

Mukherjee, I., and Large, R. R. (2016) Application of Pyrite Trace Element Chemistry to Exploration for SEDEX Style Zn-Pb Deposits: McArthur Basin, Northern Territory, Australia. Ore Geol. Rev. (in press) http://dx.doi.org/10.1016/j.oregeorev.2016.08.004.

Oberthur T., Cabri L.J., Weiser T.W., McMahon G., Muller P. (1997) Pt, Pd and other trace elements in sulfides of the main sulfide zone, Great Dyke, Zimbabwe: a reconnaissance study. Can. Mineral. 35, 597–609.

Oehlert, A. M., Swart, P. K. (2014) Interpreting carbonate and organic carbon isotope covariance

in the sedimentary record. Nature Communications (2014), 5:4672.
Ozima, M., Podosek, F.A. (2002) Noble Gas Geochemistry. Cambridge University Press (300 pp.).
Pacevski A., Moritz R., Kouzmanov K., Marquart K., Zivkovic P. and Cvetkovic L. (2012) Texture and composition of Pb-bearing pyrite from the Coka Marin polymetallic deposit, Serbia, controlled by nanoscale inclusions. Can. Mineral. 50, 1–20.
Palenik C S., Utsunomiya S., Reich M., Kesler S.E., Ewing R.C. (2004) "Invisible" gold revealed: direct imaging of gold nanoparticles in a Carlin-type deposit. Am. Mineral. 89, 1359–1366.
Parada, M. A., López-Escobar, L., Oliveros, V., Fuentes, F., Morata, D., Calderón, M., Aguirre, L., Féraud, G., Espinoza, F., Moreno, H., Figueroa, O., Muñoz-Bravo, J., Troncoso Vásquez, R., Stern, C. R. (2007) Andean magmatism. In: Moreno, T., Gibbons,W. (Eds.), The geology of Chile, 21–114. The Geological Society, London, pp. 115–146.
Pérez, Y. D. (1999) Fuentes de aguas termales de la Cordillera Andina del Centro-Sur de Chile (39–42oS). Boletin, vol. 54. Servicio Nacional de Geologia y Mineria, p. 65.
Pérez-Flores, P., Cembrano, J., Sánchez, P. (2014) Local Stress fields and paleo-fluid distribution within a transtensional duplex: An example from the northern termination of the Liquiñe-Ofqui Fault System. Abstract T26C 4697 AGU fall Meeting San Francisco, EE.UU
Pérez-Flores, P., Cembrano, J., Sánchez-Alfaro, P., Veloso, E., Arancibia, G., Roquer, T. (2016) Tectonics, magmatism and paleo-fluid distribution in a strike-slip setting: insights from the northern termination of the Liquiñe–Ofqui Fault System, Chile. Tectonophysics 680, 192–210.
Peterson E.C. and Mavrogenes J.A. (2014) Linking high-grade gold mineralisation to earthquake-induced fault-valve processes in the Porgera gold deposit, Papua New Guinea. Geology 42, 5, 383–386.
Piña R., Gervilla F., Barnes S.J., Ortega L., and Lunar R. (2013) Platinum-group elements-bearing pyrite from the Aguablanca Ni-Cu sulphide deposit (SW Spain): A LA-ICP-MS study. Eur. J. Mineral. 25, 241–252.
Planer-Friedrich B., Lehr C., Matschullat J., Merkel B. J., Nordstrom D. K. and Sandstrom M. W. (2006) Speciation of volatile arsenic at geothermal features in Yellowstone National Park. *Geochim. Cosmochim. Acta* 70, 2480–2491.
Pokrovski G. S., Kara S. and Roux J. (2002) Stability and solubility of arsenopyrite, FeAsS, in crustal fluids. *Geochim. Cosmochim. Acta* 66, 2361–2378.
Pokrovski G.S., Zakirov I.V., Roux J., Testemale D., Hazemann J.L., Bychkov A.V. and Golikova G. V. (2002) Experimental study of arsenic speciation in vapor phase to 500 °C: implications for As transport and fractionation in low-density crustal fluids and volcanic gases. Geochim. Cosmochim. Acta 66, 3453–3480.
Pokrovski G.S., Roux J. and Harrichoury J.C. (2005) Fluid density control on vapor–liquid partitioning of metals in hydrothermal systems. Geology 33, 657–660.
Pokrovski G. S., Hazemann J. L., Testemale D., Roux J. and Tella M. (2005) Transport of metalloids by low-density hydrothermal fluids: Insights from X-ray absorption spectroscopy. *Geochim. Cosmochim. Acta Suppl.* 69, A734.
Pokrovski G.S., Borisova A.Y. & Bychkov A.Y. (2013) Speciation and transport of metals and metalloids in geological vapors. Rev. Mineral. Geochem. 76, 165–218.
Potent, S. (2003) Kinematik und Dynamik neogener Deformationsprozesse des su¨dzentralchilenischen Subduktionssystems, no¨ rdlichste Patagonische Anden (37–40S). Ph.D Thesis, Universitat Hamburg, 169 pp.
Pritchard M. E., Jay J. A., Aron F., Henderson S. T. and Lara L. E. (2013) Subsidence at southern Andes volcanoes induced by the 2010 Maule, Chile earthquake. Nat. Geosci. 6, 632–636.
Pudack C., Halter W. E., Heinrich C. A., and Pettke T. (2009) Evolution of Magmatic Vapor to

Gold-Rich Epithermal Liquid: The Porphyry to Epithermal Transition at Nevados de Famatina, Northwest Argentina. Econ. Geol. 104, 449-477.

Qian G., Brugger J., Testamale D., Skiner W., and Pring A. (2012) Formation of As(II)-pyrite during experimental replacement of magnetite under hydrothermal conditions. Geochim.Cosmochim. Acta 100, 1–10.

Radcliffe D. & McSween H.Y. (1969) Copper zoning in pyrite from Cerro de Pasco, Peru: a discussion. Am. Mineral. 54, 1216-1217.

Radic J. P. (2010) Las cuencas cenozoicas y su control en el volcanismo de los Complejos Nevados de Chillán y Copahue- Callaqui (Andes del Sur, 36–39ªS). Andean Geol. 37, 220–246.

Ray M. C., Hilton D. R., Muñoz J., Fischer T. P. and Shaw A. M. (2009) The effects of volatile recycling, degassing and crustal contamination on the helium and carbon geochemistry of hydrothermal fluids from the Southern Volcanic Zone of Chile. *Chem. Geol.* 266, 38–49.

Reich M., Kesler S.E., Utsunomiya S., Palenik C.S., Chryssoulis S., and Ewing R.C. (2005) Solubility of gold in arsenian pyrite. Geochim.Cosmochim. Acta 69, 2781–2796.

Reich M., Utsunomiya S., Kesler S.E., Wang L.M., Ewing R.C., and Becker U. (2006) Thermal behavior of metal nanoparticles in geologic materials: Geology 34, 1033–1036.

Reich, M., Chryssoulis, S.L., Deditius, A., Palacios, C., Zúñiga, A., Weldt, M., and Alvear, M. (2010) "Invisible" silver and gold in supergene digenite (CuS). Geochim. Cosmochim. Acta 74, 6157–6173.

Reich M., Hough R., Deditius A., Utsunomiya S., Ciobanu C., and Cook N.J. (2011) Nanogeoscience in ore systems research: Principles, methods and applications. Ore Geol. Rev. 42, 1–5.

Reich M., Deditius A., Chryssoulis S., Li J.W., Ma C.Q., Parada M.A., Barra F., and Mittermayr F. (2013) Pyrite as a record of hydrothermal fluid evolution in a porphyry copper system: A SIMS/EMPA trace element study. Geochim. Cosmochim. Acta 104, p. 42–62.

Reich M., Simon A., Deditius A., Barra F., Chryssoulis S., Lagas G., Tardani D., Knipping J., Bilenker L.,, Sánchez-Alfaro P., Roberts M.P. and Munizaga R. (2016a). Trace elemnt signature of pyrite from the Los Colorados Iron Oxide-Apatite (IOA) deposit, Chile: a missing link between Andean IOA and Iron Oxide Copper-Gold systems? Econ. Geol 111, pp. 743–761.

Reich M., Large R., Deditius A. (2016b) New advances in trace element geochemistry of ore minerals and accessory phases. Ore Geol. Reviews (in press).

Reyes a. G., Trompetter W. J., Britten K. and Searle J. (2002) Mineral deposits in the Rotokawa geothermal pipelines, New Zealand. *J. Volcanol. Geotherm. Res.* 119, 215–239.

Richards J. P. (2011) Magmatic to hydrothermal metal fluxes in convergent and collided margins. *Ore Geol. Rev.* 40, 1–26.

Richards, J.P. (2013) Giant ore deposits formed by optimal alignments and combinations of geological processes: Nature Geoscience, v. 6, no. 11, p. 911–916, doi: 10.1038/ngeo1920

Richards J. P. (2015) The oxidation state, and sulfur and Cu contents of arc magmas: Implications for metallogeny. *Lithos* 233, 27–45.

Rosenau M., Melnick D., Echtler H. (2006) Kinematic constraints on intra-arc shear and strain partitioning in the southern Andes between 38°S and 42°S latitude. Tectonics 25, 1–16.

Roulleau E., Tardani D., Sano Y., Takahata N., Vinet N., Berrios C., Bravo F., Muñoz C, Sanchez J. (2016) New insight of noble gas and stable isotopes of geothermal/hydrothermal fluids at Caviahue-Copahue Volcanic Complex: boiling steam separation and water-rock interaction at shallow depth. Journal of Volcanology and Geothermal Research 328, 70-83.

Rowland, J.V., Sibson, R.H. (2004). Structural controls on hydrothermal flow in segmented rift system, Taupo Volcanic Zone, New Zealand. Geofluids 4, 259-283.

Rowland, J.V., and Simmons, S.F. (2012) Hydrologic, Magmatic, and Tectonic Controls on Hydrothermal Flow, Taupo Volcanic Zone, New Zealand: Implications for the Formation of Epithermal Vein Deposits. Econ. Geol. 107, 427-457.

Rusk B.G., Reed M.H. and Dilles J.H. (2008) Fluid inclusion evidence for magmatic-hydrothermal fluid evolution in the porphyry copper–molybdenum deposit at Butte, Montana. Econ. Geol. 103, 307–334.

Sánchez P., Pérez-Flores P., Arancibia G., Cembrano J., Reich M. (2013) Crustal deformation effects on the chemical evolution of geothermal systems: the intra-arc Liquiñe–Ofqui fault system, Southern Andes. Int. Geol. Rev. 55, 1384–1400. 939.

Sánchez-Alfaro P., Reich M., Arancibia G., Pérez-Flores P., Cembrano J., Driesner T., Lizama M. Rowland J., Morata D., Heinrich C. A., Tardani D., Campos E. (2016a) Physical, chemical and mineralogical evolution of the Tolhuaca geothermal system, southern Andes, Chile: insights into the interplay between hydrothermal alteration and brittle deformation. J.Volcanol. Geoth. Res. 324, 88–104.

Sánchez-Alfaro P., Reich M., Driesner T., Cembrano J., Arancibia G., Pérez-Flores P., Heinrich C. A., Rowland J., Tardani D., Lange D., Campos E. (2016b) The optimal windows for seismically-enhanced gold precipitation in the epithermal environment. Ore Geol. Rev. 79, 463–473.

Sano, Y., Wakita, H. (1988) Helium isotope ratio and heat discharge rate in the Hokkaido Island, Northeast Japan. Geochem. J. 22, 293–303.

Sano, Y., Marty, B. (1995) Origin of carbon in fumarolic gas from island arcs. Chem Geol 119:265-274.

Sano, Y., Williams, S. N. (1996) Fluxes of mantle and subducted carbon along convergent plate boundaries. Geophys Res Lett 23:2749-2752.

Sano, Y., Nishio, Y., Sasaki, S., Gamo, T., Nagao, K. (1998) Helium and carbon isotope systematics at Ontake volcano, Japan. Journal of geophysical research 103 (B10), 23863–23873.

Sano, Y., Takahata, N., Nishio, Y., Fischer, T. P., Williams, S. N. (2001) Volcanic flux of nitrogen from the Earth. Chem Geol 171:263-271.

Sano, Y., Takahata, N., Seno, T. (2006) Geographical Distribution of $^{3}He/^{4}He$ Ratios in the Chugoku District. Southwestern Japan. Pure Appl. Geophys. 163, 745–757.

Sano, Y., Tokutake, T., Takahata, N. (2008) Accurate measurement of atmospheric helium isotopes. Analytical Sciences 24, 521–525.

Sano Y., Fischer T. P. (2013) The analysis and Interpretation of Noble Gases in Modern Hydrothermal Systems. In: The Noble Gases as Geochemical Tracers. Advances in Isotope Geochemistry. (ed Burnard P.) 249–317 (Springer-Verlag).

Sano Y., Marty B., Burnard P. (2013) Noble gases in the atmosphere. In: The Noble Gases as Geochemical Tracers. Advances in Isotope Geochemistry (ed Burnard P.) 17–31 (Springer-Verlag).

Saunders J.A. (1990) Colloidal transport of gold and silica in epithermal precious-metal systems: evidence from the Sleeper deposit, Nevada. Geology 18, 757–760.

Schmid-Beurmann P. and Bente K. (1995): Stability properties of the CuS2–FeS2 solid solution series of pyrite type. Mineral. Petrol. 53, 333-341.

Sepúlveda, F., Dorsch, K., Lahsen, A., Bender, S., Palacios, C. (2004) The chemical and isotopic composition of geothermal discharges from the Puyehue-CordónCaulle area (40.5°S), Southern Chile. Geothermics 33, 655–673.

Sepúlveda, F., Lahsen, A., Powell, T. (2007) Gasgeochemistry of the CordónCaulle geothermal system, Southern Chile. Geothermics 36, 389-420.

Shimazaki H. & Clark L.A. (1970) Synthetic FeS2–CuS2 solid solution and fukuchilite-like

minerals. Can. Mineral. 10, 648-664.
Shoji T., Iwano H., Kaneda H., Takenouchi S. (1989) Trace elements in pyrite from Kirishima geothermal field and their availability for exploration. J. Geotherm. Res. Soc. Jpn. 11, 31–42.
Shoji T., Kaneda H., Takano Y. (1999) Minor element geochemistry in the Yanaizu-Nishiyama geothermal field, Northeastern Japan. Geotherm. Resour. Counc. Trans. 23, 405–406.
Sibson, R.H. (1994) Crustal stress, faulting and fluid flow, in Parnell, J., ed., Geological Society Special Publication, v. 78, no. 1, p. 69–84.
Sibson, R.H. (1996) Structural permeability of fluid-driven fault-fracture meshes. J. Struct. Geol. 18, 1031–1042.
Sibson, R.H. (2001) Seismogenic framework for hydrothermal transport and ore deposition. Rev. Econ. Geol. 14, 25-50.
Sibson, R. H., Rowland, J.V. (2003) Stress, fluid-pressure, and structural permeability in seismogenic crust, North Island, New Zealand. Geophys. J. Int. 154, 584-594
Sillitoe R. and Hedenquist J. (2003) Chapter 18 Linkages between Volcanotectonic Settings , Ore-Fluid Compositions , and Epithermal Precious Metal Deposits. *Soc. Econ. Geol.* 10, 315–343.
Simmons S. F. and Browne P. R. L. (2000) Hydrothermal minerals and precious metals in the Broadlands-Ohaaki geothermal system: Implications for understanding low-sulfidation epithermal environments. *Econ. Geol.* 95, 971–999.
Simmons, S. F. & Brown, K. L. (2006) Gold in magmatic hydrothermal solutions and the rapid formation of a giant ore deposit. Science 314, 288–291.
Simmons S. F. and Brown K. L. (2007) The flux of gold and related metals through a volcanic arc, Taupo Volcanic Zone, New Zealand. *Geology* 35, 1099–1102.
Simmons S. F., Brown K. L., Browne P. R. L. and Rowland J. V. (2016a) Gold and silver resources in Taupo Volcanic Zone geothermal systems. *Geothermics* 59, 205–214.
Simmons S. F., Brown K. L. and Tutolo B. M. (2016b) Hydrothermal transport of Ag, Au, Cu, Pb, Te, Zn, and other metals and metalloids in New Zealand geothermal systems: Spatial Patterns, Fluid-mineral equilibria, and implications for epithermal mineralization. *Econ. Geol.* 111, 589–618.
Simon G., Huang H., Penner-Hahn J.E., Kesler S.E. and Kao L.S. (1999) Oxidation state of gold and arsenic in gold-bearing arsenian pyrite. Am. Miner. 84, 1071–1079.
Simon A.C., Pettke T., Candela P.A., Piccoli P.M., and Heinrich C.A. (2006) Cu partitioning in a melt-vapor-brine-magnetite-pyrrhotite assemblage. Geochim. Cosmochim. Acta 70, 5583–5600.
Simon A. C., Pettke T., Candela P. A., Piccoli P. M., and Heinrich C. A. (2007) The partitioning behavior of As and Au in S-free and S-bearing magmatic assemblages. Geochim. Cosmochim. Acta, 71, 1764–1782.
Skinner B. J., White D. E., Rose H. J., Mays R. E. (1967) Sulfides associated with the Salton Sea geothermal brine. Econ. Geol. 62, 316–330.
Soltani Dehnavi A., Lentz D. R., and McFarlane C. R. M. (2015) LA-ICPMS analysis of volatile trace elements in massive sulphides and host rocks of selected VMS deposits of the Bathurst mining camp, New Brunswick: Methodology and application to exploration. Geological Survey of Canada Open File 7853, 214.
Somoza R. and Ghidella M. E. (2005) Convergencia en el margen occidental de América del sur durante el Cenozoico: Subducción de las placas de Nazca, Farallón y Aluk. *Rev. la Asoc. Geol. Argentina* 60, 797–809.
Steadman, J. A., Large, R. R., Meffre, S., Olin, P. H., Danyushevsky, L. V., Gregory, D. D.,

Belousov, I., Lounejeva, E., Ireland, T. R., and Holden, P. (2015) Synsedimentary to Early Diagenetic Gold in Black Shale-Hosted Pyrite Nodules at the Golden Mile Deposit, Kalgoorlie, Western Australia. Econ. Geol. 110, 5, 1157-1191.

Stefánsson A. and Arnórsson S. (2002) Gas pressures and redox reactions in geothermal fluids in Iceland. *Chem. Geol.* 190, 251–271.

Stelling J., Botcharnikov R. E., Beermann O. and Nowak M. (2008) Solubility of H2O- and chlorine-bearing fluids in basaltic melt of Mount Etna at T = 1050-1250 °C and P = 200 MPa. *Chem. Geol.* 256, 101–109.

Stern, C. R. (1991) Role of subduction erosion in the generation of the Andean magmas. Geology 19, 78–81.

Stern, C. R., Moreno, H., López-Escobar, L., Oliveros, V., Clavero, J. E., Lara, L. E., Naranjo, J. A, Parada, M. A., Skewes, M. A. (2007) Chilean volcanoes. In: Moreno, T., Gibbons, W. (Eds.), The geology of Chile, 21–114. The Geological Society, London, pp. 147–178.

Sun W., Arculus R. J., Kamenetsky V. S. and Binns R. a (2004) Release of gold-bearing fluids in convergent margin magmas prompted by magnetite crystallization. *Nature* 431, 975–978.

Sung Y. H., Brugger J., Ciobanu C. L., Pring A., Skinner W. and Nugus M. (2009) Invisible gold in arsenian pyrite and arsenopyrite from a multistage Archean gold deposit: sunrise Dam Eastern Goldfields Province, Western Australia. Miner. Deposita 44, 765–791.

Tanner D., Henley R. W., Mavrogenes J.A., Holden P. (2016) Sulfur isotope and trace element systematics of zoned pyrite crystals from the El Indio Au–Cu–Ag deposit, Chile. Contr. Mineral. Pet. 171 (4), 1-17

Tardani D., Reich M., Roulleau E., Takahata N., Sano Y., Pérez-Flores P., Sánchez-Alfaro P., Cembrano J., Arancibia G. (2016). Exploring the structural controls on helium, nitrogen and carbon isotope signatures in hydrothermal fluids along an intra-arc fault system. Geochim. Cosmochim. Acta 184, 193–211.

Tassara, A., Gotze, H. J., Schmidt, S., Hackney, R. (2006) Three-dimensional density model of the Nazca plate and the Andean continental margin. Journal of geophysical research, Vol. 111, b09404.

Tassara A. and Yañez G. (2003) Relación entre el espesor elástico de la litosfera y la segmentación tectónica del margen andino (15- 47°S). *Andean Geol.* 30, 159–186.

Thiele R., Lahsen A., Hugo M., Varela J., Munizaga F. (1987) Estudio geológico regional a escala 1:100.000 de la Hoya Superior y Curso Medio del Río Bío-Bío. Centrales Quitramán, Huequecura, Aguas Blancas, Pangue, Ralco y Llanquén. Depto. de Geología-ENDESA (In spanish).

Tossell J. A., Vaughan D. J., Burdett J. K. (1981) Pyrite, marcasite, and arsenopyrite-type minerals: crystal chemical and structural principles. Phys. Chem. Miner. 7, 177– 184.

Varekamp, J. C., DeMoor, J. M., Merrill, M. D., Colvin, A. S., Goss, A. R. (2006) Geochemistry and isotopic characteristics of the Caviahue–Copahue volcanic complex, Province of neuquen, Argentina. Geological Society of America Special Paper 407, 317–342.

Vaughan D. J., Craig J. R. (1978) Mineral Chemistry of Metal Sulfides. Cambridge Univ. Press, Cambridge.

Vaughan J. P. and Kyin A. (2004) Refractory gold ores in Archean greenstones, Western Australia: mineralogy, gold paragenesis, metallurgical characterization and classification. Mineral. Mag. 68, 255–277.

Vogel, J. C., Grootes, P. M., Mook, W. G. (1970) Isotopic fractionation between gaseous and dissolved carbon dioxide. Z. Phys. 230, 255–258.

Wallace P. J. (2005) Volatiles in subduction zone magmas: Concentrations and fluxes based on melt inclusion and volcanic gas data. *J. Volcanol. Geotherm. Res.* 140, 217–240.

Wilkinson, J. J., Stoffell, B., Wilkinson, C. C., Jeffries, T. E., and Appold, M. S. (2009) Anomalously metal-rich fluids form hydrothermal ore deposits. Science 323, 764-767.

Williams-Jones A. E., and Heinrich C. A. (2005) Vapor transport of metals and the formation of magmatic-hydrothermal ore deposits. Economic Geology 100th Anniversary Volume 1905–2005 100, 1287–1312.

Williams-Jones A. E., Migdisov A. A., Archibald S. M., and Xiao Z. (2002) Vapor transport of ore metals, in Hellmann, R., and Wood, S.A., eds., Water-rock interactions, ore deposits, and environmental geochemistry. A tribute to David A. Crerar. Geochemical Society Special Publication 7, 279–305.

Zajacz Z. (2007) Mass transfer during volatile exsolution in magmatic systems: Insights through methodological developments in melts and fluid inclusion analysis [Ph.D. thesis]. ETH Zürich Monograf 17448, 169.

Zajacz Z., Halter W. (2009) Copper transport by high temperature, sulfur-rich magmatic vapor: Evidence from silicate melt and vapor inclusions in a basaltic andesite from the Villarrica volcano (Chile). Earth Planet. Sci. Lett. 282, 115–121.

Zajacz Z., Seo J. H., Candela P. A., Piccoli P. M. and Tossell J. A. (2011) The solubility of copper in high-temperature magmatic vapors: A quest for the significance of various chloride and sulfide complexes. Geochim. Cosmochim. Acta 75, 2811–2827.

Zelenski M. E., Fischer T. P., de Moor J. M., Marty B., Zimmermann L., Ayalew D., Nekrasov A. N. and Karandashev V. K. (2013) Trace elements in the gas emissions from the Erta Ale volcano, Afar, Ethiopia. *Chem. Geol.* 357, 95–116.

Appendix A1. *Geochemistry of major and trace elements of lavas from Tolhuaca, Copahue, Callaqui and Lonquimay volcanoes from Southern Volcanic Zone of Chile.*

Sample name	Location	SiO2	Al2O3	Fe2O3	MnO	MgO	CaO	Na2O	K2O	TiO2	P2O5	LOI	Total	Sc	Be	V	Ba	Sr	Y	Zr	Cr	Co	Ni	Cu	Zn	Ga	Ge	As	Rb	Nb
		%	%	%	%	%	%	%	%	%	%	%	%	ppm	ppm	ppm	ppm	ppm	ppm	ppm	ppm	ppm	ppm	ppm	ppm	ppm	ppm	ppm	ppm	ppm	ppm
NV-TOL-3	Tolhuaca vn.	57,1	16,68	8,71	0,1	4	7,6	3,73	1,3	1,02	0,26	0,1	101	24	1	193	325	435	27	144	90	36	40	80	70	16	1	12	37	3
NV-TOL 1	Tolhuaca vn.	55,8	17,32	8,85	0,1	4,2	7,8	3,8	1,3	1,07	0,25	0,1	101	26	1	183	100	21	40	80	80	16	1	12	36	457	26	145	3	b.d.
NV-TOL 2	Tolhuaca vn.	54,2	16,52	10,08	0,2	3,8	8,1	3,61	1	1,18	0,24	0,3	99	30	b.d.	253	30	34	20	110	80	17	1	10	26	475	24	120	2	b.d.
DT-COP-SUM-1	Copahue vn.	55,3	17	9,03	0,1	4,4	8,1	3,54	1,8	1,15	0,28	-0,4	100	25	2	200	406	519	25	184	60	22	30	60	70	17	1	b.d.	54	6
DT-COP-SUM-2	Copahue vn.	54,7	16,89	9,18	0,1	4,5	7,8	3,54	1,9	1,21	0,29	-0,4	100	26	2	206	413	513	25	200	60	43	30	60	70	17	1	b.d.	56	6
NV-COP-PREGLA-1A	Copahue vn.	56,5	16,3	8,55	0,1	3,6	6,6	3,77	2	1,28	0,37	0,4	100	23	2	178	484	494	29	211	60	32	30	40	80	17	1	b.d.	57	8
NV-COP-PREGLA-1B	Copahue vn.	56,2	16	8,36	0,1	3,5	6,6	3,76	2	1,24	0,37	0,4	99	22	2	178	469	490	30	203	60	40	30	40	70	17	1	5	58	7
NV-COP-PREGLA-1C	Copahue vn.	56,7	16,37	8,45	0,1	3,6	6,5	3,68	2	1,29	0,37	0,1	99	22	2	174	480	490	29	210	60	29	30	40	110	17	1	b.d.	55	8
NV-COP-PREGLA-1D	Copahue vn.	56,5	16,37	8,32	0,1	3,6	6,5	3,75	2	1,27	0,36	0,2	99	22	2	174	480	491	28	207	60	32	40	50	80	17	1	b.d.	57	7
NV-COP-PREGLA-2A	Copahue vn.	60,5	15,33	7,91	0,1	1,9	4,2	4,3	3,4	1,41	0,47	-0,2	99	17	2	120	696	349	40	358	b.d.	20	b.d.	30	70	17	1	7	109	12
NV-COP-PREGLA-2B	Copahue vn.	60,3	15,11	7,88	0,1	1,8	4,2	4,07	3,3	1,38	0,47	-0	99	17	2	124	666	349	38	346	b.d.	12	b.d.	40	80	17	1	8	102	11
NV-COP-PREGLA-2C	Copahue vn.	60,7	15,04	7,55	0,1	1,9	4,3	4,1	3,3	1,41	0,46	-0,1	99	17	2	116	669	347	39	358	b.d.	29	b.d.	30	80	17	b.d.	8	108	12
NV-CAV-MEL-1	Copahue vn.	55,9	16,62	8,27	0,1	3,8	7,2	3,55	2	1,13	0,28	0,7	100	22	1	180	471	504	24	176	60	29	30	50	70	16	1	b.d.	54	5
CQ-2	Callaqui vn.	51,1	19,87	8,82	0,1	4,9	9,7	3,67	0,9	1,05	0,18	0,3	101	21	b.d.	210	244	1064	12	70	40	24	30	80	70	18	b.d.	b.d.	15	1
CQ-8	Callaqui vn.	52,3	19,4	8,39	0,1	4,5	9,3	3,62	1	1,01	0,18	0,5	100	20	b.d.	212	256	1004	13	76	40	23	30	60	80	18	b.d.	b.d.	17	2
VV-18	Callaqui vn.	51,2	18	9,79	0,1	3,3	8,5	3,41	0,8	1,11	0,2	2	98	28	1	240	315	591	25	85	40	17	b.d.	80	80	17	1	b.d.	20	2
LON-5-04	Lonquimay vn.	58,7	16,63	9,63	0,2	2	5,4	5,28	1,1	1,22	0,36	-0,3	100	25	1	50	366	478	33	122	b.d.	8	b.d.	10	100	18	1	9	21	2
CF02-05B	Lonquimay vn.	58,4	16,46	10,59	0,2	2,1	5,6	5,12	1	1,22	0,48	-0,5	101	26	1	48	349	492	34	115	b.d.	9	b.d.	20	110	19	1	9	21	2
CF02-04A	Lonquimay vn.	58,1	16,3	10,29	0,2	2	5,6	5,03	1	1,23	0,46	-0,4	100	26	1	45	345	484	34	113	b.d.	9	b.d.	20	110	19	1	9	20	2

Appendix A1. *Continue*

Mo	Ag	In	Sn	Sb	Cs	La	Ce	Pr	Nd	Sm	Eu	Gd	Tb	Dy	Ho	Er	Tm	Yb	Lu	Hf	Ta	W	Tl	Pb	Bi	Th	U	Ir	Ru	Rh	Pt	Pd	Au	Re
ppm	ppm	ppm	ppm	ppm	ppm	ppm	ppm	ppm	ppm	ppm	ppm	ppm	ppm	ppm	ppm	ppm	ppm	ppm	ppm	ppm	ppm	ppm	ppm	ppm	ppm	ppm	ppm	ppb	ppb	ppb	ppb	ppb	ppb	ppb
b.d.	b.d.	b.d.	2	1,1	3,5	13	29	4,1	18	4,5	1,1	4,5	0,7	4	0,8	2,5	0,4	2,4	0,4	3,5	0,2	117	0,1	11	b.d.	3,6	1,2	b.d.	b.d.	b.d.	b.d.	b.d.	b.d.	b.d.
b.d.	b.d.	2	0,9	3,4	333	13	29	4,1	18	4,5	1,2	4,7	0,7	4,1	0,9	2,7	0,4	2,5	0,3	3,5	0,2	b.d.	0,1	11	b.d.	3,7	1,3	b.d.	b.d.	b.d.	b.d.	1	1	b.d.
b.d.	b.d.	1	0,8	2,5	276	12	28	3,9	17	4,1	1,2	4,3	0,6	3,9	0,8	2,4	0,4	2,2	0,3	3	0,2	83	b.d.	9	b.d.	2,6	0,9	b.d.	b.d.	b.d.	b.d.	b.d.	b.d.	b.d.
b.d.	b.d.	b.d.	2	b.d.	2,5	21	45	6	25	5,4	1,4	4,5	0,7	4	0,8	2,3	0,3	2,1	0,3	4,1	0,4	2	0,2	11	b.d.	6,8	2	b.d.	b.d.	b.d.	b.d.	b.d.	b.d.	b.d.
b.d.	0,5	b.d.	2	0,5	2,7	23	48	6,3	26	5,4	1,3	4,8	0,7	4,2	0,8	2,4	0,4	2,4	0,4	4,5	0,5	138	0,2	11	b.d.	7	2,1	b.d.	b.d.	b.d.	b.d.	b.d.	b.d.	b.d.
b.d.	0,6	b.d.	2	0,6	2,6	27	57	7,4	31	6,3	1,5	5,7	0,9	4,7	0,9	2,7	0,4	2,4	0,4	4,8	0,6	93	0,2	12	b.d.	7,9	2,2	b.d.	b.d.	b.d.	b.d.	b.d.	b.d.	b.d.
b.d.	0,6	b.d.	2	0,6	2,4	27	57	7,5	31	6,5	1,5	5,8	0,9	4,8	0,9	2,7	0,4	2,7	0,4	4,7	0,5	136	0,2	12	b.d.	7,7	2,1	b.d.	b.d.	b.d.	b.d.	b.d.	b.d.	b.d.
2	0,6	b.d.	2	b.d.	2,2	27	56	7,3	30	6,2	1,6	5,6	0,8	4,7	0,9	2,6	0,4	2,6	0,4	5	0,6	77	0,1	12	b.d.	7,8	2,2	b.d.	b.d.	b.d.	b.d.	b.d.	b.d.	b.d.
b.d.	b.d.	b.d.	2	0,6	2,5	26	55	7,1	29	6,5	1,5	5,4	0,8	4,6	0,9	2,7	0,4	2,4	0,4	4,8	0,6	93	0,2	13	b.d.	7,8	2,2	b.d.	b.d.	b.d.	b.d.	b.d.	b.d.	b.d.
3	1	b.d.	3	0,8	5,3	40	85	11	44	8,5	1,6	7,4	1,1	6,4	1,2	3,7	0,5	3,5	0,5	7,6	0,9	76	0,4	18	b.d.	15	4,2	b.d.	b.d.	b.d.	b.d.	b.d.	b.d.	b.d.
3	0,9	b.d.	3	0,8	3,3	40	84	11	44	8,9	1,6	7,5	1,1	6,4	1,3	3,8	0,6	3,4	0,5	7,8	0,8	3	0,4	18	b.d.	14	4,1	b.d.	b.d.	b.d.	b.d.	b.d.	b.d.	b.d.
3	1	b.d.	3	0,7	5,4	40	86	11	43	8,7	1,7	7,7	1,1	6,2	1,2	3,7	0,5	3,5	0,5	8	0,9	140	0,4	20	b.d.	14	4,1	b.d.	b.d.	b.d.	b.d.	b.d.	b.d.	b.d.
b.d.	b.d.	b.d.	2	0,5	3,1	23	46	5,9	24	5	1,3	4,4	0,6	3,8	0,8	2,3	0,4	2,1	0,3	3,9	0,5	86	0,3	12	b.d.	7	2,1	b.d.	b.d.	b.d.	b.d.	b.d.	b.d.	b.d.
b.d.	b.d.	b.d.	1	b.d.	1	12	25	3,2	15	3,2	1	2,7	0,4	2	0,4	1,1	0,2	1,1	0,2	1,6	0,1	b.d.	b.d.	8	b.d.	3	1	1	b.d.	b.d.	b.d.	b.d.	2	b.d.
b.d.	b.d.	b.d.	1	b.d.	1,2	12	26	3,6	16	3,5	1,1	3,1	0,4	2,4	0,4	1,2	0,2	1	0,2	2	0,1	b.d.	b.d.	11	b.d.	3,4	1,1	1	b.d.	b.d.	b.d.	b.d.	b.d.	b.d.
b.d.	b.d.	b.d.	b.d.	b.d.	1,2	13	27	3,9	18	4,3	1,2	4,4	0,7	3,9	0,8	2,3	0,3	2,2	0,3	2,2	0,1	b.d.	b.d.	6	b.d.	2,5	0,8	b.d.	b.d.	b.d.	b.d.	b.d.	b.d.	b.d.
b.d.	b.d.	b.d.	1	0,7	2	14	32	4,6	22	5,3	1,7	5,7	0,9	5,1	1,1	3,2	0,5	3,1	0,5	3,1	0,2	1	b.d.	11	b.d.	2,6	0,9	b.d.	b.d.	b.d.	b.d.	b.d.	b.d.	b.d.
b.d.	b.d.	b.d.	2	0,8	1,9	14	33	4,8	23	5,9	1,8	6	0,9	5,6	1,1	3,2	0,5	3	0,4	2,8	0,2	b.d.	b.d.	11	b.d.	2,5	0,9	b.d.	b.d.	b.d.	b.d.	b.d.	b.d.	b.d.
b.d.	b.d.	b.d.	1	0,8	1,9	14	33	4,8	23	5,9	1,8	6,1	0,9	5,5	1,1	3,3	0,5	3	0,5	2,9	0,1	b.d.	b.d.	12	b.d.	2,4	0,9	b.d.	b.d.	b.d.	b.d.	b.d.	b.d.	b.d.